Determining the innermost structure of quasars by microlensing: Measuring, simulating and interpreting light curves of multiple quasars

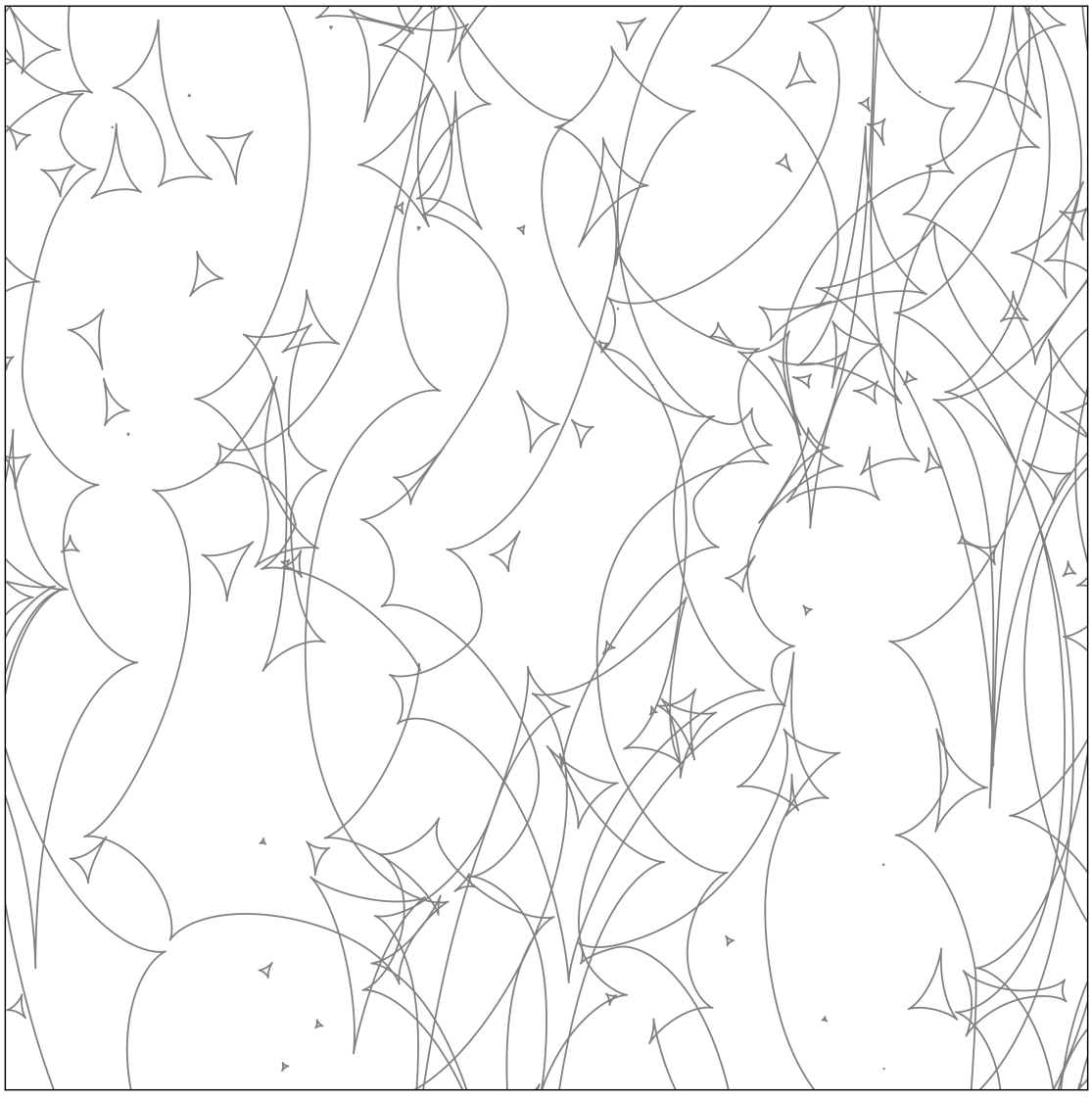

Christian Matthias Sorgenfrei

cover image: $10\,R_{\rm E} \times 10\,R_{\rm E}$ of microlensing caustics for image B of HE0435-1223

Dissertation

submitted to the

Combined Faculty of Mathematics, Engineering and Natural Sciences

of the Ruprecht-Karls-Universität Heidelberg

for the degree of

Doctor of Natural Sciences

Put forward by

CHRISTIAN MATTHIAS SORGENFREI

born in Freiburg im Breisgau, Germany

Oral examination: 29 January 2026

Determining the innermost structure of quasars by microlensing: Measuring, simulating and interpreting light curves of multiple quasars

Referees: Prof. Dr. Joachim Wambsganß
Prof. Dr. Christian Fendt

Für Annette und Matthias,
die mir ihre Begeisterung für Physik weitergegeben haben.

Abstract

This thesis aims at measuring quasar microlensing light curves and applying them to constrain the structure of quasar accretion disks. Thus, data was taken in two photometric filters at the Las Cumbres Observatory, using their global network of 1 m telescopes since 2014. In the first part, applying difference imaging analysis together with point spread function photometry aided with *Gaia* data, we measure the light curves of the multiple images of eight gravitationally lensed quasars in the R and V band, covering almost ten years with in total 1872 epochs. For each quasar, we determine difference curves of the time delay corrected light curves. This removes the intrinsic quasar brightness variations present in all images with only uncorrelated microlensing variability of the individual images remaining. We find these additional variations, attributed to the source size depended microlensing of the individual images by compact objects in the lens galaxy, throughout our whole data set.

For the second part of this thesis, we focus on the prominent microlensing signal in image B of the quadruple quasar HE0435-1223, revealed through our difference curves. The variations appear to be chromatic, i.e. depend on the filter, with higher amplitude fluctuations in the V band. This is expected, since the hotter central region of the accretion disk experiences more microlensing variation due to its smaller size. To quantify this observation, by means of microlensing simulations, we are able to infer that the accretion disk of HE0435-1223 is indeed larger in radius by factors of $1.24^{+0.08}_{-0.20}$, $1.42^{+0.11}_{-0.22}$ and $1.43^{+0.10}_{-0.23}$ in the R with respect to the V band, depending on the disk model, in agreement with the expectation from thin accretion disk theory, though with a tendency towards a shallower temperature profile. Additionally, we find disk half-light radii of 0.7 to 1.0 Einstein radii, corresponding to average inclined disk scale radii of around $\log \langle R_{2500}/\mathrm{cm} \rangle \simeq 16.4^{+0.5}_{-0.7}$ at 2500 Å in the quasar rest-frame.

Zusammenfassung

Ziel dieser Arbeit ist es Lichtkurven von gelinsten Quasaren zu messen und diese für Rückschlüsse auf deren Akkretionsscheiben zu verwenden. Hierfür wurden Daten in zwei Filtern mit 1 m Teleskopen des Las Cumbres Observatoriums seit 2014 erhoben. Im ersten Teil der Arbeit werden mittels Differenzbildanalyse, Photometrie mit Punktbildfunktionen und *Gaia* Daten somit die Lichtkurven der Mehrfachbilder von acht solcher gravitativ gelinsten Quasaren im R und V Filter bestimmt, die sich über beinahe 10 Jahre erstrecken. Für jeden Quasar werden Differenzkurven der Lichtkurven berechnet, da dies jene Helligkeitsveränderungen entfernt, welche vom Quasar selbst stammen. Somit bleiben nur zwischen den einzelnen Quasarbildern unkorrelierte Veränderungen übrig. Wir finden diese zusätzlichen Variationen, die dem quasaren Mikrolinseneffekt (ausgelöst durch Sterne in der Linsengalaxie) zugeschrieben werden können, in unserem gesamten Datensatz.

Im zweiten Teil widmen wir uns den Differenzkurven des Vierfachquasars HE0435-1223, insbesondere Bild B, in dem unsere Daten ein deutliches Mikrolinsensignal zeigen, welches chromatisch ist, d.h. vom Filter abhängt. Wie erwartet finden wir stärker ausgeprägte Helligkeitsveränderungen im V Filter, da der Mikrolinseneffekt für kleinere Quellen – wie dem heißen zentralen Teil der Scheibe – stärker ist. Um diese Beobachtung zu quantifizieren führen wir Mikrolinsensimulationen durch, aus denen wir schließen können, dass die Akkretionsscheibe von HE0435-1223 im R Filter tatsächlich (je nach Model) vom Radius 24% bis 43% größer ist. Dies stimmt mit dem theoretisch erwarteten Größenunterschied einer dünnen Standardmodelscheibe überein, tendiert jedoch leicht zu einem flacheren Temperaturprofil. Zusätzlich messen wir Scheibenhalblichtradien von 0.7 bis 1.0 Einsteinradien, was ungefähr einem Skalenradius $\log \langle R_{2500}/\mathrm{cm} \rangle \simeq 16.4^{+0.5}_{-0.7}$ bei 2500 Å im Ruhesystem des Quasars entspricht.

Contents

List of Figures

List of Tables

1. Fundamentals of quasar microlensing

According to Einstein's famous equation $E = mc^2$, even small mass objects contain enormous amounts of energy. However, this energy cannot easily be extracted. While typical chemical reactions release just tiny fractions of it (around $\sim \mathrm{eV}/(uc^2) \simeq 10^{-9}$ for typical binding energies and atomic masses u), nuclear fission and even more so nuclear fusion of elements in stars can release significant amounts of energy (around 0.7% from hydrogen via the proton-proton chain, see e.g. Frank et al. 2002). Gravity however can accomplish more. As objects with mass m are falling in a gravitational field towards the central mass M with radius R, they convert their potential into kinetic energy, which can be released by collisions with other objects, thus heating up the material and radiating away energy ΔE_{acc}. This phenomenon is called accretion, and, to simplify, using Newtonian physics (assuming a full conversion of the potential energy) gives

$$\Delta E_{\mathrm{acc}} = GMm/R. \tag{1.1}$$

Thus, if M/R of the central object is large, so is ΔE_{acc}. Naturally, ideal objects that come to mind due to their large and compact mass are black holes. From a simplified estimate, inserting the Schwarzschild radius $2GM/c^2$ of a black hole for R, it follows that half of the in-falling object's rest mass would be released. However, including relativistic corrections and instead using the innermost stable circular orbit for R, estimates vary but generally are around $0.06\,mc^2 \lesssim \Delta E_{\mathrm{acc}} \lesssim 0.42\,mc^2$ depending on the rotation of the black hole and additional assumptions (Thorne 1974; Rees 1984; Laor & Netzer 1989; Frank et al. 2002).

This is the process at work in the center of quasars, where matter is accreted onto the central black hole in a disk, and thus is releasing these enormous amounts of energy resulting in the brightest observable sources in the universe (Frank et al. 2002; Padovani et al. 2017). As discussed in the next section, much knowledge has already been accumulated about the general structure of these objects, though obtaining direct and firm constraints on them remains challenging, since the central quasar regions are not resolved. Different techniques have been employed to gain

insights (e.g. reverberation mapping; see Horne et al. 2021 and references therein). However, in this work, we employ the power of *quasar microlensing* to 'zoom' into the central quasar structure (see e.g. Schneider et al. 2006; Schmidt & Wambsganss 2010; Vernardos et al. 2024, for comprehensive reviews), for which we go through the necessary fundamentals in this chapter. Altogether, the thesis is structured as follows:

After summarizing here in Chapter 1 the – for this work – necessary fundamentals of quasars and their structure with a focus on accretion disks, as well as gravitational lensing and their combination, i.e. quasar microlensing, we come to Part I, focusing on measuring quasar light curves. There, we start with an overview of the eight quasars that have been observed within a survey specifically designed for our purposes (Chapter 2), describe the data reduction in detail (Chapter 3), present and discuss our quasar light curves (Chapter 4), as well as the resulting difference curves unveiling microlensing variations in our data (Chapter 5).

In Part II we turn to our promising data of the quadruple quasar HE0435-1223 and conduct a microlensing analysis to draw conclusions on its accretion disk. This analysis consists of our microlensing simulations to fit the data (Chapter 6) and the subsequent analysis, with interpretation and discussion of the results (Chapter 7). Finally, we summarize and conclude this thesis with Chapter 8.

1.1. Quasars

Quasars are among the brightest objects in the universe, radiating with luminosities of up to $\sim 10^{41}$ W emitted over the full range of the electromagnetic spectrum from the radio to γ-rays. In the current understanding, the source of this enormous energy release is a central super massive black hole (SMBH, $M \gtrsim 10^6\,\mathrm{M}_\odot$) accreting matter as discussed above (see e.g. Netzer 2015; Padovani et al. 2017).

Since the discovery of the first quasar 3C 273 by Schmidt (1963), who observed such a *quasi-stellar radio source* at significant redshift, the field studying these quasi-stellar objects (QSOs) and related targets grew strongly. They are found in large numbers as bright compact sources at the centers of overshone host galaxies and are located at large cosmic distances with high redshifts (in a few examples up to or even more than $z \simeq 7$) and for instance play an important role in the evolution and growth of (their host) galaxies (Urry & Padovani 1995; Bower et al. 1998; Di Matteo et al. 2005). As, compared to the larger distance, their size (depending on the specific part of a quasar's structure) is only on the order of $\sim 10^{13}$ to 10^{20} cm (ranging from below mere light days to a few parsec; see e.g. Frank et al. 2002; Netzer 2015), these objects are largely unresolved and appear as point sources in observations.

In today's picture, i.e. the 'unified AGN model' (Antonucci 1993; Urry & Padovani 1995), quasars are part of the larger class of active galactic nuclei (AGN), including e.g. also radio-quiet quasars, Seyfert galaxies, radio galaxies and others. In this model, these objects with (in part) different observed properties, have essentially a shared overall structure, however observed at different viewing angles (see also e.g. Netzer 2015; Padovani et al. 2017 and references therein for more details). In this framework, the structure of AGNs can generally be described as follows (see e.g. Fig. 7.2 in Frank et al. 2002 and especially Fig. 3 in Vernardos et al. 2024 for detailed depictions of the following structures).

In the center, the already mentioned SMBH has formed an accretion disk extending from around its innermost stable circular orbit at around $\sim 10^{13}$ cm emitting from the X-ray, outwards to $\sim 10^{16}$ cm radiating in the UV and optical (see Sect. 1.2). Additionally, surrounding the black hole is a X-ray corona, and perpendicular to the accretion disk (for radio loud AGNs), large jets originate from the black hole. The spectra of quasars also contain broad emission features resulting from the broad line region (BLR) consisting of high-velocity (leading to the broadening) dense gas clouds ionized by radiation from the accretion disk. At the outer parts surrounding the accretion disk, a dusty torus at ~ 0.1 to around 10 parsec, can obscure emission of the more central structures depending on the observing angle (though not for the more face-on quasars). Above and outside this region, the narrow line region (NLR) is located with ionized lower density and low velocity gas clouds adding narrow emission lines (again, we refer to Antonucci 1993; Urry & Padovani 1995; Netzer 2015; Padovani et al. 2017 and others for comprehensive overviews on AGN structure). In the rest-frame of a quasar, its emission in the UV and optical is dominated by the emission of the accretion disk (see also e.g. Vernardos et al. 2024). Therefore, observing at the corresponding wavelengths (depending on the quasars redshift), one can study this inner structure, which is the component of quasars this works focuses on.

1.2. Shakura-Sunyaev thin accretion disk model

For the rest of this thesis we will focus solely on parts of the innermost structure of quasars, i.e. their accretion disks powered by the central SMBH. Therefore, here we go through the later needed theoretical aspects of quasar accretion disks, mainly their temperature and brightness profile, as well as their size.

In their pioneering work, Shakura & Sunyaev (1973) introduced a theoretical model for a geometrically thin (but optically thick) viscous disk, accreting matter at a mass rate $\dot{M}$ onto the central massive object with mass M (in the case of quasars a SMBH),

which has since become a widely used model for accretion disks in general including for quasars. For the details on the calculations we refer to their publication, as well as e.g. to the textbook by Frank et al. (2002), but in the end, this thin disk model predicts a temperature profile of the accretion disk (i.e. temperature as a function of radius r of a circular symmetric disk) following

$$T(r) = \left(\frac{3GM\dot{M}}{8\pi\sigma r^3} \left[1 - \sqrt{\frac{r_{\rm in}}{r}} \right] \right)^{1/4} , \tag{1.2}$$

where G is the gravitational constant and σ is the Stefan-Boltzmann constant. This profile can be simplified for sufficiently large radii $r \gg r_{\rm in}$ far outside the disk's inner edge at $r_{\rm in}$ (i.e. ignoring the inner cut-off term in square-brackets by setting $r_{\rm in} = 0$, as well as different regimes, where this is result takes on modified forms as depicted in Fig. 12 of Shakura & Sunyaev 1973) to the power-law

$$T(r) \propto r^{-\beta} \quad \text{with} \quad \beta = 3/4. \tag{1.3}$$

Here we have introduced the general (negative) temperature profile slope β for later reference, as some alternative or modified accretion disk models (see e.g. the slim disk model by Abramowicz et al. 1988, models like Novikov & Thorne 1973 including relativistic effects, or magnetic stress at the inner edge as in Agol & Krolik 2000, or wind models such as Li et al. 2019, and many more; see Sect. 2.9.2 of Vernardos et al. 2024 for an overview) predict values deviating from $\beta = 3/4$ of the thin disk model by Shakura & Sunyaev (1973) in both directions (corresponding to steeper $\beta > 3/4$ or shallower $\beta < 3/4$ temperature profiles; see e.g. Cornachione & Morgan 2020).

From this temperature profile, an according brightness profile for thermally radiating accretion disks can be derived. Introducing a scale radius r_s, at which the disk temperature $T(r_s)$ is equal to $T_0 := hc/(k_B\lambda_0)$ for some reference wavelength λ_0 (with the speed of light c, the Planck constant h and the Boltzmann constant k_B), the thin disk temperature profile from Eq. 1.3 becomes $T(r) = T_0(r/r_s)^{-3/4}$. Moreover, assuming that the disk radiates as a black body $B_\lambda(\lambda, T)$ with temperature $T = T(r)$ at each annulus r according the temperature profile, we arrive at a spectral radiance (in $\mathrm{W\,m^{-2}\,sr^{-1}\,\mathring{A}^{-1}}$) in terms of emitted wavelengths λ over the extend of the disk:

$$B_\lambda(\lambda, r) := B_\lambda(\lambda, T(r)) = \frac{2hc^2}{\lambda^5} \left[\exp\left(\frac{\lambda_0}{\lambda} \left(\frac{r}{r_s} \right)^{3/4} \right) - 1 \right]^{-1} . \tag{1.4}$$

Observing such a disk through a photometric filter, thus integrating $B_\lambda(\lambda, r)$ over the filter transmission profile (with a central filter wavelength λ_c corresponding to a rest-frame wavelength of λ_0), leads to a brightness profile $B(r)$ as measured in that

filter. Assuming the filter width to be small $\Delta\lambda \ll \lambda_c$, effectively measuring only at one wavelength and thus $B(r) \simeq B_\lambda(\lambda_0, r)\Delta\lambda$, results in the disk's brightness profile:

$$B(r) = \frac{2hc^2\Delta\lambda}{\lambda_0^5}\left[\exp\left(\left(\frac{r}{r_s}\right)^{3/4}\right) - 1\right]^{-1}, \tag{1.5}$$

i.e. power radiated away into a solid angle per disk area at a to the filter corresponding rest-frame wavelength of λ_0.

To determine the size of the before introduced scale radius r_s, comparing the original temperature profile from Eq. 1.2 (again ignoring the inner edge), with the reduced form from above (i.e. $T(r) = T_0(r/r_s)^{-3/4}$), results in an explicit relation between T_0 and r_s in terms of the physical constants from Eq. 1.2. Furthermore, expressing T_0 in terms of λ_0 according to its definition above and inserting the Stefan-Boltzmann constant $\sigma = 2\pi^5 k_B^4/(15h^3c^2)^{-1}$, we find for the size of the scale radius

$$r_s = \left(\frac{45GM\dot{M}\lambda_0^4}{16\pi^6 hc^2}\right)^{1/3} \simeq 9.7{\cdot}10^{15}\,\mathrm{cm} \times \left(\frac{\lambda_0}{\mu\mathrm{m}}\right)^{4/3} \times \left(\frac{M}{10^9 M_\odot}\right)^{2/3} \times \left(\frac{L}{\eta L_\mathrm{E}}\right)^{1/3}, \tag{1.6}$$

which again is the disk size, where the temperature matches the rest-frame wavelength λ_0.[1] Most importantly for this work, we note that the size of the thermally emitting accretion disk of quasars following Eq. 1.6 thus depends on the central filter wavelength $\lambda_c = \lambda_0(z_\mathrm{S} + 1)$, including the redshift z_S of the source[2], according to

$$r_s \propto \lambda_c^{4/3}, \tag{1.7}$$

which can also directly be seen by applying Wien's law to Eq. 1.3. This dependence of the observed size of the accretion disk on the used photometric filter is one of the main targets of interest for this thesis.

Finishing this section on the model by Shakura & Sunyaev (1973), the brightness profile can be used to determine the luminosity of thin quasar accretion disks, which can be converted to an estimate of the scale size based on an observed luminosity. Therefore, the brightness profile in Eq. 1.5 is integrated over the extent of the disk (and solid angle) to find the disk's luminosity in the quasar rest-frame.[3] We then

[1] We additionally have inserted typical values in the second part of Eq. 1.6, having introduced the luminosity L in units of the Eddington luminosity $L_\mathrm{E} = 4\pi GMm_\mathrm{p}c/\sigma_\mathrm{T}$ (with the proton mass m_p and Thomson scattering cross-section σ_T), as well as the accretion disk efficiency $\eta = L/(\dot{M}c^2)$, to get an order of magnitude estimate (see Poindexter & Kochanek 2010a; Morgan et al. 2010).

[2] For aspects on cosmology we refer e.g. to Bartelmann (2019).

[3] This results in $L \simeq 2.58 \times 16\pi^2 r_s^2 hc^2\Delta\lambda/\lambda_0^5$ (the numerical factor comes from the r-integration; see e.g. Kochanek 2004), generating a flux $F = L\lambda_0^2/(4\pi c D_\mathrm{S}^2)$, with the angular diameter distance to the source D_S, as well as switching from wavelength to frequency-space. Here, typically D_S is given in Hubble radii $r_H = c/H_0$, with $H_0 = 70.0\,\mathrm{km\,s^{-1}\,Mpc^{-1}}$; see footnote 2.

express the resulting flux in magnitudes m and introduce typical reference values. Thus, similarly as in e.g. Morgan et al. (2010) and Vernardos et al. (2024), including the disk's inclination i (to correct for general disk orientations; $i = 90°$ means face-on) and the source redshift, we arrive at the luminosity-based scale size

$$r_s \simeq \frac{4.9 \cdot 10^{15}\,\mathrm{cm}}{\sqrt{\cos(i)}} \times \left(\frac{\lambda_c}{\mu\mathrm{m}}\right)^{3/2} \times \left(\frac{zpt}{3631\,\mathrm{Jy}}\right)^{1/2} \times \frac{D_\mathrm{S}}{r_H} \times 10^{-0.2(m-19)}, \tag{1.8}$$

where zpt is the zero-point of the magnitude system in Jansky. Let us mention already at this point, that it turns out that measurements of the accretion disk size of quasars inferred from microlensing simulations using brightness profiles such as the one introduced here with Eq. 1.5 – which is the approach we will follow in Part II of this thesis – are systematically and consistently larger than luminosity-based disk size estimates from Eq. 1.8, with possible solutions including changing the temperature profile from Eq. 1.3 to smaller β values (see e.g. Morgan et al. 2010, 2018; Cornachione & Morgan 2020, and our analysis and discussion in Chapter 7).

1.3. Gravitational lensing: strong and micro

The history of gravitational lensing – maybe surprisingly – had started *before* Albert Einstein finished his General Theory of Relativity (GR) in 1915. Estimates by Johann von Soldner (1804) treating light as test particle in the Newtonian equations, as well as later by Einstein (1911) using his Special Theory of Relativity already resulted in *half* of the correct deflection angle $\hat{\alpha}$ by which the direction of the trajectory of light passing by a mass M at a distance ξ is changed, which is given by

$$\hat{\alpha} = \frac{4GM}{c^2\xi} \tag{1.9}$$

as calculated with GR (Einstein 1916). Inserting the mass and radius of the sun gives a deflection angle of 1.75 arcsec as confirmed by Arthur Eddington's famous solar eclipse expedition in 1919 (Dyson et al. 1920).

Further developments included e.g. investigations into the magnification of a background by a foreground star, with the background star lensed into a luminous ring (today 'Einstein ring') or split into two images depending on the exact configuration of the system (Einstein 1936), as well as the application of this idea to galaxies acting as lenses by Fritz Zwicky (1937a,b). Developing this idea further, one sees that quasars as introduced in Sect. 1.1 can then be lensed into multiple images as well, if (from our point of view) situated behind one such lens galaxy (see e.g. the comment

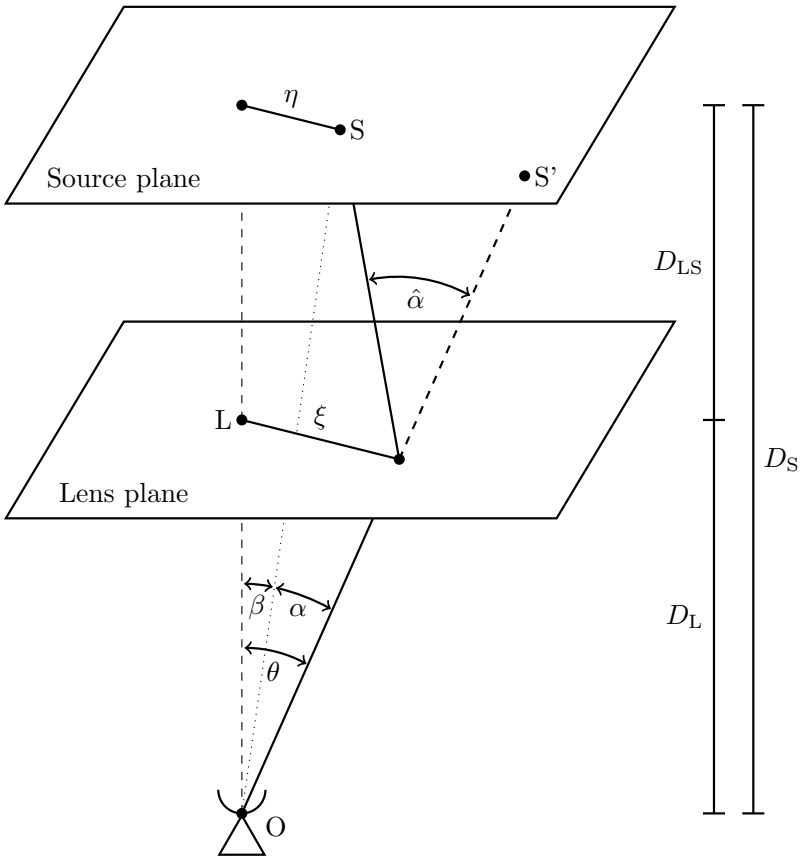

Figure 1.1.: Simplified diagram of gravitational lensing (reproduced from Bartelmann & Schneider 2001 and adapted orientating on Schmidt & Wambsganss 2010) to derive the lens equation, following the description in the main text.

at the end of Refsdal 1964), which was confirmed by the discovery of the double quasar Q0957+561 (Walsh et al. 1979). For more detailed and in-depth overviews on these and additional aspects of the history and fundamentals of gravitational lensing we refer to Schneider et al. (2006) and Schmidt & Wambsganss (2010), which most of the following introduction in this section is based on (see also e.g. Bartelmann & Schneider 2001 and Saha et al. 2024).

The deflection of light by the point mass M from Eq. 1.9 needs generalization for extended sources without circular symmetry (see e.g. Bartelmann & Schneider 2001), which we include later. We further assume that all relevant deflections can be thought to happen in one plane between source and observer (i.e. we use the so-called 'thin lens approximation'), while in principle all matter and energy in the vicinity of the light's path from source to observer contributes.

The resulting general lensing situation is sketched in Fig. 1.1, describing the propagation of light originating from a source S at β (which should actually be two-dimensional angular coordinates; see e.g. Bartelmann & Schneider 2001 and Schneider et al. 2006) relative to the lens L deflecting it (according to Eq. 1.9) and thus

reaching the observer O from direction θ creating there the image S' of S. Introducing the angular diameter distances D_S, D_L, and D_LS from observer to source, observer to lens, as well as lens to observer (see footnote 2), we find from Fig. 1.1:

$$\theta D_\mathrm{S} = \beta D_\mathrm{S} + \hat{\alpha} D_\mathrm{LS} \tag{1.10}$$

assuming small deflection angles $\hat{\alpha} \ll 1$ (valid for all astrophysical purposes). Introducing the reduced deflection angle $\alpha(\theta) := (D_\mathrm{LS}/D_\mathrm{S})\hat{\alpha}(\xi)$ with $\xi = D_\mathrm{L}\theta$ (Fig. 1.1) we find the 'lens equation':

$$\beta(\theta) = \theta - \alpha(\theta), \tag{1.11}$$

which, by inserting α and Eq. 1.9 becomes $\beta(\theta) = \theta - \theta_\mathrm{E}^2/\theta$, where we have introduced the Einstein angle

$$\theta_\mathrm{E} = \sqrt{\frac{4GM}{c^2}\frac{D_\mathrm{LS}}{D_\mathrm{L} D_\mathrm{S}}}, \tag{1.12}$$

i.e. the angular radius of the luminous ring mentioned before emerging in the perfectly symmetric situation $\beta = 0$ (see Eq. 1.11). Inserting typical redshifts for source z_S and lens z_L (i.e. of quasars behind lens galaxies such as the ones we will focus on, see Table 2.1, and converting them to angular distances using a cosmological model), as well as the mass M of a massive galaxy into Eq. 1.12, leads to Einstein angles on the scale of $\theta_\mathrm{E} \sim \sqrt{M/(10^{12} M_\odot)}$ arcsec (see e.g. Schmidt & Wambsganss 2010), corresponding to typical separations of quasar images. This is the so-called 'strong lensing' regime. While for a stellar lensing scenario (gravitational lensing by stars with $M \simeq M_\odot$ in a lens galaxy additionally lensing a quasar image) we find $\theta_\mathrm{E} \sim 10^{-6}\sqrt{M/M_\odot}$ arcsec, i.e. deflections on the order of *micro*arcseconds, eponymous for 'microlensing'. This (Eq. 1.12 in general) can be converted to a distance in the source plane to find the 'Einstein radius' $R_\mathrm{E} = D_\mathrm{S}\theta_\mathrm{E}$, which we will use a lot especially in Part II of this thesis (see e.g. Eq. 6.1 for the microlensing Einstein radius central for our analysis).

Generally, following Schneider et al. (2006), extending to non-symmetric systems and thus switching to two-dimensional notation (as already indicated in Fig. 1.1), as well as considering an extended lens (essentially elevating Eq. 1.9 to an integral including the surface mass density Σ of the lens)[4], the lens equation (Eq. 1.11) becomes

$$\boldsymbol{\beta} = \boldsymbol{\theta} - \boldsymbol{\nabla}\psi, \tag{1.13}$$

where we have introduced the deflection potential $\psi(\boldsymbol{\theta}) = \pi^{-1} \int d^2\boldsymbol{\theta}' \kappa(\boldsymbol{\theta}') \ln|\boldsymbol{\theta} - \boldsymbol{\theta}'|$,

[4] To be more precise, the deflection angle becomes $\hat{\boldsymbol{\alpha}}(\boldsymbol{\xi}) = 4G/c^2 \int d^2\boldsymbol{\xi}' \Sigma(\boldsymbol{\xi}')(\boldsymbol{\xi} - \boldsymbol{\xi}')/|\boldsymbol{\xi} - \boldsymbol{\xi}'|^2$, where $\boldsymbol{\xi}$ is the now two-dimensional coordinate in the lens plane (see Fig. 1.1). In this generalized expression, instead of the lens mass M, the surface mass density $\Sigma(\boldsymbol{\xi}) = \int dz \rho(\boldsymbol{\xi}, z)$ appears, where z is the direction perpendicular to the lens plane and ρ is the mass density of the lens.

which generates the two-dimensional reduced deflection angle $\boldsymbol{\alpha}(\boldsymbol{\theta}) = \boldsymbol{\nabla}\psi$. Here we also have introduced the convergence $\kappa(\boldsymbol{\theta}) = \Sigma(D_\mathrm{L}\boldsymbol{\theta})/\Sigma_\mathrm{cr}$, i.e. the surface mass density normalized by the critical surface mass density $\Sigma_\mathrm{cr} = \frac{c^2}{4\pi G}\frac{D_\mathrm{S}}{D_\mathrm{L}D_\mathrm{LS}}$. From this version of the lens equation and deflection potential, one can arrive at other relevant aspects, such as the time delay function $\tau(\boldsymbol{\theta},\boldsymbol{\beta}) = \tau_\mathrm{geom}+\tau_\mathrm{grav}$, which explains the time delay a certain light path from source to observer experiences due to the geometry of the system τ_geom, as well as the gravitational Shapiro delay τ_grav,[5] but we refer to the aforementioned reviews for the details.

Continuing with this generalized version of the lens equation, the Jacobian matrix of the lens mapping is given by

$$\mathcal{A}(\boldsymbol{\theta}) = \frac{\partial\boldsymbol{\beta}}{\partial\boldsymbol{\theta}} = \left(\delta_{ij} - \frac{\partial^2\psi(\boldsymbol{\theta})}{\partial\theta_i\partial\theta_j}\right)_{(i,j)} = \begin{pmatrix} 1-\kappa-\gamma_1 & -\gamma_2 \\ -\gamma_2 & 1-\kappa+\gamma_1, \end{pmatrix} \tag{1.14}$$

with the components of the so-called shear $\gamma = \sqrt{\gamma_1^2+\gamma_2^2}$, with $\gamma_1 = (\psi_{,11}-\psi_{,22})/2$, $\gamma_2 = \psi_{,12} = \psi_{,21}$ and similarly $\kappa = (\psi_{,11}+\psi_{,22})/2$ for the already introduced convergence, where $\psi_{,ij} = \partial^2\psi(\boldsymbol{\theta})/(\partial\theta_i\partial\theta_j)$ was used as short-hand. The inverse of the determinant of the Jacobian gives the magnification of the source

$$\mu = \frac{1}{\det\mathcal{A}(\boldsymbol{\theta})} = \frac{1}{(1-\kappa)^2-\gamma^2}. \tag{1.15}$$

Here, 'critical curves', i.e. lines in the lens plane at which the magnification is (formally) infinite, are found at $\det\mathcal{A}(\boldsymbol{\theta}) = 0$. For later reference, mapping them with the lens equation into the source plane, one finds the corresponding so-called 'caustics'.

To finish this introduction into the basics of gravitational lensing, when observing targets (such as quasars) lensed by a foreground galaxy, their light experiences shear and convergence from the lens galaxy. The latter is typically modeled by the resulting convergence of smooth matter κ_smooth, i.e. from the lens galaxies dark matter halo. Additionally, the source's light is microlensed by all compact objects (such as stars) in the vicinity to its light path, i.e. these objects are acting as additional convergence of $\kappa_\star$ on the source light. The total convergence is then given by $\kappa = \kappa_\star + \kappa_\mathrm{smooth}$. Combining the previous steps, we find the form of the lens equation in the case of a large number N of compact objects with masses m_i situated at $\boldsymbol{\theta}_i$ in the lens plane that are generating the additional microlensing with convergence $\kappa_\star$ on top of the

[5] This gives rise to the time delays between the multiple images of the strongly lensed quasars, e.g. $\Delta t_\mathrm{AB} = \tau(\boldsymbol{\theta}_\mathrm{A},\boldsymbol{\beta}) - \tau(\boldsymbol{\theta}_\mathrm{B},\boldsymbol{\beta})$ for two images A and B (see Sect. 1.4 and Table 2.1), with $\tau(\boldsymbol{\theta},\boldsymbol{\beta}) = (1+z_\mathrm{L})D_\mathrm{L}D_\mathrm{S}/(cD_\mathrm{LS})[(\boldsymbol{\theta}-\boldsymbol{\beta})^2/2-\psi(\boldsymbol{\theta})]$, where the Fermat potential in square-brackets has vanishing gradient equivalent to the lens equation (Eq. 1.13) and z_L is the lens' redshift.

lensing of their host galaxy with convergence $\kappa_{\rm smooth}$ and shear γ as:

$$\boldsymbol{\beta} = \begin{pmatrix} 1-\kappa_{\rm smooth}-\gamma_1 & -\gamma_2 \\ -\gamma_2 & 1-\kappa_{\rm smooth}+\gamma_1, \end{pmatrix} \boldsymbol{\theta} - \frac{D_{\rm LS}}{D_{\rm L} D_{\rm S}} \frac{4G}{c^2} \sum_{i=1}^{N} \frac{m_i(\boldsymbol{\theta}-\boldsymbol{\theta}_i)}{|\boldsymbol{\theta}-\boldsymbol{\theta}_i|^2}. \quad (1.16)$$

Here, essentially the first term gives the linearized contribution of strong lensing via $\mathcal{A}\cdot\boldsymbol{\theta}$, as the N microlenses are in the vicinity of the strong lensing light path, and the second term includes the additional effect from these microlenses. Again note, that this introduction is based on reviews and such, mostly on Schneider et al. (2006); Schmidt & Wambsganss (2010); Saha et al. (2024); Vernardos et al. (2024) and we refer the reader to these for more details.

Ultimately, gravitational lensing as described here occurs under different circumstances. As already mentioned, through the dependence of the Einstein angle on the square-root of the lenses mass (Eq. 1.12), lensing by objects with stellar masses leads to deflection angles and image separations on the order of microarcseconds, more than challenging to resolve in any context. However, the resulting time-variable (through the relative motion of the different components) source brightness magnification from the unresolved microimages is not only central for microlensing on the extragalactic scale we are interested in (Sect. 1.4), but also for planetary microlensing – a method to detect exoplanets complementary to many other detection methods (see Mao & Paczynski 1991, the first detection by Bond et al. 2004 and e.g. Tsapras 2018) or in general galactic microlensing (e.g. searching for compact dark matter candidates, see Paczynski 1986 and e.g. Wambsganss et al. 2000).

On the other end of the lens mass spectrum is strong lensing, where background objects (such as quasars or galaxies) are lensed by galaxies or even galaxy clusters, leading to multiple images separated on the scale of arcseconds, magnified and deformed in their shape into luminous arcs (Schmidt & Wambsganss 2010). In Fig. 1.2, we show the effect that strong lensing by an elliptical lens (e.g. a galaxy) has on a background source (for our purposes a quasar) located at different positions $\boldsymbol{\beta}$, with four examples, based on Schmidt (2020)[6]. The described effects are apparent, i.e. there are different numbers of (deformed, separated or merging) images depending on the position in the source plane relative to the caustics that are separating areas of different image multiplicity (i.e. crossing them adds or removes two images: compare the blue and the purple source). Observed examples for the depicted four configurations with two to four quasar images can be found e.g. in our data set in Part I of this thesis (see Fig. 2.1).

[6] The lecture notes including `python` codes for figures are available at https://wwwstaff.ari.uni-heidelberg.de/mitarbeiter/rschmidt/papers/Jena_Proceedings_Schmidt.html.

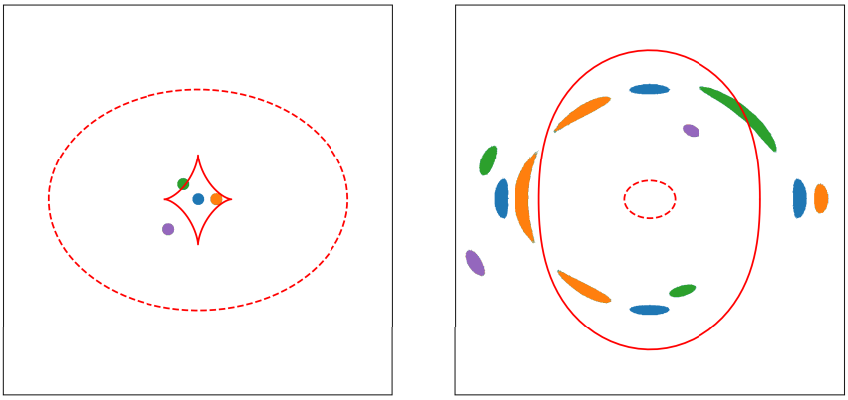

Figure 1.2.: Sources lensed by an elliptical lens. On the left, the source plane with four sources (representing possible quasar positions), as well as the central 'tangential' and the outer 'radial' caustics are depicted (in red) for an elliptical lens (representing a galaxy, located at the center). On the right, the corresponding critical curves are shown together with the different multiple images for each of the four source positions with the four common image configurations – cross (blue), cusp (orange), fold (green; note the two merging images) and double (purple) – which we also see for our targeted quasars in Chapter 2. The Figure was made using `python` code from Schmidt (2020) Fig. 3 (based on Schneider et al. 2006; Narayan & Bartelmann 1996).

To conclude these remarks on strong lensing, not only double or quadruple quasar configurations are possible: SDSS J1004+4112 (with the so far longest time delay of over six years, see Muñoz et al. 2022), a – by a whole galaxy cluster – strongly lensed quasar is visible as four images plus an additional faint fifth image (as theoretically expected by the odd-number theorem, see Burke 1981). Furthermore, even systems with six quasar images have been observed (see e.g. the 'Einstein zigzag lens' from Dux et al. 2025 where one quasar is being lensed into six images by two galaxies at different redshifts). For other aspects such as astrometric microlensing and weak gravitational lensing, however, we refer to the aforementioned reviews. Finally, before continuing in the next section with the one application of strongly lensed quasar we focus on in this work, note that other strong lensing applications will be mentioned at the beginning of Chapter 5.

1.4. Quasar microlensing

Bringing together several aspects from the previous sections, it becomes evident, that strongly lensed quasars offer a method to study their inner structure, i.e. their accretion disk. Here we go through this argument of central importance to this thesis similar as in Sorgenfrei et al. (2025) and refer to the previously mentioned reviews (especially Schmidt & Wambsganss 2010; Vernardos et al. 2024) for further details.

A subset of all quasars are observed as multiply imaged quasars, i.e. they are strongly lensed (Sect. 1.3), since coincidentally, they are located (from an observer's point of view) behind some massive galaxy, which acts as strong gravitational lens. As already mentioned, such a system was first discovered by Walsh et al. (1979) with Q0957+561, a double quasar. Today, more than 230 confirmed lensed quasars are known (Ducourant et al. 2018, see also e.g. footnote 30). By measuring the light curves of their multiple images (i.e. the images brightness with time) and correcting for the time delays of the individual images (Sect. 1.3), two kinds of brightness variations in the images' light curves can be distinguished:

1. There are correlated brightness variations occurring simultaneously in *all* (time delay corrected) images. Therefore, they are intrinsic to the quasar itself, e.g. due to disk instabilities (see e.g. Frank et al. 2002; Vanden Berk et al. 2004).

2. Additional uncorrelated brightness variations can be found in the light curves of the individual images. These therefore cannot originate from the quasar. However, as we are looking at multiple light paths, they can be attributed to individual processes along these individual lines of sight. Thus, they can arise in the lens galaxy, where the individual images' light paths are separated by large distances and therefore are independent (which we will revisit in Sect. 5.1).

While the first kind, i.e. the intrinsic variations, are necessary for measuring time delays (e.g. Kundić et al. 1995; Giannini et al. 2017; Millon et al. 2020a) and thus also for constraining the Hubble constant using time delay cosmography (Refsdal 1964; Kundić et al. 1997; TDCOSMO Collaboration et al. 2025), the second type of brightness variations are the main focus in this work. As described, they are caused by the effect of gravitational lensing by stars (and potentially other compact objects) in the lensing galaxy in the vicinity of the individual quasar images, i.e. their origin is microlensing (Sect. 1.3, especially Eq. 1.16). The brightness variations in time from this 'quasar microlensing' arise through the combination of relative motions of the quasar, the lens galaxy (including its stars), as well as the observer, which combined are acting as time-varying magnifications on the individual images over time scales of weeks, months and years (see e.g. Chang & Refsdal 1979; Schmidt & Wambsganss 2010; Mosquera & Kochanek 2011; Vernardos et al. 2024). This phenomenon of quasar microlensing was detected for the first time in the quadruple quasar Q2237+0305 (Irwin et al. 1989; Corrigan et al. 1991), i.e. the famous 'Einstein Cross' discovered by Huchra et al. (1985), which is also a target in our observation campaign (see Sorgenfrei et al. 2024, and Chapter 2).

The combined effect of microlensing (Sect. 1.3) from many compact objects following Eq. 1.16 can be described by a source plane pattern containing the in position

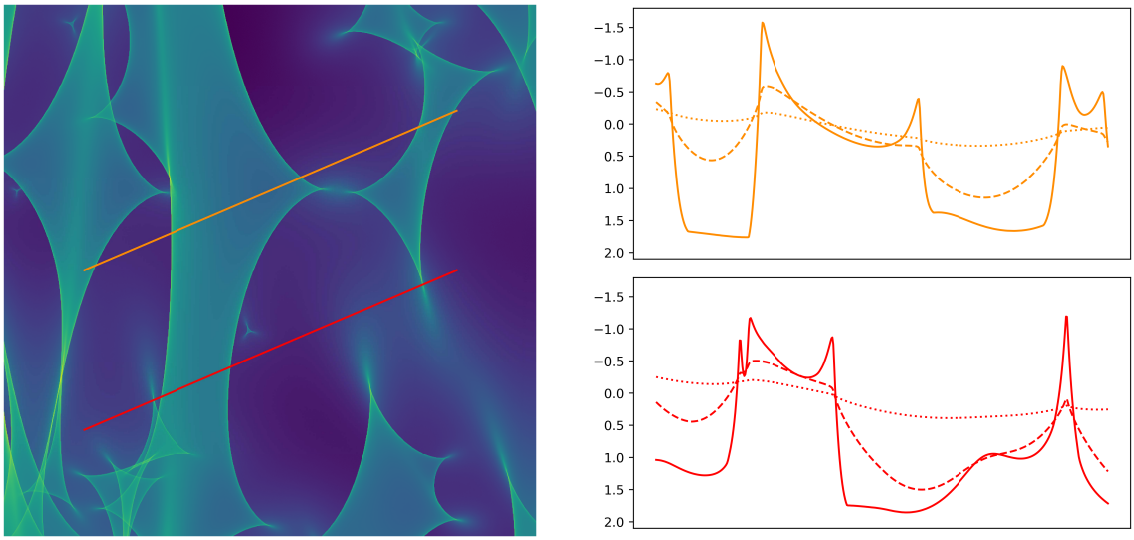

Figure 1.3.: Source size effect on the microlensing signal (inspired from Schmidt & Wambsganss 2010). On the left, $5\,R_\mathrm{E} \times 5\,R_\mathrm{E}$ of a magnification map (i.e. our caustic pattern of HE0435-1223, image B for $\kappa_\star/\kappa = 0.3$; see Chapter 6) is shown, with two example tracks. On the right, the to each track corresponding light curves are shown (in magnitudes over time or distance along the tracks), using three different source sizes (of a thin disk from Eq. 1.5; again, see Chapter 6 for the specifics) with solid, dashed and dotted lines, corresponding to $r_s = 0.01$, 0.1 and $1.0\,R_\mathrm{E}$, respectively.

varying resulting magnification of a point source (e.g. Kayser et al. 1986; Wambsganss et al. 1990, and see the left panel of Fig. 1.3 for such a magnification map), with characteristic caustic lines present throughout the patterns, where formally (again for point sources) the magnification becomes infinite (Eq. 1.15; see also the cover picture of this thesis, where part of caustic pattern used for our analysis is depicted as described in Sect. 7.4). For extended sources, the microlensing signal is given by the averaged magnification values over the extend of the source according to its size and brightness profile. The extended source effectively moves (as described above) through the pattern resulting in varying (size-averaged) magnification values and thus the microlensing-induced light curves, which we demonstrate in Fig. 1.3.[7]

Finally, this dependence on the source size means that the microlensing signals in quasar light curves can be used to infer properties of the structure of quasars, such as the size of their accretion disks, as has been done by e.g. Kochanek (2004); Poindexter & Kochanek (2010a); Morgan et al. (2010, 2018); Cornachione et al. (2020b); Rivera et al. (2024) and others. Therein, disk sizes in scale radii r_s are measured (as introduced in Sect. 1.2), i.e. where the disk's temperature corresponds to the photometric filter (with central filter wavelength λ_c) through which the light curves were observed.

[7] This can be explored *interactively* with 'The Scrolling Infinite Lightcurve' by Robert Schmidt, available at `https://dc.g-vo.org/inflight/res/lc1/ui/fixed` (GAVO Data Center 2007).

As derived in Sect. 1.2, if the thin disk model of Shakura & Sunyaev (1973) applies, $r_s \propto \lambda_c^{4/3}$ (i.e. Eq. 1.7), assuming a thin disk radiating as black body at all radii according to the temperature profile (Eq. 1.3). However, as mentioned, other models could apply, thus also modifying Eq. 1.7. Therefore, and of utmost importance for this project, this (or a corresponding) dependence of the measured size on the used photometric filter means that by observing in multiple bands the temperature profile of the accretion disk (i.e. the slope β in Eq. 1.3) is accessible as well (Wambsganss & Paczynski 1991; Anguita et al. 2008; Eigenbrod et al. 2008a; Poindexter et al. 2008; Mosquera et al. 2009; Cornachione et al. 2020a). In the end, this is what we are most interested in. Consequently, measuring this effect of the accretion disk's temperature profile on the light curves was the main goal of the analysis we conducted (using our own quasar microlensing data from Part I) in Sorgenfrei et al. (2025), which is described in detail in Part II of this thesis.

Part I.

Measuring quasar light curves

2. Overview of the eight quasars observed with LCO

In light of the recent first look event of the *Vera C. Rubin Observatory*, with some first preliminary images released to the public in July 2025[8], a new area for time-domain astronomy has begun. With its Legacy Survey of Space and Time (LSST), which will observe the southern sky for ten years with a cadence of only a few days with the largest camera ever built, an unprecedented number and quality of observations of all kinds of astronomical objects and events that are changing with time in the night sky will be obtained (Bianco et al. 2022). This clearly will have an huge impact on quasar microlensing (amongst many other fields), since not only new gravitationally lensed quasars will be found, but also high quality light curves of more of these systems then ever will be available for analysis. Additionally, since LSST will obtain data in six optical filters (u, g, r, i, z, and y, covering not only the optical, but also small parts of UV and NIR), these light curves will be ideal to investigate the structure of quasar accretion disks using chromatic quasar microlensing (see Ivezić et al. 2019 or e.g. the simulations by Neira et al. 2020, which imply that potentially hundreds of high magnification events will be observed with LSST per year).

Monitoring of lensed quasars has been conducted for quite some time. To name a few examples, there are early observations of the Einstein Cross by Irwin et al. (1989, including the first detection of microlensing), Corrigan et al. (1991) and Ostensen et al. (1996). There is 12 years of V band data of the same system by the Optical Gravitational Lensing Experiment OGLE[9] (Woźniak et al. 2000a; Udalski et al. 2006), as well as published data of three lensed quasars in R and V from MiNDSTEp (i.e. Microlensing Network for the Detection of Small Terrestrial Exoplanets, Giannini et al. 2017; Giannini 2017). A treasure chest is the data set of COSMOGRAIL[10] (i.e. the COSmological MOnitoring of GRAvItational Lenses, Millon et al. 2020a), with 15 years of monitoring in the R band, publishing light curves of the images of 18 quasars.

[8] https://rubinobservatory.org/gallery/collections/first-look-gallery

[9] The OGLE data is available at https://ogle.astrouw.edu.pl/cont/4_main/len/huchra/ including the published data from 1997 on, as well as additional data taken in 2007 and 2008.

[10] https://www.epfl.ch/labs/lastro/scientific-activities/cosmograil/

There are some multi-band observations of the Einstein Cross by Goicoechea et al. (2020), as well as many more observations and published data of individual lensed quasars in various (but mostly single) bands at different epochs.

A survey of multiple quasars to measure microlensing light curves using moderate size robotic telescopes at an existing facility was envisioned by Schmidt & Wambsganss (2010). In the end, this idea became our quasar microlensing program targeting eight gravitationally lensed quasars with the robotic 1 m telescopes of the Las Cumbres Observatory (LCO[11], Brown et al. 2013) starting in 2014, with data taken in two bands in order to be able to detect not only microlensing, but *chromatic* microlensing.

2.1. Las Cumbres Observatory: observing at LCO

As described in Sorgenfrei et al. (2024, 2025), this project utilized R and V band data obtained with LCO, a global network of various robotic telescopes (see Brown et al. 2013). Data of eight lensed quasars – namely HE1104-1805, HE2149-2745, Q2237+0305, HE0435-1223, HE0047-1756, Q0142-100, RXJ1131-1231 and WFI2033-4723 – were taken since 2014 with 1 m telescopes at five locations of LCO, with the majority of observations coming from Cerro Tololo, Chile; but also portions (depending on the quasar) from Sutherland, South Africa; Siding Springs, Australia; McDonald, USA; as well as Teide, Spain.

The 1 m telescopes of LCO are of Ritchey-Chrétien Cassegrain configuration with mounted Sinistro cameras[12]. Their field of view is about 26.5 arcmin×26.5 arcmin with a pixel scale of $s = 0.389$ arcsec/pixel and they have a read-out noise of around 8 e^-, a dark current of 0.002 e^-/pixel/s and a gain of 1.0 e^-/ADU. We use observations with typical exposure times of 180 s. The two filters chosen for our observations are standard R and V band Johnson-Cousins/Bessell filters, with central filter wavelengths and widths of $\lambda_c(R) = 6407$ Å and $\Delta\lambda(R) = 1580$ Å, as well as $\lambda_c(V) = 5448$ Å and $\Delta\lambda(V) = 840$ Å (Bessell 2005 and the information provided by LCO, see footnote 12). More details on the data obtained with LCO will be given in chapter 3.

Before proceeding with an overview of the eight quasars, in Fig. 2.1 we present images of the eight quasars as they appear in our 'best' LCO observations (which are the so-called DIA reference images in R and V from the data reduction in Sect. 3.3, i.e. images combined from multiple low seeing, high S/N observations), to give a first impression of the LCO images and the quasar image configurations.[13]

[11] https://lco.global/
[12] See https://lco.global/observatory/instruments/ and links therein.
[13] For reference, *Hubble* space telescope (*HST*) observations of all eight lensed quasars are available on the CASTLES webpage https://lweb.cfa.harvard.edu/castles/ (Falco et al. 2001).

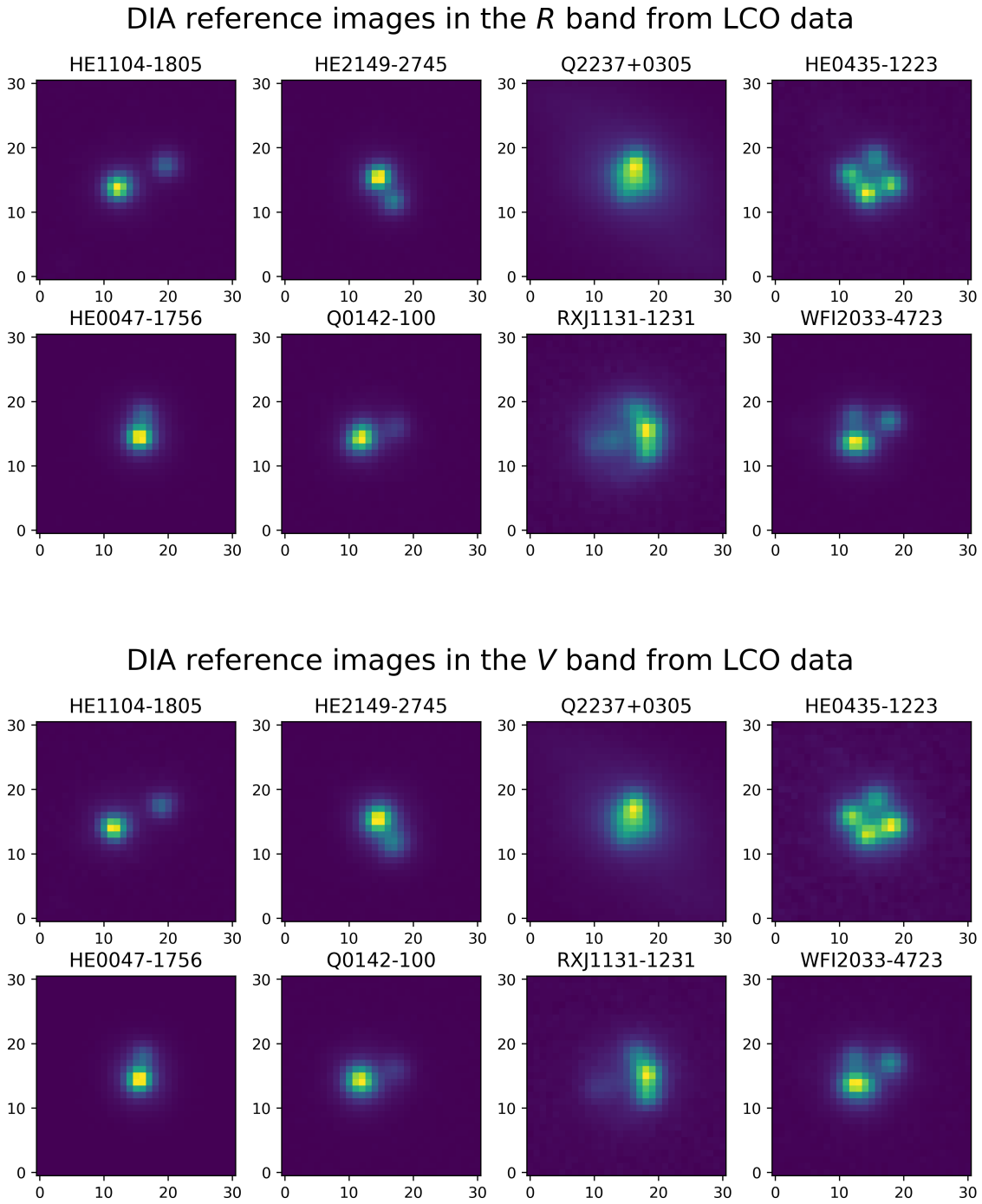

Figure 2.1.: Here, the eight lensed quasars (doubles on the left and quads on the right) as observed with LCO are presented. Shown are cutouts of their DIA reference images (see Sect. 3.5) zoomed in and centered on the quasars in the R band (upper panel) and the V band (lower panel), where north is down and east is right. The color scale is linear in flux, from the minimum (blue) to the maximum (yellow) flux value, for each individual image. The eight lensed quasars are among the brightest systems with apparent magnitudes in the optical of up to around ~ 17 mag as can be seen more precisely in the light curves in Chapter 4. The side lengths of the cutouts are 31 pixels, i.e. approximately 12 arcsec.

2.2. LCO quasar microlensing program targets

In this section, we give an overview of the eight lensed quasars we target with LCO to measure their light curves (see Sorgenfrei et al. 2024 and Sorgenfrei et al. 2025 for the first four quasars) and summarize some main properties in Table 2.1, including the discovery papers of the systems identifying them as lensed quasars, their type (see Fig. 1.2 or e.g. Neira et al. 2025), the involved redshifts, as well as image separations and time delays (see Sect. 1.3). Main reasons for the selection of quasars were image separation, visibility and their comparably high brightnesses (see Chapter 4).

We point out that throughout this work, all time delays are given with respect to quasar image A in days, such that they are to be added to the MJDs of the other images for the correct time delay shift. Hence, given two images A and B, a negative time delay $\Delta t_{\mathrm{AB}} < 0$ means that image A leads compared to image B, i.e. intrinsic quasar variability is first observable in image A, and thus all data points of image B would have to be shifted to earlier times to be in sync with image A.

Table 2.1.: Overview of lensed quasars observed with LCO

Quasar	discovery paper	z_{S}	z_{L}	type	$\theta\,['']$	time delays [days]
HE1104-1805	Wisotzki et al. (1993)	2.319	0.729	double	3.19	$\Delta t_{\mathrm{AB}} = 152.2 \pm 3.0$
HE2149-2745	Wisotzki et al. (1996)	2.033	0.603	double	1.70	$\Delta t_{\mathrm{AB}} = -39.0^{+14.9}_{-16.7}$ $\Delta t_{\mathrm{AB}} \simeq -70$ to -85 $\Delta t_{\mathrm{AB}} = -103 \pm 12$
Q2237+0305	Huchra et al. (1985)	1.695	0.0394	cross	1.78	all $\Delta t \simeq 0$
HE0435-1223	Wisotzki et al. (2002)	1.693	0.454	cross	2.54	$\Delta t_{\mathrm{AB}} = -9.0 \pm 0.8$ $\Delta t_{\mathrm{AC}} = -0.8^{+0.8}_{-0.7}$ $\Delta t_{\mathrm{AD}} = -13.8 \pm 0.8$
HE0047-1756	Wisotzki et al. (2004)	1.678	0.407	double	1.43	$\Delta t_{\mathrm{AB}} = -7.6 \pm 1.8$
Q0142-100	Surdej et al. (1987)	2.719	0.491	double	2.23	$\Delta t_{\mathrm{AB}} = -97.7^{+16.1}_{-15.5}$
RXJ1131-1231	Sluse et al. (2003)	0.658	0.295	cusp	3.23	$\Delta t_{\mathrm{AB}} = 1.6^{+0.7}_{-0.7}$ $\Delta t_{\mathrm{AC}} = -1.0^{+1.2}_{-1.2}$ $\Delta t_{\mathrm{AD}} = -92.5^{+1.9}_{-1.8}$
WFI2033-4723	Morgan et al. (2004)	1.662	0.661	fold	2.53	$\Delta t_{\mathrm{AB}} = 36.2^{+0.7}_{-0.8}$ $\Delta t_{\mathrm{AC}} = -23.3^{+1.2}_{-1.4}$

Note: Additional references beside the discovery papers are given in the main text. $\theta\,['']$ is the maximum image separation in arcseconds (the exact relative image positions are given in Table 3.1). The 'type' (double, cross, cusp and fold) refers to the image configuration from strong lensing (source position relative to caustics) as explained in Sect. 1.3 and Fig. 1.2. The three conflicting time delays of HE2149-2745 are discussed in the main text. For comparison, two extensive lists of (many more) lensed quasars can be found under `https://lweb.cfa.harvard.edu/castles/` and `https://research.ast.cam.ac.uk/lensedquasars/`.

Note that the order in which the quasars are presented and discussed throughout this work follows generally Table 2.1. This is roughly the order in which they were worked on for this project (and *not* a sorting e.g. based on their right ascension) together with some consideration for displaying reasons in this thesis.

2.2.1. HE1104-1805

The gravitationally lensed double quasar HE1104-1805, discovered by Wisotzki et al. (1993) within the Hamburg/ESO survey (HES), has a redshift of $z_S = 2.319$, while the lensing galaxy is located at redshift $z_L = 0.729$ (Lidman et al. 2000). The large separation of the two images of 3.19 arcsec (Lehár et al. 2000) and faint lens galaxy (see Fig. 2.1) made this object a good first target for light curve extraction (i.e. to develop and test the various data reduction steps). However, as will be shown, the time delay of $\Delta t_{AB} = (152.2 \pm 3.0)$ days, where image B leads (Poindexter et al. 2007), together with seasonal observation gaps, creates problems for detecting microlensing in data of this system. Nevertheless, microlensing has been detected and analyzed in this system (Schechter et al. 2003; Chartas et al. 2009). Morgan et al. (2010) have found an accretion disk size of $\log(R_s/\mathrm{cm}) = 15.9^{+0.2}_{-0.3}$ in the quasar rest-frame wavelength corresponding to the used filter from their microlensing analysis.[14]

2.2.2. HE2149-2745

HE2149-2745 is a double quasar with broad absorption lines. It was discovered by Wisotzki et al. (1996) in HES, with redshifts of quasar and lens galaxy of $z_S = 2.033$ and $z_L = 0.603$, respectively (Eigenbrod et al. 2007). The two images are separated only by 1.7 arcsec (see Fig. 2.1). The time delay was determined as $\Delta t_{AB} = (-103 \pm 12)$ days by Burud et al. (2002), with image A leading. Reanalyzing the same data, Eulaers & Magain (2011) reported an alternative time delay of about $\Delta t_{AB} \simeq -70$ to -85 days and thus concluded that these delays are unreliable. Evaluating data taken over 15 years at the *Leonhard Euler* 1.2 m Swiss Telescope by the COSMOGRAIL programme, Millon et al. (2020a) found strong evidence for a time

[14] Note that Morgan et al. (2010) presents R_{2500} values (i.e. Shakura-Sunyaev thin disk scale radii r_s from Sect. 1.2, including an mean inclination of $\langle i \rangle = 60°$ – thus, by projection, increasing the actual disk size – and correcting to a rest-frame wavelength of $\lambda = 2500$ Å for comparison) in their Fig. 1 – their famous 'quasar accretion disk size to black hole mass relation' (updated e.g. in Morgan et al. 2018; Rivera et al. 2024) – to compare different systems and values from different methods. In their Table 1, however, they give their inclined scale radii R_s (measured with quasar microlensing) with respect to the photometric filter wavelength in the quasar rest-frame, e.g. $\lambda_0 = 2110$ Å for HE1104-1805. Thus, these values have to be corrected via Eq. 1.7 to 2500 Å. However, this reference wavelength is chosen such, that for a system at typical redshift observed in the optical, this correction does not change the R_s size value much, e.g. for HE1104-1805 we find $\log(R_{2500}/\mathrm{cm}) \approx 16.0$.

delay of $\Delta t_{\mathrm{AB}} = -39.0^{+14.9}_{-16.7}$ days. However, the large and uncertain range of the various time delays in HE2149-2745 leads to multiple possible difference curves and therefore uncertain microlensing signals. Nevertheless, in Chapter 4 we do find a long term trend independent of the applied time delay and consistent with the difference curve from Millon et al. (2020a).

2.2.3. Q2237+0305

Q2237+0305, famously known as the 'Einstein Cross', was discovered by Huchra et al. (1985). The four images of the quasar at $z_{\mathrm{S}} = 1.695$ appear in cross configuration around the center of a barred spiral galaxy at $z_{\mathrm{L}} = 0.0394$ known as Huchra's lens. They are located approximately on a circle with a radius of just around 0.9 arcsec, thus the four point sources and the galaxy bulge are situated very close in a region only somewhat larger than the typical seeing disk in the optical. Therefore source blending and strong light contamination from the lens galaxy are serious issues in the system.[15] On the one hand, this makes the system difficult to study. On the other hand, the images apparent location inside the bulge of the lens galaxy also means that microlensing is likely at all times, since the light of the quasar images travels through the central and thus densely populated parts of the lens galaxy (Kayser & Refsdal 1989).

We set $\Delta t = 0$ days for the time delays of all combinations between the four images. This is a reasonable simplification, since various estimates for time delays as obtained or predicted with different techniques are (almost) all under a day and of the order of just a few hours (see e.g. the model predictions by Schneider et al. 1988; Wambsganss & Paczynski 1994; Schmidt et al. 1998, the results from analysis of *Chandra X-Ray Observatory* data by Dai et al. 2003, as well as Vakulik et al. 2006; Koptelova et al. 2006; Berdina & Tsvetkova 2018), while our light curves span over 10 years, making them negligible.[16] Also, shifting these light curves by a few uncertain hours for microlensing determination introduces additional uncertainty from the then necessary interpolation, while vanishing time delays mean that microlensing can be extracted immediately, as will be shown later.

In fact, quasar microlensing was first detected in Q2237+0305 (Irwin et al. 1989; Wambsganss et al. 1990; Corrigan et al. 1991) and since then has a long history of being observed in this system (e.g. by Ostensen et al. 1996 and OGLE: Woźniak

[15] Only in our best observations the cross shape of the four images is visible, e.g. in Fig. 2.1, while the lens galaxy is still very prominent. The full beauty of the system can be seen e.g. in *HST* images: https://esahubble.org/images/potw1204a/.

[16] Of note is that while determining time delays in 18 systems of COSMOGRAIL data, (Millon et al. 2020a) do *not* find estimates for Q2237+0305 due to the dominate nature of microlensing in the system, which is an issue for all observation based time delay measurements in Q2237+0305.

et al. 2000a,b; as well as Giannini 2017, Goicoechea et al. 2020 and many more). X-ray microlensing has been studied by Zimmer et al. (2011), while using OGLE data of the Einstein Cross, optical quasar microlensing was studied e.g. by Kochanek (2004) – who developed the microlensing analysis method (in the following referred to as the 'Kochanek light curve fitting method' or simply the 'Kochanek method') we are using in Part II (see Sect. 6.2) and Sorgenfrei et al. (2025) – as well as by Anguita et al. (2008), Eigenbrod et al. (2008a), Poindexter & Kochanek (2010a,b) and others. For example, Morgan et al. (2010) using the Kochanek method, find $\log(R_s/\mathrm{cm}) = 15.6 \pm 0.3$ (see also footnote 14) from their microlensing analysis for the accretion disk size.

2.2.4. HE0435-1223

The quadruply imaged quasar HE0435-1223 was discovered in HES by Wisotzki et al. (2002). Similar to the Einstein Cross, the four quasar images are visible in the cross configuration, but with wider image separations of up to 2.54 arcsec. HE0435-1223 is located at a redshift $z_\mathrm{S} = 1.693$ (Sluse et al. 2012) and is lensed by an elliptical foreground galaxy at $z_\mathrm{L} = 0.454$ (Eigenbrod et al. 2006). This lens galaxy is clearly identifiable for instance in *HST* data (Courbin et al. 2011), but is not very prominent in our LCO observations (see Fig. 2.1). This simplifies our analysis compared to the Einstein Cross, since light contamination from the lens galaxy does not has to be considered in the early steps of the data reduction. The time delays between the four images were precisely determined by COSMOGRAIL as $\Delta t_\mathrm{AB} = (-9.0 \pm 0.8)$ days, $\Delta t_\mathrm{AC} = -0.8^{+0.8}_{-0.7}$ days and $\Delta t_\mathrm{AD} = (-13.8 \pm 0.8)$ days, with bright image A leading (Millon et al. 2020a, updating the values of Courbin et al. 2011 and Bonvin et al. 2017 by using additional observation seasons). COSMOGRAIL data was also used by Bonvin et al. (2017) to measure the Hubble constant H_0 within the H0LiCOW project.[17]

Microlensing in HE0435-1223 has already been found and studied (see e.g. Blackburne & Kochanek 2010; Blackburne et al. 2011; Ricci et al. 2011; Braibant et al. 2014), focusing e.g. on the BLR using emission line profiles, on anomalous flux ratios or flux and colour variations, as well as applying the histogram or the Kochanek light curve fitting methods. Using the latter, Morgan et al. (2010) measured an accretion disk size of $\log(R_s/\mathrm{cm}) = 15.7^{+0.5}_{-0.7}$. This system, presenting the LCO light curves, as well as extracting and analyzing the microlensing signal, is the main focus in our publication Sorgenfrei et al. (2025) and will be the main topic in Part II of this thesis.

[17] The so-called 'H_0 Lenses in COSMOGRAIL's Wellspring' (H0LiCOW) project focusing on time-delay cosmography, see also Suyu et al. (2017) and `https://shsuyu.github.io/H0LiCOW/site/`.

2.2.5. HE0047-1756

The doubly imaged quasar HE0047-1756 first described by Wisotzki et al. (2004) is located at redshift $z_S = 1.678$ (Sluse et al. 2012) and lensed by a galaxy at $z_L = 0.407$ (Eigenbrod et al. 2006). The two images are separated by ~ 1.43 arcsec. Giannini et al. (2017) first measured the time delay and found $\Delta t_{AB} = -7.6 \pm 1.8$ from five years of data taken by the MiNDSTEp collaboration at the 1.54 m Danish telescope. The recent time delay estimates from COSMOGRAIL (Millon et al. 2020a) using the *Leonhard Euler* 1.2 m Swiss Telescope are in agreement. While Sluse et al. (2012) found evidence for microlensing of the BLR, both optical data sets (Giannini et al. 2017; Millon et al. 2020a) show the presence of slow long-term microlensing of the quasar accretion disk.

2.2.6. Q0142-100

Q0142-100 (also known as UM673) is a doubly imaged quasar as first recognized by Surdej et al. (1987) (previously, it had already been detected as high redshift quasar by MacAlpine & Feldman 1982), located at redshift $z_S = 2.719$ and lensed by an elliptical galaxy at redshift $z_L = 0.491$ (Eigenbrod et al. 2007). The image separation is about 2.2 arcsec and the time delay between the two images was first measured by Koptelova et al. (2012), and then by Oscoz et al. (2013) – finding no clear or only minor evidence for microlensing in the system, respectively – and consecutively updated in close agreement to $\Delta t_{AB} = -97.7^{+16.1}_{-15.5}$ by Millon et al. (2020a).

2.2.7. RXJ1131-1231

The quadruply imaged quasar RXJ1131-1231 is located at redshift $z_S = 0.658$ and lensed by an elliptical galaxy at $z_L = 0.295$ (see the discovery letter by Sluse et al. 2003, as well as Sluse et al. 2007). The four images appear in cusp configuration, i.e. 3 images are very close together separated only by around ~ 1 arcsec (see Table 3.1), and image D on the opposite side of the lens at a separation of 3.23 arcsec relative to image A (see Fig 2.1). Time delays have been first measured in Morgan et al. (2006), then corrected by Tewes et al. (2013) with longer light curves spanning nine observational seasons, and were finally updated with six more years of data by Millon et al. (2020a). The latter study finds $\Delta t_{AB} = 1.6^{+0.7}_{-0.7}$, $\Delta t_{AC} = -1.0^{+1.2}_{-1.2}$ and $\Delta t_{AD} = -92.5^{+1.9}_{-1.8}$, which we adopt. Microlensing has been studied in this system (e.g. Chartas et al. 2009) with Morgan et al. (2010) measuring an accretion disk size of $\log(R_s/\mathrm{cm}) = 15.3 \pm 0.2$.

2.2.8. WFI2033-4723

Finally, WFI2033-4723, a quadruply lensed quasar discovered by Morgan et al. (2004), is located at a redshift of $z_S = 1.662$ (Sluse et al. 2012). The quasar is lensed by an early-type galaxy at $z_L = 0.661$ (Eigenbrod et al. 2006), separating the four images by up to ~ 2.5 arcsec in a fold configuration. Time delays were estimated consistently by Vuissoz et al. (2008), Morgan et al. (2018) and the COSMOGRAIL collaboration (Bonvin et al. 2019), where we use the most recent values from the latter publication, i.e. $\Delta t_{AB} = 36.2^{+0.7}_{-0.8}$ and $\Delta t_{AC} = -23.3^{+1.2}_{-1.4}$. As done usually in this system, they treat the close image pair A1 and A2 as a blend (similarly, the two images appear as one elongated image in our LCO observations; see Fig. 2.1), i.e. the combined image $A = A1 + A2$ is considered (Bonvin et al. 2019 finds $\Delta t_{A1A2} = -1.0^{+3.1}_{-2.7}$ consistent with zero time delay). Multiple studies have detected and or analyzed microlensing in this system (e.g. Sluse et al. 2012; Giannini et al. 2017; Motta et al. 2017). Morgan et al. (2018) measured an accretion disk size of $\log(R_s/\mathrm{cm}) = 15.86^{+0.25}_{-0.27}$ using the Kochanek method.

3. Data reduction

In this chapter, the reduction steps applied to our LCO observations are described, starting from the retrieval of the data to the final determination of the quasar light curves. As described in Chapter 2, we monitored eight strongly lensed quasars (see Sects. 2.2.1 to 2.2.8 and Table 2.1 for a compact overview) since 2014 in the R and V band with the 1 m telescopes of LCO, in order to determine the light curves of their multiple images. Parts of the content presented here was already published in our method paper (Sorgenfrei et al. 2024; see also Sorgenfrei et al. 2025 for a compact summary). Besides providing more details and discussing recent developments, in this thesis, we describe the reduction method applied to the full data set, while in the two publications, only data of four of the eight quasars was reduced and discussed (namely HE1104-1805, HE2149-2745, Q2237+0305 and HE0435-1223). The general plan of the data reduction is summarized in the following and each step is described in detail in one of the seven corresponding sections:

Sect. 3.1: Data of the eight quasars is requested and afterwards retrieved from LCO via `python` scripts. Subsequent validation of these images filters out a large number of – for various reasons – 'bad images'.

Sect. 3.2: All images are aligned with respect to an astrometric reference image using the `ISIS` package[18] from Alard & Lupton (1998) and Alard (2000). The alignment routine was modified to incorporate *Gaia* proper motion data (Gaia Collaboration et al. 2016, 2023) to correct the star positions used by `ISIS` to achieve accurate image alignment.

Sect. 3.3: Single observations taken in the same night by the same telescope are stacked into a 'combined image'. Additionally, for each quasar and band, a high signal-to-noise (S/N) and small seeing 'reference image' is produced for a later step using the best available images (see Fig. 2.1).

Sect. 3.4: The position of quasar image A and each frame's point spread function (PSF) are extracted from the combined images using our modified version of the `GALFIT` software version 2.0.3 from Peng et al. (2002), where *HST* data is used to fix the relative quasar image positions.

[18] `ISIS` is available at `http://www2.iap.fr/users/alard/package.html`.

Sect. 3.5: Difference image analysis (DIA) carried out with so-called `hotpants` software[19] by Becker (2015) is used to create 'difference images'. In DIA, the reference image from the penultimate step, transformed with a space-varying convolution kernel, is subtracted from all combined images. Therefore, the resulting difference images should contain only brightness variations of the individual quasar images.

Sect. 3.6: The fluxes of the quasar images are extracted using `GALFIT` once again, however, this time on the difference images, where the PSF and quasar model position are fixed from before, again making use of *Gaia* data.

Sect. 3.7: Finally, the *difference* fluxes from the previous step do not contain the full flux at each epoch, as reference images were subtracted. Therefore, individual quasar image flux offsets are determined in the reference images, once more using PSF photometry with `GALFIT`. These offsets are then added to the corresponding quasar image fluxes. Converting to magnitudes, this results in the final quasar image light curves.

Finishing this overview, we note that the reduction pipeline to determine our LCO light curves of lensed quasars is similar to Giannini et al. (2017) and Giannini (2017). However, a main difference is that *Gaia* data was used to improve the astrometry, which became relevant due to the long-term observation campaign and the LCO image quality. Furthermore, the `ISIS`, `GALFIT` and `hotpants` codes had to be adapted to be better suited for various features of the LCO data, such as the low number density of stars in the field of view, the multiple quasar images and the size of the data set. Note that all steps of the data reduction are either implemented in `python` or are `python` scripts that run `ISIS`, `GALFIT` and `hotpants` on the data. The whole pipeline (though *without* the modified `GALFIT` code) is available on GitHub[20] or linked otherwise.

3.1. LCO data

As described in Sect. 2.1, images of the eight quasars (see Fig. 2.1) were taken at LCO by Robert W. Schmidt and Joachim Wambsganß since 2014. Observations of the targets are requested according to their visibility in the night sky over the year using a `python` script. Other factors deciding whether an image is actually taken by LCO include the remaining allocated time for the project in each half year, priority settings, requests from other groups and the brightness of the moon. These factors

[19] The software package `hotpants` is a newer implementation of the DIA algorithm by Alard & Lupton (1998) and Alard (2000), available at `https://github.com/acbecker/hotpants`.
[20] `https://github.com/sorgenfrei-c95/qsoMLdiffcurves`

explain the observation gaps that will be apparent in the light curves presented in Chapter 4. There is for instance the irregular spacing of the epochs especially early in the campaign (since then most steps had to be done completely manually), the larger gap in 2017 (resulting from scheduling issues), and of course the regular yearly gaps according to the quasars right ascension.

The first image was taken at 56 789.24 MJD, i.e. on May 12, 2014. Since then, data has been collected of all eight quasars and currently still is. The observations are downloaded via a `python` script checking for the quasar coordinates. The last time that data has been downloaded was at the end of January 2024[21], the most recent observation was at 60 336.04 MJD, i.e. on January 24, 2024. Therefore, the observations as presented in this thesis cover a range of close to 10 years. This is planed to be expanded in the future, since more than one year of new data is already available and the program continues further.

After retrieving the observations[22], immediately a larger number of bad images were flagged through automatic checks. Then, in parts also by manual inspection of the flagged images, typically those with multiple problems were deleted. Typical problems include (1) wrong or no filter leading to immediate exclusion, (2) very short exposure times, (3) false image shapes, (4) an airmass of more than 1.5 corresponding to an zenith angle of $\sim 48°$, (5) the moon being nearby, (6) a median-estimated high background, (7) bad pointing accuracy or wrong target leading to the quasar not being located roughly in the image center and (8) generally corrupted images with parts missing or fully empty images due to unknown observational failures. Most of these problems come together and degrade the image quality to a point, where they are not meaningfully usable. Of all 16076 downloaded images, 9876 raw images were taken into consideration for the next steps of the data reduction, i.e. 6200 (coincidentally, this is not a rounded number) were deemed 'bad images' at this point. However, three quarters of those images seem to be observations of other research groups of various close-by targets or our quasars in different filters. They are thus actually not bad images *per se*, just not ones needed for our campaign. Some of the remaining raw images had further problems such as bad seeing, being defocused (among other optical aberrations) or somehow imaged the sky multiple times slightly dithered.

[21] Actually, the last data download was conducted on March 25, 2024 – the date of the full moon before eastern (Schmidt 2022), a natural observational gap, not only because of the holidays. Unfortunately, due to data right issues, only data until the end of January was downloaded.

[22] The downloaded LCO observations (or 'raw images') are already corrected for bias, dark current and flat field by LCO. However, in the early (pre-2017) LCO intern data reduction pipeline 'e90', an off-center pixel-line was apparently overwritten, which we corrected for by averaging over the neighboring lines (see `trimming.py` in our reduction pipeline in footnote 20). Note that this line never affected the quasars or chosen reference stars. Nevertheless, a correction is necessary to have the correct relative star positions and raw image shapes, essential for image alignment (Sect. 3.2).

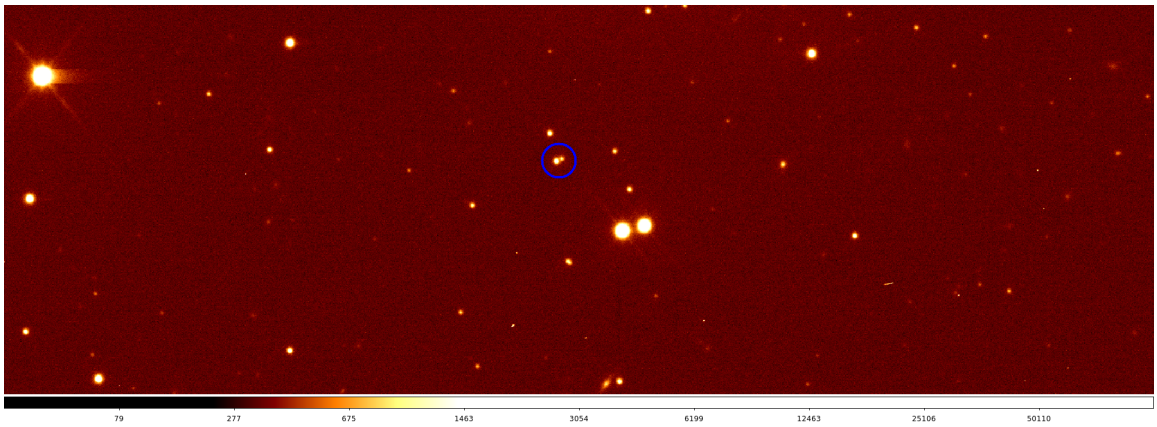

Figure 3.1.: Example observation of HE1104-1805. Shown is a single R band LCO observation of HE1104-1805 (where north is down and east is right). The color scale shows the counts logarithmically. The original image has a size of 4096×4096 pixels, i.e. ~ 26.5 arcmin $\times$ 26.5 arcmin, however, for displaying reasons, here we only show the central part of the image covering about ~ 10.3 arcmin $\times$ 3.5 arcmin. The double quasar is *not* the two bright sources clearly visible in the center of the image, but is located slightly above and to the left, marked with the blue circle.

Those were filtered out in the following steps, since manual inspection of all images was not possible, do to the large number of remaining images.

Before continuing, in Fig. 3.1 we show part of a high quality raw image of HE1104-1805, which was the first quasar worked on for this project. The larger separation of the two images (see Table 2.1) and no strong lensing galaxy present in the LCO data made this object a suitable first target, on which most of the reduction pipeline was initially developed. Visible is not only the quasar, but a field of foreground stars with a – for all our targets – typical number and distribution of stars, as well as a few image artifacts, such as cosmic rays and saturated pixels.

3.2. Image alignment and *Gaia* proper motion data

For all consecutive steps of the data reduction as outlined at the beginning of this chapter, it is important that all single observations are properly aligned (or 'registered') on a shared coordinated system. For example, this is clearly needed for an accurate stacking of individual images from each observation night and for applying DIA to the resulting combined images, as mismatches here would lead to unusable results. The single observations as retrieved from LCO are roughly centered on the targeted quasars, however, due to LCO's pointing accuracy and small unavoidable orientation issues (as well as some dithering tests in the early phase of the observational campaign), it is necessary to conduct a thorough alignment of all images.

To this end, as stated previously, the ISIS software was used (see footnote 18 and Alard & Lupton 1998; Alard 2000). ISIS determines the positions of a large number of stars in all images of one data set (i.e. one quasar in one band). It then aligns all images relative to one another by applying appropriate transformations to the individual images in order to minimize the sum of squared star position deviations. More concretely, in a first step, ISIS identifies an as large as possible number of stars ($i = 1, ..., N \simeq 500$ to 1000 stars in our case) in an astrometric reference image (which were selected manually; see Fig. 3.1 showing part of the R band reference image of HE1104-1805) and determines all their positions $\boldsymbol{r}_i^{\mathrm{ref}}$. Subsequently, the positions of these stars $\boldsymbol{r}_i$ are determined in each raw image as well. Finally, minimizing the star position deviations with respect to the astrometric reference image $\boldsymbol{\Delta r}_i = \boldsymbol{r}_i - \boldsymbol{r}_i^{\mathrm{ref}}$, all images are corrected by individual shifting, rotating and scaling them accordingly.

However, since our raw images are taken up to ~ 10 years apart, the relative star positions change due to their proper motions, which makes it difficult for ISIS to achieve proper image alignment. We therefore needed to resolve this issue and have presented our resulting method in Sorgenfrei et al. (2024), which incorporates the stars proper motions from *Gaia* into ISIS in order to improve the alignment significantly. As time domain astronomy is now conducted on increasingly larger scales, most famously via the Legacy Survey of Space and Time (LSST) at the *Vera C. Rubin Observatory*, including proper motion data to improve image alignment in studies might be relevant and an idea to consider in the future.

This issue of the proper motions of the reference stars affecting the alignment quality was first noted when data of the first three quasars (ultimately in preparation for Sorgenfrei et al. 2024) was reduced. Accompanying the aligned images, ISIS generates diagnostic status files called '`log_interp2`'. Here, in comparison to earlier experiences with ISIS, the reported alignment quality values (mainly the dispersions in Eq. 3.2) appeared to be less accurate than expected. Data reduction was continued nevertheless, however, in the difference images (from DIA as described in the overview at the beginning), the problem became obvious.

In Fig. 3.2 we show several zoom-ins of example difference images, with the stars proper motions overplotted using *Gaia* data (Gaia Collaboration et al. 2023). Clearly visible is that some of the stars did not just remain as negative or positive values (as expected if they were variables), but that they display flux sign changes inside their PSFs expanse, resulting in a dipole structures. Their proper motion direction, as indicated with the arrows, is in most of the cases orthogonal to the terminator separating the negative and positive values, i.e. pointing in the direction of the dipole.

What apparently happened is that, in the time between the compared observations, the stars moved due to their proper motion. Therefore, their PSFs could not be

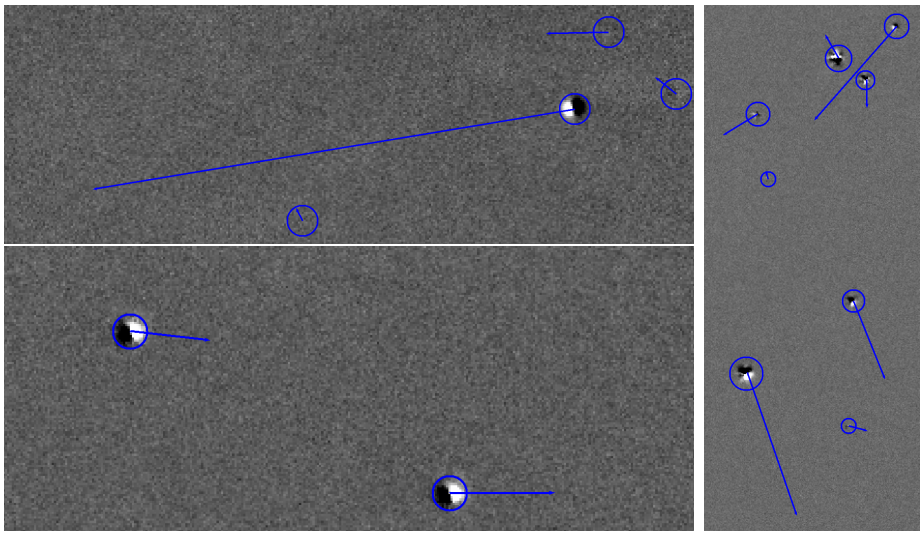

Figure 3.2.: Examples of remaining star dipole structures in difference images of HE1104-1805 with *Gaia* proper motion data shown as blue arrows indicating the direction (their length is proportional to the absolute proper motion, see Fig. 3.3).

perfectly subtracted in DIA and the dipole structure remained (a simplified picture would be the difference of two identical 2D-gaussians with one having its position slightly shifted off-center). This discovery has already been made by Skowron et al. (2014), who showed that using this effect, it is possible to determine proper motions directly from DIA. For us however, this posed a problem: the shifted star positions degraded the image alignment quality of `ISIS`, especially also leading to inconsistent quasar positions, as the reference stars fundamentally *cannot* be matched.

Let us now turn to our solution as described in Sorgenfrei et al. (2024). As the star positions relative to the reference image (additionally to the original raw image misalignment) are influenced by their proper motions, this alignment issue depends on the time difference between each raw image t and the reference image t^{ref}, i.e. $\Delta\tilde{t} := t - t^{\mathrm{ref}}$. Since we choose a high S/N and low seeing image (typically ~ 1.3 arcsec) for each target as reference image (see Fig. 3.1, which shows the astrometric reference image for the HE1104-1805 R band data set), they are of better quality as most other images. Therefore we applied the following correction to these reference images.

We utilized proper motion values from *Gaia* data release 3 (Gaia Collaboration et al. 2023, DR3[23]) of those stars in our fields with Renormalized Unit Weight Error RUWE < 1.4 (Lindegren 2018) and whose proper motions have S/N ≥ 5 to correct their reference image positions in the calculations of `ISIS`. In preparation, the stars in the neighborhood of the lensed quasar from the *Gaia* DR3 data were matched to the stars detected and used by `ISIS` (see Fig. 3.3). This leads to a list of star

[23] https://gea.esac.esa.int/archive/

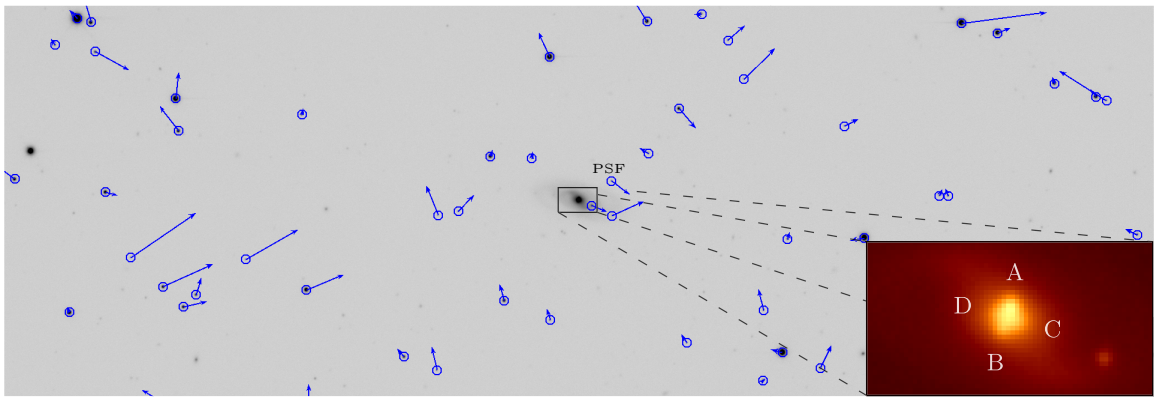

Figure 3.3.: R band image of Q2237+0305 in inverted gray scale. North is down, east is right and the field size is ~ 12.4 arcmin $\times$ 4.2 arcmin. The blue arrows depict the stars proper motions $\boldsymbol{\mu}_i$ from *Gaia* DR3 data; the high eastward proper motion star in the top right has $\mu \approx 55.4$ mas/year. The PSF star is labeled. In the lower right, a zoom into the central part, where the Einstein Cross is situated, is shown (~ 25.3 arcsec $\times$ 13.6 arcsec; image names A to D are indicated), using the R band DIA reference image (see Fig. 2.1). This figure is published in Sorgenfrei et al. (2024).

positions as detected by `ISIS`, additionally including their *Gaia* proper motions in the local tangent plane in right ascension $\mu_{\alpha^\star,i} = \mu_{\alpha,i} \cos\delta_i$ and declination $\mu_{\delta,i}$. For each raw image, $\Delta\tilde{t}$ and the list of proper motions of all stars were determined. We then propagate all star position values from the reference image taken at time t^{ref} to the positions where they would be at the time t of the current raw image with

$$\boldsymbol{r}_i^{\mathrm{ref}}(t) = \boldsymbol{r}_i^{\mathrm{ref}}(t^{\mathrm{ref}}) + \boldsymbol{\mu}_i \Delta\tilde{t} \quad \text{with} \quad \boldsymbol{\mu}_i = (\mu_{\alpha^\star,i}, \mu_{\delta,i})^\top, \tag{3.1}$$

where the proper motions $\mu_{\alpha^\star,i}$ and $\mu_{\delta,i}$ are converted to units of pixel/years using the pixel scale $s = 0.389$ arcsec/pixel (Sect. 2.1).[24] `ISIS` then continues running unchanged, simply using the corrected star positions $\boldsymbol{r}_i^{\mathrm{ref}}(t)$ from Eq. 3.1 in the reference image to align the current raw image at time t to the reference image.[25]

This method was applied to all images in our 16 datasets. Quantifying the quality of image alignment, Figs. 3.4 and 3.5 show the dispersions σ of the star position deviations with respect to reference images $\boldsymbol{\Delta r}_i$ measured *after* alignment by `ISIS`:

$$\sigma = \sqrt{\sigma_x^2 + \sigma_y^2} = \sqrt{\frac{1}{N-1}\sum_i^N (\boldsymbol{\Delta r}_i - \boldsymbol{\Delta\bar{r}})^2}, \tag{3.2}$$

[24] Our pixel coordinates $\boldsymbol{r} = (x, y)^\top$ are related to equatorial coordinates via $(\alpha, \delta)^\top = s\hat{R}(x, -y)^\top$ with $\hat{R}$ representing a matrix leading to only small rotations of less than 1°.

[25] Note, that this does *not* move the stars to the correct positions. We just modified the positions `ISIS` uses to calculate the necessary corrections. Dipole structures will still remain in the difference images and those stars should not be used as 'stamps' in the DIA method. The main goal was to improve overall image alignment such that quasar image positions are as stable as possible.

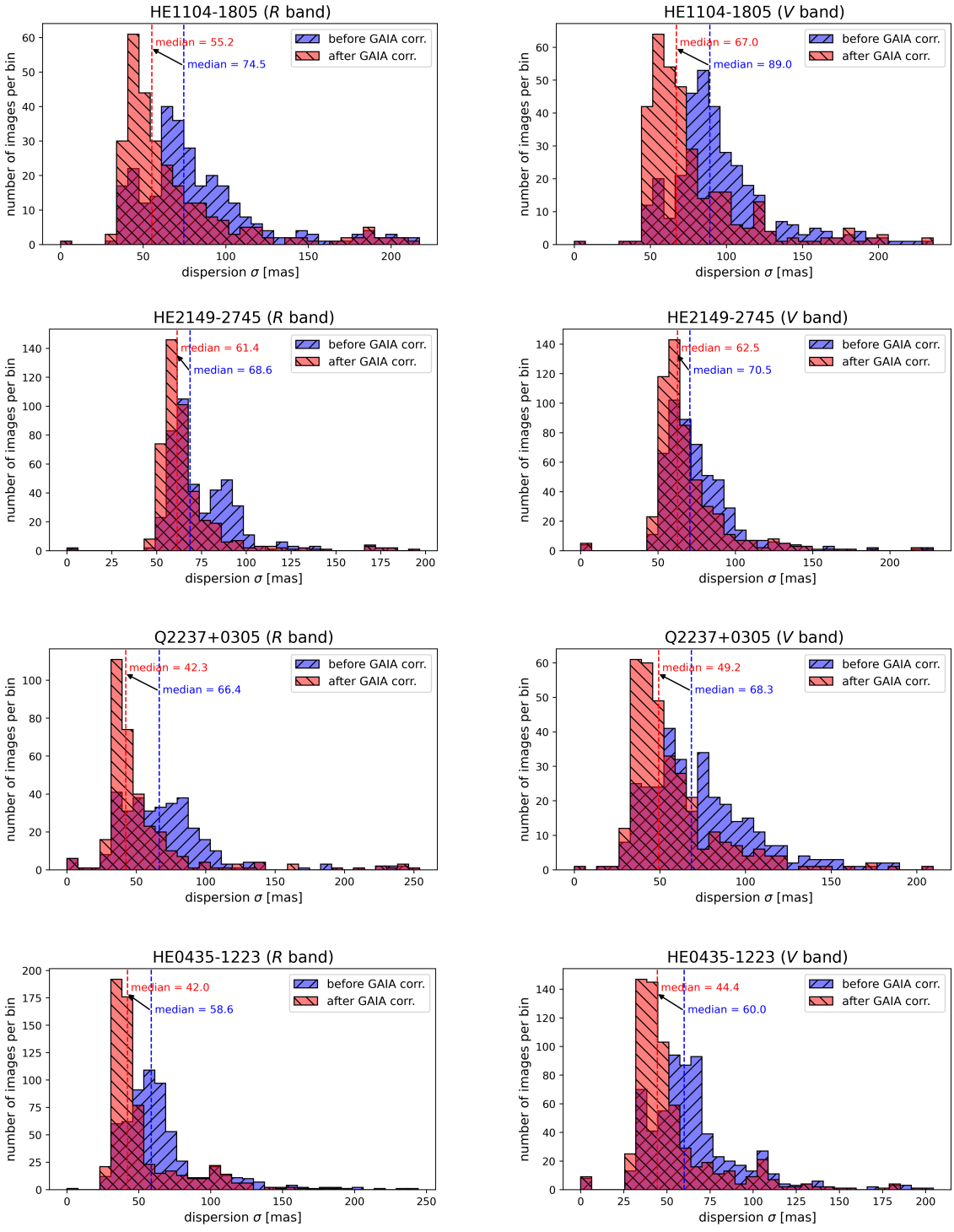

Figure 3.4.: Results of the alignment of all images of HE1104-1805 (first row), HE2149-2745 (second row), Q2237+0305 (third row) and HE0435-1223 (fourth row) in the R (left column) and V (right column) band. Shown are the dispersions σ as defined in Eq. 3.2, i.e. the standard deviation of all star position distances in mas between an aligned image and the reference image for all aligned images without (blue) and with (red) the method using *Gaia* proper motion data. The improvement of the median dispersion over all images is shown by the dashed vertical lines.

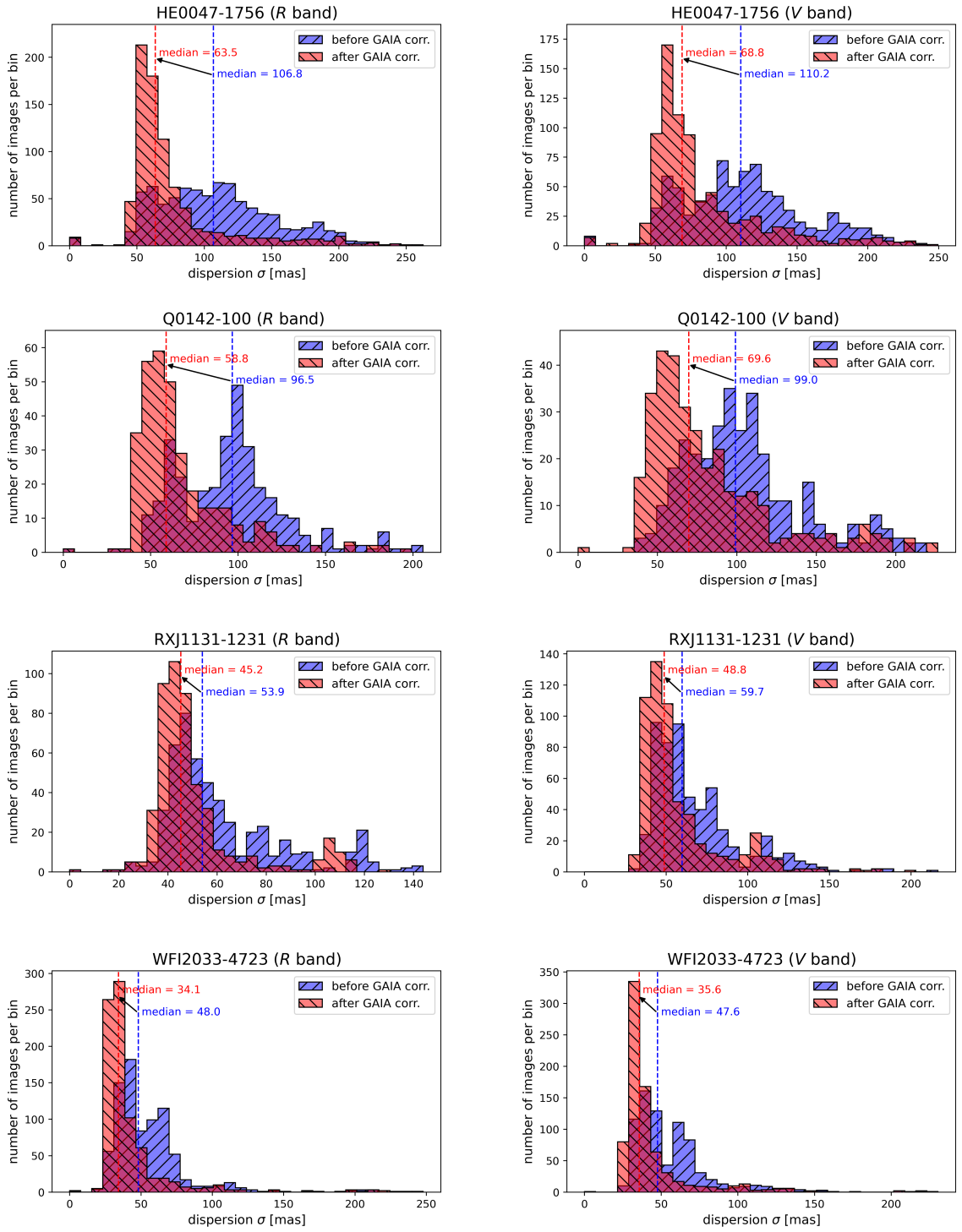

Figure 3.5.: Same as Fig. 3.4, but for HE0047-1756 (first row), Q0142-100 (second row), RXJ1131-1231 (third row) and WFI2033-4723 (fourth row), again in the R (left column) and V (right column) band.

where $\boldsymbol{\Delta\bar{r}}$ is the average star deviation vector that ideally would vanish. The dispersions σ are calculated for each image from σ_x and σ_y, i.e. the dispersions in x and y pixel-direction as determined by `ISIS` (and given as output in its so-called previously mentioned '`log_interp2`'-files). In Figs. 3.4 and 3.5, the dispersion results when applying and in contrast *not* applying the correction are compared. The median dispersions are shown as well, demonstrating that the level of alignment improved significantly using *Gaia*. For instance, for HE0435-1223, the median dispersion improved from $\langle\sigma\rangle \sim 59\,\mathrm{mas}$ before to $\sim 43\,\mathrm{mas}$ after this correction (Fig. 3.4). Averaged over all data sets, image alignment improved by about 27 % with our method.

3.3. Image combination

Typically, either three or four (but up to $\sim$ eight) single observations of the same target were taken in a night in the same filter, mostly with exposure times of 180 s each (and generally not deviating from this by more than $\pm 60\,\mathrm{s}$). As a next step, these were combined into one image per night to improve the S/N. In rare cases, where data was collected at multiple locations in a night, these observations were *not* combined into one image, but treated separately for the different telescopes. Simultaneously to creating the combined images, error images were calculated, since these are needed for `GALFIT` and `hotpants` to work properly and reliably in the following steps.

The images are combined, and the associated error image is calculated, using Eqs. 3.3 and 3.4 below. These equations describe a weighted mean, including rejecting the $N_{\mathrm{rej}}/2$ minimum and $N_{\mathrm{rej}}/2$ maximum values at every pixel position of the N photometrically scaled individual images (i.e. a 'min-max-rejection') in order to remove bad pixels e.g. due to cosmic rays (in most cases we use $N_{\mathrm{rej}} = 2$). For example, for $N = 3$ images, our method is simply a median stack of the observations, where they are slightly rescaled to an even brightness level. The photometric scales s_i measure the relative general brightness and exposure of the observations. They are of the order of one and are determined by aperture photometry of multiple (~ 20) reference stars in the field (checked for non-variability over time with respect to each other) via $s_i = \mathrm{median}\left[F_1^j / F_i^j\right]$, where F_i^j is the flux of reference star j in image i and the median is evaluated over all stars j. The weights ω_i of the single images were chosen to be the inverse of the photometric scales s_i, i.e. $\omega_i = s_i^{-1}$. This was done to increase the contribution of images with higher S/N, which achieved this for instance through coincidentally better observing conditions or longer exposure times.[26]

[26] This choice has the advantage of roughly being a proxy for inverse variance weighting, which results in the smallest variance of all possible weights for a weighted average (which can be shown with a Lagrange multiplier to include the normalization condition). Using Poisson statistics for

Therefore, the combined image $\bar{z}$ is given by

$$\bar{z}(x,y) = \frac{\sum_{i=1}^{N-N_{\mathrm{rej}}} \omega_i s_i z_i(x,y)}{\sum_{i=1}^{N-N_{\mathrm{rej}}} \omega_i} = \frac{\sum_{i=1}^{N-N_{\mathrm{rej}}} z_i(x,y)}{\sum_{i=1}^{N-N_{\mathrm{rej}}} s_i^{-1}} \quad \text{with} \quad \omega_i = \frac{1}{s_i}. \tag{3.3}$$

The z_i are the background b_i reduced single images d_i, i.e. $z_i = d_i - b_i$, i counts over the sorted values of $s_i z_i$, where the min-max-rejection is already applied and (x, y) are the individual pixel positions. By using Gaussian error propagation on Eq. 3.3 and Poisson statistics i.e. $\Delta d_i(x,y) = \sqrt{d_i(x,y)}$, we obtain the error image:

$$\Delta\bar{z}(x,y) = \frac{f_{\mathrm{rej}}}{\sum_{i=1}^{N-N_{\mathrm{rej}}} s_i^{-1}} \sqrt{\sum_{i=1}^{N-N_{\mathrm{rej}}} \left[d_i(x,y) + \Delta b_i^2 + \bar{z}(x,y)^2 \frac{\Delta s_i^2}{s_i^4} \right]}. \tag{3.4}$$

Here, a correction factor $f_{\mathrm{rej}} = \frac{\text{noise of background in combined image}}{\text{median background of error image with } f_{\mathrm{rej}}=1}$ of the min-max-rejection is included (which typically is about one), as well as errors of the background flux Δb_i and the scale Δs_i, with all three terms being determined statistically.[27] Using the same combining method, additionally, for each data set, a few (~ 10) best images (in terms of seeing, S/N, etc.) were combined in the same way to create reference images for DIA (see Fig. 2.1) needed for Sect. 3.5 (see also Sorgenfrei et al. 2024).

3.4. PSF photometry with GALFIT

Subsequently, in preparation for applying DIA, our method uses PSF photometry with GALFIT on the combined images $\bar{z}(x,y)$ and associated error images $\Delta\bar{z}(x,y)$ from Eqs. 3.3 and 3.4. As described in Sorgenfrei et al. (2024), the goal is *not* to extract the light curves, but to determine the position of quasar image A and the PSF for every night.[28] These will be needed when applying PSF photometry with GALFIT on the difference images in Sect. 3.6 (where positions and PSFs cannot be determined). The PSF is a 30×30 pixel region around a star near the quasar, which we select for each data set. The GALFIT version (Peng et al. 2002, version 2.0.3) we use, has been modified to include our multiple quasar model as in Giannini et al. (2017).[29] This

the variance of the fluxes and approximating it by s_i for all pixels (i.e. the typical brightness level, ignoring a proportionality constant, unimportant due to normalization) one finds $\omega_i \simeq s_i^{-1}$.

[27] Note that, since we did not want to rely on IRAF anymore, most of this reduction step was implemented in python using astropy (http://www.astropy.org), which still had some major issues (e.g. with aperture photometry), when this was coded around 2021/22. Together with the data quality, this explains most of the choices taken in this section (and other reduction steps).

[28] For WFI2033-4723, quasar image B position was used as the reference position, since image A is actually a blend of the fold pair A1 and A2 (see Sect. 2.2.8 and Table 3.1).

[29] Our version of GALFIT had actually been further adapted to work in flux-space, not magnitude-space, using Cash's C-statistic (see Sect. 3.2 and Appendix A of Zimmer et al. 2011).

Table 3.1.: Quasar image position separations

separations [arcsec]		B−A	C−A	D−A	G−A
HE1104-1805	$\Delta\alpha^\star$	2.901(3)			
	$\Delta\delta$	−1.332(3)			
HE2149-2745	$\Delta\alpha^\star$	0.890(3)			
	$\Delta\delta$	1.446(3)			
Q2237+0305	$\Delta\alpha^\star$	−0.673(3)	0.635(3)	−0.866(3)	−0.075(4)
	$\Delta\delta$	1.697(3)	1.210(3)	0.528(3)	0.939(3)
HE0435-1223	$\Delta\alpha^\star$	−1.476(3)	−2.467(3)	−0.939(3)	
	$\Delta\delta$	0.553(3)	−0.603(5)	−1.614(3)	
HE0047-1756	$\Delta\alpha^\star$	0.232(3)			
	$\Delta\delta$	−1.408(3)			
Q0142-100	$\Delta\alpha^\star$	2.145(3)			
	$\Delta\delta$	−0.613(3)			
RXJ1131-1231	$\Delta\alpha^\star$	0.030(3)	−0.588(3)	−3.105(3)	−2.032(8)
	$\Delta\delta$	1.187(3)	−1.120(3)	0.878(3)	0.586(6)
		A1−B	A2−B	C−B	
WFI2033-4723	$\Delta\alpha^\star$	−2.196(3)	−1.482(3)	−2.114(3)	
	$\Delta\delta$	1.261(3)	1.376(3)	−0.277(3)	

Note: For each quasar, the relevant image and lens galaxy position separations on the sky in right ascension $\Delta\alpha^\star = \Delta\alpha\cos\delta$ in the local tangent plane and declination $\Delta\delta$ are given in arcseconds with uncertainties of the final digit in brackets. All separations are measured with respect to quasar image A (except for WFI2033-4723 where its images A1, A2 and C are measured with respect to B) and are determined from the values on the CASTLES webpage (see footnote 30) based on *HST* data (Falco et al. 2001). For usage in `GALFIT` with our multiple PSF quasar model, these relative positions are converted to pixel differences with $(\alpha, \delta)^\top = s \cdot (x, -y)^\top$ (see footnote 24). The values for the first four quasars were already given in Sorgenfrei et al. (2024) and Sorgenfrei et al. (2025).

model consists of two or four copies of the PSF arranged in the orientation and with fixed relative distances (with respect to quasar image A) of the quasar images. The relative coordinates of the images as given in Table 3.1 are taken from the CASTLES webpage[30], which uses *HST* data (Falco et al. 2001). Then, `GALFIT` fits our quasar model to all combined images by minimizing the sum of squared differences of data and model flux (χ^2_{red}) returning the fluxes of the quasar images and the position of image A (see also Giannini 2017), as well as residuals, χ^2_{red} and background flux.

As an example, in Fig. 3.6 we show PSF photometry results of HE0435-1223 for

[30] The webpage `https://lweb.cfa.harvard.edu/castles/` of the CfA-Arizona Space Telescope LEns Survey of gravitational lenses (CASTLES, Falco et al. 2001) by C. S. Kochanek, E. E. Falco, C. Impey, J. Lehar, B. McLeod and H.-W. Rix currently contains data of over 100 lensed quasars.

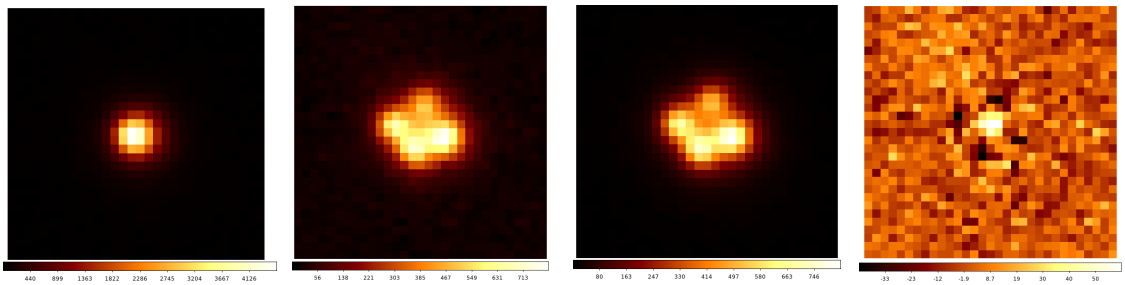

(a) PSF **(b)** data **(c)** model **(d)** residuals

Figure 3.6.: GALFIT example of HE0435-1223 in the *R* band from September 29, 2016: **(a)** the PSF star, **(b)** the combined LCO data of that night, **(c)** the quasar model made with GALFIT using four copies of the PSF fitted to the quasar images with the relative positions fixed with *HST* data and **(d)** the residuals between data and model. Shown are the fluxes in each pixel with linear scale (though note that the ranges of the colour bars below the images differ) and **(b)**, **(c)** as well as **(d)** show the same region of the frames.

one epoch. In the residuals, one sees that the model build from four copies of the PSF star (see Table 3.1) accurately fitted the data, except for some small amount of excess light from the lens galaxy. This worked accordingly for all epochs and all data sets. A similar plot depicting PSF photometry applied to HE1104-1805 is available in Sorgenfrei et al. (2024), together with a more detailed description of this process for the first three quasars. In general, for the four double quasars, the lens galaxies were not visible in our LCO data (see Fig. 2.1; but faintly in e.g. *HST* images), therefore we did not account for them in our GALFIT model. This was performed similarly for the quadruple quasars, except for Q2237+0305, since there, the quasar images can barely be isolated in our data due to of the bright core of the lens (see Figs. 2.1 and 3.3). Therefore, for the Einstein Cross, we had to include a galaxy model, since otherwise, the fits by GALFIT would not converge. We used the model described in the PhD thesis of Emanuela Giannini (Giannini 2017) consisting of (1) a de Vaucouleurs profile (i.e. a Sérsic profile with fixed Sérsic index of $n = 4$) and (2) an exponential profile ($n = 1$) representing the galactic bulge and the galactic disk, respectively:

$$I(r) = I_e \exp\left\{-b_n\left[\left(\frac{r}{r_e}\right)^{1/n} - 1\right]\right\} \propto \begin{cases} e^{-b_4\, r^{1/4}} & \text{for } n = 4 \\ e^{-b_1\, r} & \text{for } n = 1, \end{cases} \tag{3.5}$$

where $I_e = I(r_e)$ is the free brightness parameter and $b_n \approx 2n - 1/3$ is chosen such that r_e is the half-light radius. The radial coordinate is replaced by $r = \theta_1^2 + \theta_2^2/q^2$, where $(\theta_1, \theta_2)^\top = \hat{R}(\varphi)(x, y)^\top$, with $\hat{R}(\varphi)$ a rotation matrix. We used the values from Giannini (2017, see Sect. 9.2 and especially Table 9.2) to fix the half-light radii ($r_e = 4.7$ and $10.4\,$pixels), the galaxy orientation ($\varphi = 58.36°$) and the axis ratio

($q = 0.65$), but the relative positions and brightnesses are free (however, we find the same average magnitude difference of ~ 0.9 mag between both galaxy components).

Originally, a galaxy model was only included for Q2237+0305. However, after a problematic comparison of the resulting light curves of RXJ1131-1231 with literature data (Millon et al. 2020a) and subsequent checking of the residuals of PSF photometry on the difference images (Sect. 3.6), it became clear that also for RXJ1131-1231, including a galaxy model in this step is similarly important for finding optimal quasar positions.[31] For RXJ1131-1231, the galaxy model from Suyu et al. (2013) was adopted.[32] Once again, the galaxy position was free for `GALFIT` to fit, with an initial guess motivated by the value from Table 3.1. This lead to improved light curves due to the refined (i.e. shifted by ~ 0.3 pixel) best-fit quasar model positions, which significantly changed the PSF photometry of the difference images (Sect. 3.6).

Continuing with the method as described in Sorgenfrei et al. (2024), in Fig. 3.7 we show the positions of image A of several of our quasars as determined with `GALFIT` (as data points for the x and y directions respectively). These quasar image A positions $\boldsymbol{r}_{\mathrm{QSO}}(t)$ are following lines with non-vanishing slopes. However, since we have aligned the images (and showed that this has worked well, see Figs. 3.4 and 3.5), the positions of quasars (situated at cosmic distances) should not change with time. The found linear trends in the quasar positions originate from the proper motion of each data sets PSF star, moving inside its fixed 30×30 pixel box over the ten years, and consequently, the position of this box changes with time, as it is fitted to a non-moving quasar. In the figure, the plotted lines are *not* fits to the data points, but lines with slopes calculated from the *Gaia* DR3 (Gaia Collaboration et al. 2023) proper motion of the PSF star $\boldsymbol{\mu}_{\mathrm{PSF}}$. The position offset $\bar{\boldsymbol{r}}_0$ of each line is fixed with the median of all proper motion corrected positions. These lines, calculated from *Gaia* proper motion data of the PSF star, are then used as true quasar image A positions:

$$\bar{\boldsymbol{r}}_{\mathrm{QSO}}(t) = \bar{\boldsymbol{r}}_0 + \boldsymbol{\mu}_{\mathrm{PSF}}\tau(t) \quad \text{with} \quad \bar{\boldsymbol{r}}_0 = \mathrm{median}\left[\boldsymbol{r}_{\mathrm{QSO}}(t) - \boldsymbol{\mu}_{\mathrm{PSF}}\tau(t)\right], \tag{3.6}$$

where $\tau(t) = t - 2014.0\,\mathrm{years}$. These improved quasar positions $\bar{\boldsymbol{r}}_{\mathrm{QSO}}(t)$ are used instead of the data points $\boldsymbol{r}_{\mathrm{QSO}}(t)$, since they fit well to the data. Additionally, as the median of the positions was taken, these are preferable values, since the (PSF star proper motion corrected) quasar positions must be constant. The $\bar{\boldsymbol{r}}_{\mathrm{QSO}}(t)$ are kept

[31] In Appendix A (Fig. A.6) we show a light curve comparison of our data, where the galaxy model was used, with the COSMOGRAIL data (Millon et al. 2020a), together with two image-cutouts centered on the quasar, depicting the effect of the galaxy model on the PSF photometry residuals.

[32] See Eq. 15 and Table 1 in Suyu et al. (2013): we use their best-fit (one galaxy component) values converted to our coordinates and units in Eq. 3.5, i.e. an orientation angle of $\varphi = 301.6°$, an axis ratio of $q = 0.85$, a half-light radius of $r_e = 0.93$ pixel and a Sérsic-index of $n = 1.6$.

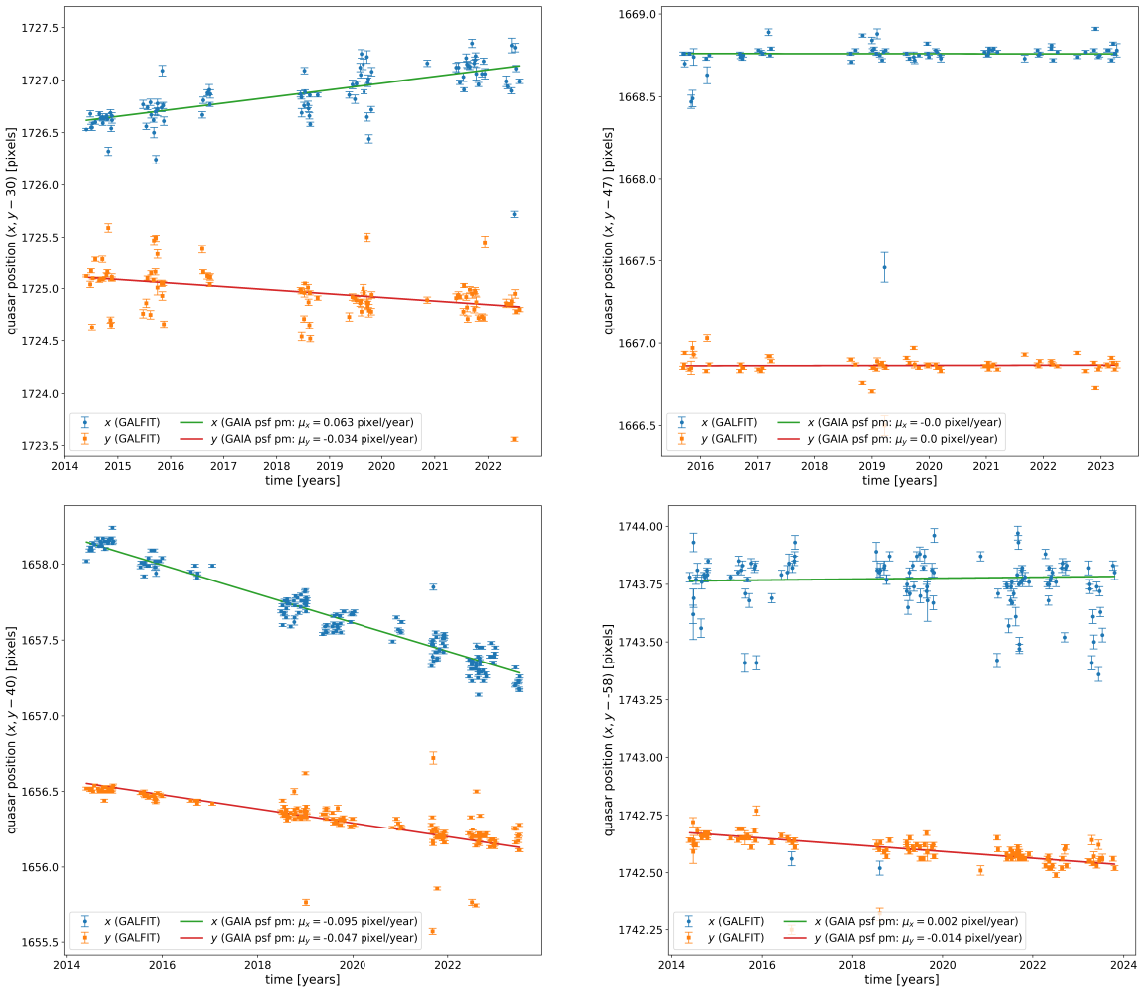

Figure 3.7.: Examples of quasar image A positions $\boldsymbol{r}_{\mathrm{QSO}}(t)$ with time as determined by GALFIT. Shown are the x and y pixel image A positions of Q2237+0305 in R (upper left), HE0435-1223 in R (upper right), HE0047-1756 in R (lower left) and the image B positions of WFI2033-4723 in V (lower right) as data points. The lines are *not* fits to these data points, but simply $\bar{\boldsymbol{r}}_{\mathrm{QSO}}(t)$-lines with the PSF star proper motion $\boldsymbol{\mu}_{\mathrm{PSF}}$ from *Gaia* data as slope and the median proper motion corrected position as overall offset $\bar{\boldsymbol{r}}_0$ (see Eq. 3.6). This was done for all 16 datasets and these resulting lines were used to fix the quasar model position when applying PSF photometry to the difference images (see Sect. 3.6). In the last data update, these lines were used unchanged and applied directly to the new difference images to have consistent positions and fits.

fixed in the subsequent light curve determination from the difference images.

We have used *Gaia* proper motion data to improve the image alignment (see Sect. 3.2 and Figs. 3.4 and 3.5) and the quasar position (see Sect. 3.4 and Fig. 3.7). In Fig. 3.8, we present how these two usages of *Gaia* proper motion data combined typically improved and stabilized our light curve quality. The left and right panels compare parts of the light curves of Q2237+0305 in the V band (from 2018 to 2022) without and with these *Gaia* improvements (see also Sorgenfrei et al. 2024).

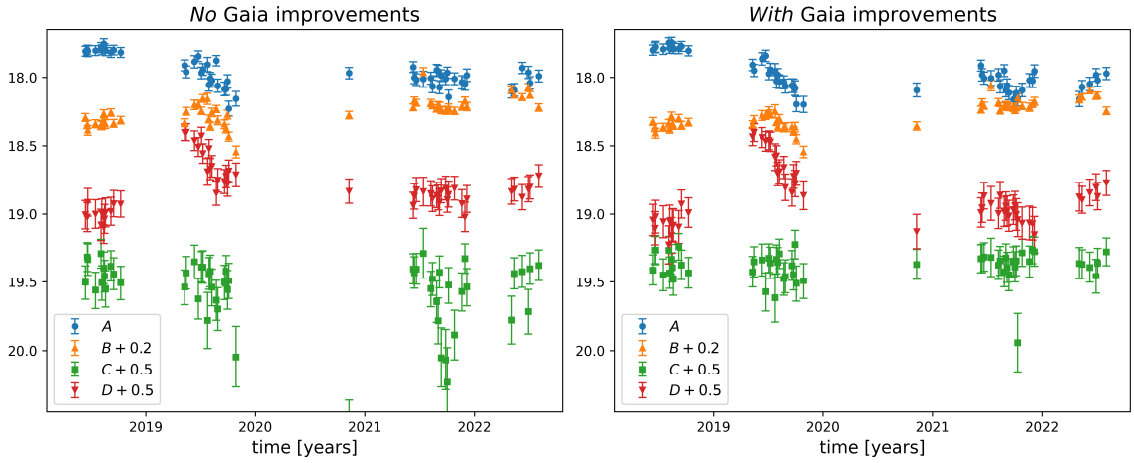

Figure 3.8.: Comparison of the light curves of Q2237+0305 in the V band without (left panel) and with (right panel) the combined effects from using *Gaia* proper motion data. For both plots, the same magnitude offsets were added to the different images to separate the light curves. This figure was published in Sorgenfrei et al. (2024).

3.5. Difference imaging analysis

Following Sorgenfrei et al. (2024), in the next step, DIA was applied to all combined images to obtain difference images. The difference images essentially are the combined images minus the DIA reference image (from Sect. 3.3). However, since the reference image has by construction a better seeing than the combined images, `hotpants` convolves it with a space-varying convolution kernel. This kernel is estimated from the PSFs of 5×5 so-called 'stamps', which are 31×31 pixel boxes centered on these stars. The stamps are distributed over the whole frame to estimate the PSF for all $(x, y)^\top$. The 5×5 stamps are chosen by `hotpants` from a selection of acceptable stars itself determined by `hotpants`. Importantly, we can modify this list to ensure that the quasar images are not included, as this would remove quasar light from the difference images. This is the main reason we use `hotpants` (Becker 2015) and not directly `ISIS` (Alard & Lupton 1998; Alard 2000), which `hotpants` is based on. Exclusion of the quasar from the list of stamps was simply not possible in `ISIS` and thus our signal would have been lost. Furthermore, `hotpants` could be adapted to our low numbers of field stars and proved to be more flexible in choosing stamp stars.

Continuing with the space-varying convolution kernel, DIA requires specifying σ values of three Gaussian components of the kernel function. We set these to 0.8, 2.4 and 4.0 pixel, adapted to the range of typical seeing values obtained with LCO telescopes (compare e.g. with Giannini et al. 2017; Giannini 2017). Moreover, each of the Gaussian components is multiplied with polynomials of order 4, 3 and 2, respectively. The spatial variation of the kernel function over the 5×5 stamp regions

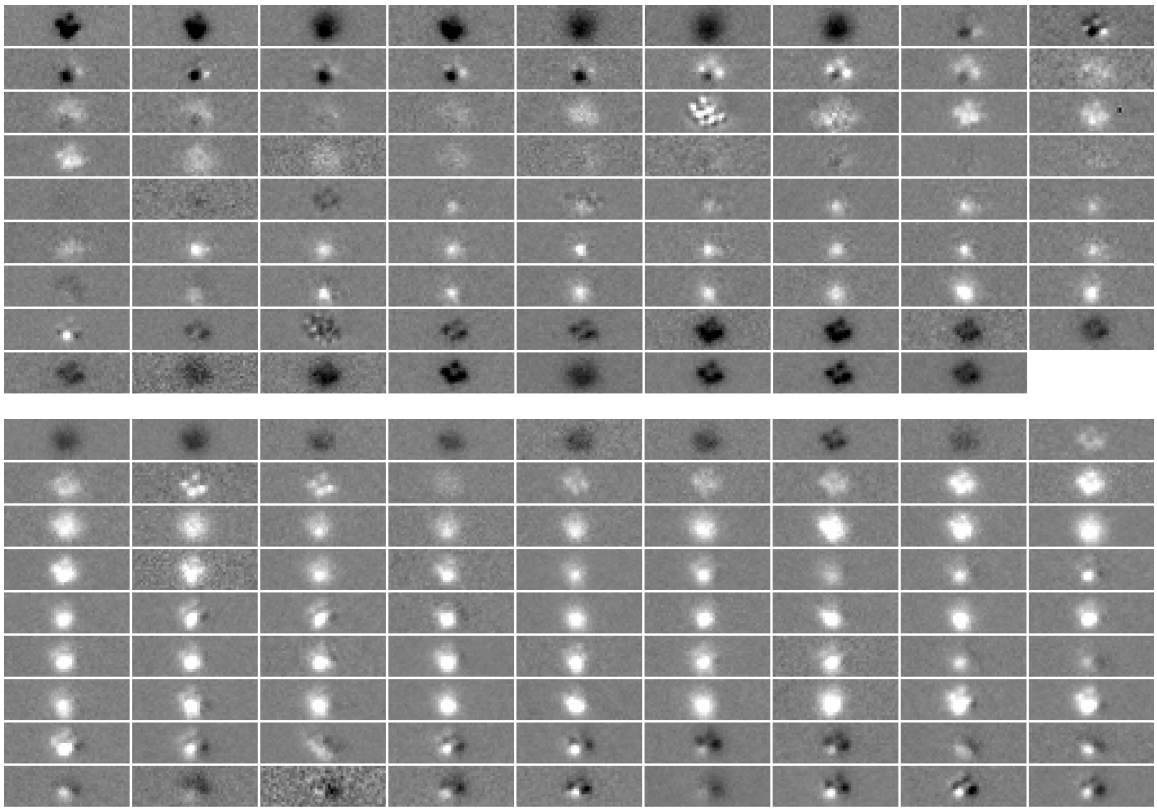

Figure 3.9.: Difference images of HE0435-1223 in R (upper panel) and V (lower panel), both from mid 2014 (each upper left) to early 2024 (each lower right). Shown is the remaining flux in each pixel relative to the corresponding reference image (see Fig. 2.1) linearly in grey scale, where white means brighter and black darker.

of our frames is interpolated with a polynomial of order 2. Finally, the background flux is allowed to vary spatially with a polynomial of order 2 as well.[33]

This subtraction removes all constant sources in the image and especially removes all the light from the lens galaxy. Therefore, the remaining brightness variation is due to changes of the quasar images with respect to the DIA reference image, which will be measured in the next section. In Fig. 3.9, we show time series of the R and V difference images of HE0435-1223 (see Sorgenfrei et al. 2024, for another example).

For the Einstein Cross, a further improvement of the light curves was achieved through splitting the data into two intervals that overlap in 2018. We then only worked with reference images of the respective intervals and carried out the DIA separately. This lead to two light curves (for all images), which overlap in 2018, the year where we linked the brightnesses from times ≥ 2018 to those < 2018. Apparently, for this data set, the time period over which observations were taken otherwise was too great and the influence from the proper motions accumulated.

[33] See e.g. Narayan et al. 2016; Giannini et al. 2017 for other `hotpants` usages and Alard & Lupton 1998; Alard 2000; Bramich 2008; Bramich et al. 2013 for more details on DIA theory.

Furthermore, the analysis of the data of Q0142-100 proved difficult, especially for the faint image B. Testing multiple possibilities (e.g. trying various different list of stamps and also different stamp grids such as 4×4) did not improve the quality of the data. So unfortunately, we had to keep the results as they were, which will be shown in the next chapter, where the final light curves are presented and discussed.

3.6. PSF photometry revisited

As a natural first idea on how to continue, one could imagine using aperture photometry on the quasar images in the reference images. Since only light from these images ideally remains in the images and especially the light from the lens galaxy is not present anymore, this seems possible at first glance. However instead, PSF photometry was used once again, now on the difference images. This is done not only because we know the PSFs from a previous step (which makes it simple and accurate), but mainly because the quasar images typically overlap due to their small separations (see Table 2.1) and possibly even have different signs in the difference images, which makes aperture photometry unfeasible (see also Fig. 3.9).

Applying PSF photometry on the difference images, now using the fixed quasar model positions from the *Gaia* position line (Eq. 3.6), as well as the PSF (from Sect. 3.4) to construct the quasar model, was again performed using `GALFIT`. Note that, this time, since we are working with difference images, the galaxy models were not used anymore in the cases where they had been included before (Q2237+0305 and RXJ1131-1231). For all data sets, only the two or four images of the quasar model were fitted, plus a constant sky background checked to be consistent with zero. Fit residuals and reduced χ^2-values were monitored as well. For the most part, there were little residuals left and $\chi^2_{\mathrm{red}} \lesssim 2$. However, to consistently remove a few last 'bad' data points, we chose a different metric described in the next section.

At this point, let us demonstrate the power of DIA by showcasing an comparison of a light curve from just applying PSF photometry on the combined images and stopping after that step (Sect. 3.4) versus a light curve extracted with PSF photometry from the difference images as described until this step. In Fig. 3.10 this is shown for a part of the Q2237+0305 data. The improvement of light curve quality is evident and nicely illustrates the impact that DIA has on our lensed quasar light curves, which is why it is used not only in quasar lensing (Woźniak et al. 2000a; Giannini et al. 2017; Sorgenfrei et al. 2024), but also in planetary microlensing (e.g. Albrow et al. 2009; Mróz et al. 2025), for supernovae (Narayan et al. 2016) and in the future LSST at the *Vera C. Rubin Observatory* (see e.g. Liu et al. 2024).

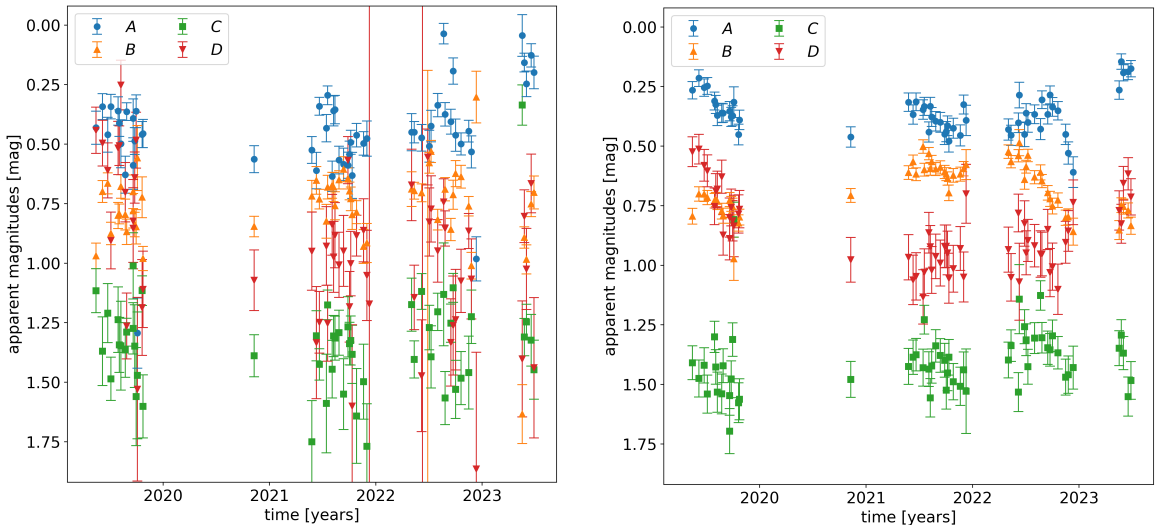

Figure 3.10.: Direct PSF photometry (left panel) versus PSF photometry of the difference images (right panel). For this comparison, parts of the R band data of Q2237+0305 was used as an example. Note the same magnitude and time ranges (i.e. 2.0 mag with an arbitrary overall magnitude offset and early 2019 to mid 2023).

3.7. Reference image offsets and finalization of the light curves

Due to our usage of DIA, the quasar flux values $F_X^{\mathrm{DIA}}(t)$ from the last step are all missing constant flux offsets F_X^{ref} from the subtracted reference image (for each quasar, band and quasar image, abbreviated as subscript X here). These reference flux offsets have to be determined and added to the difference fluxes to calculate proper fluxes and magnitudes. We therefore again used `GALFIT`, i.e. apply PSF photometry to the quasar images in the reference images (for each quasar and each band), with the position of our multiple quasar image model as free parameter and the PSF fixed from the respective PSF star. In the case of Q2237+0305 and RXJ1131-1231, the galaxy models were included. The resulting fluxes F_X^{ref} were added as offsets to the light curves from the difference images $F_X^{\mathrm{DIA}}(t)$.

To convert to magnitudes, the zero points of the apparent magnitude scales were determined by the median brightness of several (~ 20) stars (where PSF photometry was used one final time) in each quasars R and V band DIA reference images, relative to their apparent magnitudes, which we calculated from *Gaia* G, G_{bp} and G_{rp} data (see Table C.2 in Riello et al. 2021). These zero points (ranging from ~ 27.02 mag to 29.53 mag) were included as magnitude offsets m_0, finally resulting in the quasar light curves:

$$m_X(t) = -2.5 \log_{10} \left(F_X^{\mathrm{DIA}}(t) + F_X^{\mathrm{ref}} \right) + m_0. \tag{3.7}$$

Table 3.2.: Additional systematic errors σ_0[mag] of the zero points m_0

	he1104	he2149	q2237	he0435	he0047	q0142	rxj1131	wfi2033
R	0.12	0.04	0.04	0.03	0.04	0.03	0.02	0.02
V	0.30	0.02	0.07	0.02	0.03	0.02	0.02	0.01

Note: Here, the estimated 1σ-errors of the zero points are listed. Only abbreviated quasar names are given for displaying reasons. They refer to the eight quasars in the order used throughout this thesis and as presented in Sects. 2.2.1 to 2.2.8.

Using Gaussian error propagation, the 1σ-uncertainties of the light curves $m_X(t)$ were calculated as

$$\Delta m_X(t) = \frac{2.5}{\ln(10)} \sqrt{\left[\left(\Delta F_X^{\mathrm{DIA}}(t)\right)^2 + \left(\Delta F_X^{\mathrm{ref}}\right)^2 \right]} \times \left(F_X^{\mathrm{DIA}}(t) + F_X^{\mathrm{ref}} \right)^{-1}, \tag{3.8}$$

with X again being a stand-in for each quasar, quasar image and band combination. Note that the light curve errors as calculated here in Eq. 3.8, which we always quote (e.g. in Chapter 4, Figs. 4.1 to 4.8, Tables B.1 and B.2 in Appendix B, as well as in Sorgenfrei et al. 2024, 2025 and GAVO Data Center 2025) do *not* include the uncertainties of the zero points m_0. We excluded them, as they are only systematically affecting all data points in the same way and thus are not relevant for the difference curves we consider later for our microlensing analysis in this work. However, if for some other research question the exact and absolute values of the apparent magnitudes of our light curves are important, it is necessary to add to each uncertainty from Eq. 3.8 the systematic errors σ_0 of the zero points m_0 in quadrature, i.e.

$$\Delta \widetilde{m}_X(t) = \sqrt{\Delta m_X^2(t) + \sigma_0^2}, \tag{3.9}$$

using the values from Table 3.2, to obtain the correct magnitude errors $\Delta \widetilde{m}_X(t)$.

In accordance with Sorgenfrei et al. (2024), from the final quasar light curves, a small number of epochs with data points that have unreasonably high uncertainties were removed. These outliers with significant larger errors were identified in logarithmic histograms of the uncertainties of each data set as determined with Eq. 3.8. The thresholds $\Delta m_X^{\mathrm{max}}$ beyond which epochs were removed are given in Table 3.3, together with the total number of removed epochs.

This concludes the data reduction. Together with the number of images from two intermediate steps of the data reduction, the final number of epochs per quasar and band are given in Table 3.4. In total, this amounts to 1872 LCO quasar light curve epochs, corresponding – on average – to an observation of one of the quasars in either filter on every second day in the ten years of observations.

Table 3.3.: Chosen maximum magnitude errors with number of removed epochs

	he1104	he2149	q2237	he0435	he0047	q0142	rxj1131 ABC	rxj1131 D	wfi2033
$\Delta m_X^{\max}$ [mag]	0.04	0.05	0.10	0.05	0.03	0.06	0.05	0.16	0.05
# removed, R	2	2	0	1	16	3	0	10	6
# removed, V	4	8	0	1	28	10	4	16	8

Note: In the case of RXJ1131-1231, image D was treated independently of the other images, due to highly different uncertainties. Also, the quasar abbreviations from Table 3.2 are used.

Table 3.4.: Number of images at intermediate steps and final number of epochs

	he1104	he2149	q2237	he0435	he0047	q0142	rxj1131	wfi2033
# raw images, R	495	682	399	677	946	357	510	868
# raw images, V	512	609	406	697	949	367	583	819
# combi./diff., R	126	177	115	80	207	83	86	127
# combi./diff., V	130	154	114	81	199	82	86	118
# final epochs, R	124	175	115	79	191	80	86	121
# final epochs, V	126	146	114	80	171	72	82	110

Note: In the upper two rows denoted 'raw images', the number of observations *after* the initial sorting out (as described in Sect. 3.1) are given. Of these in total 9876 images, a large number of images were further removed by the aligning step (Sect. 3.2) and visual inspection. Then, the remaining images were stacked into combined images (often 4 images, see Sect. 3.3). Consequently, the numbers in the middle two rows are much lower, counting the combined images used for PSF photometry and DIA (Sects. 3.4, 3.5 and 3.6), thus also giving the number of difference images. Most importantly, the last two rows give the final number of epochs in our LCO quasar light curves (see Chapter 4), after removing some remaining epochs (see Sect. 3.7 and Table 3.3; in the case of RXJ1131-1231's faint image D, a few extra data points were removed and only 76 in R and 70 in V remained).

3.8. Current developments

In the next chapter, we present and discuss our quasar light curves, as they were determined using the techniques described here. However, at this point, it is noteworthy that parts of our data reduction pipeline were recently tested on simulated data. We – lead by Robert Schmidt, who chiefly conducted that analysis – took part in the 'pixel to light curve challenge' posed by Neira et al. (2025). There, a data set containing simulated observations of lensed quasars (of the four types introduced in Sect. 1.3, with varying image separations, as well as host and lens galaxy brightnesses) over several epochs was generated. The data set is provided as simulated CCD cutouts of these quasars and several reference stars in their vicinity. It is designed to have typical properties of the future LSST data, such as cadence, CCD gaps (sometimes removing individual reference stars from the data) and resolution.

As this promised to be a great test of the methods we applied to the LCO data, we took the challenge. Starting with our reduction, no proper motions were used for the stars, so the whole *Gaia* data part of our reduction did not apply. Image combination was not necessary either. First, Robert Schmidt had to create full images from the 'mosaic' of star and quasar cutouts, since `ISIS` works with regular full field observations.[34] Applying `ISIS` to the simulated data, we found and reported an issue in data regarding the quasar image positions and the overall coordinate system, which was then fixed by Favio Neira.

Continuing with our reduction pipeline, when we wanted to apply our `GALFIT` version to the properly aligned images in order to determine the quasar image positions for DIA, it unfortunately turned out that developments in the local computer infrastructure and the `gcc` compilers made continued usage of `GALFIT` at least very difficult. Therefore, Robert Schmidt created the necessary lensed quasar PSF fitting algorithms in `python`, especially using `astropy`.[35] Then, DIA could be applied as previously described and finally PSF photometry carried out with fixed image positions. In the end, plausible and consistent light curves could be extracted rather quickly and only minor additional adjustments to our codes were necessary. Currently, we are waiting for the results of the challenge, which are planned to be published as a follow-up paper. However, from private communications with Favio Neira, it became clear that our method is well suited to extract the relative brightness light curves, even though, as suspected, it does not handle the absolute brightness offsets as good as other methods (Sect. 3.7). Nevertheless, if confirmed, these are still very promising news in regards to our LCO light curves, as the absolute offsets do not matter for the difference curves and subsequent microlensing studies (Sorgenfrei et al. 2025).

Importantly, through this digression, it became obvious that switching from `GALFIT` to `astropy` is not only sensible, but a necessary step for the future of our LCO light curves. We plan to use this new method for future updates of our light curves. Since the start of February 2024 (as the last update contained data until the end of January; see footnote 21), a large number of new LCO observations of the eight quasars are available. Including these will lengthen our light curves by over one and a half years and thus will presumptively increase the number of epochs by $\sim 15\%$, potentially even reaching a point where overlap with future LSST data is possible.

[34] The cutouts have the advantage of a greatly reduced disk space and might also be better tailored to other light curve determination methods, such as `STARRED` (see Millon et al. 2024), who participated as well. Also, with real data, star cutout positions could be corrected with proper motion data, similar to our method from Sect. 3.2 and Sorgenfrei et al. (2024), but *actually* changing the positions (in comparison to footnote 25). This has the potential to greatly improving the DIA, as no dipoles as in Fig. 3.2 should remain and the quality and number of stamps would be increased.

[35] The code used for our contribution is available at `https://bwgit.de/hd-tf119/plc_challenge`.

4. Quasar light curves

In this chapter we present the light curves for our lensed quasar sample, which is one of the main results of this thesis. The light curves consist of the apparent magnitudes of the quasar images with time, almost covering 10 years from May 2014 to January 2024, following the data reduction from the previous chapter.

4.1. LCO light curves

Figures 4.1 to 4.8 show the final light curves of the eight quasars we obtained with LCO as introduced in Chapter 2. In all plots, the light curves are corrected for the respective time delays using the values given in Table 2.1. This allows a direct comparison of the signal in the various images.

Previous versions of the light curves of the three quasars HE1104-1805, HE2149-2745 and Q2237+0305 were already published in Sorgenfrei et al. (2024). The light curves of HE0435-1223 as presented in this thesis were published in Sorgenfrei et al. (2025). As of mid 2025, the current versions of the light curves of these first four quasars are also publicly available at the German Astrophysical Virtual Observatory GAVO Data Center (2025). In the future, additional data points (see Sect. 3.8) are planned to be made available there as well. The light curves of the other quasars (HE0047-1756, Q0142-100, RXJ1131-1231 and WFI2033-4723) are so far unpublished and presented here for the first time. Additionally, as they are of central importance to this thesis, the light curves of HE0435-1223 are tabulated in Appendix B, together with more details on the data availability of the light curves of all eight quasars.

4.1.1. HE1104-1805, HE2149-2745 and Q2237+0305

As described in Sorgenfrei et al. (2025), the light curves of HE1104-1805, HE2149-2745 and Q2237+0305 were updated with respect to Sorgenfrei et al. (2024) to include data until January 2024 (see also Sect. 3.1 and footnote 21). At that time, the final light curves of all eight quasars were determined simultaneously, in order to have the same time range for all quasars. Thus all three data sets include additional epochs at the end (in 2023 and 2024) with respect to Sorgenfrei et al. (2024). However,

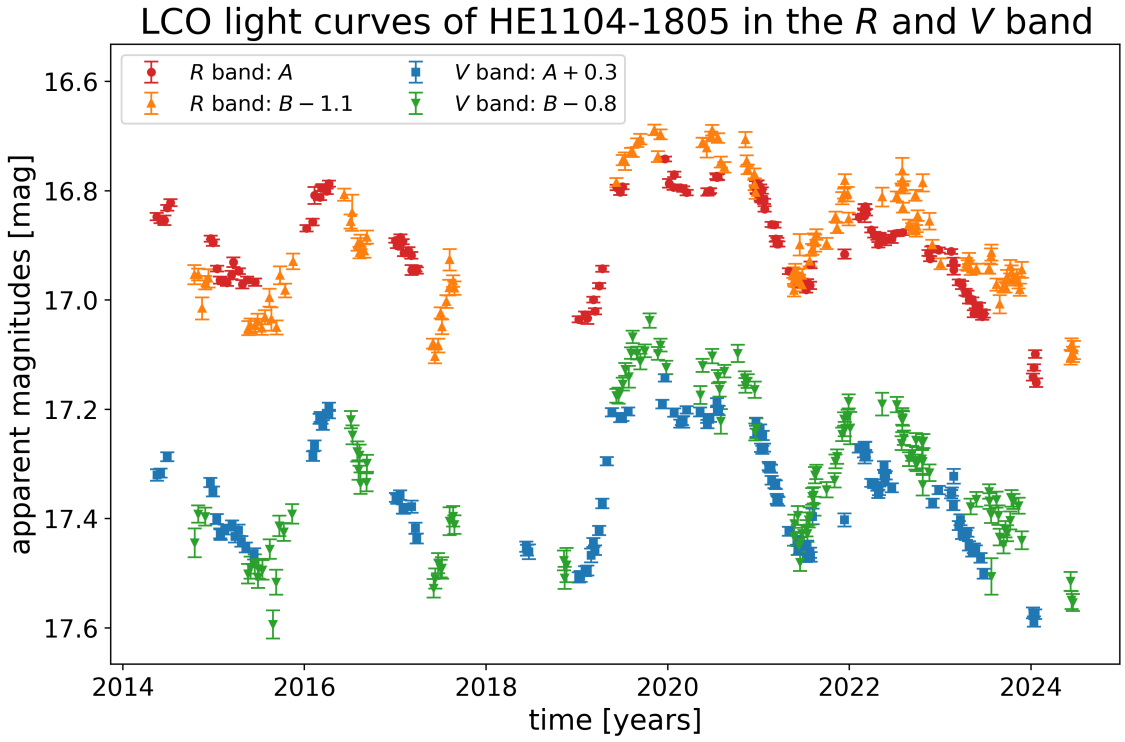

Figure 4.1.: Light curves of HE1104-1805. Shown are the time delay corrected light curves of the two images of HE1104-1805 in the R band (upper curves) and V band (lower curves), where magnitude offsets were added to reveal the intrinsic quasar variability and to separate the two filters.

especially for HE1104-1805 (and to a smaller extend for HE2149-2745) more data points from the start of our campaign (from 2014 to 2016) were added to our light curves as well, due to improvements in the method to access all available data from our LCO campaign. These 'new' (i.e. final for the purpose of this thesis) light curves for HE1104-1805 consist of 124 R and 126 V band data points (see Fig. 4.1), for HE2149-2745 of 175 R and 146 V band data points (Fig. 4.2) and for Q2237+0305 of 115 R and 114 V data points (Fig. 4.3), which is overall a plus of $\sim 39\%$ with respect to Sorgenfrei et al. (2024). Furthermore, the resulting light curves for HE2149-2745 changed (mainly by a small magnitude offset in the V band, but to some extend also in the shape of the curves) due to an improved alignment, quasar position and consecutive difference imaging from a reselection of the reference image and a more adequate PSF-cutout.

The light curves of HE1104-1805 as shown in Fig. 4.1 clearly show a strong intrinsic quasar variability in both bands (e.g. the sawtooth shape in 2014 to 2018 with an amplitude of ~ 0.3 mag or the double bump around the year 2020), since by using magnitude offsets the light curves of both images can be overlayed quite well for the most part. Of course, this systems approximately half year time delay (see Table 2.1;

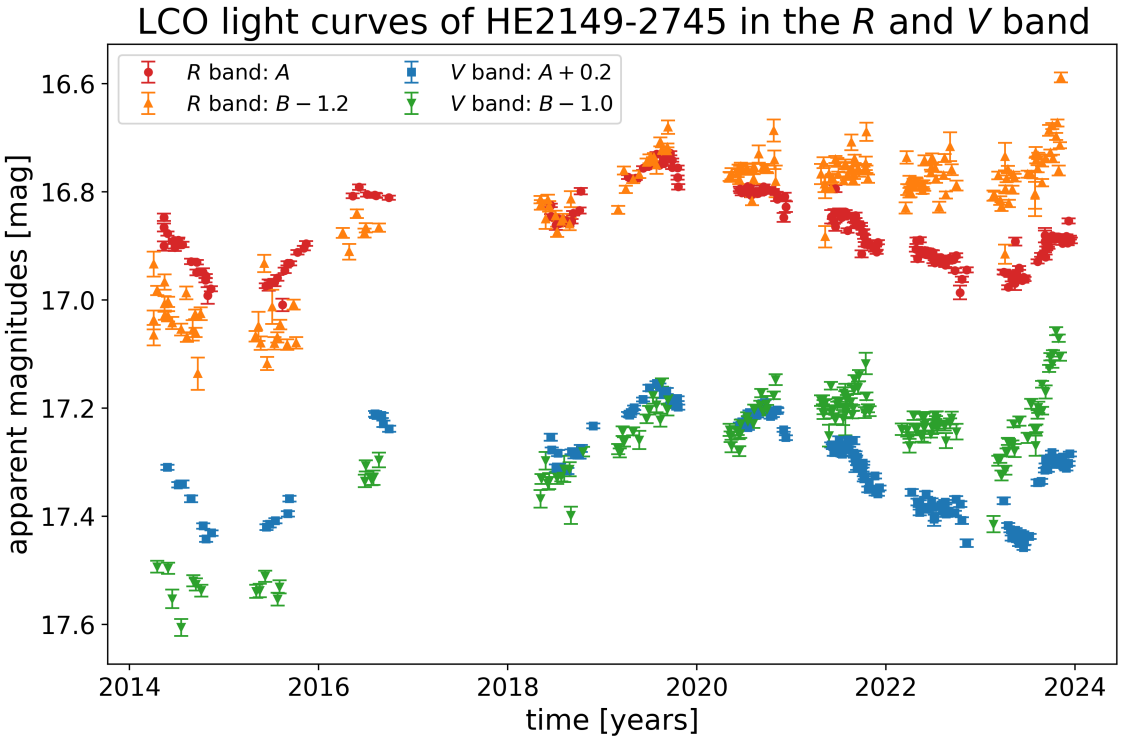

Figure 4.2.: Light curves of HE2149-2745. Shown are the light curves of the two images of HE2149-2745 in the R band (upper curves) and V band (lower curves). Magnitude offsets were added to approximately match the light curves between 2018 and 2020. The light curves of image B are shifted using the time delay value from Millon et al. (2020a). Note however, that for HE2149-2745 two more possible and contested time delay estimates exist (Burud et al. 2002; Eulaers & Magain 2011).

value from Poindexter et al. 2007) together with the seasonal observation gaps from our LCO program, leads to little overlap of images A and B in time. This makes an extraction of potential microlensing signals difficult, since only a few data points will remain for a difference curve. Still, as a well separated and bright double quasar, this was an ideal first target at the start of this project to get familiar with the data and to begin developing the necessary data reduction steps as described in Chapter 3.

Figure 4.2 shows the light curves of both images of HE2149-2745 in both bands, where the first corresponding time delay in Table 2.1 (i.e. the time delay from Millon et al. 2020a) was used for visualization (the other two possible time delays simply lead to the light curves of image B being shifted slightly more to the left).

Investigating the different proposed time delays for this system did not lead to a result. Matching the curves manually does not obviously disqualify one of the proposed time delays since no clearly intrinsic sharp peaks are present in all light curves (e.g. in the observational seasons of 2018 to 2021, image A displays some peaks and drops, while image B consists mostly of rising parts and might be affected by microlensing

as the two images begin to diverge). Our attempt to use the `PyCS3` software (COSMOGRAIL[36]: Tewes et al. 2013; Millon et al. 2020a,b), written for light curve shifting and time delay estimation, was not successful and we thus were not able to constrain the time delay further from our data.

Nevertheless, at least some long-term intrinsic quasar variability is identifiable, where – compared to HE1104-1805 – images A and B overlap a lot more in time (for all possible time delays). Additionally, microlensing is distinctly visible from 2020/2021 on, where image A becomes fainter, while image B stays roughly constant and finally even rises stronger than image A before 2024. In the data before the gap of 2017/2018, image B is clearly fainter than later (note the magnitude offsets to match the curves of A and B in 2018 to 2020). This fits the long-term trend and suggests a slow brightness increase of image B relative to image A over the whole observation period that could be attributed to microlensing.

Figure 4.3 shows the light curves of the four images of Q2237+0305, where the curves from the two different photometric filters are separated into two panels. Note again, for this quasar, all time delays are set to zero (Sect. 2.2.3), which means that there is perfect overlap of the multiple curves, making it easy to calculate difference curves for microlensing determination in this system. Throughout the whole observational campaign, the images brightness variations appear to be uncorrelated, except for a shared brightness decline in 2019 in images A, B and part of C (plus maybe in D). This indicates that the images of Q2237+0305 are affected by microlensing at all times in agreement with numerous works as discussed in Sect. 2.2.3.

4.1.2. HE0435-1223

The LCO data of HE0435-1223, its reduction and subsequent microlensing analysis are published in Sorgenfrei et al. (2025), including the light curves as shown in Fig. 4.4. They contain 79 epochs in the R band and 80 epochs in the V band for all four images. The light curves of images B, C and D are shifted in time by the delays given in Table 2.1. Immediately, intrinsic quasar brightness variations are visible in all four images and both bands. Focusing on images A, C and D, the overall shape of the light curves, i.e. a general brightness increase until 2018 and consecutive decrease, as well as the brightness peaks in 2018/2019 and in 2022 are highly similar and their magnitude differences appear relatively constant (especially for C and D), or in the case of image A, are only changing slowly.

Image B displays the same overall behavior, but in addition a strong magnification relative to the other three images can be observed: initially, its apparent magnitude

[36] https://cosmograil.gitlab.io/PyCS3/index.html

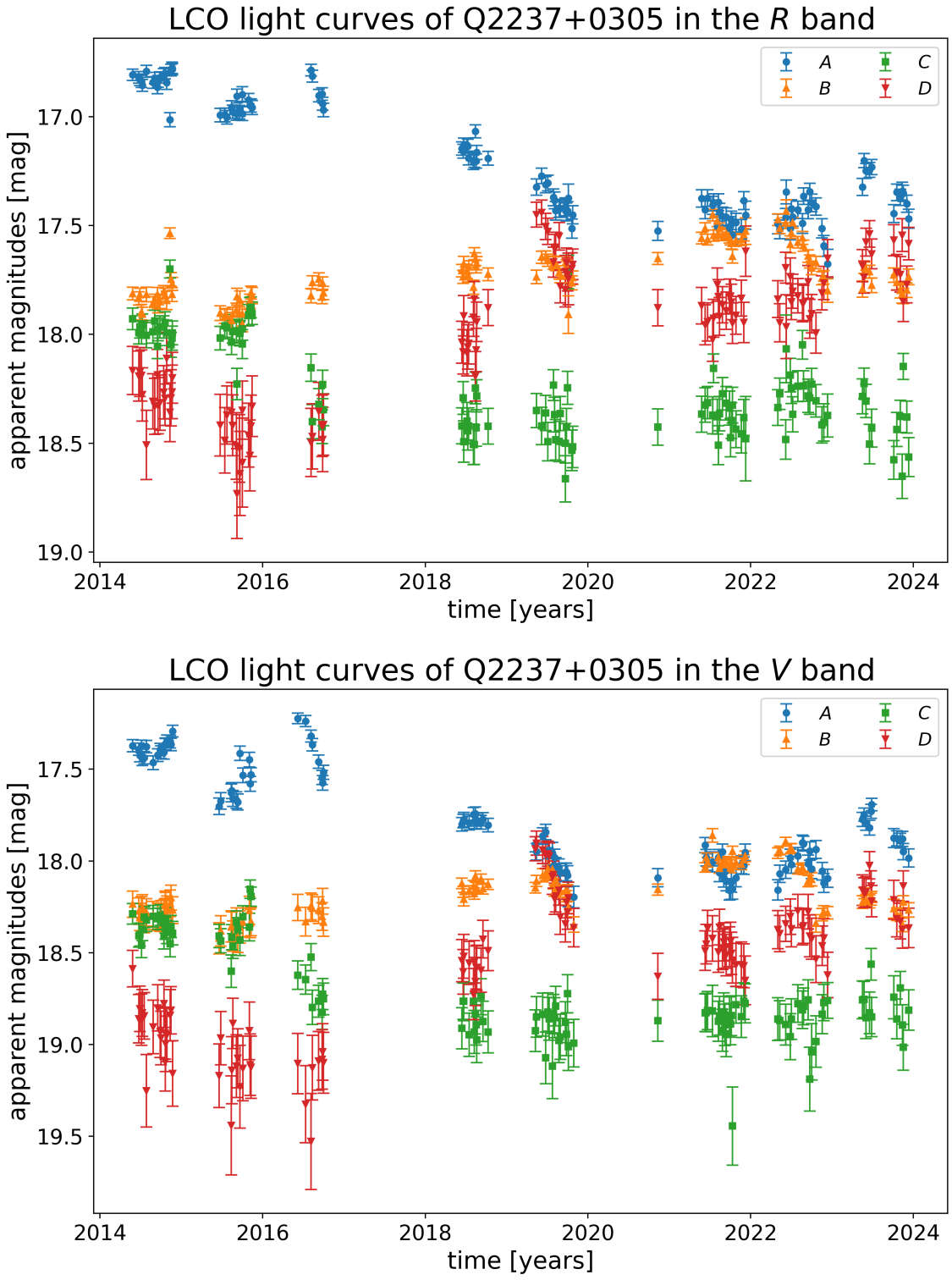

Figure 4.3.: Light curves of Q2237+0305. Shown are the light curves of the four images of the Einstein Cross in the R band (upper panel) and V band (lower panel). The data of both filters is plotted with the same time range. Moreover, no time delays were applied (see Sect. 2.2.3), as well as no magnitude offsets.

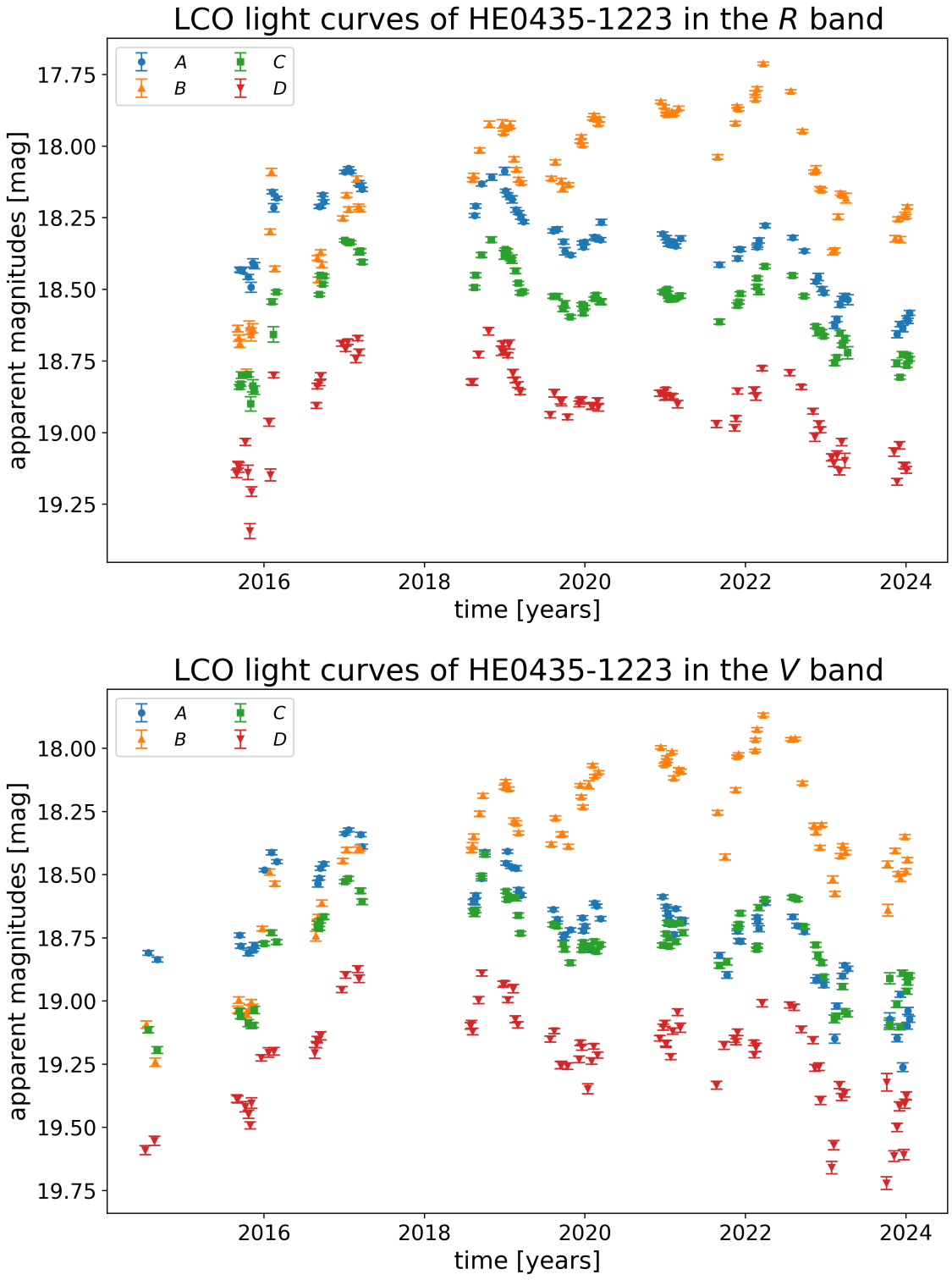

Figure 4.4.: Light curves of HE0435-1223. Shown are the time delay corrected light curves of the four images of HE0435-1223 in the R band (upper panel) and V band (lower panel), using the same time range, as already published in Sorgenfrei et al. (2025). The data is given in Appendix B, Tables B.1 and B.2.

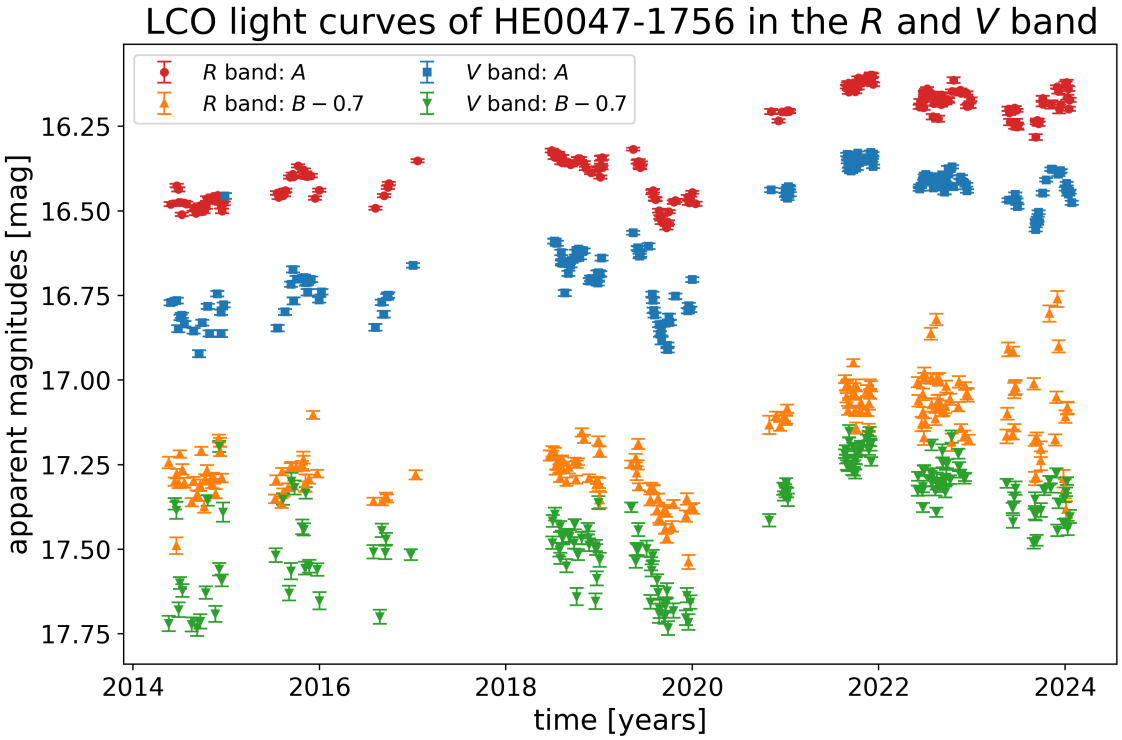

Figure 4.5.: Light curves of HE0047-1756. Shown are the time delay corrected light curves of the two images of HE0047-1756 in the R band and V band. Both light curves of image A are displayed above the two light curves of the fainter image B.

lies between those of images A and C (in R) or comparable to that of image C (in V), but later surpasses image A clearly, reaching values over half a magnitude brighter than A in 2022. In absolute terms, over the full 10 years of observations the apparent magnitude of image B varies by ~ 1.1 mag in the R band and by even ~ 1.4 mag in the V band, while the other three images show variations roughly on the order of ~ 0.6 mag (in R) and ~ 0.8 mag (in V). This excess brightness variation in image B is strong evidence for microlensing, which is discussed further in the following chapters and is the main focus of Sorgenfrei et al. (2025), where we analyzed this signal.

4.1.3. HE0047-1756 and Q0142-100

The so far unpublished LCO light curves of HE0047-1756 are presented in Fig. 4.5. They are comprised of 191 epochs in the R band and 171 epochs in the V band, which is the largest number of epochs per quasar in our LCO data set. In both bands, the quality of image A (in terms of scatter between nearby data points) clearly surpasses that of the fainter image B, which appears rather noisy. However, at least for certain longer stretches of time, the scatter in image B seems mostly consistent with image A, given the associated errors (e.g. from 2018 to 2022 in both bands), though this is

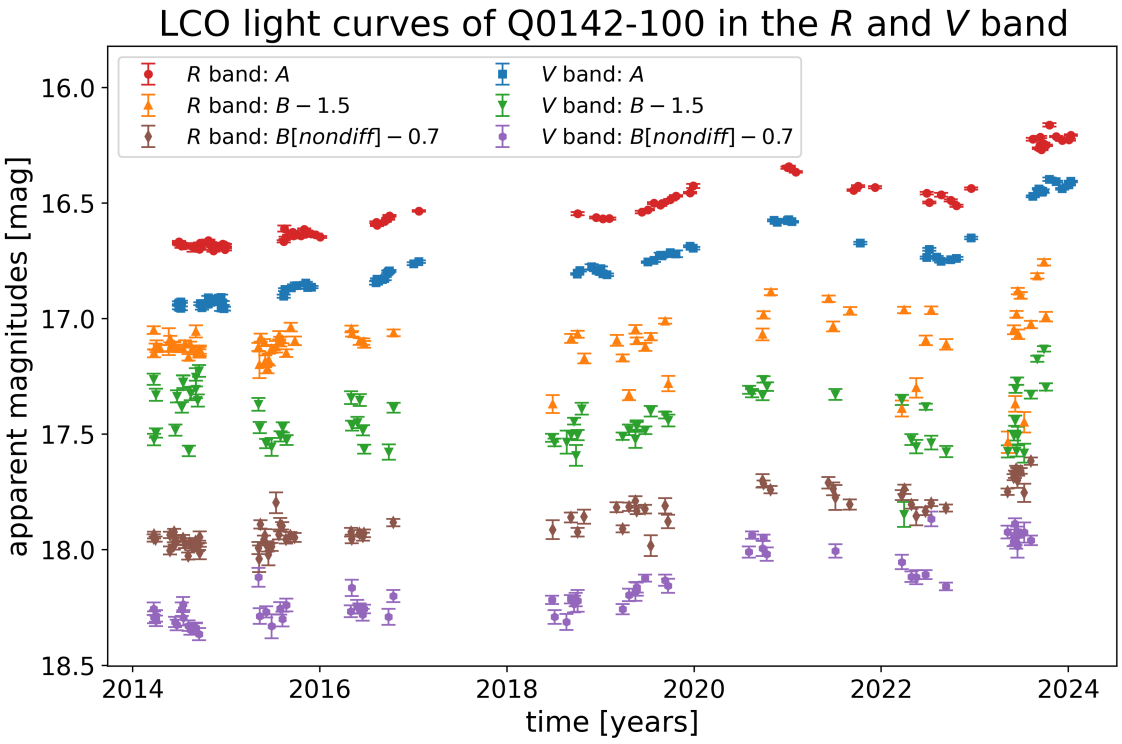

Figure 4.6.: Light curves of Q0142-100. Shown are the light curves of the two images of Q0142-100 (also known as UM673) in the R band and V band, with the light curves of image A on top, followed by the light curves of the fainter image B (shifted by a magnitude offset). Additionally, results for image B from *not* using DIA, but just PSF photometry on the combined epoch images are shown below as comparison.

certainly not the case for the early part of the V band and the late part of the R band. It is thus very difficult to detect microlensing in our data. Still, the intrinsic quasar light curve shared by all four curves is clearly visible, where the small time delay (Table 2.1) first determined by Giannini et al. (2017) leaves a lot of overlap in time between the images.

In Fig. 4.6 we show the time delay corrected data of our last double quasar Q0142-100, with 80 R and 72 V band epochs. Again, our method worked well in determining the light curve for the bright image A, but the noise and scatter was much more significant in the case of the fainter image B. Although, also here, there are time intervals with better S/N, such as in 2014 to 2017 in R, as well as 2018 to 2022 in V. As discussed in Sect. 3.5, different settings of the DIA did not resolve remaining problems with image B. Highly unusual is that the regular photometric data of image B from the combined images for this system, i.e. not using DIA, appears less noisy and more consistent overall (which is not at all the case for all other studied systems, where the LCO light curve quality from DIA clearly surpasses direct PSF photometry; see Fig. 3.10). Nevertheless, intrinsic quasar variability is identifiable.

4.1.4. RXJ1131-1231 and WFI2033-4723

The light curves of RXJ1131-1231 are shown in Fig. 4.7. They consist of 86 data points in the R and 82 in the V band, but only for images A, B and C, each. For the fainter image D, on the other side of the lens galaxy, which we measured below 19 mag down to ~ 21 mag, the number of data points is reduced further, certainly related to its low brightness and its position closer to the galaxy (see Sect. 3.6), thus for image D the number of epochs are only 76 in R and 70 in V.

Intrinsic quasar variability is again clearly visible in this object. Especially the three close images A, B and C with very small time delays (see Table 2.1) have similar light curves, with the same general behavior and features (such as steep slopes in 2014 and 2015, as well as the v-shape in 2019) and a few distinctions (e.g. the overall brightness, some intraseasonal variation and the additional trend of image B, which slowly gets fainter, at least in the R band). The larger time delay of faint image D with respect to image A leads to less overlap, but the general shape still matches with the other curves even though the scatter of data points is more prominent.

Finally, in Fig. 4.8 we present the time delay corrected light curves of WFI2033-4723. The final light curves consist (in all images) of 121 epochs in the R band and 110 epochs in the V band. The extremely close image pair A1 and A2 was fitted regularly with two PSFs as described in Sect. 3.4, however as mentioned before, light exchange[37] can be problematic in this case, which is why often the combination of both fluxes is stated. We do both, thus for both the R and V band we show *five* light curves, namely those of image A1, A2, $\mathrm{A} = \mathrm{A1} + \mathrm{A2}$, B and C (where again the somewhat misleading but typical notation of image A means adding the *fluxes* – not magnitudes – of images A1 and A2 together). The result is a high quality light curve for this combined image A, which has little noise and no clear outliers, but also the individual curves of A1 and A2 are of good quality. Fortunately, the light curves of images B and C are (upon visual inspection) of high quality as well, which makes this a promising data set for future analysis.

All five curves in both bands display clearly correlated intrinsic quasar variability over the whole LCO observations. The light curves can be matched quite well (which can be seen directly for images A2 and B, as their overall magnitudes are very similar). Still, on closer inspection uncorrelated variability is present as can be see in the difference curves, that potentially can be attributed to quasar microlensing.

[37] As an example, light exchange is what likely happened in one epoch in 2022 in the R band in Fig. 4.8. At MJD 59 737.4097 two data points, one of A1 (in blue) and one of A2 (in orange), are visible somewhat distant from the rest of their respective light curves and are closer together in brightness – however the combined flux above (image A in green) shows no outlier. This is consistent with image A2 having taken some light of A1 in the PSF fit, due to the blending issue.

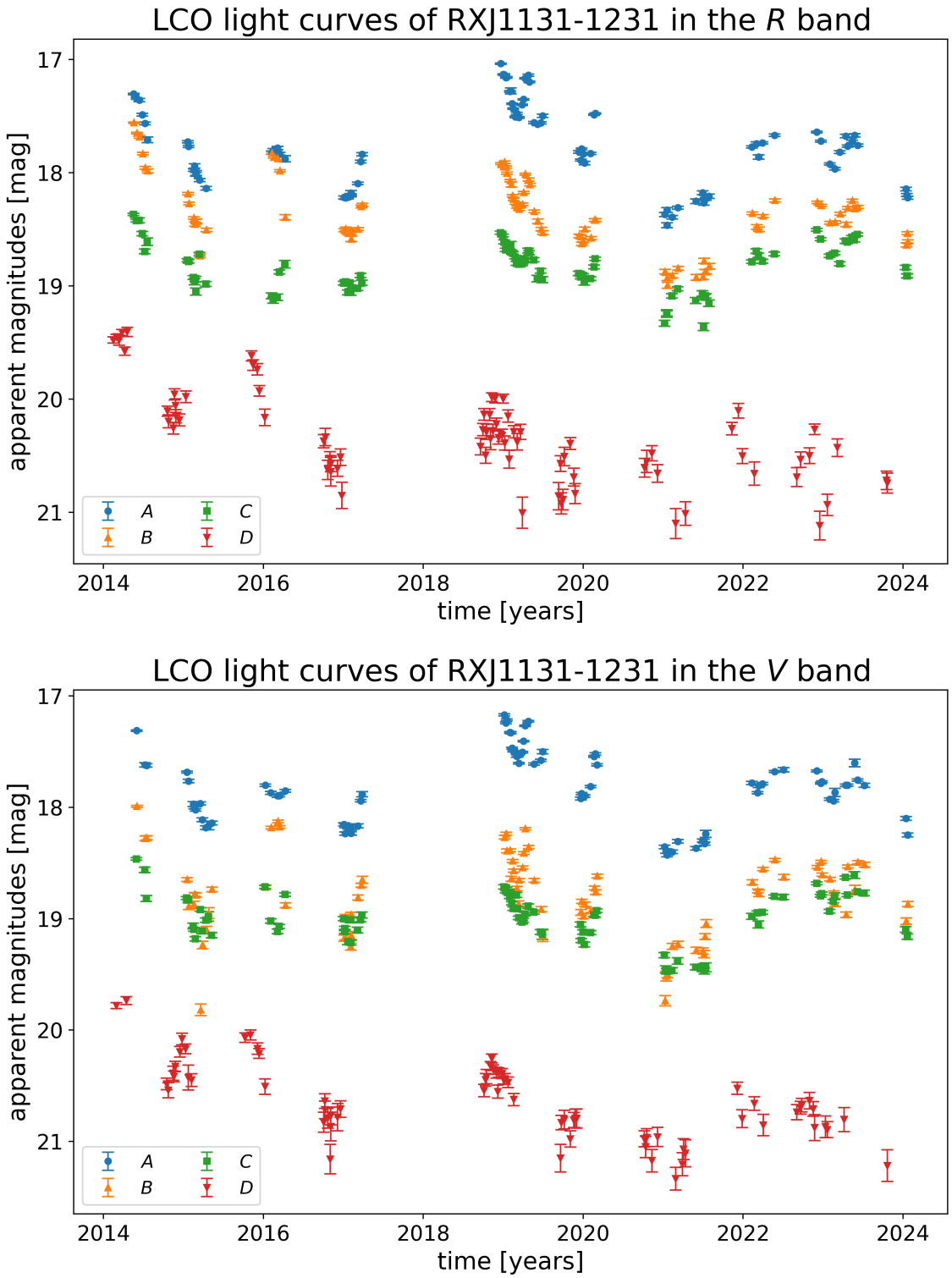

Figure 4.7.: Light curves of RXJ1131-1231. Shown are the time delay corrected light curves of the four images of RXJ1131-1231 in the R band (upper panel) and V band (lower panel), plotted with the same time range and no magnitude offsets.

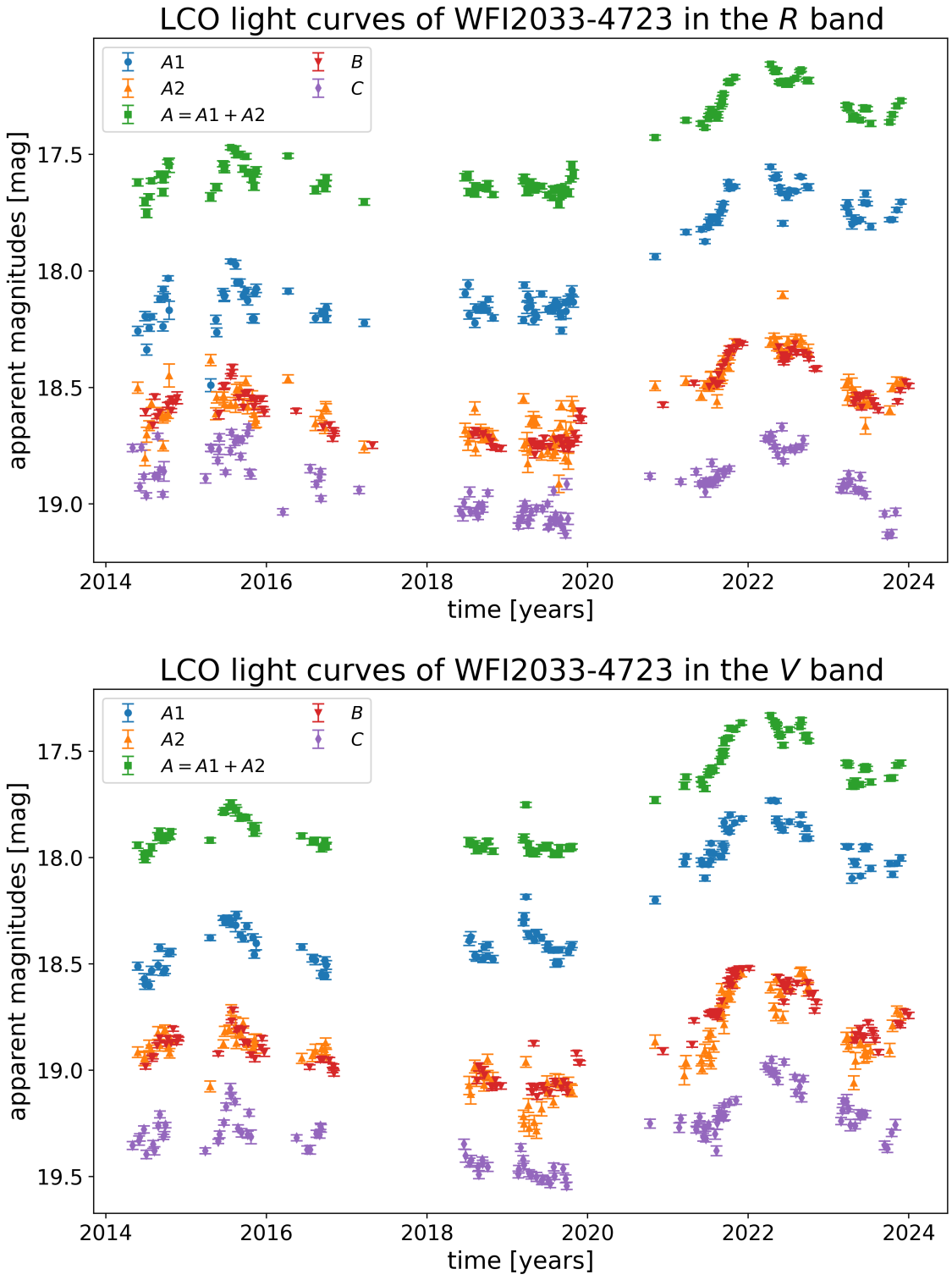

Figure 4.8.: Light curves of WFI2033-4723. Shown are the time delay corrected light curves of the four images of WFI2033-4723 (A1, A2, B and C) as well as the combined image A = A1 + A2 (where the fluxes of the close image pair is added together) in the R band (upper panel) and V band (lower panel), plotted with the same time range.

4.2. Comparison with published light curves

All eight systems have been monitored by other research groups in the past (see Chapter 2). However, only for a few, there is data in either the R or V band that is overlapping with the time range of our observing campaign. Comparing to these data sets, we generally find agreement of the light curves of the quasar images in the shared observing seasons. Here we give a few examples of such comparisons.

First, as the main object of interest for Part II and Sorgenfrei et al. (2025), in Fig. 4.9 we show a comparison of our HE0435-1223 light curves with COSMOGRAIL data (Millon et al. 2020a) in the R band. Our light curves can be matched well to their data in both overlapping seasons (and to the single COSMOGRAIL epoch in late 2018), except for a few outliers, without relative offsets between the four images.

Unfortunately, one example, where there is no data overlap in time, is within our research group, i.e. the MiNDSTEp data of Q2237+0305, HE0047-1756 and WFI2033-4723 by Emanuela Giannini (Giannini et al. 2017; Giannini 2017), where data was obtained from 2008 to 2012 at the 1.54 m Danish telescope at La Silla/ESO (European Southern Observatory). Still, in Fig. 4.10, we compare our LCO V band light curves of WFI2033-4723 to the ones from MiNDSTEp (a similar comparison can be made in the R band). Even though there is no overlap in time, after adding a shared magnitude offset of 16.6 mag to all MiNDSTEp curves, our LCO data seem to naturally continue the trends, relative magnitude differences and typical features of their light curves.

In Appendix A (Fig. A.3), we show a similar comparison to the MiNDSTEp data for HE0047-1756, again with no overlap in time. However, as already mentioned (in Chapter 2), there are lots of data sets of the Einstein Cross, e.g. by COSMOGRAIL (Millon et al. 2020a), Liverpool-Maidanak observations (Goicoechea et al. 2020) and most importantly from OGLE (Woźniak et al. 2000a; Udalski et al. 2006). Combined with the MiNDSTEp data and our LCO data, we can create long light curves covering more than a quarter of a century (from 1997 to 2024) in the V band (while there is no OGLE R band data), where only small magnitude offsets have been applied to some of the curves to achieve an adequate matching. This is shown in Fig. 4.11.

Additionally to the HE0047-1756 MiNDSTEp and LCO comparison, two more light curve comparisons are presented in Appendix A, both where we compare our data to the R band data from COSMOGRAIL (Millon et al. 2020a). There is the (in Sect. 3.4) already mentioned comparison for RXJ1131-1231 in Fig. A.6 and finally, Fig. A.1 depicts the comparison for HE2149-2745. In both comparisons with COSMOGRAIL data, it is clear that their data is of higher quality (especially for HE2149-2745, image B). Still, the light curves match well in the shared observing seasons.

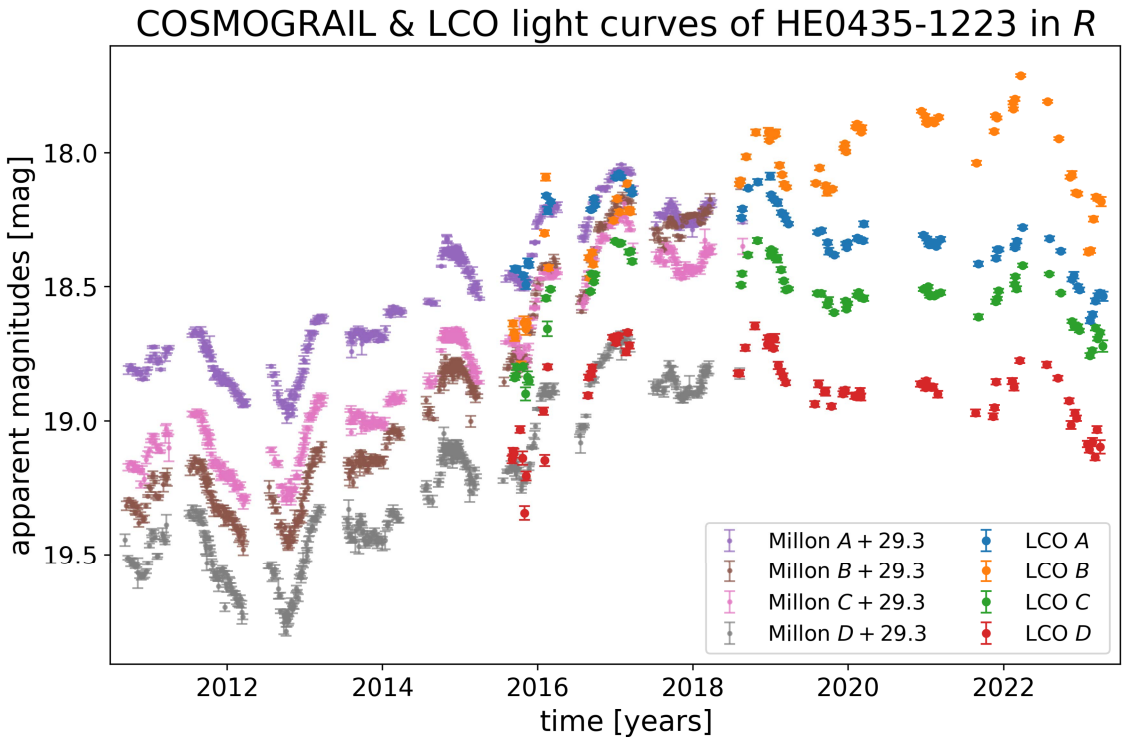

Figure 4.9.: Comparison of COSMOGRAIL (2003-2018) and LCO (2014-2024) light curves of HE0435-1223 in the R band (shown is only the data in 2010-2023).

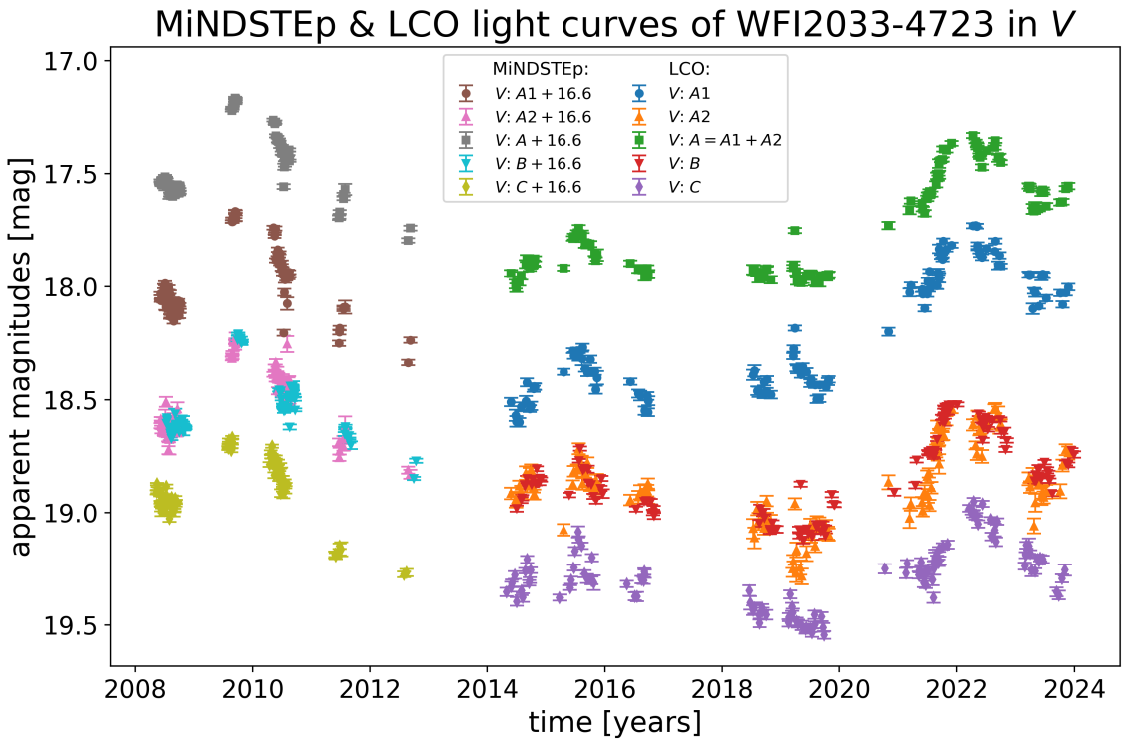

Figure 4.10.: Comparison of MiNDSTEp (2008-2012) and LCO (2014-2024) light curves of WFI2033-4723 in the V band.

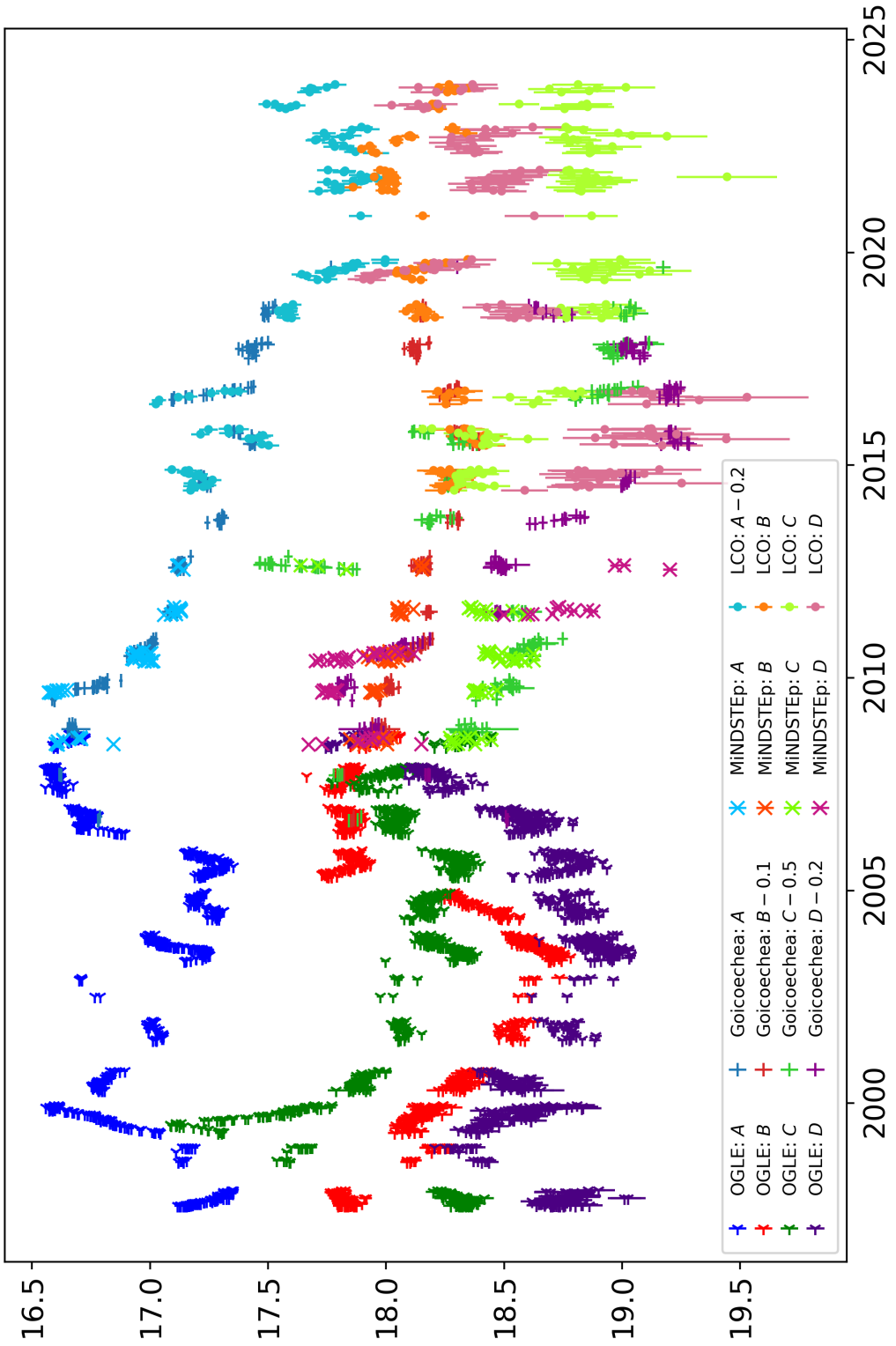

Figure 4.11.: More than a quarter century of the Einstein Cross – light curve comparison of Q2237+0305 in the V band. Shown are the apparent magnitudes of the images with time in years (image rotated for displaying reasons) from four different data sets: OGLE (1997-2008), Liverpool-Maidanak (2006-2019), MiNDSTEp (2008-2012) and our LCO data (2014-2024). A few small magnitude offsets had to be included to match the light curves, which mostly appears to be very successful.

5. Unveiling the microlensing content: difference light curves

Strongly lensed quasars can be used for various applications, such as studying the lens galaxy (see e.g. Shajib et al. 2024 for an overview of cosmological applications of strong lensing – not only of quasars, but e.g. also of supernovae – by galaxies in general) and investigating the dark matter distributions or possible substructures in the lens (see e.g. Mao & Schneider 1998; Wambsganss et al. 2000; Xu et al. 2015; Nierenberg et al. 2024 or Vegetti et al. 2024 and references therein). Also, there is time delay cosmography (e.g. Refsdal 1964; Bonvin et al. 2017; Birrer et al. 2024; TDCOSMO Collaboration et al. 2025) to measure the *Hubble* constant H_0, time delay determination in general (e.g. Vanderriest et al. 1989; Giannini et al. 2017; Millon et al. 2020a) and finally quasar microlensing (e.g. Chang & Refsdal 1979; Kochanek 2004; Schmidt & Wambsganss 2010; Morgan et al. 2018; Vernardos et al. 2024).[38]

We focus on the latter, i.e. studying the structure of quasars, specifically their accretion disks, through the magnifying glass that is microlensing, using our LCO light curves. In order to analyze and interpret quasar microlensing events, we first have to detect and isolate them in our data set. This 'unveiling' of the microlensing content in our light curves is presented in this chapter.

5.1. Theory and Method

5.1.1. Basic concept

In order to extract potential microlensing content from the quasar light curves presented in the last chapter, we calculate the magnitude differences between the light curves of pairs of images, i.e. we calculate so-called 'difference curves'. If the light curves of the individual images are corrected for the time delays (due to the different light travel paths from strong lensing, see Sect. 1.3), the unknown intrinsic quasar

[38] Multiple reviews cited here are part of an open access *Space Science Reviews* series covering the various aspects of 'Strong Gravitational Lensing', giving an in-depth, current and comprehensive overview of the field; see https://link.springer.com/collections/jafbihjfcj.

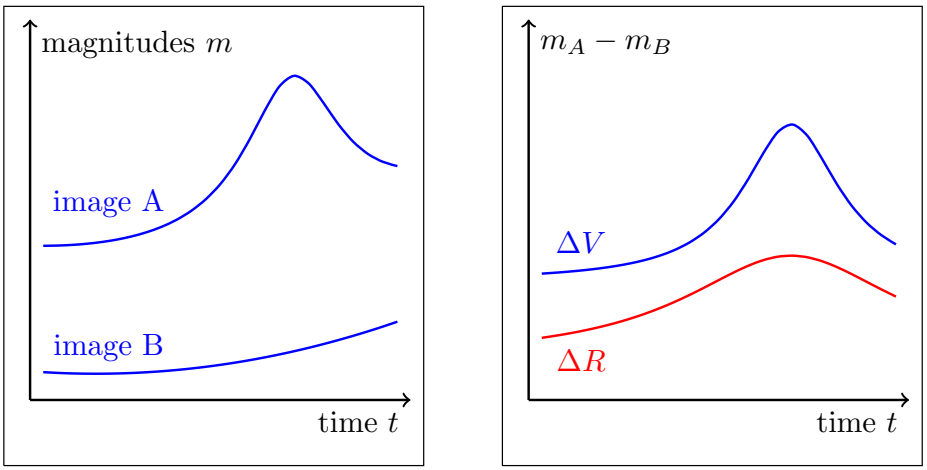

Figure 5.1.: Schematic idealized difference curve. On the left, two hypothetical time delay corrected V band light curves of two images A and B of a lensed quasar are sketched continuously in time. On the right, the upper blue curve ΔV shows their difference curve, removing the brightness variation shared by both images (i.e. the slow rise visible on the left) and thus revealing the 'microlensing event' (i.e. the bump). The lower red curve ΔR shows a possible corresponding difference curve in the R band (with an arbitrary offset); essentially a smoothed version, as one would expect from a larger quasar size for that filter (see Sect. 1.4 and Fig. 1.3).

variability present in all images is removed (e.g. Kochanek 2004; Anguita et al. 2008, and many others). This is illustrated in Fig. 5.1: two image's (time delay corrected) light curves $m_A(t)$ and $m_B(t+\Delta t_{\mathrm{AB}})$ are shown. Here, image A exhibits an additional variation, representing a microlensing event $\mu_A(t)$, on top of the shared slow increase of both images, i.e. the intrinsic quasar variability $I(t)$. Calculating the difference, the microlensing content is revealed.[39] Formalizing this idea, the light curves (i.e. magnitudes as a function of time; compare with Eq. 3.7) of the two example images can then generally be written as:

$$m_A^X(t) = I^X(t) + C_A + \mu_A^X(t) \quad \text{and} \quad m_B^X(t) = I^X(t - \Delta t_{\mathrm{AB}}) + C_B + \mu_B^X(t), \tag{5.1}$$

where the superscript X denotes the passband and we included possible microlensing content μ_B in image B. Thus, in the difference curve – besides a for us irrelevant constant offset from the different strong lensing magnifications of the two images C_A and C_B – only microlensing remains:

$$\Delta X_{AB}(t) := m_A^X(t) - m_B^X(t + \Delta t_{\mathrm{AB}}) = \mu_A^X(t) - \mu_B^X(t + \Delta t_{\mathrm{AB}}) + C_A - C_B. \tag{5.2}$$

[39] Generally, quasar microlensing events are not separated cleanly, but overlap and independently can be present in all images simultaneously, as it is e.g. the case with Q2237+0305 (see Sect. 2.2.3). This leads to difference curves containing overlapping microlensing events from both images, with no immediate way of matching them to the image they originated from.

Since microlensing in the two images is completely unrelated $\mu_A^X \neq \mu_B^X$, a non-constant difference $\Delta X_{AB}(t)$ exposes the presence of microlensing. Here, it is also apparent that potential colour variations of the quasar itself (i.e. unequal time derivatives of the intrinsic R and V band brightnesses $\dot{I}^R(t) \neq \dot{I}^V(t)$, do *not* affect the microlensing signal in the difference curves and *cannot* mimic chromatic microlensing since $I^X(t)$ has canceled completely.[40] However, something else at least in principal can mimic microlensing – extinction. Before continuing, note that all of this discussion of course does not only hold for a double quasars images A and B, but *all* images and image combinations ($m_\alpha - m_\beta$ with images $\alpha \neq \beta$) of the lensed quasars.

5.1.2. The role of extinction and other potential contaminants

In principle, all astrophysical phenomena that might occur in the vicinity of the quasar images can result in contaminated data. For instance, dust along the line of sight to the images decreases their brightness and can cause additional variability in the light curves (see e.g. Yonehara et al. 2008). We can neglect extinction in the Milky Way, as well as extinction in the quasar host galaxy, because there, the light paths of the individual images are not separated by large physical distances (Vernardos et al. 2024). Thus, this kind of extinction affects all light curves in one filter in the same way and therefore cancels out in Eq. 5.2, if we add extinction terms from those locations to Eq. 5.1. However, doing so for the extinction in the lens galaxy will not lead to cancellation of terms, since in the lens galaxy the light paths are physically separated by distances on the scale of the lens galaxy itself, i.e. kiloparsecs. There, dust content cannot be expected to be identical and therefore two extinction terms $E_A^X(t)$ and $E_B^X(t)$ added to the light curves (Eq. 5.1) will end up in the difference curve (Eq. 5.2) in a similar way as the microlensing content, potentially time and filter depend as well. However, if the time dependence of these two additional extinction terms is weak (i.e. on longer time scales) compared to the short time scales of typical microlensing variations of down to mere weeks (Sect. 1.4), then extinction just introduces constant offsets in the different filters $E_A^X - E_B^X$, which are irrelevant for our analysis (similar as the magnification offsets C_A and C_B in Eq. 5.2).

So far, in quasar microlensing light curve analyses, differential extinction is only occasionally taken into account: e.g. Burud et al. (2002) studied the influence of extinction on their data using spectra, concluding with a preference for microlensing

[40] Note that calculating differences of one image with itself in different filters leads to curves, e.g. $\Delta A^{RV}(t) := m_A^R(t) - m_A^V(t) = \mu_A^R(t) - \mu_A^V(t) + I^R(t) - I^V(t)$, containing not only the chromatic microlensing signal from just that image, but also quasar colour variations (and differential galactic extinction $E_A^R(t) - E_A^V(t)$ from the next section). These colour curves, as well as their differences ($\Delta A^{RV} - \Delta B^{RV} = \Delta R_{AB} - \Delta V_{AB}$, removing all intrinsic terms and constant offsets), are sometimes considered to disentangle the various signals present (see e.g. Giannini et al. 2017).

as origin for observed signals. Similar, Eigenbrod et al. (2008b) find only constant extinction contributions (with the same consequence as the time scale argument mentioned above). Also, by showing that microlensing simulations do reproduce the light curves (e.g. by using the method by Kochanek 2004), microlensing generally is the preferred explanation for observed variations (Yonehara et al. 2008) and typically solely considered in analyses (e.g. Poindexter & Kochanek 2010a; Morgan et al. 2010). As discussed in Chapter 3 of Vernardos et al. 2024, describing the different analysis methods in detail including extinction aspects, when using single epoch methods focusing on flux ratios or emission line shapes, corrections with microlensing-free baselines (as proxies for the extinction content) are included. Similarly, in the histogram method (e.g. Forés-Toribio et al. 2024) light curves from the infrared, corresponding to the largest scales of the quasar unaffected by microlensing, are included.

Additionally, reverberation of the continuum flux by the BLR is discussed as the source of high frequency variations in light curve data. A first analysis focusing on this effect first proposed by Sluse & Tewes (2014) has been done by Paic et al. (2022), but has not been incorporated into the standard microlensing analysis method since.[41]

5.1.3. Light curve interpolation

Contrary to Fig. 5.1, measured light curves are of course *not* continuous functions in time. The shifting in time these measured discrete light curves according to their time delays means that a difference is not directly calculable, since the data points of the involved light curves in general are not at same times anymore (except for Q2237+0305, where the time delays vanish, see Table 2.1). Thus, interpolation between the data points is required. This necessary interpolation creates several issues:

1. First of all, both the exact choice of interpolation scheme (linear, cubic, etc.), as well as the errors of the time delays creates additional uncertainty on the values of the interpolated curve.

2. Additionally, the choice of which curve to interpolate to the epochs of the other in each pair can have influence on the resulting difference as well (where only one curve should be interpolated, since interpolating both would create twice as many, non-independent data points).

3. Next, especially at observational gaps (but also inside seasons) there is the question of the maximum separation in time over which one chooses to interpolate and whether extrapolation at the edges of longer gaps is justifiable.

[41] See Morgan et al. (2010); Rivera et al. (2023, 2024) for discussions on BLR reverberation, treating this effect as a constant 30% flux contaminant, but not including the frequency aspect.

4. The uncertainty of the involved time delays adds to the uncertainty of the light curve (especially a problem for HE2149-2745 in our data set, see Sect. 2.2.2).

5. Finally, time delays that shift one light curve mostly into the seasonal observation gaps (which are quite extended in our LCO data) of the other image would of course leave us with little of a difference curve to continue working with.

This final problem especially occurred in HE1104-1805, where its time delay of approximately half a year left only little overlap in the shifted curves, and thus only a few data points could be calculated for the difference curve. However, for other quasars, with smaller time delays, such as HE0435-1223, this is not a relevant problem since the slightly shifted light curves leave large overlaps.

Regarding the first two points, we decided to use linear interpolation of the typically brighter images to the fainter ones. In general, image A was interpolated to the (time delay corrected) epochs of image B (and for the quadruple quasars also to) C and D, as well as image B to images C and D and finally image C to image D. In a few cases, we also include comparisons with difference curves that were interpolated the other way around.

Referring to the third point, interpolation between data points is only done if they are separated by ≤ 30 days (except for HE1104-1805, where we increased that limit slightly by three and a third days, due to the already mentioned problems with its half-year time delay, i.e. to gain a few more data points at the small overlaps especially for the comparison between interpolating image A or image B). Furthermore, no extrapolation into observational gaps is used. Note, that these previous points mean, that the number of data points vastly differs not only for the eight quasars, but also between the different image pairs within a quasar's data set.

Lastly, regarding the fourth point, we tested the influence of the uncertainties of the time delays on the difference curves for HE0435-1223 for its analysis in Sorgenfrei et al. (2025). The errors of the time delays are less than a day (0.8 days, see Table 2.1), which is negligible compared to all other error sources. Indeed, incorporating the errors of the time delays, we have created and checked 1000 difference curves. They appear highly similar, with only small magnitude changes typically around 0.003 mag as well as small error changes on the same order, which is why we neglect it (also, because the systematic error of 0.05 mag included later clearly covers this level of uncertainty; see Sect. 6.2).

The uncertainties (e.g. $\Delta m_{A,\,\mathrm{interp.}}$) of the interpolated light curves (e.g. $m_{A,\,\mathrm{interp.}}$) are estimated from Monte Carlo sampling. To be explicit, we draw 2048 magnitude values at each (uninterpolated) epoch according to the data points magnitude values and errors assuming Gaussian distributions. We then interpolate those 2048 light

curves and measure the spread (i.e. standard deviation) at the new epochs.

Finally, the difference curves then simply are the (time delay corrected) differences between an image's light curve and the suitably interpolated light curve of another image (essentially Eq. 5.2), e.g.:

$$B - A := m_B(t + \Delta t_{\mathrm{AB}}) - m_{A,\,\mathrm{interp.}}(t), \tag{5.3}$$

$$C - B := m_C(t + \Delta t_{\mathrm{AC}}) - m_{B,\,\mathrm{interp.}}(t + \Delta t_{\mathrm{AB}}), \tag{5.4}$$

with the other combinations following accordingly. The uncertainties of the difference curves are determined with standard Gaussian error propagation, i.e. for instance the error of Eq. 5.3 is given by $\Delta(B - A) = \sqrt{(\Delta m_B)^2 + (\Delta m_{A,\,\mathrm{interp.}})^2}$. This is done for all 16 data sets. The resulting difference curves are presented in the next section.

5.2. Difference curves from LCO data

In Figs. 5.2, 5.3, 5.4 and 5.5, the difference light curves of the double quasars HE1104-1805 and HE2149-2745, as well as the quadruple quasars Q2237+0305 and HE0435-1223 are presented. The remaining four quasar's difference curves are shown in Figs. A.4, A.5, A.7 and A.8 (in Appendix A, together with a few comparison plots from Sect. 4.2). Note that the difference curves of HE0435-1223 are already published in Sorgenfrei et al. (2025), while the other quasar's difference curves are all unpublished. Going through our results, most of the difference curves of the eight quasars are clearly non-constant (i.e. $\Delta X_{AB}(t) \neq$ const. in Eq. 5.2), thus very likely displaying quasar microlensing, following the arguments in the previous section (Sect. 5.1):

- The difference curves for HE1104-1805 in Fig. 5.2 only contain a few data points (consistent for interpolating either image) due to the time delay as discussed in Sect. 5.1.3. Nevertheless, the curves are non-constant indicating the presence of microlensing (which has already been detected in this system; see Sect. 2.2.1).
- Using all three possible time delays for HE2149-2745 (see Table 2.1 and Sect. 2.2.2), in Fig. 5.3 clear microlensing is exposed in our LCO data as suspected in Sect. 4.1.1, where $B - A$ increases by around to 0.4 mag over the ten years independently of the time delay. This makes it an interesting target for a microlensing analysis, potentially restraining the time delay if simulations would prefer one difference curve over the other two. Also, in Fig. A.2, we compare our R band difference curve of HE2149-2745 to one we obtain using COSMOGRAIL data (Millon et al. 2020a). Our data matches and naturally continues their data (i.e. the rising microlensing signal), again independent from the delay.

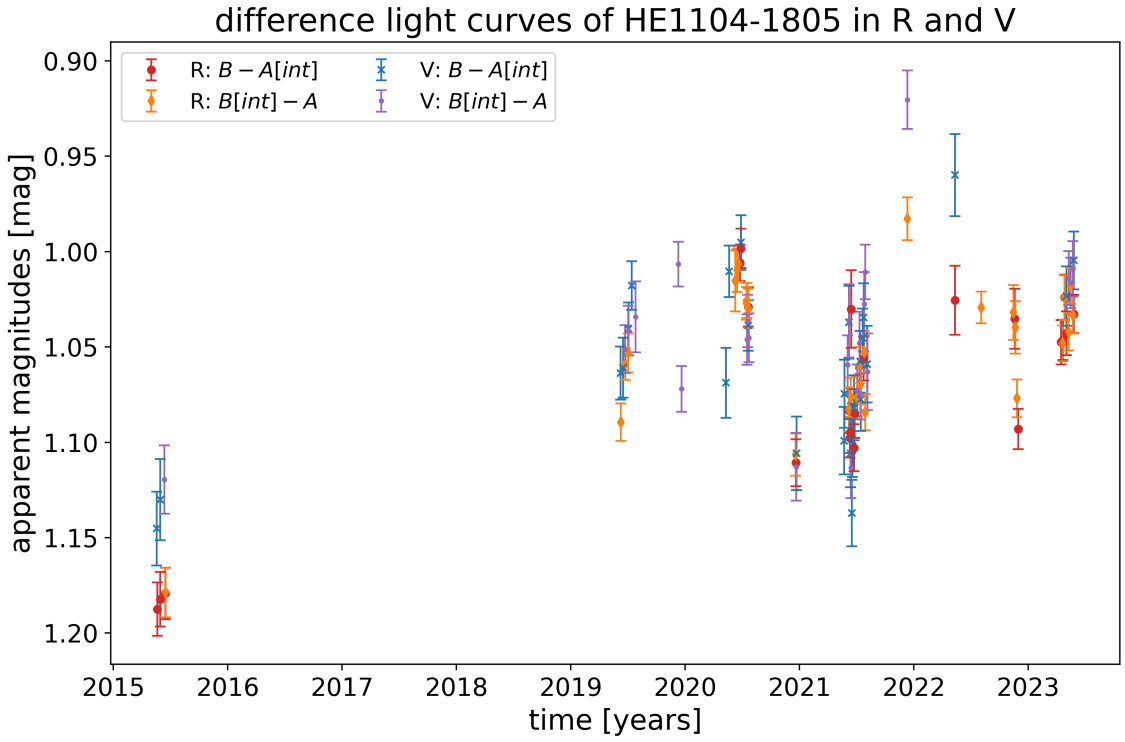

Figure 5.2.: Difference curves of HE1104-1805. Shown are $B - A$ differences, once with the light curves of image A interpolated to the epochs of image B and vice versa, both in R (red circles and orange diamonds) and V (blue crosses and violet dots).

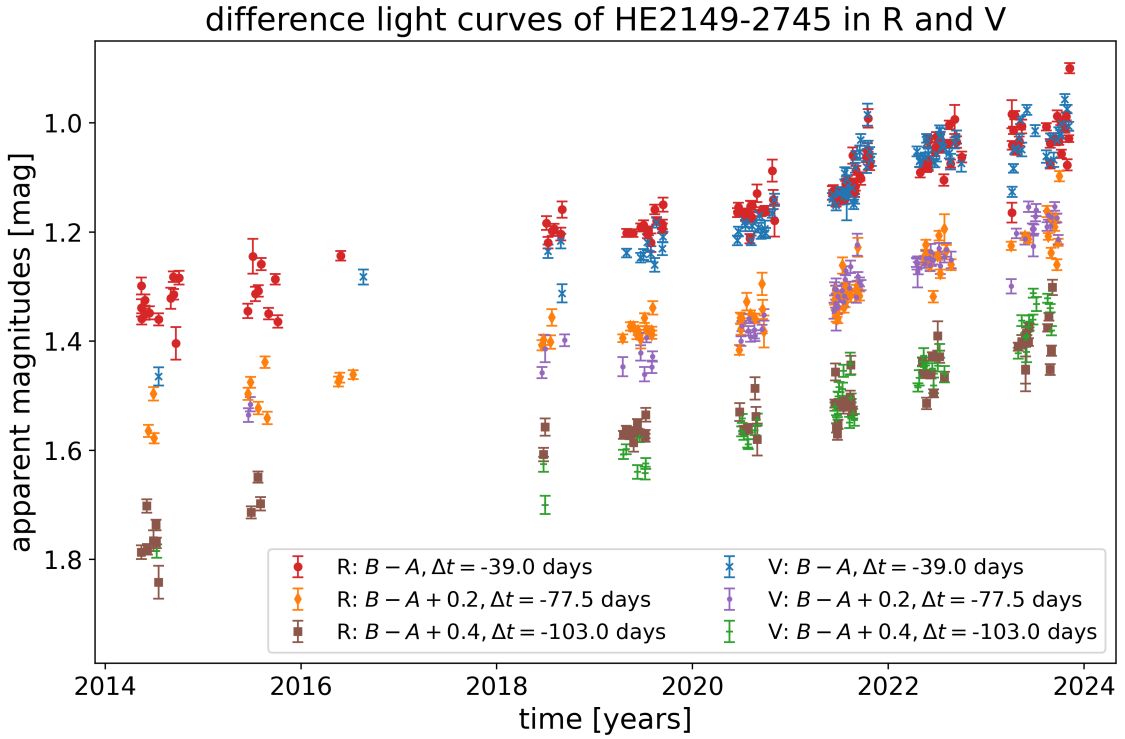

Figure 5.3.: Difference curves of HE2149-2745. Shown are $B - A$ differences in R and V, determined for each time delay from Table 2.1 separated by magnitude offsets.

- The six image difference combinations for Q2237+0305 (in both bands) are presented in Fig. 5.4, where no interpolation was necessary due to the negligible time delays (Sect. 2.2.3). Clearly, all four quasar images are constantly affected by microlensing (also see Sect. 4.1.1), as known, observed and studied for a long time (Sect. 2.2.3 and the quarter-century-long light curves in Fig. 4.11).
- Fig. 5.5, clearly shows the microlensing signal in the LCO data of HE0435-1223 as already described in Sect. 4.1.2: all three combinations of difference curves with respect to image B show a prominent microlensing variation. Colour effects are also visible as the variation has an amplitude that is larger in the V, than in the R band. This is the *chromatic microlensing* signal analyzed in Sorgenfrei et al. (2025). Note also that the other combinations also display variations, though smaller ones. As the $D-C$ curves are mostly flat (implying no microlensing), they likely originate in image A as a brightness-decreasing long-term microlensing signal ($\sim 0.05\,\mathrm{mag/yr}$). This is the reason why in Sorgenfrei et al. (2025) – as well as in Part II of this thesis – we focused on the $B-C$ curve instead of e.g. the $B-A$ curve, as the latter includes microlensing signals from both lines of sight, making it more difficult to analyze.
- The R and V band $B-A$ difference curves for HE0047-1756 are shown in Fig. A.4. Due to the high level of noise (from image B, see Fig. 4.5), a detection of (chromatic) microlensing in our data is very difficult (and mostly independent of which image is being interpolated) and seems questionable at best.
- Similar as for HE1104-1805, there remains only a small number of data points in the difference for Q0142-100 in Fig. A.5. Together with the issues regarding image B (see Sect. 3.5 and Fig. 4.6), this makes any detection (or non-detection) difficult to claim in our data (see also Sect. 2.2.6).
- Due to the larger time delay with respect to image D, the RXJ1131-1231 differences in Fig. A.7 of the other images contain a larger number of data points, which do expose microlensing variation, especially in the $B-A$ curve.
- Finally, in Fig. A.8, all difference combinations for WFI2033-4723 are shown, not only with respect to the combined image A, but also to A1 and A2 (see Sect. 4.1.4). A long-term linear trend over $\sim 0.3\,\mathrm{mag}$ is present in all combinations with respect to image A (and A1), thus revealing microlensing in our data, as has been detected by others in this system (see Sect. 2.2.8).

This concludes Part I of this thesis, having presented our measurements and reduction of LCO data of eight lensed quasars to determine their light and subsequent difference curves exposing microlensing signals, whose analysis is the goal of Part II.

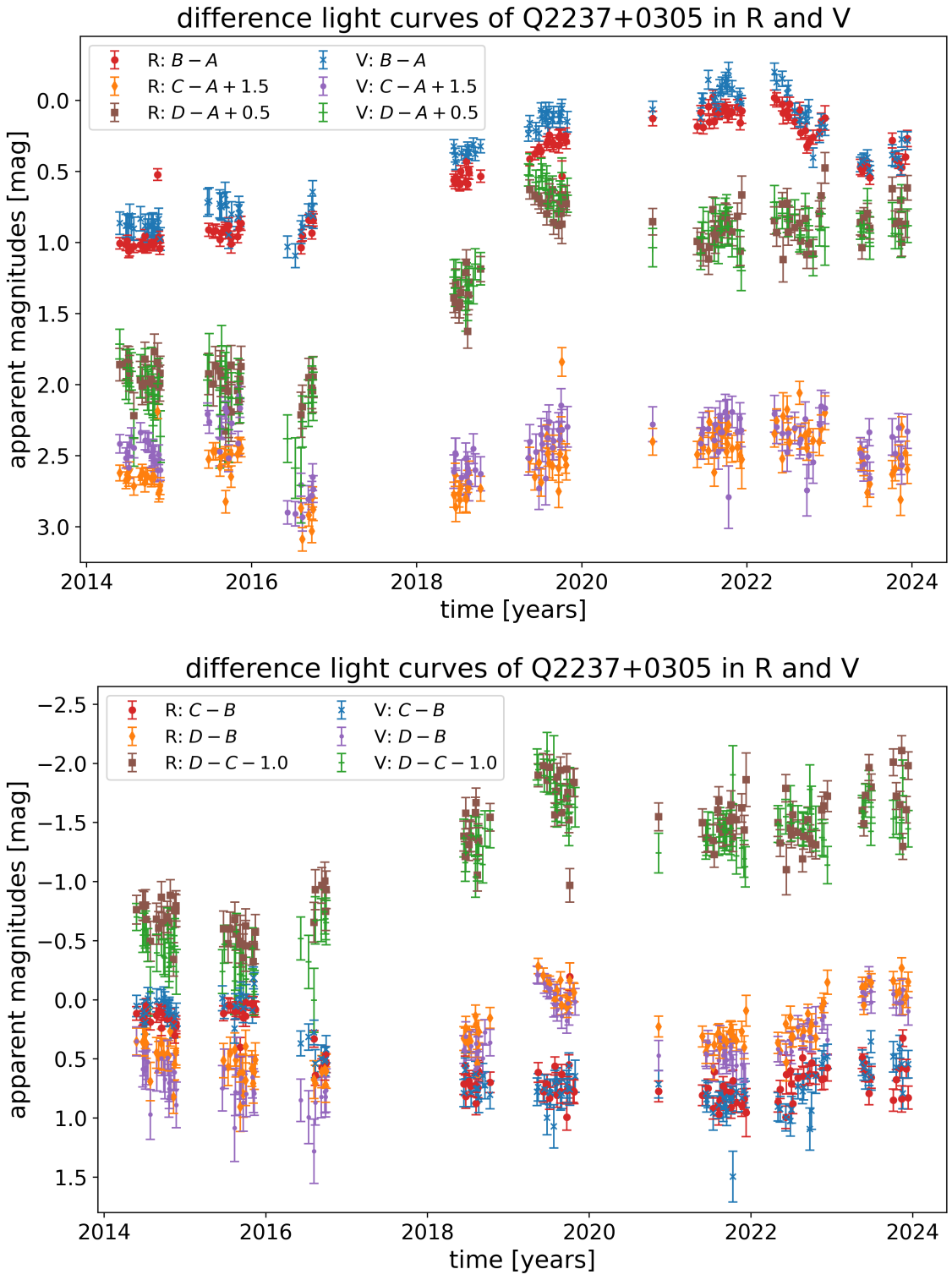

Figure 5.4.: Difference light curves of Q2237+0305. Shown are all six combinations of differences of pairs of the four light curves ($B-A$, $C-A+1.5$ mag and $D-A+0.5$ mag on the top and $C-B$, $D-B$ and $D-C-1.0$ mag on the bottom) in the R band (red circles, orange diamonds and brown squares) as well as the V band (blue crosses, violet dots and green minuses).

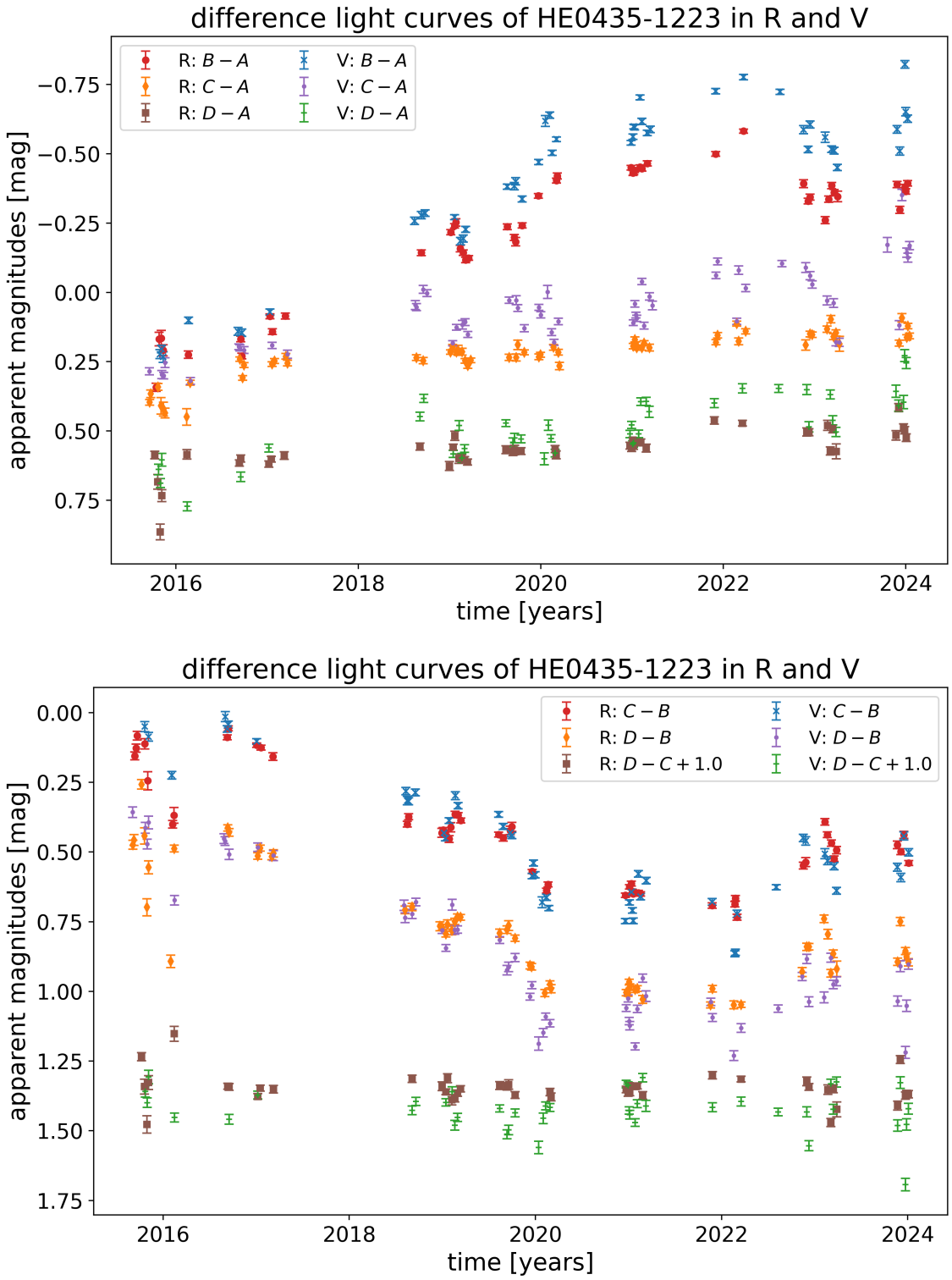

Figure 5.5.: Difference light curves of HE0435-1223. Shown are the six combinations of differences of all pairs of the four light curves ($B-A$, $C-A$ and $D-A$ in the top panel and $C-B$, $D-B$ and $D-C+1.0$ mag in the bottom panel), each in the R and the V band (with the same colour and symbol scheme as Fig. 5.4). For reference, in the aforementioned order of difference curves, there are 48/46, 60/55, 45/41, 51/49, 58/54, 45/41 data points in R/V. This figure is adapted from Sorgenfrei et al. (2025).

Part II.

Simulating and interpreting quasar microlensing curves

6. Microlensing simulations

Part I of this thesis culminated with the presentation of the difference curves, thus revealing the microlensing content we captured with our LCO observation campaign of eight lensed quasars in two photometric filters over ten years. However, the envisioned goal of this survey was not only to just detect chromatic quasar microlensing, but furthermore to analyze and interpret the data with respect to quasar accretion disk theory. This is the objective of Part II.

The LCO difference curves of most of the eight quasars, as described and discussed in Sect. 5.2, exhibit microlensing. However, since the data quality, the size of each quasar's data set and the significance of the uncovered microlensing signals varied among them, not all were considered for further analysis. Additionally, as this project's time was naturally limited, one system with the most promising data was chosen for analysis. We especially considered the data of HE2149-2745, Q2237+0305 and HE0435-1223, due to their comparatively strong microlensing signals and high data quality, and finally selected our data of HE0435-1223 (Fig. 5.5) for subsequent microlensing analysis. This data has the advantage of clearly exposing a – in comparison with Q2237+0305 rather isolated – strong microlensing event in image B (around 0.7 to 0.8 mag in the $C - B$ curve of Fig. 5.5, noticeable already in the light curves in Sect. 5.2), including a chromatic effect (the variation is larger in the V band) and no issues with the time delays in comparison to HE2149-2745. However, as described in Sects. 4.1.2 and 5.2, some microlensing is also present in image A, but not (or at most very little) in images C and D. Thus, the $C - B$ and $D - B$ curves (i.e the upper four curves in the lower panel of Fig. 5.5) are best suited for analysis, as their microlensing signal originates chiefly from one line of sight, avoiding a combinatorial explosion from simultaneously simulating microlensing in all four images (as would be necessary for Q2237+0305, see e.g. Kochanek 2004). Therefore, we restricted ourself to the $B - C$ curve of HE0435-1223[42], as described in Sorgenfrei et al. (2025).

In order to analyze this chromatic microlensing signal in image B of HE0435-1223, we simulated microlensing light curves of image B and fitted them to our $B - C$ data (assuming that no microlensing variation is present in image C). This was done using

[42] We use the negative of Eq. 5.4, i.e. $B - C = -(C - B)$, inverting the magnitude-axis in Fig. 5.5 for the respective curves to have microlensing in image B as positive term in this difference.

the (in the field well known) 'Kochanek light curve fitting method' (Kochanek 2004), which has been utilized in a plethora of studies investigating microlensing in the light curves of many lensed quasars (e.g. by Anguita et al. 2008; Eigenbrod et al. 2008a; Morgan et al. 2010, 2018; Cornachione et al. 2020b; Rivera et al. 2024). We were thus able to draw conclusions on the accretion disk of HE0435-1223. This analysis was presented in Sorgenfrei et al. (2025), therefore parts of this chapter have already been published there.

6.1. Magnification patterns

6.1.1. Calculating microlensing maps with `Teralens`

Simulating microlensing light curves following the Kochanek method (Kochanek 2004) requires the generation of source-plane microlensing magnification patterns (or 'maps') with the microlensing parameters of the involved quasar images. Since these maps, depicting microlensing caustic patterns (see Sects. 1.3 and 1.4), are also central to other methods (see e.g. Forés-Toribio et al. 2024, for an application within the related histogram method) and extragalactic microlensing in general, multiple algorithms have been developed over the years to calculate them (see Vernardos et al. 2024, Sect. 2.7 for an overview and descriptions of the individual methods).

Instead of analytically solving the lens equation, determining caustics and the (micro-)lensing magnification throughout the source plane, typically the inverse ray shooting technique is employed (Kayser et al. 1986). In short, microlenses are distributed in the lens plane. Then, a grid of light rays are propagated backwards from the observer through the lens plane (where they are deflected according to the lens equation; Eq. 1.16) into the source plane. There, per pixel (labeled with index-pair ij), the number of rays N_{ij} (i.e. a flux), relative to the number if there were no lenses N_{rays}, is an approximation for the magnification N_{ij}/N_{rays} that an object located at this pixel-position would experience. As this is computationally expensive, Wambsganss (1990, 1999) developed an hierarchical tree code called `microlens`, drastically speeding up the calculations by appropriately grouping together microlenses at larger distances to a ray. Other methods have been developed (e.g. Kochanek 2004, Fourier method and Mediavilla et al. 2006, Polygon method). Using inverse ray shooting directly on graphics processing units (GPUs), the GERLUMPH team (Vernardos & Fluke 2013; Vernardos et al. 2014)[43] produced an enormous set of magnification maps for a wide parameter range (used e.g. by Vernardos & Tsagkatakis 2019, and others).

[43] Maps from GERLUMPH (GPU-Enabled, High-Resolution, cosmological MicroLensing parameter survey) are available at `https://gerlumph.swin.edu.au/`.

Recently, another fast GPU-based approach was published (Weisenbach 2025a,b)[44], however we opted to use yet another code parallelized for GPUs: `Teralens`.

Developed by Alpay (2019), `Teralens` essentially is a newer implementation of the hierarchical tree code of the inverse ray shooting technique from Wambsganss (1990, 1999), however, as already mentioned, fully parallelized for GPUs.[45] To our knowledge, the analysis in Sorgenfrei et al. (2025) is the first published usage of `Teralens` (see also Weisenbach 2025b) and the speed (a few minutes for the maps described in the following section) and resulting quality are remarkable. In the earlier stages of testing the code, we have successfully verified a few maps by comparing them to maps generated with `microlens`. Note for usage that the shear direction as defined for `Teralens` is rotated by $\pi/2$ in comparison to `microlens` (Wambsganss 1999). Additionally, we have included an output of N_{rays} to `Teralens` to convert the maps N_{ij} from counts to the magnitude scale $\mu_{ij} = -2.5 \log_{10}(N_{ij}/N_{\mathrm{rays}})$. All microlensing magnification maps as described in the following and used for our analysis were produced by running `Teralens` on the bwForCluster supercomputer BinAC.[46]

6.1.2. Magnification maps for HE0435-1223, image B

Following the analysis in Sorgenfrei et al. (2025), for image B of HE0435-1223, we fixed the total convergence and shear to $\kappa = 0.539$ and $\gamma = 0.602$ (Schechter et al. 2014) and varied the fraction of compact matter $\kappa_\star$ in steps of 0.1 from $\kappa_\star/\kappa = 0.1$ to 1.0 (the convergence is composed of contributions from compact and smooth matter $\kappa = \kappa_\star + \kappa_{\mathrm{smooth}}$; see Sect. 1.3). We assumed equal masses of $M = 1 M_\odot$ for all microlenses in the lens plane (as did e.g. Anguita et al. 2008), since microlensing results are (mostly) independent from the mass distribution (Lewis & Irwin 1996).[47] Also, as usual (due to the extreme computational costs), we use static lens mass distributions, i.e. ignoring the movement of the stars causing the lensing in this step, since it has been shown that this can just be incorporated as a constant factor into the absolute velocity distribution (this has been investigated by Kundić & Wambsganss 1993; Wambsganss & Kundić 1995; see also Kochanek 2004 and Sect. 7.3).

We produced ten statistically independent magnification maps (by having `Teralens` generate independent distributions of microlenses using different random seeds for each individual map, which all have also different $\kappa_\star$) with sizes of 8000^2 pixels cov-

[44] https://github.com/weisluke/microlensing/
[45] `Teralens` is available and documented in detail at https://github.com/illuhad/teralens.
[46] https://wiki.bwhpc.de/e/BinAC
[47] Still, many in the field (e.g. Kochanek 2004; Morgan et al. 2018; Rivera et al. 2024) do include mass distributions for the lenses (such as initial mass functions by Salpeter 1955; Kroupa 2002) for their analysis or investigate the mass distribution itself (Wyithe et al. 2000; Wyithe & Turner 2001). However, after some initial test with `Teralens` we decided against this extra complication.

ering $40\,R_\mathrm{E} \times 40\,R_\mathrm{E}$, thus with a resolution of $200\,\mathrm{pixel}/R_\mathrm{E}$. Using a flat cosmology (see footnote 2) with $H_0 = 70.0\,\mathrm{km\,s^{-1}\,Mpc^{-1}}$, $\Omega_{\mathrm{m},0} = 0.3$, and the redshifts from Sect. 2.2.4 (see also Table 2.1), the source-plane Einstein radius (which scales with the square root of the unknown mean mass $\langle M \rangle$ of the microlenses; Eq. 1.12) corresponds to

$$R_\mathrm{E} = \sqrt{\frac{4G\langle M \rangle}{c^2}\frac{D_\mathrm{S} D_\mathrm{LS}}{D_\mathrm{L}}} \simeq 5.42 \times 10^{16} \sqrt{\langle M \rangle / M_\odot}\ \mathrm{cm}, \tag{6.1}$$

where D_S, D_L, and D_LS are the angular diameter distances from observer to source, observer to lens, and lens to source (see Fig. 1.1). The $\kappa_\star/\kappa = 0.5$ `Teralens` map is shown on the left in Fig. 6.3 and $\kappa_\star/\kappa = 0.3$ and 0.8 are used for Fig. 6.4.

6.1.3. Including the source profile: convolved maps

As described in Sect. 1.4, the apparent source size – connected to our main focus: the quasar's temperature profile – strongly influences the observed microlensing signal (Fig. 1.3). As derived in Sect. 1.2 (Eq. 1.5) inserting the temperature profile (Eq. 1.3) of a quasar accretion disk from Shakura & Sunyaev (1973) into Planck's law (assuming a small filter width) results in a radial surface brightness profile

$$B(r) \propto \left[\exp\left(\left(\frac{r}{r_s}\right)^{3/4}\right) - 1\right]^{-1}, \tag{6.2}$$

with a characteristic scale radius r_s where the temperature $T(r_s) = hc/(k_B \lambda_0)$ matches the filter wavelength in the quasar rest-frame λ_0 (see Sect. 1.2). However, for simplicity (e.g. when applying a convolution) this profile is often replaced with a Gaussian brightness profile

$$B(r) \propto \exp\left(-\frac{r^2}{2r_s^2}\right), \tag{6.3}$$

with a (different) scale radius r_s. Substituting Eq. 6.2 therewith can be done, as Mortonson et al. (2005) showed (using various models) that it is primarily the overall disk size measured in half-light radii $r_{1/2}$ that is important for the effect microlensing has on the light curves, rather than the detailed shape of the brightness profile. This was later confirmed by Vernardos & Tsagkatakis (2019) using a deep machine learning approach. Nevertheless, we considered both profiles, mostly, to stay compatible with others (as most studies use one of them), but also since the resulting light curves do look different at least on the smaller scales. Also, while the thin disk has a pole and falls off slowly, the Gaussian disk is unphysical, but computationally advantageous.

Since the publication of the thin disk model by Shakura & Sunyaev (1973), many modifications to it have been proposed and developed (see Sect. 1.2 and e.g. Cornachione & Morgan 2020; Vernardos et al. 2024 for compact overviews). Therefore, for our analysis we also include a third profile: an in terms of $\beta < 3/4$ shallower temperature profile (compared with Eq. 1.3). These shallower profiles have been measured and predicted, as well as invoked to explain the typically observed disk size discrepancy, with the disk appearing larger in microlensing studies than expected from their luminosity (Poindexter et al. 2008; Morgan et al. 2010, 2018; Li et al. 2019; Cornachione et al. 2020a; Cornachione & Morgan 2020, the latter work concluding that microlensing studies favor shallower profiles by comparing results of 15 lensed quasars). As a compromise between these and other studies and models, for our third model we set the slope in Eq. 1.3 to $\beta = 1/2$ (even though there are also some predictions and measurements of steeper disks) and refer to it as the 'slim' accretion disk profile (referring to Abramowicz et al. 1988, whose model has $\beta \approx 1/2$, approximated from their Fig. 11, as has been noticed by Cornachione & Morgan 2020).[48] This, through the same derivation (Sect. 1.2), leads to the slim disks brightness profile:

$$B(r) \propto \left[\exp\left(\sqrt{\frac{r}{r_s}}\right) - 1\right]^{-1}. \tag{6.4}$$

Note, that its (also different) scale radius r_s is the radius where the filter wavelength matches the disk's temperature as for the thin disk (Eq. 6.2), but its theoretical size (Eq. 1.6) has to be modified depending on the specific theory (e.g. Li et al. 2019).

Finally, we want to remark again, that – for all three models – we do *not* include the physically necessary inner cutoff term (where at radius $r_{\rm in}$ the accretion disk ends and the matter falls into the black hole), which was already predicted by Shakura & Sunyaev (1973) in the thin disk profile (see Eq. 1.2). Including such a term for our profiles and simulations vastly increases the parameter space, since different unknown black hole masses (resulting in different $r_{\rm in}$) would have to be tested. Also $r_{\rm in} \ll r_s$, so neglecting the central part does not change much of the brightness distribution. In fact, convincing discoveries of 'black-hole shadows'[49] have not been achieved with microlensing analyses (with coming the closest to this goal being probably Mediavilla et al. 2015), as the small changes to the light curves simply cannot be distinguished with current data qualities. Furthermore, a disk inclination would decrease the apparent size of the central region compared to a flat face-on viewed disk, diminishing

[48] This slim accretion disk model, i.e. $\beta = 1/2$, also corresponds to $s = 1$ in the wind model by Li et al. (2019), while the standard thin disk model is recovered with $s = 0$.

[49] See the impressive very-long-baseline radio interferometry results by Event Horizon Telescope Collaboration et al. (2019, 2022), revealing the black-hole shadows of M87* and Sagittarius A*.

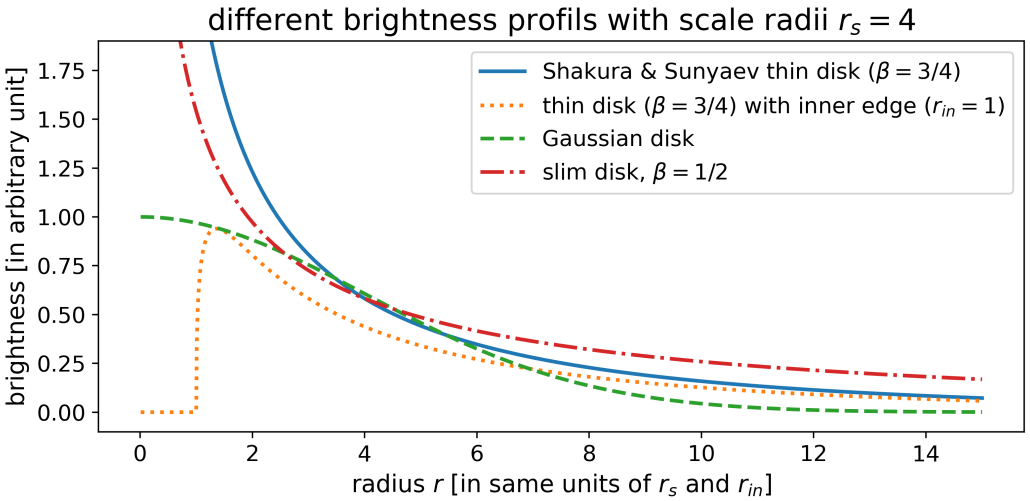

Figure 6.1.: Comparison of radial surface brightness profiles. Shown is the thin accretion disk profile without the inner cutoff term (blue, solid line; Eq. 6.2) as used for the simulations, and for comparison, the complete profile (orange, dotted line) including $r_{\rm in} > 0$ (Eq. 1.2), which we did *not* use. Also shown are the other two used profiles, i.e. the Gaussian disk (green, dashed line; Eq. 6.3), as well as the slim disk profile (red, dash-dotted line; Eq. 6.4), both again without inner cutoff terms. Note, that the slim disk ($\beta = 1/2$) is shallower than the thin disk ($\beta = 3/4$) and how the shapes of the profiles are very similar for large radii $r \gg r_s$ (independent of $r_{\rm in}$).

the effect further. Note that we also do *not* include the disk's inclination (and orientation), as this would again drastically increase the parameter space (except for a simple effective size change of the final results from an average inclination as typically done). Additionally, from AGN theory (see Sect. 1.1) and microlensing studies (Poindexter & Kochanek 2010a), it is clear that the inclinations of the accretion disks of the studied quasars should be more face-on than edge-on. This simplification, as well as ignoring inner edge effects by setting $r_{\rm in} = 0$, are typically done throughout the field (e.g. Kochanek 2004; Morgan et al. 2010; Cornachione et al. 2020b; Paic et al. 2022). The three radial brightness profiles (Eqs. 6.2, 6.3 and 6.4) are compared in Fig. 6.1 (together with one example of an inner cutoff term).

These profiles have different overall sizes as measured in half-light radii $r_{1/2}$, the relevant quantity as mentioned earlier (Mortonson et al. 2005; Vernardos & Tsagkatakis 2019). Integrating the three profiles, assuming circular symmetry

$$\int_0^{r_{1/2}} 2\pi r B(r) dr = \frac{1}{2} \int_0^{\infty} 2\pi r B(r) dr, \tag{6.5}$$

results in half-light radii of $r_{1/2} \simeq 2.44 r_s$ for the Shakura-Sunyaev thin disk profile (Eq. 6.2), $r_{1/2} = \sqrt{2 \ln 2} r_s \simeq 1.18 r_s$ for the Gaussian disk (Eq. 6.3) and $r_{1/2} \simeq 12.27 r_s$ for the slim disk profile (Eq. 6.4), all three viewed face-on (see Fig. 6.2).

We produced circularly symmetric 2D-profiles or kernels (extending out to $r_{\rm out} = 10r_s$ or at most $10\,R_{\rm E}$ for computational reasons) as a model for the brightness of face-on quasar accretion disks. Here, for each pixel at distance r to a central pixel, its value is given by the profiles $B(r)$. Then, each kernel is normalized to unity, to ensure that in the following step light is only redistributed (from a point source being magnified by the microlensing maps from Sect. 6.1.2 to extended disks). Applying the convolution theorem, we thus convolved our 10 ($\kappa_\star/\kappa$ varying) magnification patterns for image B with these kernels made from 80 different r_s for each disk model (the thin, the Gaussian and the slim disk), in total yielding 2400 convolved maps.

As described in Sorgenfrei et al. (2025), the 80 scale size values were chosen non-logarithmically over a large range.[50] We used the same values as scale radii for the thin disk (Eq. 6.2) and the Gaussian disk (Eq. 6.3), starting with 0.5, 1, 2, 3, 4, 6, 8, and 10 pixels, continuing in steps of 5 pixels up to 200 pixels, 10 pixel-steps up to 400 pixels, 20 pixel-steps up to 600 pixels, and finally 50 pixel-steps up to 800 pixels. Therefore, our analysis tests disks with scale radii as small as $0.0025\,R_{\rm E}$ and as large as $4.0\,R_{\rm E}$, corresponding to half-light radii (see Eq. 6.5) of $r_{1/2} \simeq 0.0029\,R_{\rm E}$ or $0.0056\,R_{\rm E}$ (around the pixel scale) up to $r_{1/2} \simeq 4.71\,R_{\rm E}$ or $8.96\,R_{\rm E}$ for the Gaussian and thin disks half-light radii, respectively. Since we calculated $r_{1/2}$ of the slim disk (Eq. 6.4) to be significantly larger than for the other two models, we rescaled all 80 slim disk's scale radii to a tenth of the previous r_s values (therefore ranging from 0.05 pixels to 80 pixels, i.e. slim disk scale radii of $0.000\,25\,R_{\rm E}$ to $0.4\,R_{\rm E}$ corresponding to $r_{1/2} \simeq 0.0031\,R_{\rm E}$ to $4.91\,R_{\rm E}$; also $r_{\rm out} = 100r_s$), to have comparable half-light radii.

Notably, numerically determined half-light radii of the kernels do not perfectly agree with the theoretical sizes as calculated from Eq. 6.5. For the smaller disks, deviations come from the pixelation (as their size is on the order of the pixel scale) and for the largest maps (limited to 4000^2 pixels for computational reasons as mentioned before) the numerical $r_{1/2}$ values do not increase enough anymore, since larger parts of the disk's outskirts are missing. This restricted the size range (together with the pixel scale and the total size of the maps) and we selected it, as well as $r_{\rm out}$, such that these issues are negligible for (most) of the tested sizes (see Fig. 6.2).[51] Note that for the rest, the theoretical half-light disk radii $r_{1/2}$ from Eq. 6.5 were used. Finally, as a comparison and an example, Fig. 6.3 shows one of the unconvolved `Teralens` maps together with two convolved versions of it, both using Shakura-Sunyaev thin disk kernels, once for $r_{1/2} \approx 0.3\,R_{\rm E}$ and once for $r_{1/2} \approx 1.0\,R_{\rm E}$.

[50] See Anguita et al. (2008); Eigenbrod et al. (2008a), for similar choices. Initially, we actually tested working only with ≤ 20 logarithmically-spaced sizes, as done typically (e.g. Kochanek 2004; Morgan et al. 2018). However, the final choice of size values became necessary for a successful determination of disk size *ratios*, which will be explained in the next chapter (see Sect. 7.2).

[51] For the Gaussian disk there is essentially no problem – a clear advantage of this unphysical model.

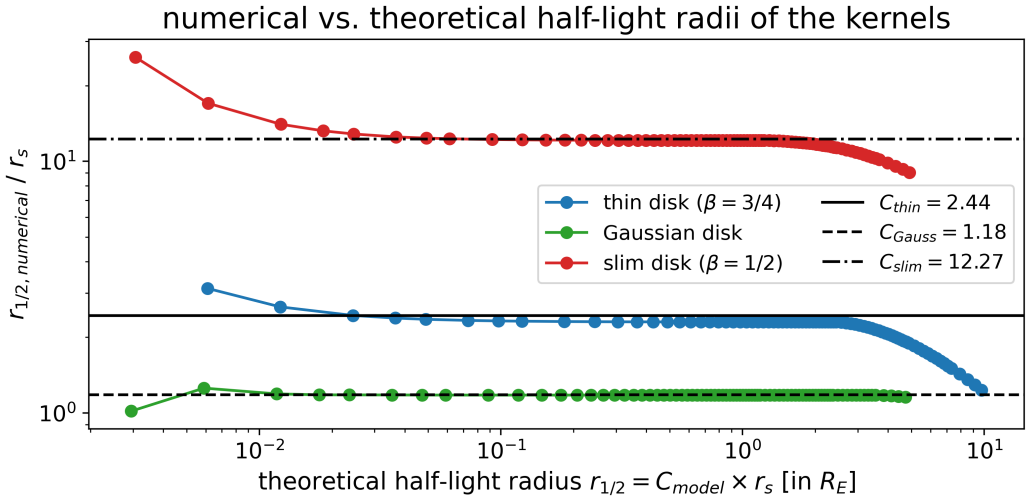

Figure 6.2.: Comparison of the disk kernel's half-light radii. Shown for each theoretical half-light radius $r_{1/2}$ (defined by Eq. 6.5; i.e. the scale radius r_s times a model dependent constant C_{model}) as dotted lines for the three models (thin disk in blue, Gaussian disk in green and slim disk in red) are the numerically determined half-light radii of all 2D-kernels relative to the r_s value, they were computer for. The non-logarithmic spacing of the 80 size values and the per model (slightly) different disk sizes in $r_{1/2}$ are visible. As described, there are some deviations for the smallest and largest models, but in general, the produced 2D-kernels reproduce the expected $r_{1/2}/r_s$-ratios (i.e. the C_{model}-values shown as black lines; see the results of Eq. 6.5, while throughout this work, we actually use more digits of these r_s-to-$r_{1/2}$ conversion factors C_{model}, i.e. 2.4356, 1.1774 and 12.2712 for the thin, Gaussian and slim disk) well, at least for the central $0.02\,R_\mathrm{E} \lesssim r_{1/2} \lesssim 3.0\,R_\mathrm{E}$, also depending on the model.

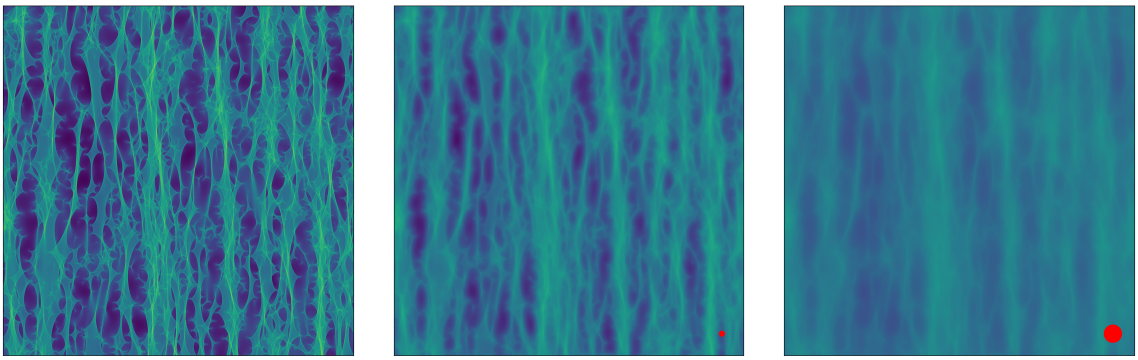

Figure 6.3.: Comparison of unconvolved and convolved HE0435-1223 magnification maps. Shown are maps ($40\,R_\mathrm{E} \times 40\,R_\mathrm{E}$) of image B for $\kappa_\star/\kappa = 0.5$ (the magnitude scale goes from 2.8 mag to −4.2 mag). On the left, the unconvolved `Teralens` map is shown. In the middle, the map is convolved with a thin disk kernel with $r_{1/2} \approx 0.3\,R_\mathrm{E}$, and on the right with $r_{1/2} \approx 1.0\,R_\mathrm{E}$ (represented by the red disks in the corner).

6.2. Kochanek light curve fitting method

As explained at the beginning of this chapter, we used the microlensing analysis method from Kochanek (2004) to study properties of HE0435-1223's accretion disk. We therefore fitted simulated microlensing light curves (generated from the magnification maps of image B of HE0435-1223) to the LCO R and V band $B-C$ difference curves, as described in Sorgenfrei et al. (2025).

Continuing with this approach, in order to extract these microlensing light curves from the 4200 convolved magnification maps from Sect. 6.1, we constructed 10^7 tracks with track lengths corresponding to ten years (slightly longer than the time interval in which data was obtained and evaluated; see Sect. 3.1) by drawing 10^7 velocities sampled from a log-uniform distribution between $0.002\,R_\mathrm{E}/\mathrm{yr}$ and $2.0\,R_\mathrm{E}/\mathrm{yr}$ (in principle limited only by the size of our magnification patterns). For these tracks, random directions and random x and y start point coordinates on the maps were drawn uniform. However, in order to avoid edge effects for the largest disks from the convolution (as it used fast Fourier transforms that assume periodical patterns – which the `Teralens` maps are not), we discarded the outer $5\,R_\mathrm{E}$ on all sides of each convolved magnification map for the next steps, leaving us with the central $30\,R_\mathrm{E} \times 30\,R_\mathrm{E}$ available for usage. Tracks whose start or end coordinates were outside this region, had their start points redrawn (but not their velocities), until they stayed within it. Thus, we generated 10^7 random tracks, located within the central $30\,R_\mathrm{E} \times 30\,R_\mathrm{E}$ of the convolved maps. Figure 6.4 shows two unconvolved magnification maps for $\kappa_\star/\kappa = 0.3$ and 0.8 generated with `Teralens` together with the first 200 of all 10^7 tracks, showcasing the range of track lengths (i.e. velocities), random directions, as well as the restriction to the central $30\,R_\mathrm{E} \times 30\,R_\mathrm{E}$.

For each compact object fraction $\kappa_\star/\kappa$, each disk size r_s, and all three disk models (i.e. the thin, the Gaussian and the slim disk model; see Eqs. 6.2, 6.3 and 6.4), we placed all 10^7 tracks on the corresponding map and linearly interpolated the magnitudes of 500 equally spaced steps along each track. The generated light curves were then compared to the R and V band $B-C$ difference curves from Sect. 5.2 (Fig. 5.5), by fixing the start time of the simulated tracks to $t_0 = 2014.5\,\mathrm{yr}$ (chosen such to cover the data) and then interpolating them to the epochs t_i of the difference curves, thus extracting two simulated microlensing curves $\mu_B(t_i)$ of image B at the same epochs of the R and V band difference curves, respectively (see Sect. 5.1, where we dropped the photometric band superscript $X \in \{R, V\}$ here and in the following). Since we assumed no microlensing along the line of sight of image C (see Sect. 5.2), we subtracted a constant offset μ_C from each simulated $\mu_B(t_i)$ curve. Analogous to Eq. 5.2 (absorbing all constant terms into μ_C), this accounts for a possible non-zero

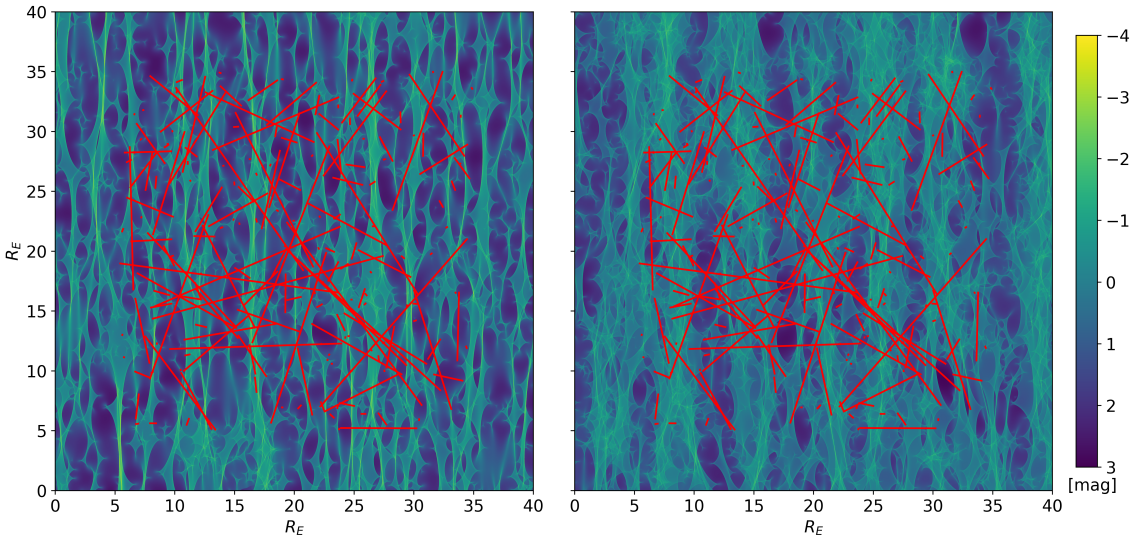

Figure 6.4.: Two magnification patterns with example tracks. Shown are the same 200 tracks (in red) on both unconvolved magnification maps, as generated with `Teralens` for image B of HE0435-1223 with $\kappa_\star/\kappa = 0.3$ (on the left) and $\kappa_\star/\kappa = 0.8$ (on the right; adapted from Sorgenfrei et al. 2025) using the same magnitude scale.

but constant microlensing signal in image C, the constant mean magnifications of both images from strong lensing, as well as other constant contributions (see Sect. 5.1.2). The offsets μ_C were chosen such that the difference of the mean magnitude values of the simulated and measured difference curves was minimized, i.e.

$$\mu_C := \big\langle \mu_B(t_i) \big\rangle - \big\langle (B-C)(t_i) \big\rangle, \tag{6.6}$$

essentially shifting each simulated light curve (in magnitude direction) to match the average magnitude of the measured difference curve.

To evaluate the fit quality for each generated light curve with respect to the difference curve data, χ^2 statistics are used. Since we are simply comparing one difference curve with one simulated curve, straightforwardly, the resulting goodness-of-fit estimator χ^2 for each track, compact object fraction $\kappa_\star/\kappa$, photometric band, disk model and disk size, totaling at $10^7 \times 10 \times 2 \times 3 \times 80 = 48 \times 10^9$ values, is given by:

$$\chi^2 = \sum_i \left[\frac{\mu_B(t_i) - \mu_C - (B-C)(t_i)}{\sigma_i} \right]^2, \tag{6.7}$$

which is Eq. 6 of Kochanek (2004) applied to our case.[52] Here, accordingly, the σ_i

[52] In the general case, Eq. 6.7 is summed over all image pairs $\alpha\beta$, therefore comparing microlensing simulations from the multiple images with all the *dependent* combinations of difference curves, as derived in Kochanek (2004, Eqs. 3 to 7). Going through the calculation, the error term σ_i is replaced by $\sigma^2_{\alpha\beta,i} = (\sum_\gamma \prod_{\delta\neq\gamma} \sigma^2_{\delta,i})/(\prod_{\eta\neq\alpha,\beta} \sigma^2_{\eta,i})$, which for two images simplifies to the error of their difference curve (as well as to Eq. 7 of Kochanek 2004 for four quasar images).

were set to the magnitude errors of the difference curve $B - C$ at epochs t_i (see Eq. 5.4 and footnote 52), however, with an in quadrature added systematic error of $\sigma_{\mathrm{sys}} = 0.05\,\mathrm{mag}$ to the 1σ errors of both light curves analogous to Kochanek (2004):

$$\sigma_i := \sqrt{\big(\Delta(B-C)(t_i)\big)^2 + 2\big(\sigma_{\mathrm{sys}}\big)^2}. \tag{6.8}$$

This was done since otherwise the number of tracks with acceptable χ^2 is far too low for any meaningful statistical analysis. These unknown systematic uncertainties had been similarly incorporated by previous studies (e.g. Kochanek 2004; Eigenbrod et al. 2008a; Poindexter & Kochanek 2010b; Morgan et al. 2018), and it unfortunately remains likewise necessary for our simulations, because our microlensing model does not explain these remaining residuals mostly from higher frequency variations (see e.g. Paic et al. 2022, for a recent discussion of the possible implications, as well as Rivera et al. 2023, 2024 as already mentioned in Sect. 5.1.2).[53]

In all 6×10^8 cases (10^7 tracks on ten independent maps for all three disk models and both bands), we determined the best-fitting disk size of the 80 tested sizes that minimizes χ^2 from Eq. 6.7. As this was done independently for R and V, and since our simulated light curves need to reproduce both the R and V band data, we added these best-size χ^2_R and χ^2_V values to a combined $\chi^2 = \chi^2_R + \chi^2_V$. This results in one χ^2 value with a best disk size in R and V for each of the 10^8 tracks, for all three models.

These 3×10^8 combined χ^2 values were then converted to 'track probabilities' $P(\chi^2)$, which are the likelihood of each simulated R and V band light curve pair. Here, as typically done in the field, not the usual $\exp(-\chi^2/2)$, but Eq. 10 from Kochanek (2004) is used as maximum likelihood estimator (see also e.g. Eigenbrod et al. 2008a):

$$P(\chi^2) \propto \Gamma\left[\frac{N_{\mathrm{d.o.f.}}}{2} - 1, \frac{\chi^2}{2f_0^2}\right], \tag{6.9}$$

where $\Gamma[a, b]$ is the 'upper incomplete gamma function'. This estimator has been introduced by Kochanek (2004) to circumvent the issue of comparing essentially unrelated light curves instead of models related to each other by continuous parameter changes. There, it is argued to use the probability density function of the χ^2-distribution (i.e. the probability $P(\chi^2|N_{\mathrm{d.o.f.}})$ of obtaining an χ^2 value from the data with $N_{\mathrm{d.o.f.}}$ degrees of freedom; see their Eq. 9). However, due to $N_{\mathrm{d.o.f.}} \gg 1$, this is sensitive to small over- or underestimations of the light curve's uncertainties σ_i. Therefore, they implicitly included a rescaling factor f into the σ_i (i.e. replacing σ_i with $f\sigma_i$ in Eq.

[53] Although this inclusion of a systematic uncertainty follows Eq. 3.9 (even using a similar value as given in Table 3.2), the origin of the additional noise is different (though unknown), as the magnitude offsets from Sect. 3.7 are irrelevant for the difference curves, which is why we have not included their errors in the first place.

6.7), thus modifying the χ^2 values to $\chi^2_f = \chi^2/f^2$, in order to average out errors in the σ_i. This averaging is done by integrating $P(\chi^2_f|N_{\mathrm{d.o.f.}})$ together with their chosen prior $P(f) \propto f$ (which means assuming an average error rescaling of $\langle f\rangle = 2f_0/3$) over f from zero to a maximum factor f_0, thus arriving at the given expression (Eq. 6.9) for the track probabilities $P(\chi^2)$.[54] In the end, the effect of switching to this maximum likelihood estimator is that a large number of well-fitting tracks contribute to the analysis (instead of just a few tracks due to the exponential when working without these considerations), since towards smaller χ^2 values, $P(\chi^2)$ rises, where $P(f_0^2 N_{\mathrm{d.o.f.}}) \simeq P(0)/2$, and flattens beyond this point for the smallest χ^2 values (see Kochanek 2004, for a more in-depth discussion). Therefore, this estimator (Eq. 6.9) enables the analysis, since otherwise no meaningful statistic can be done, which we have checked for our simulations.

For our combined R and V band $B-C$ data (with 51 and 49 data points, respectively; see Fig. 5.5), the number of degrees of freedom is $N_{\mathrm{d.o.f.}} = 98$ (since there are two fitted parameters, namely the offsets μ_C from Eq. 6.6 for each band). Kochanek (2004) used $f_0 = 1$ in relation to their typical χ^2 values. Through testing, we decided to set $f_0 = 3\min(\chi_{\mathrm{red}})/2$ (which are ~ 1.3), with the reduced $\chi^2_{\mathrm{red}} = \chi^2/N_{\mathrm{d.o.f.}}$ values, independently for the three disk models. This was done to ensure that the minimum χ^2_{red} would essentially be rescaled by $\langle f\rangle^2$ to unity for each model, allowing us to have comparable amounts of tracks with relevant track probabilities for the different disk models, even though their χ^2 distributions differ slightly.

We applied this procedure only to those tracks with $\chi^2_{\mathrm{red}} \leq 5$, which speeds up the analysis by removing models with vanishing likelihood. This is a conservative threshold, as models close to it are suppressed in their likelihood from Eq. 6.9 by many orders of magnitudes compared to the best-fit models. Afterwards, for each disk model, the $P(\chi^2)$ were normalized to one. Finally, these results were collected in a 'track library' including track number, $\kappa_\star/\kappa$, velocity, direction, the six best sizes (for the three models and two bands) and the three track probabilities. About 22.9 % of all 10^8 tracks have non-vanishing track probabilities (i.e. $\chi^2_{\mathrm{red}} \leq 5$) for the R and V band best-size estimates for at least one of the three models.

Finally, all steps in this chapter (after the initial generation of maps using `Teralens`) were implemented in `python`. These codes, i.e. to convolve the `Teralens` maps, to simulate the microlensing light curves via the Kochanek method and calculate χ^2 values, as well as to produce the track library are available on GitHub.[55]

[54] Here, it is helpful to substitute $t := \chi^2/(2f^2)$ to identify the incomplete gamma function.

[55] The `python` codes are available at https://github.com/sorgenfrei-c95/qsoMLsimcurves. Note that especially the Kochanek method part implemented in `threadedMLsim.py` is computationally expensive and has run even with parallelization for multiple days on our machines.

7. Results and discussion of the microlensing analysis of HE0435-1223

Finally, we can turn to the major promise from the title of this thesis: 'Determining the innermost structure of quasars by microlensing'. Therefore, in this chapter, we describe and discuss the analysis of the microlensing simulations from the previous chapter with its results for the accretion disk of HE0435-1223.

Previously, we had restricted the analysis of the microlensing content in our data of HE0435-1223 to the R and V band $B-C$ difference curves, having identified a strong signal in image B. From the different combinations of difference curves (Fig. 5.5) and especially the flat $D-C$ curve, we argued that we could assume image C to have *not* undergone any significant microlensing. This further simplified our analysis, as it was only necessary to simulate microlensing in image B (see Sect. 5.2 and Chapter 6).

This $B-C$ simulation (focusing on the Shakura-Sunyaev thin accretion disk brightness model from Eq. 6.2 as well as the Gaussian disk brightness model Eq. 6.3) and the subsequent analysis concluding with results on the quasar's accretion disk, were presented in Sorgenfrei et al. (2025). Therefore, parts of this chapter (i.e. parts of Sects. 7.1, 7.2, 7.3 and 7.4) are published in Sorgenfrei et al. (2025). However, throughout this chapter, we continue to include the additionally tested slim disk brightness model from the previous chapter (Eq. 6.4), simply mentioned in that study. Additionally, if the argument from above regarding the non-presence of microlensing in the $D-C$ curve holds, consistent results are expected when using the $B-D$ data instead in the simulations in Sect. 6.2, i.e. assuming no microlensing in the fainter image D. Therefore, as already mentioned in Sorgenfrei et al. (2025), we have repeated the simulations described in Chapter 6 and the subsequent analysis presented here, using the same tracks and parameters, simply comparing the simulated curves to the $B-D$ curve in Eq. 6.7. All results presented in this chapter are consistent with the results from this modification, albeit (since $B-D$ is affected more by noise due to image D being fainter) with slightly increased uncertainties.

7.1. Simulated $B-C$ microlensing light curves

In Fig. 7.1, we show a few simulated microlensing light curves as examples. For this, we use the 25 'best-fitting' simulated light curves in R and V, where best-fitting refers to those tracks with the highest likelihood $P(\chi^2)$ for certain R and V band disk sizes from Sect. 6.2, i.e. those with smallest χ^2_{red} (where the ranges of χ^2_{red} values of the displayed curves are given in the figure as well). These simulated curves are presented together with the observed R and V band $B-C$ data points, to which they were fitted to. We show these best-fitting curves individually for the Gaussian disk model (upper panel), the Shakura-Sunyaev thin disk model (middle panel) and the shallower slim disk model (lower panel).

For all disk models, it is noticeable in Fig. 7.1 that for almost all tracks the simulated V band curves in blue shows larger variations than the corresponding R band curves in red, since at the beginning the blue curves are below the red, which turns around especially around 2022, with the blue curves on top. This is consistent with an outward-decreasing temperature profile expected from accretion disk theory (Sect. 1.4) and corresponds to different measured disk sizes from both bands (or a size ratio deviating from one). More explicitly, this observation agrees with a larger disk in the R and smaller one in the V band, since larger sources show lower amplitude microlensing variations, as they average over larger parts of the microlensing map (Sect. 1.4; implemented by convolving the `Teralens` maps in Sect. 6.1.3 with disks of different sizes). Quantifying this result is the next step in our analysis as presented in the next section and one of the main results of this thesis.

As we show simulated light curves of the 25 *individually* best-fitting tracks for the three models, they are generally not the same tracks. Only one of the tracks used to produce the presented light curves coincides for all three disk models. Curves of one more track appear both in the Gaussian and the thin disk model plot, and finally, there are additionally 16 tracks shared by the best thin and slim disk tracks. This indicates the similarity of these two models, but also their shared difference with respect to the Gaussian model. Also, qualitatively, the light curves from the different models *do* appear different in shape (see Fig. 7.1), with more numerous and sharper variations in the thin and slim disk models compared to the Gaussian disk model, hinting at subtle differences between them and showing, that next to the primarily important half-light-radius (see Sect. 6.1.3), the actual shape of the brightness profile has its (small) influence as well.

Before continuing, note that, for the remaining quantitative analysis in the next sections, we consider *all* library tracks with non-vanishing $P(\chi^2)$ values from Sect. 6.2 (i.e. about 14 to 22 million tracks, depending on the model), not just these 25 best-

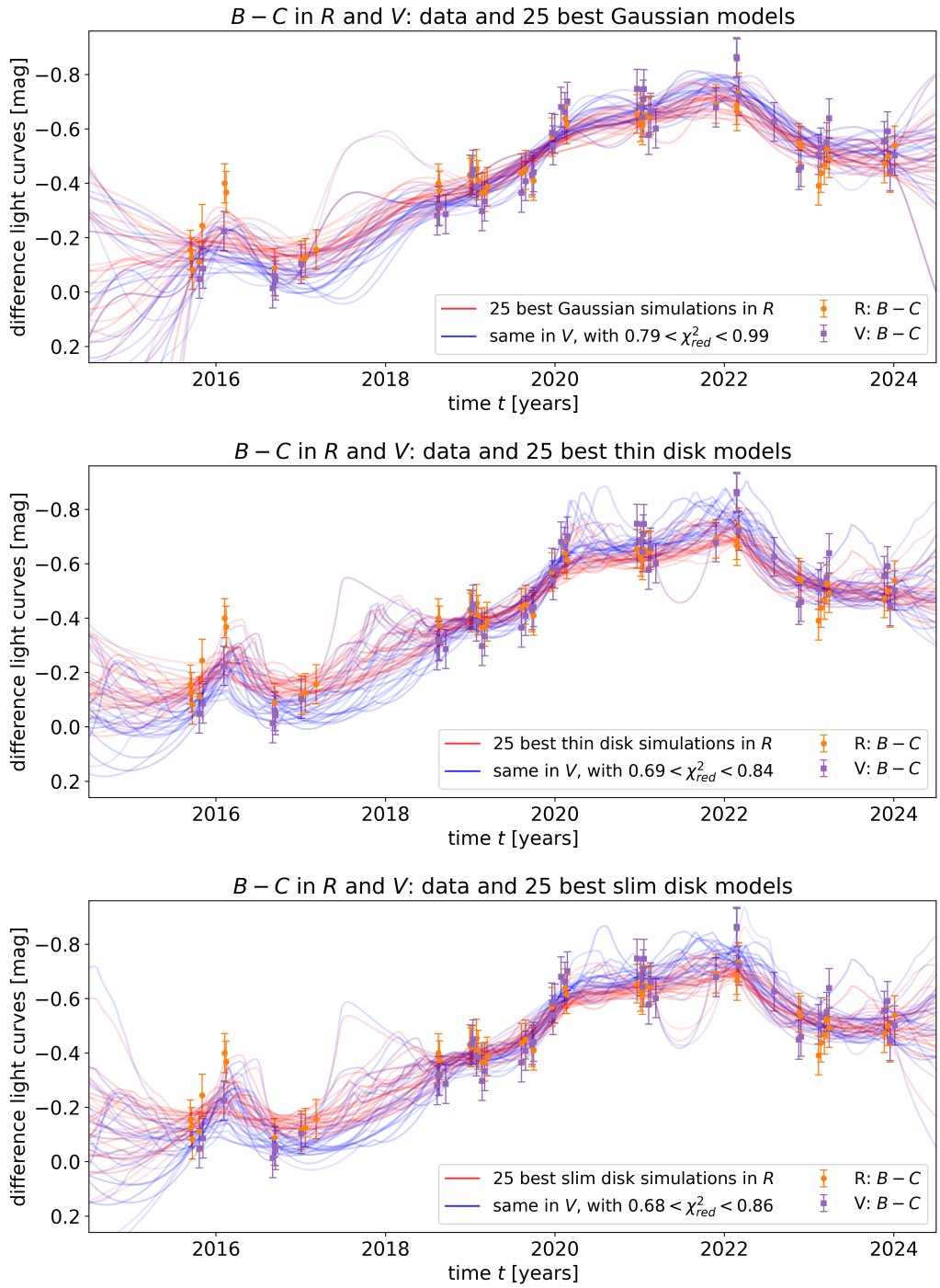

Figure 7.1.: Simulated HE0435-1223 microlensing light curves. Shown are the best-fitting simulated R and V curves (in red and blue) from the 25 tracks with the smallest $\chi^2 = \chi^2_R + \chi^2_V$ values, each for the Gaussian (top panel), the thin (middle panel) and the slim disk model (bottom panel); with the first two adapted from Sorgenfrei et al. (2025). In all three panels, the same data points are shown: our R (orange circles) and V (purple squares) band measured LCO $B-C$ difference curves (i.e. the two uppermost curves in the lower panel of Fig. 5.5, with the magnitude scale inverted), with adapted error bars including the systematic uncertainty (Eq. 6.8) as described in Sect. 6.2 and used for the χ^2 calculation (Eq. 6.7).

fitting tracks. Also, always in this analysis, the ordering of disk models of presented results is first the Gaussian disk model, then the thin disk model and lastly the slim disk model, in accordance with the order used in Sorgenfrei et al. (2025) for the first two models and to have the two 'physical' models next to each other.

7.2. Accretion disk size ratio & temperature profile

Continuing with the analysis from Sorgenfrei et al. (2025), for each of the 10^8 tracks in our track library, we can immediately determine the ratio of the source sizes in the R and V band. This size ratio $q_{R/V}$ is directly related to the temperature profile (Eq. 1.3) via the dependence of the observed size on the filter wavelength (Eq. 1.7) of a Shakura-Sunyaev disk as discussed in Sect. 1.4. For the central filter wavelengths $\lambda_c(R) = 6407\,\text{Å}$ and $\lambda_c(V) = 5448\,\text{Å}$ (see Sect. 2.1 or Bessell 2005), the expected theoretical size ratio therefore is $q^{\text{theo.}}_{R/V}(\beta = 3/4) \simeq 1.241$ (i.e. a Shakura-Sunyaev disk is expected to appear 24.1% larger in radius in the R than in the V band). For the slim disk, where we set $\beta = 1/2$, Eq. 1.7 is modified to $r_s \propto \lambda_c^2$, thus resulting in an slightly larger size ratio of $q^{\text{theo.}}_{R/V}(\beta = 1/2) \simeq 1.383$. Since the Gaussian model is not based on a specific temperature profile, no theoretical ratio can be given.[56]

While it is standard to use around 15 logarithmically spaced r_s values in simulations aimed at measuring absolute disk sizes (e.g. Kochanek 2004; Morgan et al. 2018), as detailed in Sect. 6.1.3, we chose to use 80 different values non-logarithmically (i.e. piecemeal linearly) spaced, similar to Anguita et al. (2008) and Eigenbrod et al. (2008a). These size values were selected such that their ratios were as densely and close to evenly distributed in the ratio-space as possible, in order to allow us to measure size ratios, which was not achieved in tests with fewer and logarithmically spaced values (see Fig. 7.2). Using the best-fitting R and V band sizes of all tracks in the library (Sect. 6.2), we computed each track's half-light radii fraction

$$q_{R/V} := \frac{r_{1/2}(R)}{r_{1/2}(V)} \tag{7.1}$$

independently for the three disk models (where $q_{R/V}$ is identical to a scale radii ratio, as the conversion factors from Eq. 6.5 would cancel). We then constructed

[56] Using the wavelength-size-relation from Eq. 1.3 assumes the filter widths to be small $\Delta\lambda \ll \lambda_c$ (see Sects. 1.2 and 1.4; and Sect. 2.1: in the $\Delta\lambda$ are $\sim 25\%$ and $\sim 15\%$ of the λ_c in R and V), approximating the disk's brightness by only the contributions from λ_c, but spatially originating from the whole disk according to the profiles in Sect. 6.1.3 and Eq. 1.5. Testing this assumption, the theoretical ratios were recalculated incorporating the filter transmission curves as provided by LCO (see Sect. 2.1), which did not change them significantly. Additionally, the simulations include the same assumption (via the same brightness profiles), thus being consistent with the above stated theoretical ratios.

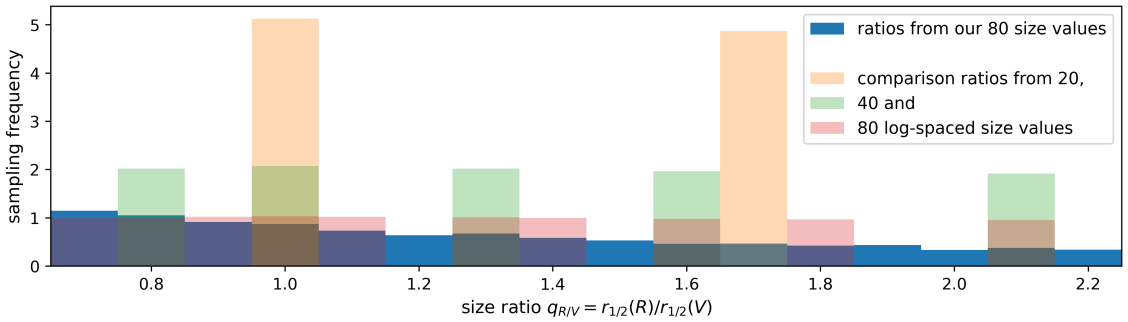

Figure 7.2.: Sampling frequency of size ratios. The blue histogram shows the binned relative number of all possible ratios of our specific choice of the 80 tested size values from Sect. 6.1.3. For comparison, in orange, green and red (using the same size range), ratios from 20, 40 and 80 logarithmically spaced size values are shown, where only a few ratios are sampled, due to the size values being spaced apart by constant factors.

histograms for $q_{R/V}$ by summing over the track probabilities $P(\chi^2)$ of all tracks in a given size ratio bin, using 16 ratio bins centered at 0.7 to 2.2 in steps of 0.1. However, despite the size value choice from above, these bins were not *exactly* evenly sampled. Therefore, we normalized each bin's probability by the number of tested source size ratios from Fig. 7.2 contributing to that particular bin, though overall, this is only a minor correction due to the specific selection of the 80 size values from Sect. 6.1.3.

Figure 7.3 – the main result of Part II – shows the resulting half-light radii ratio distributions $P\left(q_{R/V}\right)$ for the three disk models. The mean ratio values with 1σ uncertainties (as displayed) are $\left\langle q_{R/V}\right\rangle = 1.24^{+0.08}_{-0.20}$ for the Gaussian disk model, $\left\langle q_{R/V}\right\rangle = 1.42^{+0.11}_{-0.22}$ for the thin disk model and $\left\langle q_{R/V}\right\rangle = 1.43^{+0.10}_{-0.23}$ for the slim disk model, all three consistent with each other, as well as with the theoretically expected value of the thin accretion disk model by Shakura & Sunyaev (1973).[57] For reference, the respective median values (with 16^{th} and 84^{th} percentiles as errors) are $1.20^{+0.17}_{-0.12}$, $1.36^{+0.23}_{-0.13}$ and $1.38^{+0.23}_{-0.13}$. Additionally, integrating the the three models' distributions we find $P\left(q_{R/V} \geq 1\right) \approx 95\%$, 98% and 99%, respectively.

This clearly confirms the qualitative observation from Sect. 7.1, that the accretion disk of HE0435-1223 appears larger in the R than the V band and consequently, that its temperature profile is outward decreasing in accordance with Eq. 1.3.[58] It can

[57] As stated before, including the sampling frequency of ratios only affects them slightly, with the mean ratio values of the models being ~ 1.29, 1.42 and 1.47, without the correction.

[58] A conversion of the $q_{R/V}$ distributions to negative temperature profile slopes β (see Eq. 1.3) is problematic due to the small, but non-zero probabilities around the pole of (following the inverted, β-generalized Eq. 1.7) $\beta = \ln(\lambda_c(R)/\lambda_c(V))/\ln(q_{R/V})$ at $q_{R/V} = 1$ (see Fig. 7.3; just converting the mean values gives $\beta \approx 0.75$, 0.46 and 0.45, for the three models). However, the inverse slope $\zeta = 1/\beta$ (monotonically increasing as function of $q_{R/V}$), is accessible (similar as in Eigenbrod et al. 2008a): we e.g. find a probability distribution for the thin disk model with $\langle\zeta\rangle \simeq 1.96^{+0.64}_{-0.83}$, of course again compatible with thin disk theory at $\zeta = 4/3$, but somewhat shallower.

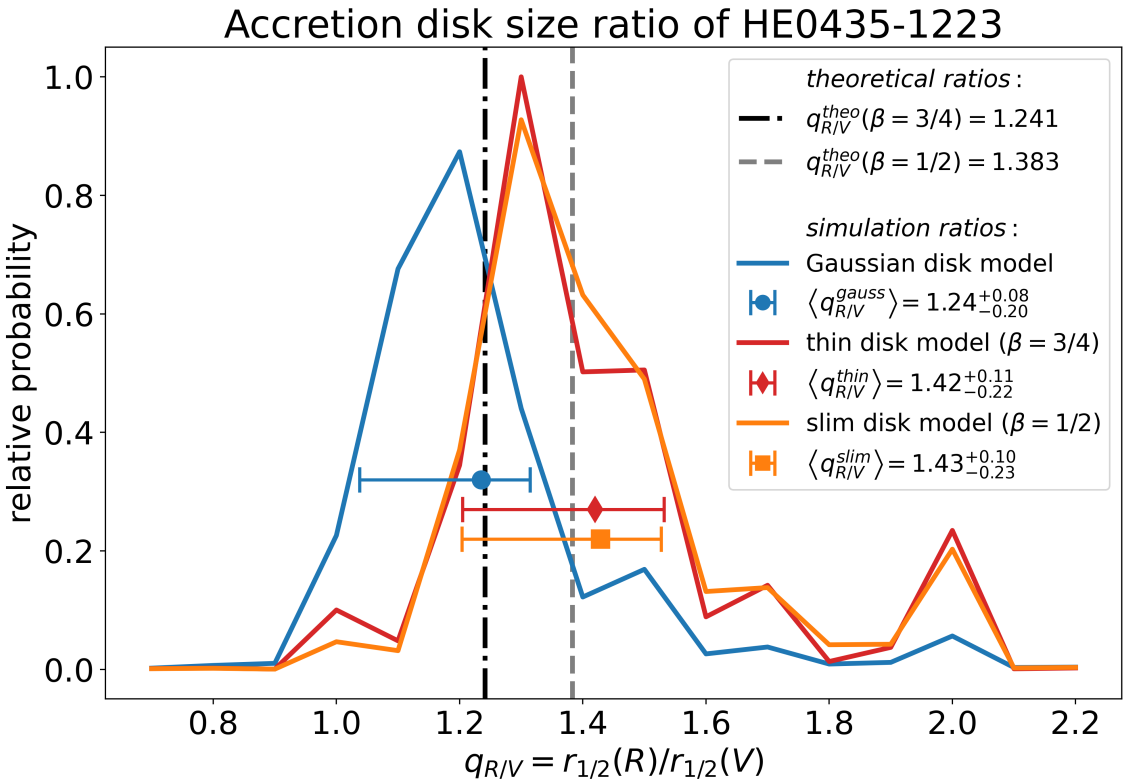

Figure 7.3.: Accretion disk size ratio distribution of HE0435-1223. Shown are the probability distributions of $q_{R/V}$ (i.e. the R to V band size ratio; Eq. 7.1) for the Gaussian (blue), thin (red) and slim disk model (orange), with corresponding mean values (blue circles, red diamonds and orange squares, respectively), each with 1σ uncertainties. Note that the mean value's position along the ordinate is arbitrary. The vertical lines indicate the theoretical values $q^{\text{theo.}}_{R/V}(\beta)$ for the thin disk (dash-dotted black line) and the slim disk (dashed gray line). Results for the first two disk models have already been similarly depicted in Sorgenfrei et al. (2025).

be noted, however, that the thin and slim disk model simulations tend to prefer a somewhat larger ratio value closer to $q^{\text{theo.}}_{R/V}(\beta = 1/2)$. This corresponds to a shallower temperature profile according to Eq. 1.3, with a negative temperature exponent closer to $\beta = 1/2$ (while still in agreement with $\beta = 3/4$ from standard thin disk theory).

Actually, this result was the main reason to include the $\beta = 1/2$ slim disk simulation (Eq. 6.4) in the first place. Since the results of the thin and slim disk models almost perfectly agree with each other and again, agree with both theoretical ratios (Fig. 7.3), we cannot distinguish them from our analysis, and thus unfortunately cannot restrict the temperature profile to either of them with our data. As stated in Sect. 6.1.3, this would have been relevant and should continue to be a target of interest for future studies, as different profiles with shallower (or also steeper than standard) profiles have not only been proposed as well as measured, but might help to resolve microlensing to luminosity size discrepancies (see Poindexter et al. 2008; Morgan

et al. 2010, 2018; Li et al. 2019; Cornachione & Morgan 2020, and references therein; see also the discussion towards the end of the following section).

7.3. Accretion disk size estimates

As done in Sorgenfrei et al. (2025), probability distributions for each model's accretion disk size (with size measured as half-light radii in units of Einstein radii) can similarly directly be inferred from our simulations. For each track in our library from Sect. 6.2, we added its track probabilities corresponding to its best-fitting $r_{1/2}(R)$ and $r_{1/2}(V)$ values to the appropriate histogram bins for the three disk models. We thus obtained six probability distributions $P(r_{1/2})$, one each model and band, shown in Fig. 7.4. From these, we find $\langle r_{1/2} \rangle = 0.91^{+2.14}_{-0.68}\,R_\mathrm{E}$ for the Gaussian model in the R band and $0.77^{+1.89}_{-0.56}\,R_\mathrm{E}$ in the V band, while the thin disk model correspondingly gives $0.98^{+2.40}_{-0.73}\,R_\mathrm{E}$ and $0.73^{+1.80}_{-0.56}\,R_\mathrm{E}$, and the slim disk has $0.97^{+2.50}_{-0.75}\,R_\mathrm{E}$ and $0.71^{+1.87}_{-0.58}\,R_\mathrm{E}$, respectively.[59] In early applications of the Kochanek method, often these microlensing analyses found smaller disk sizes in R_E (e.g. starting itself with Kochanek 2004, analyzing Q2237+0305), but e.g. recently, an accretion disk of comparable size has been found by Forés-Toribio et al. (2024) in the lensed quasar SDSS J1004+4112; also, with ~ 0.6 dex, our uncertainties are quite large.

Moreover, since each track is associated with a velocity v in R_E/yr, we constructed probability distributions $P(v)$ for the Gaussian, the thin and the slim disk model, with mean track velocities of about 0.48, 0.33 and 0.31 R_E/yr, respectively. These distributions, but with the velocities converted from units of R_E/yr to km/s using Eq. 6.1 assuming $\langle M \rangle = M_\odot$, are shown in Fig. 7.5a.

Similar as in (e.g. Kochanek 2004), combining both the size and velocity information from our simulations, we find the known linear source size–velocity degeneracy, where larger disks with higher velocities (i.e. on longer tracks, since we fixed the total duration) produce similar results smaller disks that travel slower along their shorter path. This degeneracy is one of the reasons for the broad probability distributions and the correspondingly large uncertainties of the mean values. At this point, note that we have checked the corresponding distributions of the velocity direction and the compact matter fraction $\kappa_\star/\kappa$, but find only mild and insignificant trends of higher likelihood towards velocities or tracks non-parallel to the shear direction (i.e. crossing

[59] Actually, the mean values are directly determined without binning in all six cases by summing over $r_{1/2} \cdot P(\chi^2)$ for all tracks in the library. Also, calculating mean size ratios from these average disk size values, slightly (but non-significantly) deviates from our results from the previous section, since according to 'Jensens inequality' (Jensen 1906), the ratio of means is smaller or equal than the mean of ratios. The latter is what we determined using Eq. 7.1, as we wanted to compare the two sizes of each track, rather averaging over vastly different models.

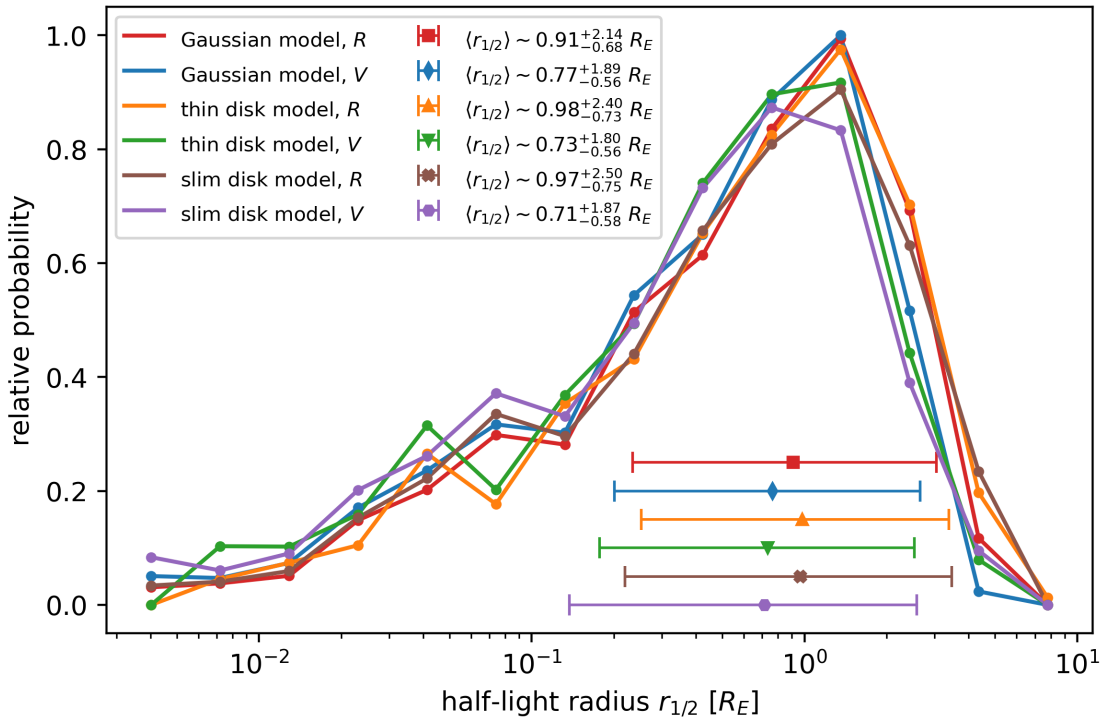

Figure 7.4.: Accretion disk size in Einstein radii of HE0435-1223. Shown are the six probability distributions for disk size in $R_{\rm E}$ from our simulations for each model and both bands. The corresponding data points with error bars show the mean size values with 1σ intervals. Note that the position of them along the ordinate is arbitrary.

the vertical dominant caustic structures in Fig. 6.4) and towards magnification maps with intermediate and higher $\kappa_\star/\kappa$ values.[60]

A possibility to convert the half-light radii $r_{1/2}$ in units of $R_{\rm E}$ to absolute accretion disk size estimates in cm by fixing the *unknown* mean microlens mass $\langle M\rangle$ in Eq. 6.1. Alternatively, assumptions can be made on the involved velocities, i.e. of the quasar

[60] Note that a few tests of including more of the LCO difference curve data from Fig. 5.5 have been conducted (next to the $B-D$ comparison as mentioned at the beginning of this chapter). These were trials of extending the analysis to include image A, i.e. a $B-A$ simulation and simultaneous $B-C$ and $A-C$ simulations. Since we argued for the presence of smaller amplitude microlensing in image A (Sect. 5.2), additional magnification maps for image A of HE0435-1223 were generated with `Teralens`. In the end, due to the combinatorial explosion (as mentioned in Chapter 6), these trials did not generate stronger limits on results in this chapter, as the number of tracks had to be reduced, leading to poor statistics (a minor tendency of slightly decreased velocity and thus size needs further investigation). However, since the map orientations differ between the images (similar to Fig. 1 in Poindexter & Kochanek 2010b for Q2237+0305), we needed to calculate the relative angles for the HE0435-1223 maps. Using the model by Kormann et al. (1994), we estimated a relative angle between image A and B of $\sim 78.3°$ (having confirmed our orientation results with similarly calculated angles for Q2237+0305 in comparison with Table 1 in Poindexter & Kochanek 2010b). Then, for each track on a map, many with the same length and corrected direction are drawn on the other. This strengthened the result for the track velocity orientation, since crossing the shear-aligned structures in image B corresponds to being about parallel to similar structures in image A, thus generating only minor microlensing from that image.

in the source plane, of the microlenses and the lens galaxy, and also of us – the observer. Comparing this prior distribution with the measured $P(v)$, this translates into a mean mass distribution of the compact objects, responsible for the microlensing, i.e. (mostly) the stars in the lens galaxy (see e.g. Sect. 5.2 of Vernardos et al. 2024, and references therein, for an in-depth overview of the history and current picture on the microlensing-objects and there masses).

In fact, a probability distribution of the average microlensing mass can be determined following the Bayesian method as introduced by Kochanek (2004, especially Eqs. 13 to 18). In brief, an effective source velocity probability density $P(v_e)$ is constructed (with v_e in km/s) by combining (the distance-weighted) velocity contributions from the observer with respect to the cosmic microwave background (CMB) in the lens plane perpendicular to the direction to the quasar $\boldsymbol{v}_0$, the stellar velocity dispersion of the microlenses in the lens galaxy $\sigma_\star$, as well as Gaussian estimates for the peculiar velocities of lens galaxy and quasar σ_e. For detailed derivations and the specific expressions (as we implemented them for our analysis in `python`) we refer the reader to Kayser et al. (1986); Kundić & Wambsganss (1993); Kochanek (2004) and the helpful schematic in Fig. 21 of Vernardos et al. 2024.[61]

This results in $P(v_e)$ for HE0435-1223 (see footnote 61), which we show in Fig. 7.5a, with an average effective velocity of $\langle v_e \rangle = 521^{+212}_{-298}\,\mathrm{km/s}$ in the source plane (with 1σ errors). Then, $P(v_e)$ is convolved with the simulation results for $P(v)$ from above (with v in R_E/yr as in Fig. 7.5a) to determine a lens mass distribution

$$P(\langle M/M_\odot \rangle) \propto \int dv_e\, P(v_e) P\Big(v = v_e \,\langle M/M_\odot \rangle^{-1/2}\Big)\,, \tag{7.2}$$

i.e. Eq. 13 in Kochanek (2004), integrating over the abscissa of Fig. 7.5a with $P(v_e)$ multiplied with either model (modified according to a range of mass values) as integrand. The resulting broad probability distributions for the average microlens mass are shown in Fig. 7.5b.

Continuing, as described in Sorgenfrei et al. (2025), we integrated these mass distributions together with the half-light radii distribution $P(r_{1/2}(R_\mathrm{E}))$ from Fig. 7.4, where similar to the velocity distributions, the conversion of $R_\mathrm{E}(\langle M \rangle)$[cm] from Eq. 6.1 has to be included to arrive at size results in cm *independent* of a specific mean mass of the microlenses. This calculation was done essentially identically to Eq. 7.2, only additionally including a uniform mass prior from 0.1 to 1.0 $M_\odot$ as typically done

[61] Courbin et al. 2011 measured $\sigma_\star = 222\,\mathrm{km/s}$ for the lens galaxy of HE0435-1223. Combining the CMB/observer contribution $\boldsymbol{v}_0$ and the stellar dispersion $\sigma_\star$ into $\bar{v}_e$ as done by Kochanek (2004), we find $\bar{v}_e \approx 392.5\,\mathrm{km/s}$. From that and $\sigma_e \approx 299.4\,\mathrm{km/s}$, using a modified Bessel function I_0, finally $P(v_e) = \frac{v_e}{\sigma_e^2} I_0\left[\frac{v_e \bar{v}_e}{\sigma_e^2}\right] \exp\left(-\frac{v_e^2+\bar{v}_e^2}{2\sigma_e^2}\right)$ can be calculated, as derived by Kochanek (2004).

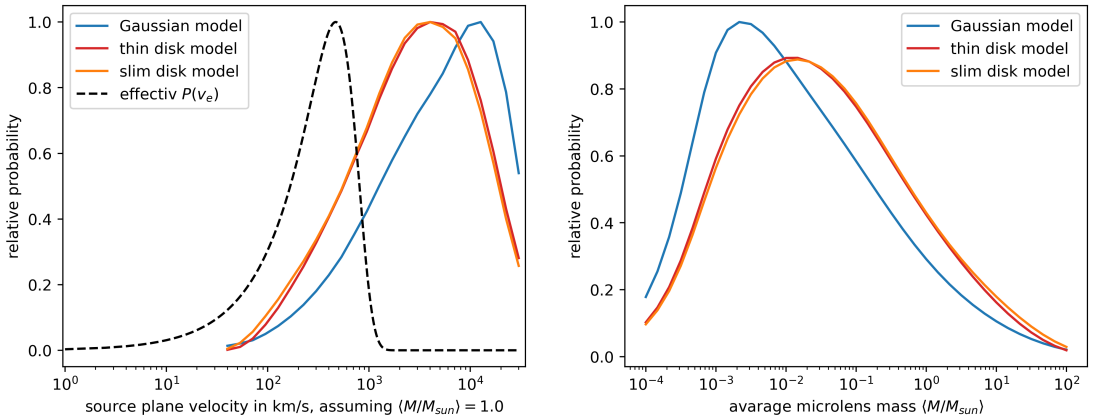

(a) Velocity distributions **(b)** Mass distributions

Figure 7.5.: Velocity and mass probability distributions. On the left, the three disk models' velocity distributions $P(v)$ in km/s (setting $\langle M\rangle = M_\odot$ in Eq. 6.1) are shown together with the effective source velocity $P(v_e)$. By therewith evaluating Eq. 7.2, on the right, the three resulting mean lens mass distributions $P(\langle M/M_\odot\rangle)$ are shown.

(e.g. Kochanek 2004; Morgan et al. 2018; Cornachione et al. 2020b; Rivera et al. 2023, having also investigated the influence of this to be minor), to restrict the calculation to more realistic mean stellar mass values (compared to the broad distribution over multiple orders of magnitudes in Fig. 7.5b as typically found by microlensing studies, e.g. giving a significant probability to a *mean* lens mass around the mass of Jupiter, in clear contradiction to typical estimates for average stellar masses):

$$P(r_{1/2}[\mathrm{cm}]) \propto \int_{0.1}^{1.0} d\langle M/M_\odot\rangle \; P(\langle M/M_\odot\rangle) P\Big(r_{1/2}[\mathrm{cm}]\,\langle M/M_\odot\rangle^{-1/2}\Big)\,. \tag{7.3}$$

We thus obtained probability distributions for the absolute size of the accretion disk of HE0435-1223 in cm for the three models. In order to compare our measured disk sizes with literature values, we converted the $r_{1/2}[\mathrm{cm}]$ sizes to the $R_{2500}[\mathrm{cm}]$ values by Morgan et al. (2010), also used e.g. in Cornachione & Morgan (2020), where disk sizes are expressed in terms of the thin disk's scale parameter r_s (see footnote 14, as well as Eqs. 6.2 and 6.5, i.e. dividing the half-light radii by 2.44) at a UV-wavelength in the quasar rest-frame of 2500 Å (using Eq. 1.7) of an inclined disk (assuming an average inclination $\langle\cos(i)\rangle = 1/2$, which increases the actual disk size by a factor of $\sqrt{2}$; see again footnote 14). Therefore, as done in Sorgenfrei et al. (2025), we converted the $r_{1/2}$ to

$$R_{2500} = \frac{\sqrt{2}\, r_{1/2}}{2.44} \times \left[\frac{2500\,\text{Å}}{\lambda_c/(z_\mathrm{s}+1)}\right]^{4/3}, \tag{7.4}$$

with the central filter wavelength λ_c (see Sect. 7.2) and the source redshift z_s (see

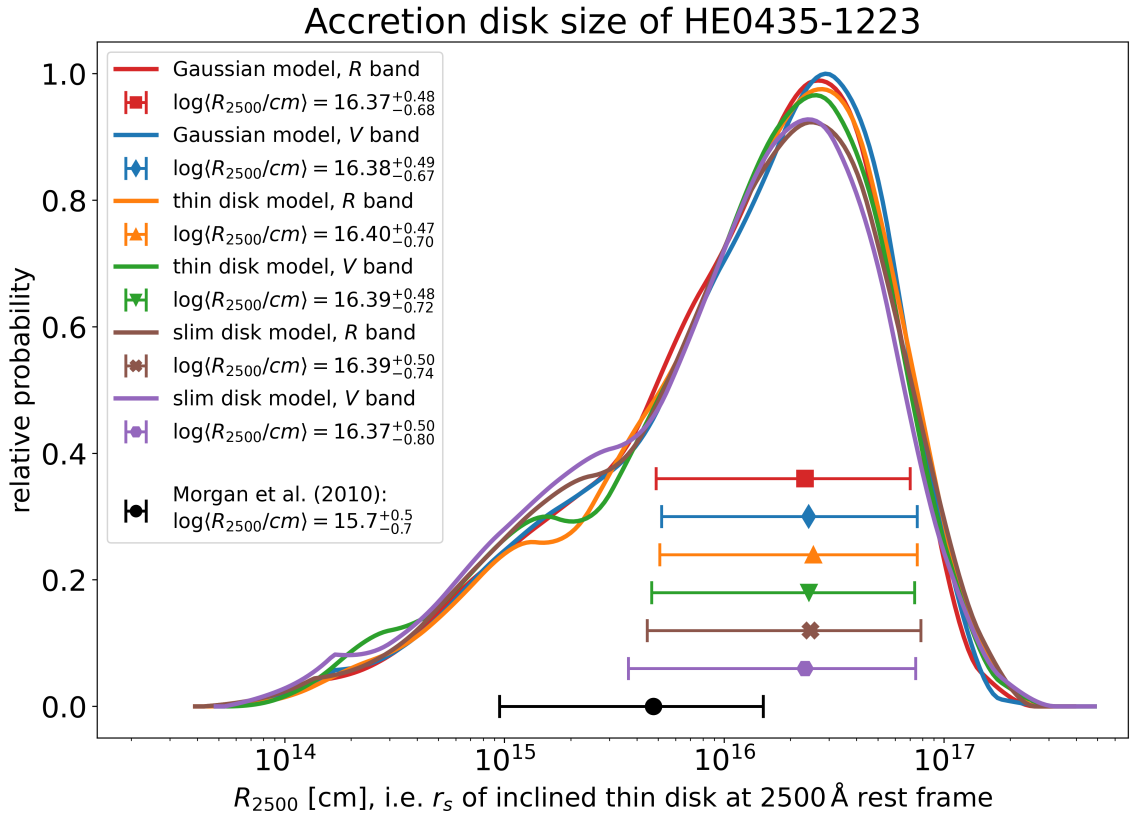

Figure 7.6.: Accretion disk size estimates R_{2500}. Shown are the probability distributions for the accretion disk size of HE0435-1223 measured in R_{2500}[cm] as defined by Eq. 7.4 from our simulations using the Gaussian disk model with the R band data (in red) and with the V band data (in blue), the thin disk model with R (in orange) and with V (in green), as well as the slim disk model with R (in brown) and with V (in purple). The in color corresponding data points with error bars, show the mean size values with 1σ intervals. Similarly, the black data point shows the microlensing size result of HE0435-1223 found by Morgan et al. (2010). The position of the mean values along the ordinate is again arbitrary. Results for the first two disk models have already been similarly depicted in Sorgenfrei et al. (2025).

Sect. 2.2.4 or Table 2.1). The resulting size distributions $P(R_{2500}[\mathrm{cm}])$ for all three models and both bands are shown in Fig. 7.6. We find $\log\langle R_{2500}/\mathrm{cm}\rangle = 16.37^{+0.48}_{-0.68}$ for the Gaussian disk in the R band and $16.38^{+0.49}_{-0.67}$ in the V band, $16.40^{+0.47}_{-0.70}$ for the thin disk in R and $16.39^{+0.48}_{-0.72}$ in V, as well as $16.39^{+0.50}_{-0.74}$ for the slim disk in R and $16.37^{+0.50}_{-0.80}$ in V, i.e. all around $R_{2500} \simeq 2.4 \cdot 10^{16}$ cm (with these findings again published already in Sorgenfrei et al. 2025, except for those from the slim disk model). If we loosen the mass prior to allow a mean stellar lens mass between 0.01 and 10.0 solar masses (instead of only 0.1 to 1.0 $M_\odot$), then these average size estimates all increase by 0.4 dex (with their errors slightly increased as well), essentially only jointly shifting the size distributions towards larger disks.

For comparison, note that Morgan et al. (2010) found an accretion disk size of $\log \langle R_{2500}/\mathrm{cm} \rangle = 15.7^{+0.5}_{-0.7}$ for HE0435-1223 from their microlensing analysis (see Sect. 2.2.4; actually, as explained in footnote 14, they give this value as inclined thin scale radius R_s at a rest wavelength of 2600 Å, which converts to R_{2500} using Eq. 1.7 to the same significant digits), which is smaller but still in agreement with our values.[62]

Our microlensing-based disk size estimates (even more so as their microlensing-based value) are significantly larger compared to their luminosity-based estimate of $\log(R^{\mathrm{lum.}}_{2500}) \simeq 14.9 \pm 0.1$.[63] In fact, Morgan et al. (2010, 2018) show that these discrepancies are found in many systems, with microlensing-based sizes typically larger by (0.57 ± 0.08) dex as derived by Cornachione & Morgan (2020). In that study, including size estimates of 15 different systems, it is argued, that this discrepancy is resolved if the temperature profile of the quasar's accretion disk (Eq. 1.3) is flatter, around $\beta \approx 1/2$ (since then, incorporating different models, luminosity sizes are increased, while microlensing sizes remain mostly unaffected; Cornachione & Morgan 2020; see also Li et al. 2019). This is – together with our results in Sect. 7.2 on the disk size ratio of HE0435-1223 $q_{R/V}$ of the thin disk model also somewhat preferring a shallower profile – the reason why we included the slim disk model (with $\beta = 1/2$; see Eq. 6.4) in this whole analysis. Note however, non of the results we found and presented in this chapter differ *significantly* for the Gaussian, thin and slim disk models, and the found ratios are compatible with either temperature profile as stated before. Therefore, further investigations into these issues of quasar accretion disk size discrepancies and their temperature profile slopes are necessary and (as mentioned at the beginning of Chapter 2) within reach with the upcoming LSST at the *Vera C. Rubin Observatory*.

[62] The disk sizes can also be expressed in terms of Schwarzschild radii $r_g = 2GM/c^2$, assuming a value for the black hole mass M of HE0435-1223. Using $M = 0.5{\cdot}10^9\,\mathrm{M}_\odot$ from Morgan et al. (2010, and references therein), we can express our accretion disk size estimate of $R_{2500} \simeq 2.4 \cdot 10^{16}$ cm as $R_{2500} \simeq 160 r_g$, however with large uncertainty. This confirms that choosing to ignore correction terms from the inner edge at r_{in} (see Sect. 1.2 and e.g. Eq. 6.2) was legitimate, since using the innermost stable circular orbit for the inner edge $r_{\mathrm{in}} := r_{\mathrm{ISCO}} = \alpha r_g$, with $\alpha = 3$ for non-rotating (Schwarzschild) and $1/2 \leq \alpha \leq 9/2$ for rotating (Kerr) black holes (e.g. Vernardos et al. 2024), means that our measured sizes are still larger than r_{in} by one to two orders of magnitudes.

[63] We can find luminosity-based size estimates from our light curves similarly with Eq. 1.8 (using again $\cos(i) = 1/2$, the central filter wavelengths from Sect. 2.1 and additionally the corresponding zero-points of 3064 Jy and 3636 Jy in R and V, respectively, as well as $D_{\mathrm{S}}/r_H \simeq 0.4075$ for HE0435-1223 with the cosmological parameters from Sect. 6.1.2). As estimates for the intrinsic magnitude of the source (corrected for magnifications from strong lensing and microlensing; see Morgan et al. 2010; Vernardos et al. 2024), we first average the light curves from Fig. 4.4 over time (where we include the systematic light curve errors from Sect. 3.7, Table 3.2, according to Eq. 3.9). Then, we remove the strong lensing magnifications magnitude offsets (Eq. 1.15, again using the κ and γ values from Schechter et al. 2014), exclude the value from image B, due to the strong microlensing event, and finally average the remaining three images for both bands resulting in $\langle m^{corr}_R \rangle \approx (20.4 \pm 0.3)$ mag and $\langle m^{corr}_V \rangle \approx (20.8 \pm 0.3)$ mag. Combining these results, we find inclined thin disk scale radii, which we again correct to 2500 Å as before, finding luminosity sizes of roughly $\log(R^{\mathrm{lum.}}_{2500}) \approx (14.8 \pm 0.1)$, in agreement with the value by Morgan et al. (2010).

7.4. Number of caustic crossings

To conclude our analysis of the microlensing signal in image B of HE0435-1223, having focused on its R to V band size ratio and its absolute size of the accretion disk of HE0435-1223 in the last sections, we now turn to the origin of the underlying variations, i.e. the microlensing caustics causing the analyzed signal in our difference curve data, as well as in our simulated light curves.

At the beginning of Sect. 7.3, we found average source-plane velocities of the quasar disk moving across the magnification patterns of 0.48, 0.33 and 0.31 R_{E}/yr for the Gaussian, thin and slim disk models. Therefore, during the approximately ten years of LCO observations as presented in Fig. 4.4, the quasar has moved around three to five Einstein radii on average. This raises the question of – statistically – how many caustics (as depicted e.g. in Fig. 6.4; see also Sects. 1.3 and 1.4) the quasar has crossed along its track in this time, as it is the averaged magnification effect of these encounters, what we have uncovered with the difference curves in Fig. 5.5, have simulated for this analysis and have drawn our presented conclusions from. To simplify, here we count caustic crossings of the simulated tracks and thus only of the disk's center. Caustics that are missed by the center or merely touch the outer parts of the disk are not counted. Consequently, the following results are lower limits.

As done in Sorgenfrei et al. (2025), to calculate the precise location of all microlensing caustics in our `Teralens` magnification maps from Sect. 6.1.2, we use the complex parametrization from Witt (1990), as implemented in `causticfinder-py`[64], using the same positions and masses of the microlenses from the `Teralens` simulations.[65] As can be seen in Fig. 7.7a, the caustics thus determined are in perfect agreement with the magnification patterns calculated with `Teralens`. Another example of caustics calculated using Witt (1990) is given as cover image of this thesis. There, a $10\,R_{\mathrm{E}} \times 10\,R_{\mathrm{E}}$ sized part for $\kappa_\star/\kappa = 0.8$ of the pure pattern of microlensing caustic lines for image B of HE0435-1223 determined here is shown.[66]

As we have set the track lengths corresponding to 10 yr in our simulations in Sect. 6.2 to match our LCO observations, we therefore counted numbers of caustic crossings N_{cc} per 10 yr. Calculating this number of intersections that each track (and thus the disk's center) has with all caustics, was done only for those tracks in our track library with non-zero probability $P(\chi^2)$. Our `python` code implementing this step is again available on GitHub.[67] In Fig. 7.7a we show one example track on an unconvolved

[64] https://github.com/rschmidthd/causticfinder-py

[65] Witt (1990) includes an additional factor of $\sqrt{|1-\kappa_{\mathrm{smooth}}|}^{-1}$ in their definition of R_{E}.

[66] It is left as an exercise for the reader to match the presented cutout of 'Witt-caustics' on the cover of this thesis to the `Teralens` magnification map on the right of Fig. 6.4.

[67] See `causticcrossingcounter.py` at https://github.com/sorgenfrei-c95/qsoMLsimcurves.

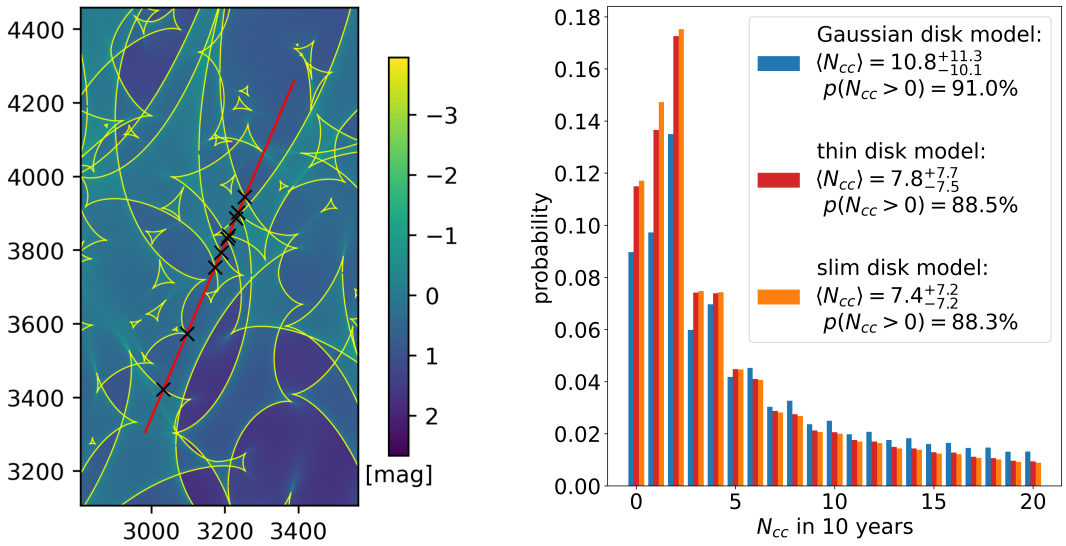

(a) Example track **(b)** Number of caustic crossings

Figure 7.7.: Number of caustic crossings N_{cc}. On the left, we show an example track (in red) on the unconvolved $\kappa_\star/\kappa = 1.0$ `Teralens` map (see Sect. 6.1.2; colour map in magnitudes, x- and y-axis in pixels) crossing $N_{cc} = 11$ (marked with black crosses) caustics (in yellow; calculated as described using Witt 1990) over the ten simulated years. On the right, we show the resulting histogram of the number of caustic crossings N_{cc} (curtailed at $N_{cc} = 20$) over all library tracks weighted by their track probability, for all three disk models. This Figure is adapted from Sorgenfrei et al. (2025), now also including the results for the slim disk model.

`Teralens` map together with the corresponding microlensing caustics as calculated with `causticfinder-py`. Additionally, N_{cc} for this specific track is indicated as well.

Similar as in the previous sections, adding each track's likelihood to the appropriate bins of a histogram of the number of caustic crossings, we obtain three probability distributions for N_{cc} for each disk model. This histogram is shown in Fig. 7.7b. We find expected numbers of caustic crossings $\langle N_{cc}\rangle$ per 10 yr of $10.8^{+11.3}_{-10.1}$, $7.8^{+7.7}_{-7.5}$ and $7.4^{+7.2}_{-7.2}$ for the Gaussian, the thin and the slim disk model, respectively (with 16^{th} and 84^{th} percentiles as uncertainties). This corresponds to approximately one caustic crossing per year. Even though the spread of these findings is large, the probability for the quasar to cross at least one caustic within the 10 yr of observations integrates in all three models to about 90%.

Of course, not all caustic crossings lead to uniquely identifiable microlensing features in the quasar light curves due to the sometimes small separation along the track in time (see Fig. 7.7a), as well as the averaging effect from the disk's brightness profile according to its source size (Sect. 6.1.3). This effectively decreases the number of *observable* caustic crossings. However, we stress again that on the other hand, the true number of N_{cc} is actually higher, since we did not include the expanse of the disk.

Given the size estimates from the last section with disk radii of almost the Einstein radius, this makes caustic crossings in image B of HE0435-1223 extremely likely at all times, explaining the microlensing signal we found in the difference curves (Fig. 5.5). Additionally, as mentioned already in Sorgenfrei et al. (2025), this might also be interesting for studying this object also in the X-ray regime (e.g. Guerras et al. 2017). There, according to Eq. 1.7, the source is expected to be much smaller than in the optical continuum region (Pooley et al. 2006; Zimmer et al. 2011; Mediavilla et al. 2015), thus leading to more variation and high magnification events in the light curves and also, since emission from these smallest scales are magnified most strongly in X-ray spectra (e.g. Reynolds et al. 2014; Chartas et al. 2017), which can help to constrain the inner edge of the disk as well as properties of the central black hole.

This concludes the analysis of the microlensing signal we discovered in our LCO data of image B of HE0435-1223 at the end of Part I of this thesis.

8. Summary and conclusion

Investigating the structure of quasar accretion disks by measuring, simulating and interpreting quasar microlensing light curves was the envisioned goal for this work. Over ten years prior to the start of the project, in Schmidt & Wambsganss (2010), a survey measuring the light curves of multiple lensed quasars using robotic telescopes was deemed the way forward to create a large data set to address these goals. 15 years later, data of eight lensed quasars in two photometric filters taken since 2014 at the Las Cumbres Observatory (LCO) has become the foundation for this thesis.

In Part I, we have measured the R and V band light curves of the multiple images of eight strongly lensed quasars introduced in Chapter 2 and observed with LCO. These quasar light curves, covering almost ten years with in total 1872 epochs, were determined using difference image analysis (DIA) in combination with point spread function (PSF) photometry. Additionally, *Gaia* data was used to correct for effects introduced by the proper motion of reference stars in the field, which became important due to the long time span and the accuracy DIA enables (which might be relevant for other uses of DIA as well), as described in Chapter 3 together with the whole data reduction method published already in Sorgenfrei et al. (2024).

The resulting data set of our LCO quasar light curves – certainly one of the main results of this thesis – are presented in Chapter 4 and are (mostly) publicly available (see Appendix B). They collectively constitute one of the larger light curve data sets covering several lensed quasars in *more* than one filter over almost ten years (for an example from a different group, we refer to the in size and data quality remarkable light curves by Millon et al. 2020a, though observed only in one filter). We have compared our light curves to literature data of the eight quasars when available, finding overall good agreement, where there is data overlap.

The LCO light curves of all quasars and their images display brightness variations, exhibiting features ranging from small-amplitude long-term changes (e.g. at least in parts of the HE2149-2745 data and essentially over the full period in Q0142-100 as well as HE0047-1756) to prominent high-amplitude short-term features (such as the sharp intraseasonal magnitude fluctuations within the data of HE1104-1805 and RXJ1131-1231) or a mixture (e.g. in HE0435-1223). In most of them, clear overall behaviors, i.e. correlated variations in all images and both bands, are visible (see e.g. the highly

similar light curves of WFI2033-4723). As explained, their origin is the quasar itself, while additional brightness variations that appear uncorrelated between the images, are attributed to microlensing of the individual quasar images. This can e.g. been seen in our data of all four images of Q2237+0305 (i.e. the Einstein Cross) with independent variations covering up to a full magnitude within our observations. It is those type of variations we are interested in, as they depend on the source size, thus probing the structure of the lensed quasars, as discussed in Chapter 1.

To extract these microlensing signals from our light curves, time delay corrected difference curves were calculated in Chapter 5, removing all the correlated variations. A particular clear microlensing signal was identified in our difference curves of HE0435-1223 as presented in Fig. 5.5. Since images A, C and D showed essentially the same intrinsic quasar variability, this microlensing signal, present in image B with an amplitude of around 0.7 to 0.8 mag over the ten observing years, was extracted with high confidence. Additionally, a clear *chromatic* feature was unveiled, i.e. the uncovered microlensing variation was stronger in the V than the R band. Again, following the arguments from Chapter 1, this is expected: the dependency of the microlensing variations on the source size in combination with the disk's temperature profile, as predicted from thin disk theory by Shakura & Sunyaev 1973, means that the more central and smaller, i.e. hotter and bluer parts experience more violent and rapid microlensing variations (e.g. Wambsganss & Paczynski 1991).

Therefore, we chose to focus on this microlensing signal in image B of HE0435-1223 for Part II of this thesis. In order to analyze and interpret this signal, in Chapter 6, we conducted microlensing simulations following the widely used light curve fitting method by Kochanek (2004). To produce microlensing magnification maps needed for our simulations we used `Teralens` (Alpay 2019), its (according to our knowledge) first published application in Sorgenfrei et al. (2025). Convolving these maps with three different accretion disk models and testing a large range of accretion disk sizes, we simulated over a billion microlensing light curves and fitted them to our data. From this comparison, the following results could be drawn in Chapter 7:

1. Our simulations were able to reproduce the measured chromatic microlensing signal. We find similar results for the three tested accretion disk models, although with some deviations, not only in the shape of simulated light curves, but also in (non-significant) tendencies in the results. Thus, from our perspective, including different models should be considered in future studies as well, even though currently the consensus in the field is that the exact profile is (at least primarily) not relevant.
2. For the R to V band size ratio of the accretion disk of HE0435-1223 we find

$\langle q_{R/V} \rangle = 1.24^{+0.08}_{-0.20}$, $1.42^{+0.11}_{-0.22}$ and $1.43^{+0.10}_{-0.23}$ for the three disk models (i.e. the Gaussian, thin and slim disk models, respectively). The results are consistent with each other, as well as with the theoretically expected ratio of 1.241 from thin accretion disk theory. As noted, the latter two models (non-significantly) prefer disks models with a more shallow temperature profile.

3. We were able to estimate the size of the accretion disk of HE0435-1223, albeit with large uncertainties (~ 0.6 dex), to around 0.7 to 1.0 Einstein radii, depending on the model and the filter. This could in all six cases consistently be converted to physical units of an inclined disk radius at around $2.4 \cdot 10^{16}$ cm (again with large uncertainties of approximately -0.7 and $+0.5$ dex). This size estimate is larger, but in agreement with the microlensing result by Morgan et al. (2010) for HE0435-1223. Also, our microlensing-based disk size is more than a magnitude larger than their additional luminosity based estimate, which we could reproduce with our light curve data.

4. Combining the previous two points, finding significantly larger microlensing than luminosity based accretion disk sizes is an observation shared throughout the field, as comprehensibly studied by Cornachione & Morgan (2020). A proposed solution is to modify the temperature profile of the thin accretion disk model towards a more shallow profile, close to one for which we have found (weak) evidence from parts of our two-band disk size ratios. Further investigation into these disk size discrepancies and possible different accretion disk temperature profiles are crucial for the progress of the field. With the upcoming Legacy Survey of Space and Time (LSST) at the *Vera C. Rubin Observatory* (which notably will also be using DIA), a large number of high quality, long-time, high cadence, multi-band observations in six filters of an unprecedented number of lensed quasars, ideal to tackle these questions, will be available for future studies and thus hopefully shed some more light on these issues.

5. Furthermore, we have determined that the accretion disk of HE0435-1223 (approximated by only its center) has to cross microlensing caustics roughly once per year to explain the discovered microlensing signal in image B from the difference curves, making HE0435-1223 a promising target for future studies.

Having investigated the inner structure of *one* quasar in our data set, we want to stress, that there are further promising microlensing signals in our LCO light curves of the eight lensed quasars only waiting to be analyzed. Especially with the upcoming LSST data in mind, we look optimistically forward to see what the future holds for chromatic quasar microlensing.

Appendix.

A. Additional light and difference curves

In this appendix, a few additional light curve comparison plots and LCO difference curves are presented, which were kept out of the main text. The order in which these extra examples for five of the eight quasars are given, follows the sequence in which the quasars and their results are presented through this work (see e.g. Table 2.1):

- Fig. A.1 shows the R band comparison of COSMOGRAIL (Millon et al. 2020a) and LCO light curves of HE2149-2745, while Fig. A.2 compares the difference curves of both campaigns, where for the latter the three time delays from Table 2.1 are used instead of only the one from COSMOGRAIL (see also Fig. 5.3).

- Fig. A.3 compares MiNDSTEp (Giannini et al. 2017) with LCO data of HE0047-1756 in the R and V band. Staying with HE0047-1756, in Fig. A.4 we present the LCO difference curves of HE0047-1756 in the R and V band. Here, we also include a comparison of interpolating either images (see Sect. 5.1.3).

- In Fig. A.5, we present the LCO difference light curves for Q0142-100, where we included also the difference, calculated from image B being determined directly from PSF photometry (see Sects. 3.4, 4.1.3 and Fig. 4.6).

- In Fig. A.6, for RXJ1131-1231 in R, light curve data of COSMOGRAIL (Millon et al. 2020a) and LCO data is shown, where the observing seasons overlap. Also presented is how the PSF photometry residuals improved by including a galaxy model for RXJ1131-1231. This addition to the PSF model was necessary to extract the depicted improved light curves (Fig. 4.7) that thus compare well to the COSMOGRAIL data (see also Sect. 3.4 and especially footnote 31).

- And finally, in Figs. A.7 and A.8, the two remaining difference curves between all quasar images of RXJ1131-1231 and WFI2033-4723, respectively, are shown.

For short descriptions and discussions of the presented data, the reader is referred to the corresponding sections in the main text, i.e. Sect. 4.2 for the light curve comparisons and Sect. 5.2 for the difference curves.

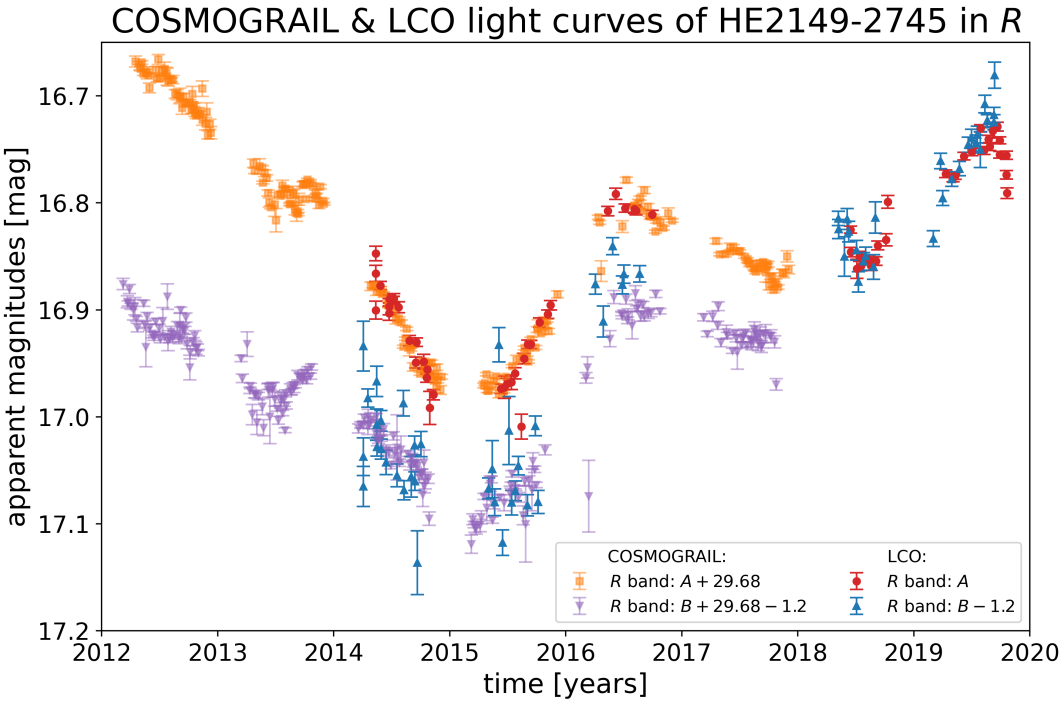

Figure A.1.: COSMOGRAIL (2003-2019) and LCO (2014-2024) comparison of HE2149-2745 in the R band. Shown are only the years 2012 to 2020 to focus on the overlapping observing seasons and used the time delay from COSMOGRAIL.

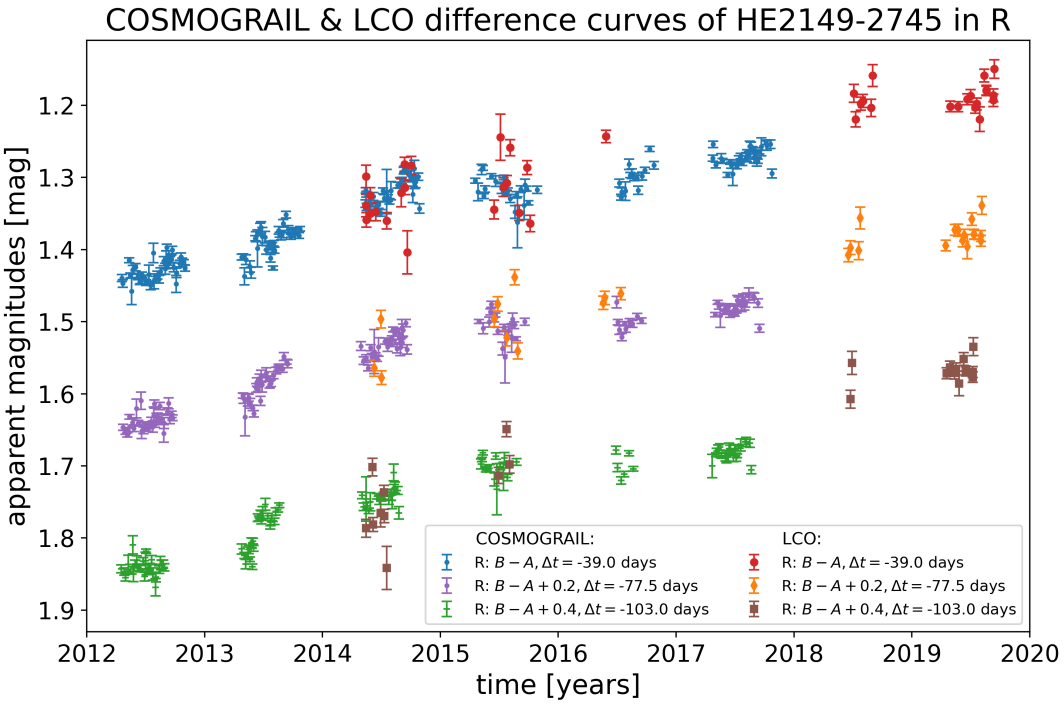

Figure A.2.: COSMOGRAIL (2003-2019) and LCO (2014-2024) comparison of difference curves of HE2149-2745 in the R band. We again restricted the plot to show only data from 2012 to 2020. The differences are calculated using the different Δt.

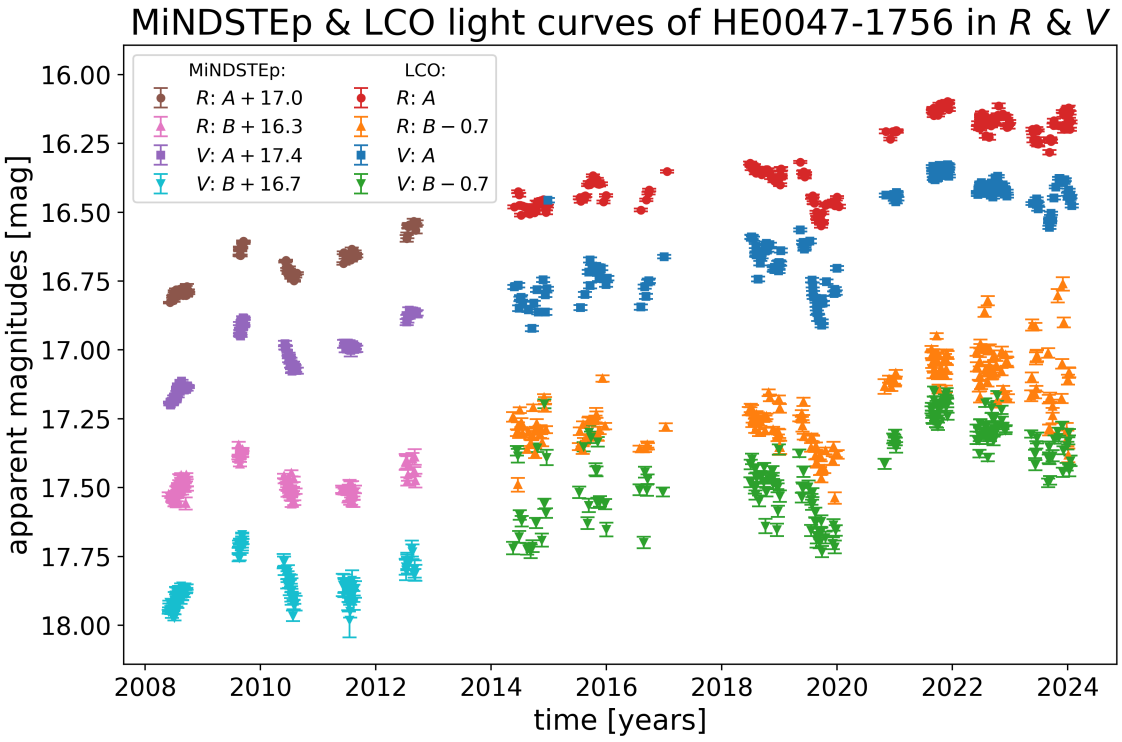

Figure A.3.: MiNDSTEp (2008-2012) and LCO (2014-2024) light curves of HE0047-1756 in the R and V band, where slightly different offsets were used for the V band.

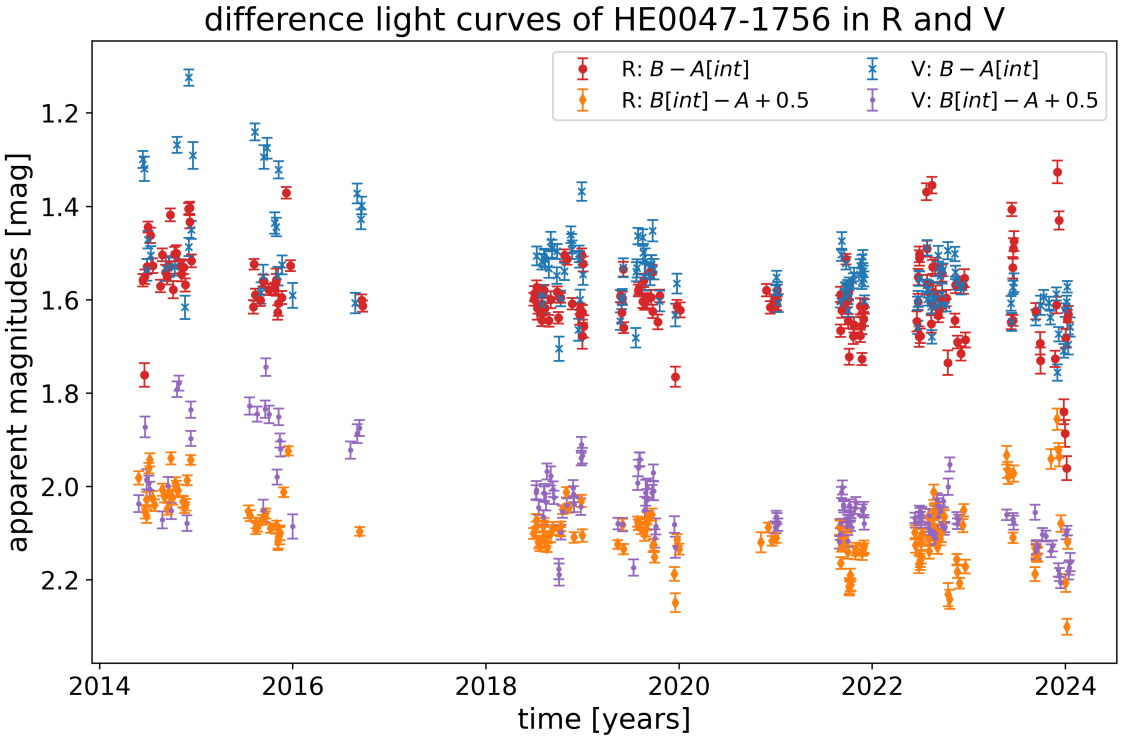

Figure A.4.: Difference curves of HE0047-1756. Shown are $B - A$ differences, once with image A interpolated to the epochs of image B and vice versa (separated by a 0.5 mag offset), both in R and V.

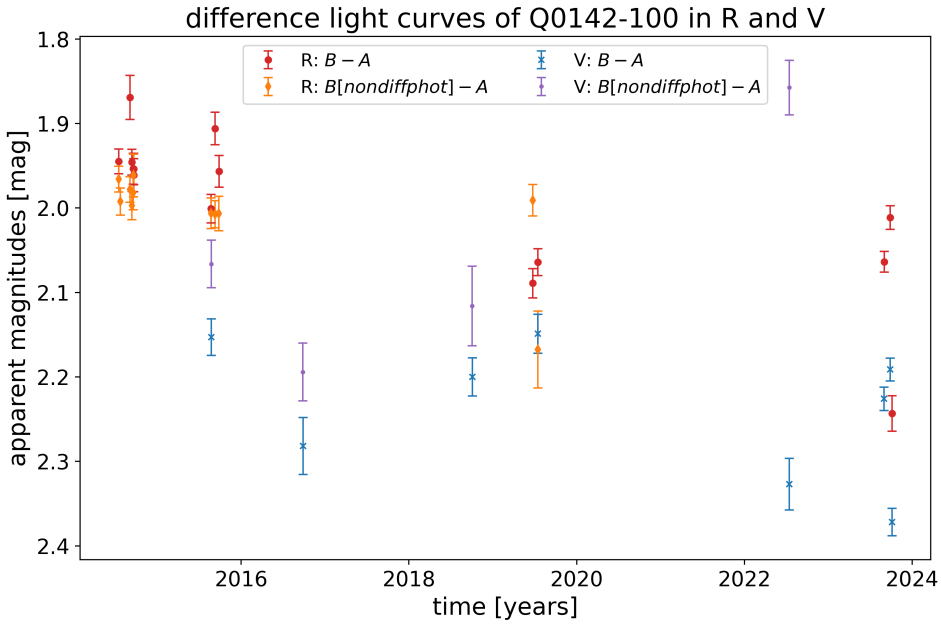

Figure A.5.: $B - A$ difference curves of Q0142-100 in R (red circles) and V (blue crosses). Additionally, the difference was calculate once more using the direct photometry light curves of image B (determined without applying DIA to the observations, see Fig. 4.6), in R (orange diamonds) and V (violet dots). No relative offsets are used.

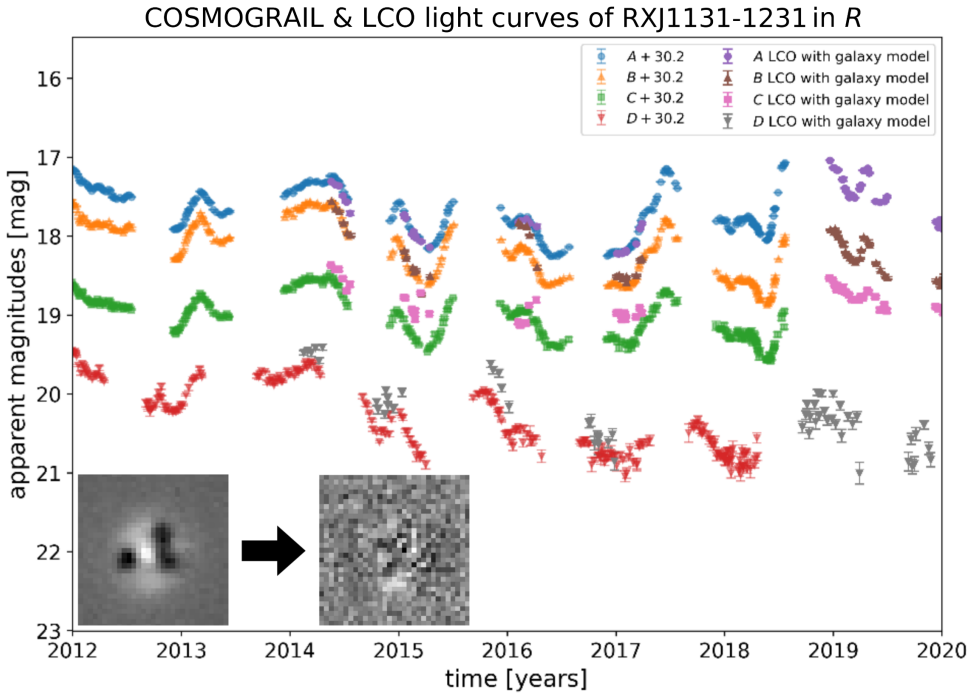

Figure A.6.: COSMOGRAIL (2003-2019) and LCO (2014-2024) comparison of RXJ1131-1231 in the R band. We restricted the plot to show only data from 2012 to 2020 to focus on the overlapping observing seasons. In the lower left, two cutouts of PSF photometry residuals, showing the improvement that comes with the galaxy model (leading to the depicted quality of light curves), are included (see Sect. 3.4).

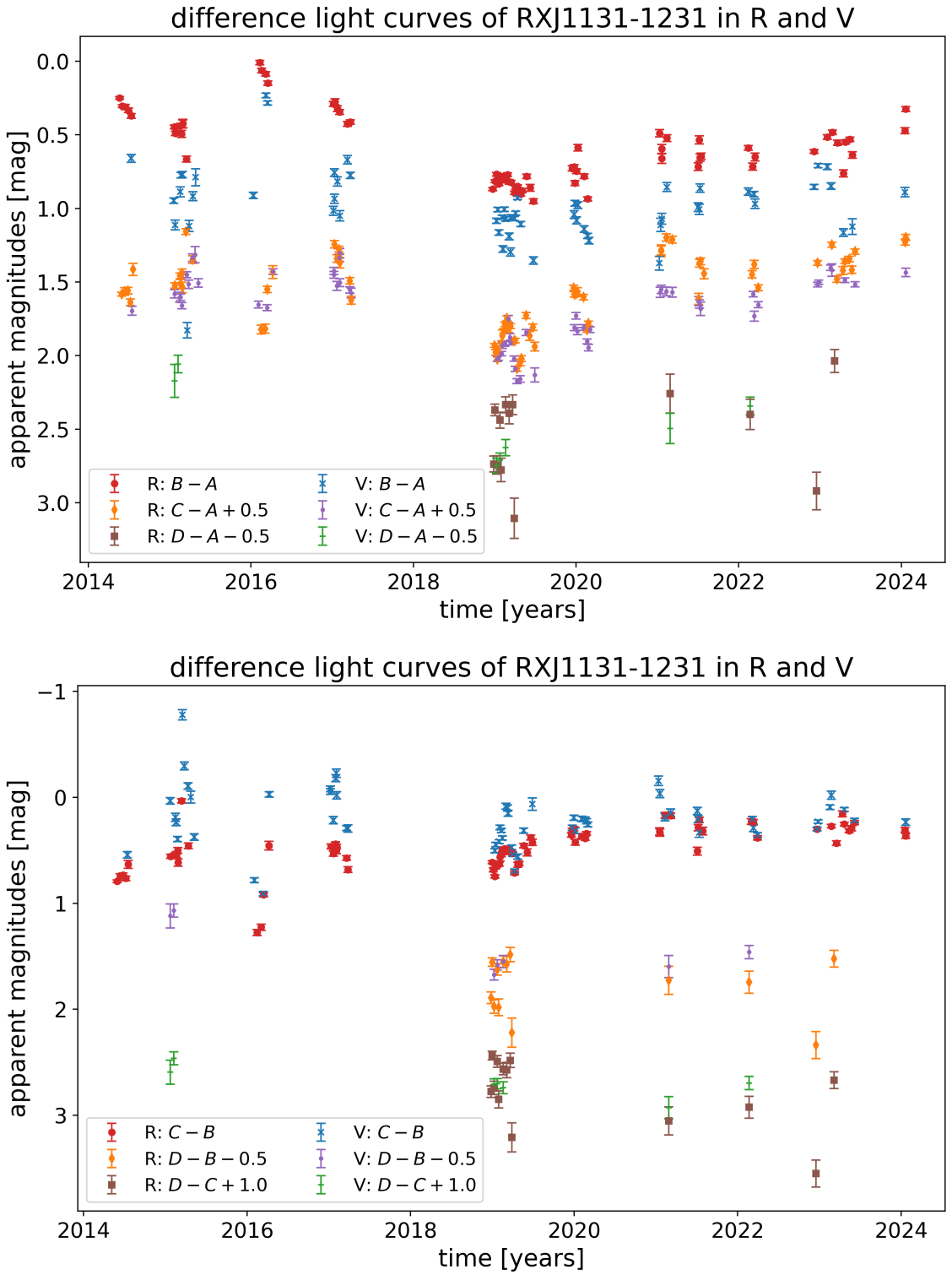

Figure A.7.: Difference curves of RXJ1131-1231. Shown are the differences $B-A$, $C-A+0.5$ mag and $D-A-0.5$ mag on the top and $C-B$, $D-B+0.5$ mag and $D-C+1.0$ mag on the bottom), all in the R and V band.

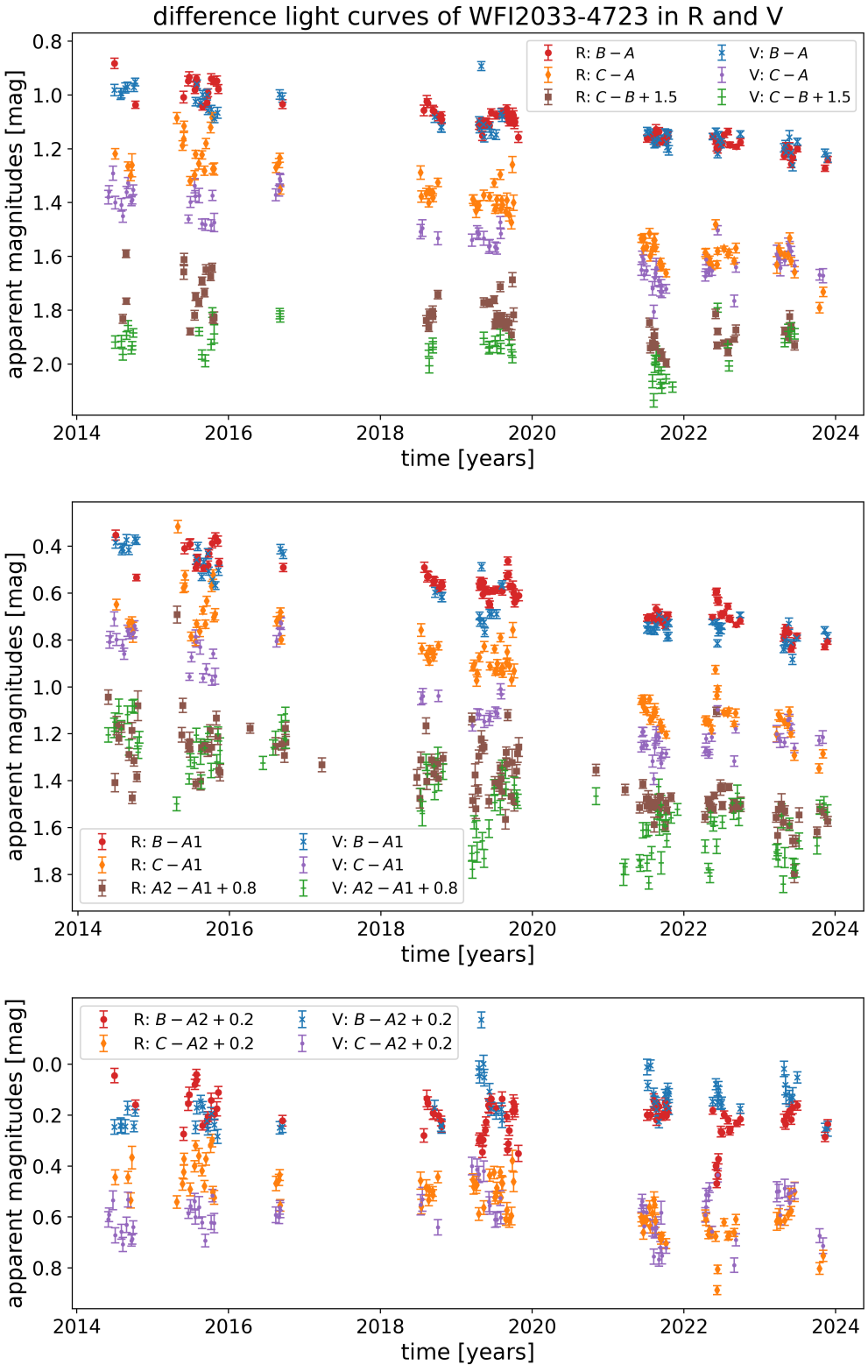

Figure A.8.: Difference curves of WFI2033-4723. Shown are the three differences $B - A$, $C - A$ and $C - B + 1.5$ mag using the combined image A = A1 + A2 on the top. In the middle panel, the differences $B - A1$ and $C - A1$ are shown, as well as $A2 - A1$. Finally, on the bottom, the two remaining differences with respect to A2 are shown (with a small overall offset for plotting reasons), all in the R and V band.

B. HE0435-1223 light curve data

In this appendix, we present the tabulated light curves of HE0435-1223 as plotted in Fig. 4.4 in the R band (Table B.1) and V band (Table B.2) and used for the microlensing analysis in Part II as published in Sorgenfrei et al. (2025). This publication also includes a reference to the Centre de Données astronomiques de Strasbourg CDS[68], where the same data is saved. Similarly, data for the earlier versions of the light curves of HE1104-1805, HE2149-2745 and Q2237+0305 published in Sorgenfrei et al. (2024) are available at CDS[69] as well. Note, that the light curves of these four quasars are also available (e.g. using `PyVO` or TOPCAT) at GAVO Data Center (2025)[70], which is where we plan to update the data as described in Sect. 3.8, likely also including the data of RXJ1131-1231 and WFI2033-4723. The remaining curves (i.e. at least those of HE0047-1756 and Q0142-100) can be provided upon request.

Table B.1.: Light curve data of HE0435-1223 in the R band

time [MJD]	A [mag]	ΔA [mag]	B [mag]	ΔB [mag]	C [mag]	ΔC [mag]	D [mag]	ΔD [mag]
57278.3919	18.4312	0.0085	18.6370	0.0113	18.8401	0.0081	19.1437	0.0137
57283.3921	18.4343	0.0076	18.6699	0.0108	18.8306	0.0077	19.1123	0.0120
57287.3403	18.4325	0.0097	18.6883	0.0142	18.7992	0.0115	19.1211	0.0167
57317.1819	18.4562	0.0083	18.7919	0.0133	18.7969	0.0089	19.0324	0.0124
57329.2909	18.4925	0.0173	18.6342	0.0236	18.8997	0.0249	19.1387	0.0251
57338.3423	18.4080	0.0146	18.6575	0.0223	18.8367	0.0213	19.3434	0.0260
57345.3257	18.4172	0.0111	18.6357	0.0162	18.8514	0.0145	19.2057	0.0165
57426.0488	18.1595	0.0072	18.2990	0.0099	18.5429	0.0087	18.9639	0.0139
57432.1096	18.2150	0.0144	18.0907	0.0126	18.6573	0.0271	19.1476	0.0209
57446.0443	18.1808	0.0062	18.4279	0.0093	18.5090	0.0065	18.7994	0.0094
57641.3990	18.2110	0.0064	18.3906	0.0084	18.5181	0.0059	18.9054	0.0102
57645.3806	18.2096	0.0063	18.4666	0.0092	18.4511	0.0058	18.8376	0.0098
57656.2744	18.1702	0.0062	18.3709	0.0085	18.4819	0.0057	18.8266	0.0097
57661.2535	18.1943	0.0069	18.4145	0.0096	18.4532	0.0066	18.8019	0.0111
57757.2081	18.0904	0.0059	18.2515	0.0079	18.3292	0.0055	18.6888	0.0091
57774.1283	18.0780	0.0061	18.1708	0.0076	18.3374	0.0056	18.7079	0.0096
57784.0903	18.0891	0.0061	18.2209	0.0086	18.3360	0.0064	18.6830	0.0092
57821.0349	18.1291	0.0089	18.1148	0.0108	18.3697	0.0100	18.7425	0.0130
57829.0557	18.1360	0.0071	18.2123	0.0095	18.3661	0.0075	18.6704	0.0088
57836.0451	18.1506	0.0072	18.2197	0.0096	18.4045	0.0080	18.7195	0.0112

[68] https://cdsarc.cds.unistra.fr/viz-bin/cat/J/A+A/703/A250 (pending as of 17 Nov. 2025)
[69] https://cdsarc.cds.unistra.fr/viz-bin/cat/J/A+A/683/A119
[70] https://dc.g-vo.org/mlcolour/q/web/form

Table B.1.: continued.

time [MJD]	A [mag]	ΔA [mag]	B [mag]	ΔB [mag]	C [mag]	ΔC [mag]	D [mag]	ΔD [mag]
58347.3320	18.2422	0.0069	18.1164	0.0077	18.4936	0.0069	18.8229	0.0095
58352.4110	18.2093	0.0076	18.1040	0.0088	18.4504	0.0082	18.8231	0.0116
58379.3404	18.1313	0.0075	18.0146	0.0088	18.3802	0.0085	18.7278	0.0114
58424.2851	18.1084	0.0110	17.9238	0.0110	18.3268	0.0101	18.6462	0.0135
58483.2072	18.0872	0.0134	17.9221	0.0146	18.3795	0.0156	18.7144	0.0162
58488.2085	18.1559	0.0059	17.9538	0.0060	18.3607	0.0055	18.6896	0.0081
58497.1754	18.1700	0.0067	17.9385	0.0072	18.3657	0.0068	18.7162	0.0096
58512.1582	18.1797	0.0062	17.9341	0.0061	18.3948	0.0058	18.7299	0.0087
58518.0325	18.1864	0.0121	17.9253	0.0125	18.3948	0.0147	18.6925	0.0158
58535.0830	18.2227	0.0082	18.0460	0.0091	18.4353	0.0094	18.7935	0.0138
58547.0239	18.2318	0.0065	18.0817	0.0070	18.4784	0.0062	18.8163	0.0096
58557.0264	18.2484	0.0071	18.1169	0.0078	18.5117	0.0074	18.8328	0.0098
58569.0144	18.2642	0.0063	18.1282	0.0066	18.5082	0.0059	18.8579	0.0093
58705.3875	18.2961	0.0069	18.1130	0.0074	18.5242	0.0071	18.9377	0.0106
58723.3345	18.2899	0.0081	18.0562	0.0086	18.5248	0.0087	18.8624	0.0129
58751.3006	18.3338	0.0086	18.1217	0.0088	18.5678	0.0092	18.8887	0.0114
58757.3558	18.3670	0.0125	18.1465	0.0132	18.5521	0.0130	18.8911	0.0158
58783.3439	18.3800	0.0069	18.1342	0.0066	18.5960	0.0061	18.9457	0.0096
58837.2554	18.3381	0.0068	17.9830	0.0059	18.5528	0.0061	18.8996	0.0098
58842.0611	18.3526	0.0079	17.9672	0.0067	18.5831	0.0075	18.8902	0.0106
58848.2154	18.3348	0.0070	17.9957	0.0063	18.5622	0.0065	18.8853	0.0101
58893.0824	18.3173	0.0068	17.9031	0.0060	18.5324	0.0065	18.9089	0.0098
58900.1177	18.3231	0.0074	17.8923	0.0063	18.5208	0.0073	18.9056	0.0113
58920.0130	18.3271	0.0078	17.9222	0.0067	18.5431	0.0074	18.8897	0.0116
58924.0322	18.2653	0.0097	17.9065	0.0086	18.5435	0.0103	18.9114	0.0132
59204.1921	18.3066	0.0071	17.8454	0.0058	18.5094	0.0067	18.8624	0.0103
59220.0665	18.3195	0.0072	17.8624	0.0061	18.5131	0.0067	18.8617	0.0103
59227.2034	18.3310	0.0071	17.8874	0.0060	18.5001	0.0066	18.8766	0.0106
59231.1236	18.3427	0.0069	17.8902	0.0054	18.5266	0.0055	18.8508	0.0085
59234.0992	18.3316	0.0074	17.8870	0.0060	18.5347	0.0067	18.8731	0.0110
59255.0818	18.3342	0.0070	17.8805	0.0059	18.5338	0.0063	18.8755	0.0095
59263.1238	18.3485	0.0073	17.8880	0.0059	18.5308	0.0062	18.8733	0.0094
59285.0298	18.3220	0.0087	17.8679	0.0072	18.5225	0.0084	18.9008	0.0127
59462.2815	18.4135	0.0085	18.0377	0.0079	18.6127	0.0092	18.9702	0.0122
59544.1960	18.3923	0.0082	17.9201	0.0069	18.5552	0.0084	18.9834	0.0116
59551.1955	18.3602	0.0074	17.8617	0.0059	18.5440	0.0065	18.9506	0.0097
59558.1121	18.3602	0.0074	17.8702	0.0063	18.5152	0.0073	18.8546	0.0104
59633.1057	18.3527	0.0078	17.8134	0.0062	18.4910	0.0074	18.8525	0.0113
59635.0820	18.3455	0.0074	17.8368	0.0062	18.4613	0.0072	18.8521	0.0110
59642.0329	18.3294	0.0086	17.7997	0.0069	18.5081	0.0095	18.8739	0.0132
59670.0125	18.2773	0.0070	17.7123	0.0053	18.4193	0.0065	18.7755	0.0086
59795.3694	18.3192	0.0074	17.8087	0.0057	18.4519	0.0064	18.7907	0.0104
59848.2984	18.3656	0.0069	17.9475	0.0054	18.5235	0.0053	18.8411	0.0083
59901.1394	18.4725	0.0078	18.0901	0.0067	18.6292	0.0064	18.9254	0.0098
59910.2973	18.4566	0.0127	18.0799	0.0117	18.6477	0.0144	19.0156	0.0145
59928.2151	18.4991	0.0083	18.1485	0.0073	18.6476	0.0070	18.9703	0.0113
59936.1925	18.5118	0.0080	18.1529	0.0070	18.6636	0.0066	18.9901	0.0104
59986.1314	18.6266	0.0100	18.3700	0.0095	18.7569	0.0089	19.0864	0.0124
59996.0983	18.6029	0.0089	18.3640	0.0087	18.7377	0.0081	19.1065	0.0122
60011.0285	18.5535	0.0099	18.2470	0.0092	18.6531	0.0094	19.0792	0.0159
60022.0121	18.5328	0.0084	18.1642	0.0074	18.6940	0.0075	19.1351	0.0125
60032.0156	18.5231	0.0088	18.1714	0.0078	18.6703	0.0078	19.0326	0.0126
60045.9814	18.5360	0.0175	18.1818	0.0171	18.7212	0.0214	19.0972	0.0255

Table B.1.: continued.

time [MJD]	A [mag]	ΔA [mag]	B [mag]	ΔB [mag]	C [mag]	ΔC [mag]	D [mag]	ΔD [mag]
60270.0786	18.6566	0.0124	18.3237	0.0113	18.7581	0.0119	19.0678	0.0143
60284.2564	18.6214	0.0090	18.2544	0.0074	18.8067	0.0068	19.1716	0.0119
60295.2129	18.6369	0.0114	18.3264	0.0106	18.7278	0.0107	19.0444	0.0128
60315.1006	18.6009	0.0081	18.2375	0.0070	18.7652	0.0068	19.1145	0.0109
60319.1758	18.6100	0.0088	18.2455	0.0074	18.7300	0.0065	19.1161	0.0112
60326.2011	18.5819	0.0084	18.2121	0.0073	18.7426	0.0072	19.1306	0.0118

Table B.2.: Light curve data of HE0435-1223 in the V band

time [MJD]	A [mag]	ΔA [mag]	B [mag]	ΔB [mag]	C [mag]	ΔC [mag]	D [mag]	ΔD [mag]
56862.3980	18.8094	0.0092	19.0934	0.0148	19.1139	0.0122	19.5905	0.0175
56903.3949	18.8356	0.0095	19.2422	0.0169	19.1938	0.0134	19.5530	0.0183
57277.3919	18.7397	0.0084	19.0339	0.0140	19.0398	0.0111	19.3863	0.0145
57282.3859	18.7823	0.0082	18.9965	0.0125	19.0605	0.0102	19.3896	0.0140
57317.1947	18.8098	0.0110	19.0487	0.0166	19.0879	0.0139	19.4184	0.0206
57332.2953	18.7996	0.0094	19.0289	0.0144	19.0969	0.0120	19.4480	0.0161
57339.3472	18.7949	0.0077	19.0057	0.0110	19.0958	0.0093	19.4925	0.0142
57345.2688	18.7801	0.0117	19.0305	0.0178	19.0356	0.0142	19.4044	0.0208
57390.2223	18.4819	0.0064	18.7131	0.0092	18.7725	0.0080	19.2250	0.0122
57423.0629	18.4116	0.0096	18.4898	0.0123	18.7300	0.0109	19.2041	0.0187
57447.0385	18.4481	0.0076	18.5356	0.0098	18.7665	0.0092	19.1992	0.0148
57633.3807	18.5364	0.0130	18.7433	0.0200	18.6999	0.0158	19.2054	0.0214
57641.3750	18.5137	0.0071	18.6866	0.0097	18.7124	0.0075	19.1727	0.0124
57645.3959	18.4746	0.0076	18.6688	0.0116	18.6825	0.0090	19.1528	0.0128
57661.2775	18.4571	0.0081	18.6128	0.0119	18.6664	0.0096	19.1382	0.0159
57757.1841	18.3373	0.0067	18.4454	0.0094	18.5276	0.0077	18.9548	0.0122
57774.1042	18.3233	0.0076	18.4019	0.0099	18.5155	0.0086	18.8968	0.0130
57829.0557	18.3415	0.0089	18.4020	0.0119	18.5638	0.0107	18.8742	0.0135
57836.0394	18.3890	0.0094	18.3944	0.0121	18.6071	0.0114	18.9122	0.0151
58342.3716	18.6073	0.0095	18.4019	0.0107	18.6443	0.0099	19.0984	0.0125
58347.4223	18.6080	0.0117	18.3864	0.0127	18.6538	0.0124	19.0922	0.0152
58352.3653	18.5822	0.0094	18.3494	0.0105	18.6396	0.0100	19.1208	0.0126
58379.3566	18.5143	0.0096	18.2584	0.0107	18.5056	0.0102	18.9969	0.0140
58394.2133	18.4109	0.0081	18.1877	0.0094	18.4198	0.0095	18.8895	0.0114
58491.1497	18.4544	0.0078	18.1537	0.0079	18.5665	0.0077	18.9338	0.0117
58497.2189	18.4081	0.0066	18.1312	0.0069	18.5979	0.0078	18.9299	0.0095
58512.1098	18.4679	0.0069	18.1605	0.0072	18.5911	0.0080	18.9953	0.0111
58536.1125	18.4751	0.0102	18.2875	0.0116	18.5916	0.0122	18.9511	0.0166
58547.0297	18.5600	0.0088	18.2960	0.0092	18.6611	0.0093	19.0718	0.0136
58557.0577	18.5818	0.0076	18.3347	0.0074	18.7324	0.0081	19.0942	0.0122
58705.4079	18.6380	0.0078	18.3797	0.0086	18.6974	0.0086	19.1511	0.0116
58723.4115	18.6763	0.0079	18.2756	0.0076	18.7032	0.0084	19.1191	0.0106
58751.3708	18.7473	0.0116	18.3411	0.0103	18.7738	0.0118	19.2536	0.0144
58757.3838	18.7378	0.0091	18.3392	0.0085	18.7955	0.0093	19.2532	0.0147
58783.2993	18.7185	0.0083	18.3883	0.0085	18.8486	0.0094	19.2578	0.0125
58837.2902	18.6707	0.0081	18.1468	0.0064	18.7975	0.0085	19.2306	0.0128
58842.1062	18.7222	0.0084	18.1923	0.0068	18.7681	0.0083	19.1660	0.0109
58849.2229	18.7035	0.0081	18.2321	0.0070	18.7869	0.0083	19.1830	0.0117
58876.0663	18.7922	0.0162	18.1442	0.0160	18.7877	0.0174	19.3473	0.0199

Table B.2.: continued.

time [MJD]	A [mag]	ΔA [mag]	B [mag]	ΔB [mag]	C [mag]	ΔC [mag]	D [mag]	ΔD [mag]
58893.1192	18.6123	0.0081	18.0677	0.0067	18.7648	0.0095	19.2375	0.0131
58903.1132	18.6242	0.0073	18.1100	0.0062	18.8038	0.0083	19.1797	0.0111
58920.0258	18.6744	0.0083	18.0950	0.0063	18.7770	0.0086	19.2140	0.0122
59204.2660	18.5876	0.0070	17.9965	0.0058	18.7795	0.0083	19.1474	0.0108
59220.1362	18.6264	0.0076	18.0647	0.0061	18.7341	0.0079	19.1038	0.0116
59227.2239	18.6525	0.0089	18.0602	0.0071	18.6907	0.0088	19.0885	0.0117
59231.1826	18.6725	0.0075	18.0353	0.0059	18.7503	0.0084	19.1673	0.0111
59234.1235	18.6957	0.0089	18.0497	0.0064	18.7831	0.0093	19.1700	0.0139
59255.0820	18.7359	0.0081	18.0152	0.0062	18.6954	0.0080	19.2205	0.0120
59263.0981	18.6346	0.0078	18.1175	0.0081	18.7652	0.0097	19.1191	0.0125
59285.0278	18.6783	0.0095	18.0848	0.0078	18.6915	0.0098	19.0446	0.0134
59297.0262	18.6831	0.0112	18.0914	0.0087	18.7303	0.0120	19.1058	0.0178
59462.3767	18.8194	0.0112	18.2543	0.0087	18.8592	0.0108	19.3335	0.0153
59496.3081	18.8971	0.0132	18.4304	0.0117	18.8446	0.0133	19.1758	0.0154
59544.2483	18.7237	0.0101	18.1646	0.0083	18.7102	0.0108	19.1494	0.0139
59551.2206	18.7622	0.0092	18.0327	0.0066	18.6969	0.0084	19.1615	0.0116
59558.1548	18.7646	0.0095	18.0246	0.0070	18.6528	0.0092	19.1241	0.0130
59633.0853	18.6683	0.0074	18.0096	0.0056	18.7950	0.0082	19.1654	0.0106
59635.1062	18.6849	0.0086	17.9657	0.0060	18.7828	0.0091	19.2128	0.0120
59642.0675	18.7137	0.0115	17.9257	0.0076	18.6304	0.0114	19.1835	0.0169
59670.0125	18.6115	0.0098	17.8677	0.0067	18.5988	0.0094	19.0085	0.0145
59795.4130	18.6671	0.0096	17.9646	0.0067	18.5900	0.0079	19.0157	0.0114
59815.4020	18.7020	0.0090	17.9627	0.0064	18.5969	0.0077	19.0249	0.0121
59848.3581	18.7259	0.0097	18.1379	0.0072	18.7059	0.0085	19.1122	0.0127
59901.1139	18.9184	0.0105	18.3056	0.0087	18.7777	0.0095	19.1553	0.0140
59910.3176	18.9083	0.0123	18.3312	0.0104	18.8195	0.0130	19.2646	0.0133
59928.2356	18.9087	0.0112	18.3927	0.0088	18.8485	0.0102	19.2597	0.0152
59936.1887	18.9362	0.0108	18.3030	0.0077	18.9050	0.0094	19.3941	0.0162
59986.0854	19.1489	0.0177	18.5195	0.0139	19.0712	0.0156	19.6594	0.0242
59996.1185	19.0199	0.0120	18.5755	0.0098	19.0595	0.0120	19.5704	0.0178
60022.0054	18.9008	0.0103	18.4256	0.0091	18.9433	0.0115	19.3329	0.0140
60032.0122	18.8586	0.0092	18.3849	0.0076	19.0411	0.0107	19.3797	0.0140
60044.9880	18.8722	0.0098	18.4123	0.0085	19.0514	0.0115	19.3658	0.0146
60236.1725	19.0859	0.0184	18.4596	0.0137	19.0937	0.0181	19.7209	0.0250
60237.2098	19.0712	0.0240	18.6405	0.0234	18.9108	0.0220	19.3216	0.0344
60270.0990	19.1472	0.0148	18.4052	0.0097	19.0124	0.0127	19.6136	0.0207
60284.2181	18.9737	0.0114	18.4963	0.0085	19.1021	0.0120	19.5003	0.0168
60295.2153	19.2626	0.0171	18.5160	0.0113	18.8899	0.0123	19.4168	0.0181
60315.1015	19.0981	0.0133	18.3495	0.0084	18.9617	0.0111	19.6083	0.0205
60319.1991	19.0394	0.0144	18.4867	0.0106	18.9255	0.0106	19.4066	0.0186
60326.1561	19.0719	0.0124	18.4420	0.0092	18.8994	0.0095	19.3756	0.0162

Publications

This work resulted in the following publications, (1) Sorgenfrei et al. (2024) mostly used in Chapter 3 and (2) Sorgenfrei et al. (2025) especially in Chapters 6 and 7:

(1) **Christian Sorgenfrei**, Robert W. Schmidt & Joachim Wambsganss: *Improving the light curves of gravitationally lensed quasars with Gaia proper motion data*. Published in *Astronomy & Astrophysics*, 683:A119, March 2024 (accepted: 12 December 2023). doi: 10.1051/0004-6361/202347381.

(2) **Christian Sorgenfrei**, Robert W. Schmidt & Joachim Wambsganss: *Detection of colour variations from gravitational microlensing observations in the quadruple quasar HE0435-1223: Implications for the accretion disc*. Accepted for publication in *Astronomy & Astrophysics*: 9 September 2025 (currently, as of 17 November 2025, in press). doi: 10.1051/0004-6361/202555933.

Bibliography

Abramowicz, M. A., Czerny, B., Lasota, J. P., & Szuszkiewicz, E. Slim Accretion Disks. *The Astrophysical Journal*, 332:646, 1988. doi: 10.1086/166683.

Agol, E. & Krolik, J. H. Magnetic Stress at the Marginally Stable Orbit: Altered Disk Structure, Radiation, and Black Hole Spin Evolution. *The Astrophysical Journal*, 528(1):161–170, 2000. doi: 10.1086/308177.

Alard, C. Image subtraction using a space-varying kernel. *Astronomy & Astrophysics Supplement Series*, 144(2):363–370, 2000. doi: 10.1051/aas:2000214.

Alard, C. & Lupton, R. H. A Method for Optimal Image Subtraction. *The Astrophysical Journal*, 503(1):325–331, 1998. doi: 10.1086/305984.

Albrow, M. D., Horne, K., Bramich, D. M., Fouqué, P., Miller, V. R., Beaulieu, J. P., Coutures, C., Menzies, J., Williams, A., Batista, V., Bennett, D. P., Brillant, S., Cassan, A., Dieters, S., Dominis Prester, D., Donatowicz, J., Greenhill, J., Kains, N., Kane, S. R., Kubas, D., Marquette, J. B., Pollard, K. R., Sahu, K. C., Tsapras, Y., Wambsganss, J., & Zub, M. Difference imaging photometry of blended gravitational microlensing events with a numerical kernel. *Monthly Notices of the Royal Astronomical Society*, 397(4):2099–2105, 2009. doi: 10.1111/j.1365-2966.2009.15098.x.

Alpay, A. Teralens – A parallel (quasar) microlensing code for multi-teraflop devices. https://github.com/illuhad/teralens, 2019.

Anguita, T., Schmidt, R. W., Turner, E. L., Wambsganss, J., Webster, R. L., Loomis, K. A., Long, D., & McMillan, R. The multiple quasar Q2237+0305 under a microlensing caustic. *Astronomy & Astrophysics*, 480(2):327–334, 2008. doi: 10.1051/0004-6361:20078221.

Antonucci, R. Unified models for active galactic nuclei and quasars. *Annual Review of Astronomy and Astrophysics*, 31:473–521, 1993. doi: 10.1146/annurev.aa.31.090193.002353.

Bartelmann, M. *Das kosmologische Standardmodell*. Springer Spektrum Berlin, Heidelberg, 2019. doi: 10.1007/978-3-662-59627-2.

Bartelmann, M. & Schneider, P. Weak gravitational lensing. *Physics Reports*, 340(4-5):291–472, 2001. doi: 10.1016/S0370-1573(00)00082-X.

Becker, A. HOTPANTS: High Order Transform of PSF ANd Template Subtraction. Astrophysics Source Code Library, ascl:1504.004, 2015. https://ui.adsabs.harvard.edu/abs/2015ascl.soft04004B.

Berdina, L. & Tsvetkova, V. S. Detection of the rapid variability in the Q2237+0305 quasar. *arXiv e-prints*, art. arXiv:1801.05650, 2018. doi: 10.48550/arXiv.1801.05650.

Bessell, M. S. Standard Photometric Systems. *Annual Review of Astronomy and Astrophysics*, 43 (1):293–336, 2005. doi: 10.1146/annurev.astro.41.082801.100251.

Bianco, F. B., Ivezić, Ž., Jones, R. L., Graham, M. L., Marshall, P., Saha, A., Strauss, M. A., Yoachim, P., Ribeiro, T., Anguita, T., Bauer, A. E., Bauer, F. E., Bellm, E. C., Blum, R. D., Brandt, W. N., Brough, S., Catelan, M., Clarkson, W. I., Connolly, A. J., Gawiser, E., Gizis, J. E., Hložek, R., Kaviraj, S., Liu, C. T., Lochner, M., Mahabal, A. A., Mandelbaum, R., McGehee, P., Neilsen, Jr., E. H., Olsen, K. A. G., et al. Optimization of the Observing Cadence for the Rubin Observatory Legacy Survey of Space and Time: A Pioneering Process of Community-focused Experimental Design. *The Astrophysical Journal Supplement*, 258(1): 1, 2022. doi: 10.3847/1538-4365/ac3e72.

Birrer, S., Millon, M., Sluse, D., Shajib, A. J., Courbin, F., Erickson, S., Koopmans, L. V. E., Suyu, S. H., & Treu, T. Time-Delay Cosmography: Measuring the Hubble Constant and Other Cosmological Parameters with Strong Gravitational Lensing. *Space Science Reviews*, 220(5): 48, 2024. doi: 10.1007/s11214-024-01079-w.

Blackburne, J. A. & Kochanek, C. S. The Effect of a Time-varying Accretion Disk Size on Quasar Microlensing Light Curves. *The Astrophysical Journal*, 718(2):1079–1084, 2010. doi: 10.1088/0004-637X/718/2/1079.

Blackburne, J. A., Pooley, D., Rappaport, S., & Schechter, P. L. Sizes and Temperature Profiles of Quasar Accretion Disks from Chromatic Microlensing. *The Astrophysical Journal*, 729(1):34, 2011. doi: 10.1088/0004-637X/729/1/34.

Bond, I. A., Udalski, A., Jaroszyński, M., Rattenbury, N. J., Paczyński, B., Soszyński, I., Wyrzykowski, L., Szymański, M. K., Kubiak, M., Szewczyk, O., Żebruń, K., Pietrzyński, G., Abe, F., Bennett, D. P., Eguchi, S., Furuta, Y., Hearnshaw, J. B., Kamiya, K., Kilmartin, P. M., Kurata, Y., Masuda, K., Matsubara, Y., Muraki, Y., Noda, S., Okajima, K., Sako, T., Sekiguchi, T., Sullivan, D. J., Sumi, T., Tristram, P. J., et al. OGLE 2003-BLG-235/MOA 2003-BLG-53: A Planetary Microlensing Event. *The Astrophysical Journal Letters*, 606(2): L155–L158, 2004. doi: 10.1086/420928.

Bonvin, V., Courbin, F., Suyu, S. H., Marshall, P. J., Rusu, C. E., Sluse, D., Tewes, M., Wong, K. C., Collett, T., Fassnacht, C. D., Treu, T., Auger, M. W., Hilbert, S., Koopmans, L. V. E., Meylan, G., Rumbaugh, N., Sonnenfeld, A., & Spiniello, C. H0LiCOW - V. New COSMOGRAIL time delays of HE 0435-1223: H_0 to 3.8 per cent precision from strong lensing in a flat ΛCDM model. *Monthly Notices of the Royal Astronomical Society*, 465(4):4914–4930, 2017. doi: 10.1093/mnras/stw3006.

Bonvin, V., Millon, M., Chan, J. H. H., Courbin, F., Rusu, C. E., Sluse, D., Suyu, S. H., Wong, K. C., Fassnacht, C. D., Marshall, P. J., Treu, T., Buckley-Geer, E., Frieman, J., Hempel, A., Kim, S., Lachaume, R., Rabus, M., Chao, D. C. Y., Chijani, M., Gilman, D., Gilmore, K., Rojas, K., Williams, P., Anguita, T., Kochanek, C. S., Morgan, C., Motta, V., Tewes, M., & Meylan, G. COSMOGRAIL. XVIII. time delays of the quadruply lensed quasar WFI2033-4723. *Astronomy & Astrophysics*, 629:A97, 2019. doi: 10.1051/0004-6361/201935921.

Bower, G. A., Green, R. F., Danks, A., Gull, T., Heap, S., Hutchings, J., Joseph, C., Kaiser, M. E., Kimble, R., Kraemer, S., Weistrop, D., Woodgate, B., Lindler, D., Hill, R. S., Malumuth, E. M., Baum, S., Sarajedini, V., Heckman, T. M., Wilson, A. S., & Richstone, D. O. Kinematics of

the Nuclear Ionized Gas in the Radio Galaxy M84 (NGC 4374). *The Astrophysical Journal Letters*, 492(2):L111–L114, 1998. doi: 10.1086/311109.

Braibant, L., Hutsemékers, D., Sluse, D., Anguita, T., & García-Vergara, C. J. Microlensing of the broad-line region in the quadruply imaged quasar HE0435-1223. *Astronomy & Astrophysics*, 565:L11, 2014. doi: 10.1051/0004-6361/201423633.

Bramich, D. M. A new algorithm for difference image analysis. *Monthly Notices of the Royal Astronomical Society*, 386(1):L77–L81, 2008. doi: 10.1111/j.1745-3933.2008.00464.x.

Bramich, D. M., Horne, K., Albrow, M. D., Tsapras, Y., Snodgrass, C., Street, R. A., Hundertmark, M., Kains, N., Arellano Ferro, A., Figuera, J. R., & Giridhar, S. Difference image analysis: extension to a spatially varying photometric scale factor and other considerations. *Monthly Notices of the Royal Astronomical Society*, 428(3):2275–2289, 2013. doi: 10.1093/mnras/sts184.

Brown, T. M., Baliber, N., Bianco, F. B., Bowman, M., Burleson, B., Conway, P., Crellin, M., Depagne, É., De Vera, J., Dilday, B., Dragomir, D., Dubberley, M., Eastman, J. D., Elphick, M., Falarski, M., Foale, S., Ford, M., Fulton, B. J., Garza, J., Gomez, E. L., Graham, M., Greene, R., Haldeman, B., Hawkins, E., Haworth, B., Haynes, R., Hidas, M., Hjelstrom, A. E., Howell, D. A., Hygelund, J., et al. Las Cumbres Observatory Global Telescope Network. *Publications of the Astronomical Society of the Pacific*, 125(931):1031, 2013. doi: 10.1086/673168.

Burke, W. L. Multiple Gravitational Imaging by Distributed Masses. *The Astrophysical Journal Letters*, 244:L1, 1981. doi: 10.1086/183466.

Burud, I., Courbin, F., Magain, P., Lidman, C., Hutsemékers, D., Kneib, J.-P., Hjorth, J., Brewer, J., Pompei, E., Germany, L., Pritchard, J., Jaunsen, A. O., Letawe, G., & Meylan, G. An optical time-delay for the lensed BAL quasar HE 2149-2745. *Astronomy & Astrophysics*, 383 (1):71–81, 2002. doi: 10.1051/0004-6361:20011731.

Chang, K. & Refsdal, S. Flux variations of QSO 0957 + 561 A, B and image splitting by stars near the light path. *Nature*, 282(5739):561–564, 1979. doi: 10.1038/282561a0.

Chartas, G., Kochanek, C. S., Dai, X., Poindexter, S., & Garmire, G. X-Ray Microlensing in RXJ1131-1231 and HE1104-1805. *The Astrophysical Journal*, 693(1):174–185, 2009. doi: 10.1088/0004-637X/693/1/174.

Chartas, G., Krawczynski, H., Zalesky, L., Kochanek, C. S., Dai, X., Morgan, C. W., & Mosquera, A. Measuring the Innermost Stable Circular Orbits of Supermassive Black Holes. *The Astrophysical Journal*, 837(1):26, 2017. doi: 10.3847/1538-4357/aa5d50.

Cornachione, M. A. & Morgan, C. W. Quasar Microlensing Variability Studies Favor Shallow Accretion Disk Temperature Profiles. *The Astrophysical Journal*, 895(2):93, 2020. doi: 10.3847/1538-4357/ab8aed.

Cornachione, M. A., Morgan, C. W., Burger, H. R., Shalyapin, V. N., Goicoechea, L. J., Vrba, F. J., Dahm, S. E., & Tilleman, T. M. Near-infrared and Optical Continuum Emission Region Size Measurements in the Gravitationally lensed Quasars Q0957+561 and SBS0909+532. *The Astrophysical Journal*, 905(1):7, 2020a. doi: 10.3847/1538-4357/abc25d.

Cornachione, M. A., Morgan, C. W., Millon, M., Bentz, M. C., Courbin, F., Bonvin, V., & Falco, E. E. A Microlensing Accretion Disk Size Measurement in the Lensed Quasar WFI 2026-4536. *The Astrophysical Journal*, 895(2):125, 2020b. doi: 10.3847/1538-4357/ab557a.

Corrigan, R. T., Irwin, M. J., Arnaud, J., Fahlman, G. G., Fletcher, J. M., Hewett, P. C., Hewitt, J. N., Le Fevre, O., McClure, R., Pritchet, C. J., Schneider, D. P., Turner, E. L., Webster, R. L., & Yee, H. K. C. Initial Light Curve of Q2237+0305. *The Astronomical Journal*, 102: 34, 1991. doi: 10.1086/115856.

Courbin, F., Chantry, V., Revaz, Y., Sluse, D., Faure, C., Tewes, M., Eulaers, E., Koleva, M., Asfandiyarov, I., Dye, S., Magain, P., van Winckel, H., Coles, J., Saha, P., Ibrahimov, M., & Meylan, G. COSMOGRAIL: the COSmological MOnitoring of GRAvItational Lenses. IX. Time delays, lens dynamics and baryonic fraction in HE 0435-1223. *Astronomy & Astrophysics*, 536:A53, 2011. doi: 10.1051/0004-6361/201015709.

Dai, X., Chartas, G., Agol, E., Bautz, M. W., & Garmire, G. P. Chandra Observations of QSO 2237+0305. *The Astrophysical Journal*, 589(1):100–110, 2003. doi: 10.1086/374548.

Di Matteo, T., Springel, V., & Hernquist, L. Energy input from quasars regulates the growth and activity of black holes and their host galaxies. *Nature*, 433(7026):604–607, 2005. doi: 10.1038/nature03335.

Ducourant, C., Wertz, O., Krone-Martins, A., Teixeira, R., Le Campion, J. F., Galluccio, L., Klüter, J., Delchambre, L., Surdej, J., Mignard, F., Wambsganss, J., Bastian, U., Graham, M. J., Djorgovski, S. G., & Slezak, E. Gaia GraL: Gaia DR2 gravitational lens systems. II. The known multiply imaged quasars. *Astronomy & Astrophysics*, 618:A56, 2018. doi: 10.1051/0004-6361/201833480.

Dux, F., Millon, M., Lemon, C., Schmidt, T., Courbin, F., Shajib, A. J., Treu, T., Birrer, S., Wong, K. C., Agnello, A., Andrade, A., Galan, A., Hjorth, J., Paic, E., Schuldt, S., Schweinfurth, A., Sluse, D., Smette, A., & Suyu, S. H. J1721+8842: The first Einstein zigzag lens. *Astronomy & Astrophysics*, 694:A300, 2025. doi: 10.1051/0004-6361/202452970.

Dyson, F. W., Eddington, A. S., & Davidson, C. A Determination of the Deflection of Light by the Sun's Gravitational Field, from Observations Made at the Total Eclipse of May 29, 1919. *Philosophical Transactions of the Royal Society of London Series A*, 220:291–333, 1920. doi: 10.1098/rsta.1920.0009.

Eigenbrod, A., Courbin, F., Meylan, G., Vuissoz, C., & Magain, P. COSMOGRAIL: the COSmological MOnitoring of GRAvItational Lenses. III. Redshift of the lensing galaxy in eight gravitationally lensed quasars. *Astronomy & Astrophysics*, 451(3):759–766, 2006. doi: 10.1051/0004-6361:20054454.

Eigenbrod, A., Courbin, F., & Meylan, G. COSMOGRAIL: the COSmological MOnitoring of GRAvItational Lenses. VI. Redshift of the lensing galaxy in seven gravitationally lensed quasars. *Astronomy & Astrophysics*, 465(1):51–56, 2007. doi: 10.1051/0004-6361:20066939.

Eigenbrod, A., Courbin, F., Meylan, G., Agol, E., Anguita, T., Schmidt, R. W., & Wambsganss, J. Microlensing variability in the gravitationally lensed quasar QSO 2237+0305 ≡ the Einstein Cross. II. Energy profile of the accretion disk. *Astronomy & Astrophysics*, 490(3):933–943, 2008a. doi: 10.1051/0004-6361:200810729.

Eigenbrod, A., Courbin, F., Sluse, D., Meylan, G., & Agol, E. Microlensing variability in the gravitationally lensed quasar QSO 2237+0305 ≡ the Einstein Cross . I. Spectrophotometric monitoring with the VLT. *Astronomy & Astrophysics*, 480(3):647–661, 2008b. doi: 10.1051/0004-

6361:20078703.

Einstein, A. Über den Einfluß der Schwerkraft auf die Ausbreitung des Lichtes. *Annalen der Physik*, 35:898, 1911. doi: 10.1002/andp.19113401005.

Einstein, A. Die Grundlage der allgemeinen Relativitätstheorie. *Annalen der Physik*, 354(7):769–822, 1916. doi: 10.1002/andp.19163540702.

Einstein, A. Lens-Like Action of a Star by the Deviation of Light in the Gravitational Field. *Science*, 84(2188):506–507, 1936. doi: 10.1126/science.84.2188.506.

Eulaers, E. & Magain, P. Time delays for eleven gravitationally lensed quasars revisited. *Astronomy & Astrophysics*, 536:A44, 2011. doi: 10.1051/0004-6361/201016101.

Event Horizon Telescope Collaboration, Akiyama, K., Alberdi, A., Alef, W., Asada, K., Azulay, R., Baczko, A.-K., Ball, D., Baloković, M., Barrett, J., Bintley, D., Blackburn, L., Boland, W., Bouman, K. L., Bower, G. C., Bremer, M., Brinkerink, C. D., Brissenden, R., Britzen, S., Broderick, A. E., Broguiere, D., Bronzwaer, T., Byun, D.-Y., Carlstrom, J. E., Chael, A., Chan, C.-k., Chatterjee, S., Chatterjee, K., Chen, M.-T., Chen, Y., et al. First M87 Event Horizon Telescope Results. I. The Shadow of the Supermassive Black Hole. *The Astrophysical Journal Letters*, 875(1):L1, 2019. doi: 10.3847/2041-8213/ab0ec7.

Event Horizon Telescope Collaboration, Akiyama, K., Alberdi, A., Alef, W., Algaba, J. C., Anantua, R., Asada, K., Azulay, R., Bach, U., Baczko, A.-K., Ball, D., Baloković, M., Barrett, J., Bauböck, M., Benson, B. A., Bintley, D., Blackburn, L., Blundell, R., Bouman, K. L., Bower, G. C., Boyce, H., Bremer, M., Brinkerink, C. D., Brissenden, R., Britzen, S., Broderick, A. E., Broguiere, D., Bronzwaer, T., Bustamante, S., Byun, D.-Y., et al. First Sagittarius A* Event Horizon Telescope Results. I. The Shadow of the Supermassive Black Hole in the Center of the Milky Way. *The Astrophysical Journal Letters*, 930(2):L12, 2022. doi: 10.3847/2041-8213/ac6674.

Falco, E. E., Kochanek, C. S., Lehár, J., McLeod, B. A., Muñoz, J. A., Impey, C. D., Keeton, C., Peng, C. Y., & Rix, H. W. The CASTLES Gravitational Lensing Tool. Vol. 237, *Astronomical Society of the Pacific Conference Series*, 2001. https://ui.adsabs.harvard.edu/abs/2001ASPC..237...25F.

Forés-Toribio, R., Muñoz, J. A., Fian, C., Jiménez-Vicente, J., & Mediavilla, E. Microlensing analysis of 14.5-year light curves in SDSS J1004+4112: Quasar accretion disk size and intracluster stellar mass fraction. *Astronomy & Astrophysics*, 691:A97, 2024. doi: 10.1051/0004-6361/202347378.

Frank, J., King, A., & Raine, D. J. *Accretion Power in Astrophysics: Third Edition*. Cambridge University Press, 2002. https://ui.adsabs.harvard.edu/abs/2002apa..book.....F.

Gaia Collaboration, Prusti, T., de Bruijne, J. H. J., Brown, A. G. A., Vallenari, A., Babusiaux, C., Bailer-Jones, C. A. L., Bastian, U., Biermann, M., Evans, D. W., Eyer, L., Jansen, F., Jordi, C., Klioner, S. A., Lammers, U., Lindegren, L., Luri, X., Mignard, F., Milligan, D. J., Panem, C., Poinsignon, V., Pourbaix, D., Randich, S., Sarri, G., Sartoretti, P., Siddiqui, H. I., Soubiran, C., Valette, V., van Leeuwen, F., Walton, N. A., et al. The Gaia mission. *Astronomy & Astrophysics*, 595:A1, 2016. doi: 10.1051/0004-6361/201629272.

Gaia Collaboration, Vallenari, A., Brown, A. G. A., Prusti, T., de Bruijne, J. H. J., Arenou, F., Babusiaux, C., Biermann, M., Creevey, O. L., Ducourant, C., Evans, D. W., Eyer, L., Guerra,

R., Hutton, A., Jordi, C., Klioner, S. A., Lammers, U. L., Lindegren, L., Luri, X., Mignard, F., Panem, C., Pourbaix, D., Randich, S., Sartoretti, P., Soubiran, C., Tanga, P., Walton, N. A., Bailer-Jones, C. A. L., Bastian, U., Drimmel, R., et al. Gaia Data Release 3. Summary of the content and survey properties. *Astronomy & Astrophysics*, 674:A1, 2023. doi: 10.1051/0004-6361/202243940.

GAVO Data Center. The Scrolling Infinite Lightcurve. http://dc.g-vo.org/inflight/res/lc1/ui/info, VO resource provided by the GAVO Data Center, 2007.

GAVO Data Center. LCO light curves of gravitationally lensed quasars. https://dc.g-vo.org/mlcolour/q/web/form, VO resource provided by the GAVO Data Center, 2025.

Giannini, E. *MiNDSTEp differential photometry of the gravitationally lensed quasars WFI2033-4723, HE0047-1756 and Q2237+0305*. PhD thesis, Ruprecht-Karls-Universität Heidelberg, 2017. doi: 10.11588/heidok.00022683.

Giannini, E., Schmidt, R. W., Wambsganss, J., Alsubai, K., Andersen, J. M., Anguita, T., Bozza, V., Bramich, D. M., Browne, P., Calchi Novati, S., Damerdji, Y., Diehl, C., Dodds, P., Dominik, M., Elyiv, A., Fang, X., Figuera Jaimes, R., Finet, F., Gerner, T., Gu, S., Hardis, S., Harpsøe, K., Hinse, T. C., Hornstrup, A., Hundertmark, M., Jessen-Hansen, J., Jørgensen, U. G., Juncher, D., Kains, N., Kerins, E., et al. MiNDSTEp differential photometry of the gravitationally lensed quasars WFI 2033-4723 and HE 0047-1756: microlensing and a new time delay. *Astronomy & Astrophysics*, 597:A49, 2017. doi: 10.1051/0004-6361/201527422.

Goicoechea, L. J., Artamonov, B. P., Shalyapin, V. N., Sergeyev, A. V., Burkhonov, O. A., Akhunov, T. A., Asfandiyarov, I. M., Bruevich, V. V., Ehgamberdiev, S. A., Shimanovskaya, E. V., & Zheleznyak, A. P. Liverpool-Maidanak monitoring of the Einstein Cross in 2006-2019. I. Light curves in the gVrRI optical bands and microlensing signatures. *Astronomy & Astrophysics*, 637:A89, 2020. doi: 10.1051/0004-6361/202037902.

Guerras, E., Dai, X., Steele, S., Liu, A., Kochanek, C. S., Chartas, G., Morgan, C. W., & Chen, B. Extended X-Ray Monitoring of Gravitational Lenses with Chandra and Joint Constraints on X-Ray Emission Regions. *The Astrophysical Journal*, 836(2):206, 2017. doi: 10.3847/1538-4357/aa5728.

Horne, K., De Rosa, G., Peterson, B. M., Barth, A. J., Ely, J., Fausnaugh, M. M., Kriss, G. A., Pei, L., Bentz, M. C., Cackett, E. M., Edelson, R., Eracleous, M., Goad, M. R., Grier, C. J., Kaastra, J., Kochanek, C. S., Krongold, Y., Mathur, S., Netzer, H., Proga, D., Tejos, N., Vestergaard, M., Villforth, C., Adams, S. M., Anderson, M. D., Arévalo, P., Beatty, T. G., Bennert, V. N., Bigley, A., Bisogni, S., et al. Space Telescope and Optical Reverberation Mapping Project. IX. Velocity-Delay Maps for Broad Emission Lines in NGC 5548. *The Astrophysical Journal*, 907(2):76, 2021. doi: 10.3847/1538-4357/abce60.

Huchra, J., Gorenstein, M., Kent, S., Shapiro, I., Smith, G., Horine, E., & Perley, R. 2237+0305: a new and unusual gravitational lens. *The Astronomical Journal*, 90:691–696, 1985. doi: 10.1086/113777.

Irwin, M. J., Webster, R. L., Hewett, P. C., Corrigan, R. T., & Jedrzejewski, R. I. Photometric Variations in the Q2237+0305 System: First Detection of a Microlensing Event. *The Astronomical Journal*, 98:1989, 1989. doi: 10.1086/115272.

Ivezić, Ž., Kahn, S. M., Tyson, J. A., Abel, B., Acosta, E., Allsman, R., Alonso, D., AlSayyad, Y., Anderson, S. F., Andrew, J., Angel, J. R. P., Angeli, G. Z., Ansari, R., Antilogus, P., Araujo, C., Armstrong, R., Arndt, K. T., Astier, P., Aubourg, É., Auza, N., Axelrod, T. S., Bard, D. J., Barr, J. D., Barrau, A., Bartlett, J. G., Bauer, A. E., Bauman, B. J., Baumont, S., Bechtol, E., Bechtol, K., et al. LSST: From Science Drivers to Reference Design and Anticipated Data Products. *The Astrophysical Journal*, 873(2):111, 2019. doi: 10.3847/1538-4357/ab042c.

Jensen, J. L. W. V. Sur les fonctions convexes et les inégalités entre les valeurs moyennes. *Acta Mathematica*, 30:175–193, 1906. https://link.springer.com/article/10.1007/BF02418571.

Kayser, R. & Refsdal, S. Detectability of gravitational microlensing in the quasar QS02237+0305. *Nature*, 338(6218):745–746, 1989. doi: 10.1038/338745a0.

Kayser, R., Refsdal, S., & Stabell, R. Astrophysical applications of gravitational micro-lensing. *Astronomy & Astrophysics*, 166:36–52, 1986. https://ui.adsabs.harvard.edu/abs/1986A&A...166...36K.

Kochanek, C. S. Quantitative Interpretation of Quasar Microlensing Light Curves. *The Astrophysical Journal*, 605(1):58–77, 2004. doi: 10.1086/382180.

Koptelova, E., Chen, W. P., Chiueh, T., Artamonov, B. P., Oknyanskij, V. L., Nuritdinov, S. N., Burkhonov, O., Akhunov, T., Bruevich, V. V., Ezhkova, O. V., Gusev, A. S., Sergeyev, A. V., Ehgamberdiev, S. A., & Ibragimov, M. A. Time delay between images of the lensed quasar UM673. *Astronomy & Astrophysics*, 544:A51, 2012. doi: 10.1051/0004-6361/201116645.

Koptelova, E. A., Oknyanskij, V. L., & Shimanovskaya, E. V. Determining time delay in the gravitationally lensed system QSO2237+0305. *Astronomy & Astrophysics*, 452(1):37–46, 2006. doi: 10.1051/0004-6361:20054050.

Kormann, R., Schneider, P., & Bartelmann, M. Isothermal elliptical gravitational lens models. *Astronomy & Astrophysics*, 284:285–299, 1994.

Kroupa, P. The Initial Mass Function of Stars: Evidence for Uniformity in Variable Systems. *Science*, 295(5552):82–91, 2002. doi: 10.1126/science.1067524.

Kundić, T. & Wambsganss, J. Gravitational Microlensing: The Effect of Random Motion of Individual Stars in the Lensing Galaxy. *The Astrophysical Journal*, 404:455, 1993. doi: 10.1086/172299.

Kundić, T., Colley, W. N., Gott, III, J. R., Malhotra, S., Pen, U.-L., Rhoads, J. E., Stanek, K. Z., Turner, E. L., & Wambsganss, J. An Event in the Light Curve of 0957+561A and Prediction of the 1996 Image B Light Curve. *The Astrophysical Journal Letters*, 455:L5, 1995. doi: 10.1086/309819.

Kundić, T., Turner, E. L., Colley, W. N., Gott, III, J. R., Rhoads, J. E., Wang, Y., Bergeron, L. E., Gloria, K. A., Long, D. C., Malhotra, S., & Wambsganss, J. A Robust Determination of the Time Delay in 0957+561A, B and a Measurement of the Global Value of Hubble's Constant. *The Astrophysical Journal*, 482(1):75–82, 1997. doi: 10.1086/304147.

Laor, A. & Netzer, H. Massive thin accretion discs. - I. Calculated spectra. *Monthly Notices of the Royal Astronomical Society*, 238:897–916, 1989. doi: 10.1093/mnras/238.3.897.

Lehár, J., Falco, E. E., Kochanek, C. S., McLeod, B. A., Muñoz, J. A., Impey, C. D., Rix, H. W.,

Keeton, C. R., & Peng, C. Y. Hubble Space Telescope Observations of 10 Two-Image Gravitational Lenses. *The Astrophysical Journal*, 536(2):584–605, 2000. doi: 10.1086/308963.

Lewis, G. F. & Irwin, M. J. The statistics of microlensing light curves. II. Temporal analysis. *Monthly Notices of the Royal Astronomical Society*, 283(1):225–240, 1996. doi: 10.1093/mnras/283.1.225.

Li, Y.-P., Yuan, F., & Dai, X. Reconciling the quasar microlensing disc size problem with a wind model of active galactic nucleus. *Monthly Notices of the Royal Astronomical Society*, 483(2): 2275–2281, 2019. doi: 10.1093/mnras/sty3245.

Lidman, C., Courbin, F., Kneib, J. P., Golse, G., Castander, F., & Soucail, G. Exploring the gravitationally lensed system HE 1104-1805: VLT spectroscopy of the lens at z=0.729. *Astronomy & Astrophysics*, 364:L62–L65, 2000. doi: 10.48550/arXiv.astro-ph/0010403.

Lindegren, L. Re-normalising the astrometric chi-square in Gaia DR2. Technical note: GAIA-C3-TN-LU-LL-124, 2018. https://www.cosmos.esa.int/web/gaia/public-dpac-documents.

Liu, S., Wood-Vasey, W. M., Armstrong, R., Narayan, G., Sánchez, B. O., & Dark Energy Science Collaboration. Testing the LSST Difference Image Analysis Pipeline Using Synthetic Source Injection Analysis. *The Astrophysical Journal*, 967(1):10, 2024. doi: 10.3847/1538-4357/ad3635.

MacAlpine, G. M. & Feldman, F. R. Discovery and spectrophotometry of high-redshift quasars. *The Astrophysical Journal*, 261:412–421, 1982. doi: 10.1086/160353.

Mao, S. & Paczynski, B. Gravitational Microlensing by Double Stars and Planetary Systems. *The Astrophysical Journal Letters*, 374:L37, 1991. doi: 10.1086/186066.

Mao, S. & Schneider, P. Evidence for substructure in lens galaxies? *Monthly Notices of the Royal Astronomical Society*, 295(3):587–594, 1998. doi: 10.1046/j.1365-8711.1998.01319.x.

Mediavilla, E., Muñoz, J. A., Lopez, P., Mediavilla, T., Abajas, C., Gonzalez-Morcillo, C., & Gil-Merino, R. A Fast and Very Accurate Approach to the Computation of Microlensing Magnification Patterns Based on Inverse Polygon Mapping. *The Astrophysical Journal*, 653(2): 942–953, 2006. doi: 10.1086/508796.

Mediavilla, E., Jiménez-Vicente, J., Muñoz, J. A., & Mediavilla, T. Resolving the Innermost Region of the Accretion Disk of the Lensed Quasar Q2237+0305 through Gravitational Microlensing. *The Astrophysical Journal Letters*, 814(2):L26, 2015. doi: 10.1088/2041-8205/814/2/L26.

Millon, M., Courbin, F., Bonvin, V., Paic, E., Meylan, G., Tewes, M., Sluse, D., Magain, P., Chan, J. H. H., Galan, A., Joseph, R., Lemon, C., Tihhonova, O., Anderson, R. I., Marmier, M., Chazelas, B., Lendl, M., Triaud, A. H. M. J., & Wyttenbach, A. COSMOGRAIL. XIX. Time delays in 18 strongly lensed quasars from 15 years of optical monitoring. *Astronomy & Astrophysics*, 640:A105, 2020a. doi: 10.1051/0004-6361/202037740.

Millon, M., Tewes, M., Bonvin, V., Lengen, B., & Courbin, F. Pycs3: A python toolbox for time-delay measurements in lensed quasars. *Journal of Open Source Software*, 5(53):2654, 2020b. doi: 10.21105/joss.02654.

Millon, M., Michalewicz, K., Dux, F., Courbin, F., & Marshall, P. J. Image Deconvolution and Point-spread Function Reconstruction with STARRED: A Wavelet-based Two-channel Method

Optimized for Light-curve Extraction. *The Astronomical Journal*, 168(2):55, 2024. doi: 10.3847/1538-3881/ad4da7.

Morgan, C. W., Kochanek, C. S., Morgan, N. D., & Falco, E. E. The Quasar Accretion Disk Size-Black Hole Mass Relation. *The Astrophysical Journal*, 712(2):1129–1136, 2010. doi: 10.1088/0004-637X/712/2/1129.

Morgan, C. W., Hyer, G. E., Bonvin, V., Mosquera, A. M., Cornachione, M., Courbin, F., Kochanek, C. S., & Falco, E. E. Accretion Disk Size Measurement and Time Delays in the Lensed Quasar WFI 2033-4723. *The Astrophysical Journal*, 869(2):106, 2018. doi: 10.3847/1538-4357/aaed3e.

Morgan, N. D., Caldwell, J. A. R., Schechter, P. L., Dressler, A., Egami, E., & Rix, H.-W. WFI J2026-4536 and WFI J2033-4723: Two New Quadruple Gravitational Lenses. *The Astronomical Journal*, 127(5):2617–2630, 2004. doi: 10.1086/383295.

Morgan, N. D., Kochanek, C. S., Falco, E. E., & Dai, X. Time-Delay Measurement for the Quadruple Lens RX J1131-1231. *arXiv e-prints*, art. astro-ph/0605321, 2006. doi: 10.48550/arXiv.astro-ph/0605321.

Mortonson, M. J., Schechter, P. L., & Wambsganss, J. Size Is Everything: Universal Features of Quasar Microlensing with Extended Sources. *The Astrophysical Journal*, 628(2):594–603, 2005. doi: 10.1086/431195.

Mosquera, A. M. & Kochanek, C. S. The Microlensing Properties of a Sample of 87 Lensed Quasars. *The Astrophysical Journal*, 738(1):96, 2011. doi: 10.1088/0004-637X/738/1/96.

Mosquera, A. M., Muñoz, J. A., & Mediavilla, E. Detection of Chromatic Microlensing in Q 2237 + 0305 A. *The Astrophysical Journal*, 691(2):1292–1299, 2009. doi: 10.1088/0004-637X/691/2/1292.

Motta, V., Mediavilla, E., Rojas, K., Falco, E. E., Jiménez-Vicente, J., & Muñoz, J. A. Probing the Broad-Line Region and the Accretion Disk in the Lensed Quasars HE 0435-1223, WFI 2033-4723, and HE 2149-2745 Using Gravitational Microlensing. *The Astrophysical Journal*, 835(2):132, 2017. doi: 10.3847/1538-4357/835/2/132.

Mróz, M. J., Poleski, R., Udalski, A., Sumi, T., Tsapras, Y., Hundertmark, M., Pietrukowicz, P., Szymański, M. K., Skowron, J., Mróz, P., Gromadzki, M., Iwanek, P., Kozłowski, S., Ratajczak, M., Rybicki, K. A., Skowron, D. M., Soszyński, I., Ulaczyk, K., Wrona, M., Abe, F., Bando, K., Bennett, D. P., Bhattacharya, A., Bond, I. A., Fukui, A., Hamada, R., Hamada, S., Hamasaki, N., Hirao, Y., Ishitani Silva, S., et al. OGLE-2015-BLG-1609Lb: A sub-Jovian planet orbiting a low-mass stellar or brown dwarf host. *Astronomy & Astrophysics*, 698:A126, 2025. doi: 10.1051/0004-6361/202453454.

Muñoz, J. A., Kochanek, C. S., Fohlmeister, J., Wambsganss, J., Falco, E., & Forés-Toribio, R. The Longest Delay: A 14.5 yr Campaign to Determine the Third Time Delay in the Lensing Cluster SDSS J1004+4112. *The Astrophysical Journal*, 937(1):34, 2022. doi: 10.3847/1538-4357/ac8877.

Narayan, G., Rest, A., Tucker, B. E., Foley, R. J., Wood-Vasey, W. M., Challis, P., Stubbs, C., Kirshner, R. P., Aguilera, C., Becker, A. C., Blondin, S., Clocchiatti, A., Covarrubias, R., Damke, G., Davis, T. M., Filippenko, A. V., Ganeshalingam, M., Garg, A., Garnavich, P. M., Hicken, M., Jha, S. W., Krisciunas, K., Leibundgut, B., Li, W., Matheson, T., Miknaitis, G.,

Pignata, G., Prieto, J. L., Riess, A. G., Schmidt, B. P., et al. Light Curves of 213 Type Ia Supernovae from the ESSENCE Survey. *The Astrophysical Journal Supplement*, 224(1):3, 2016. doi: 10.3847/0067-0049/224/1/3.

Narayan, R. & Bartelmann, M. Lectures on Gravitational Lensing. *arXiv e-prints*, art. astro-ph/9606001, 1996. doi: 10.48550/arXiv.astro-ph/9606001.

Neira, F., Anguita, T., & Vernardos, G. A quasar microlensing light-curve generator for LSST. *Monthly Notices of the Royal Astronomical Society*, 495(1):544–553, 2020. doi: 10.1093/mnras/staa1208.

Neira, F., Courbin, F., Dux, F., & Vernardos, G. LTDE: The Lens Time Delay Experiment I. From pixels to light curves. *arXiv e-prints*, art. arXiv:2504.16249, 2025. doi: 10.48550/arXiv.2504.16249.

Netzer, H. Revisiting the Unified Model of Active Galactic Nuclei. *Annual Review of Astronomy and Astrophysics*, 53:365–408, 2015. doi: 10.1146/annurev-astro-082214-122302.

Nierenberg, A. M., Keeley, R. E., Sluse, D., Gilman, D., Birrer, S., Treu, T., Abazajian, K. N., Anguita, T., Benson, A. J., Bennert, V. N., Djorgovski, S. G., Du, X., Fassnacht, C. D., Hoenig, S. F., Kusenko, A., Lemon, C., Malkan, M., Motta, V., Moustakas, L. A., Stern, D., & Wechsler, R. H. JWST lensed quasar dark matter survey - I. Description and first results. *Monthly Notices of the Royal Astronomical Society*, 530(3):2960–2971, 2024. doi: 10.1093/mnras/stae499.

Novikov, I. D. & Thorne, K. S. Astrophysics of black holes. 1973. https://ui.adsabs.harvard.edu/abs/1973blho.conf..343N.

Oscoz, A., Serra-Ricart, M., Mediavilla, E., & Muñoz, J. A. Long-term Monitoring, Time Delay, and Microlensing in the Gravitational Lens System Q0142-100. *The Astrophysical Journal*, 779(2):144, 2013. doi: 10.1088/0004-637X/779/2/144.

Ostensen, R., Refsdal, S., Stabell, R., Teuber, J., Emanuelsen, P. I., Festin, L., Florentin-Nielsen, R., Gahm, G., Gullbring, E., Grundahl, F., Hjorth, J., Jablonski, M., Jaunsen, A. O., Kaas, A. A., Karttunen, H., Kotilainen, J., Laurikainen, E., Lindgren, H., Maehoenen, P., Nilsson, K., Olofsson, G., Olsen, O., Pettersen, B. R., Piirola, V., Sorensen, A. N., Takalo, L., Thomsen, B., Valtaoja, E., Vestergaard, M., & Av Vianborg, T. Monitoring of the Einstein Cross with the Nordic Optical Telescope. *Astronomy & Astrophysics*, 309:59–64, 1996. doi: 10.48550/arXiv.astro-ph/9512103.

Paczynski, B. Gravitational Microlensing by the Galactic Halo. *The Astrophysical Journal*, 304:1, 1986. doi: 10.1086/164140.

Padovani, P., Alexander, D. M., Assef, R. J., De Marco, B., Giommi, P., Hickox, R. C., Richards, G. T., Smolčić, V., Hatziminaoglou, E., Mainieri, V., & Salvato, M. Active galactic nuclei: what's in a name? *Astronomy & Astrophysics Reviews*, 25(1):2, 2017. doi: 10.1007/s00159-017-0102-9.

Paic, E., Vernardos, G., Sluse, D., Millon, M., Courbin, F., Chan, J. H., & Bonvin, V. Constraining quasar structure using high-frequency microlensing variations and continuum reverberation. *Astronomy & Astrophysics*, 659:A21, 2022. doi: 10.1051/0004-6361/202141808.

Peng, C. Y., Ho, L. C., Impey, C. D., & Rix, H.-W. Detailed structural decomposition of galaxy

images. *The Astronomical Journal*, 124(1):266–293, 2002. doi: 10.1086/340952.

Poindexter, S. & Kochanek, C. S. Microlensing Evidence that a Type 1 Quasar is Viewed Face-On. *The Astrophysical Journal*, 712(1):668–673, 2010a. doi: 10.1088/0004-637X/712/1/668.

Poindexter, S. & Kochanek, C. S. The Transverse Peculiar Velocity of the Q2237+0305 Lens Galaxy and the Mean Mass of Its Stars. *The Astrophysical Journal*, 712(1):658–667, 2010b. doi: 10.1088/0004-637X/712/1/658.

Poindexter, S., Morgan, N., Kochanek, C. S., & Falco, E. E. Mid-IR Observations and a Revised Time Delay for the Gravitational Lens System Quasar HE 1104-1805. *The Astrophysical Journal*, 660(1):146–151, 2007. doi: 10.1086/512773.

Poindexter, S., Morgan, N., & Kochanek, C. S. The Spatial Structure of an Accretion Disk. *The Astrophysical Journal*, 673(1):34–38, 2008. doi: 10.1086/524190.

Pooley, D., Blackburne, J. A., Rappaport, S., Schechter, P. L., & Fong, W.-f. A Strong X-Ray Flux Ratio Anomaly in the Quadruply Lensed Quasar PG 1115+080. *The Astrophysical Journal*, 648(1):67–72, 2006. doi: 10.1086/505860.

Rees, M. J. Black Hole Models for Active Galactic Nuclei. *Annual Review of Astronomy and Astrophysics*, 22:471–506, 1984. doi: 10.1146/annurev.aa.22.090184.002351.

Refsdal, S. On the possibility of determining Hubble's parameter and the masses of galaxies from the gravitational lens effect. *Monthly Notices of the Royal Astronomical Society*, 128:307, 1964. doi: 10.1093/mnras/128.4.307.

Reynolds, M. T., Walton, D. J., Miller, J. M., & Reis, R. C. A Rapidly Spinning Black Hole Powers the Einstein Cross. *The Astrophysical Journal Letters*, 792(1):L19, 2014. doi: 10.1088/2041-8205/792/1/L19.

Ricci, D., Poels, J., Elyiv, A., Finet, F., Sprimont, P. G., Anguita, T., Bozza, V., Browne, P., Burgdorf, M., Calchi Novati, S., Dominik, M., Dreizler, S., Glitrup, M., Grundahl, F., Harpsøe, K., Hessman, F., Hinse, T. C., Hornstrup, A., Hundertmark, M., Jørgensen, U. G., Liebig, C., Maier, G., Mancini, L., Masi, G., Mathiasen, M., Rahvar, S., Scarpetta, G., Skottfelt, J., Snodgrass, C., Southworth, J., et al. Flux and color variations of the quadruply imaged quasar HE 0435-1223. *Astronomy & Astrophysics*, 528:A42, 2011. doi: 10.1051/0004-6361/201016188.

Riello, M., De Angeli, F., Evans, D. W., Montegriffo, P., Carrasco, J. M., Busso, G., Palaversa, L., Burgess, P. W., Diener, C., Davidson, M., Rowell, N., Fabricius, C., Jordi, C., Bellazzini, M., Pancino, E., Harrison, D. L., Cacciari, C., van Leeuwen, F., Hambly, N. C., Hodgkin, S. T., Osborne, P. J., Altavilla, G., Barstow, M. A., Brown, A. G. A., Castellani, M., Cowell, S., De Luise, F., Gilmore, G., Giuffrida, G., Hidalgo, S., et al. Gaia early data release 3 - photometric content and validation. *A&A*, 649:A3, 2021. doi: 10.1051/0004-6361/202039587.

Rivera, A. B., Morgan, C. W., Florence, S. M., Dahm, S. E., Vrba, F. J., Tilleman, T. M., Cornachione, M. A., & Falco, E. E. Optical and Near-infrared Continuum Emission Region Size Measurements in the Lensed Quasar FBQ J0951+2635. *The Astrophysical Journal*, 952(1):54, 2023. doi: 10.3847/1538-4357/acdb4f.

Rivera, A. B., Morgan, C. W., Florence, S. M., Kniezewski, K., Millon, M., Courbin, F., Dahm, S. E., Vrba, F. J., Tilleman, T. M., Cornachione, M. A., Asfandiyarov, I. M., Ehgamberdiev, S. A., & Burkhonov, O. A. Accretion Disk Size and Updated Time-delay Measurements in the

Gravitationally Lensed Quasar SDSS J165043.44+425149.3. *The Astrophysical Journal*, 964 (2):173, 2024. doi: 10.3847/1538-4357/ad3069.

Saha, P., Sluse, D., Wagner, J., & Williams, L. L. R. Essentials of Strong Gravitational Lensing. *Space Science Reviews*, 220(1):12, 2024. doi: 10.1007/s11214-024-01041-w.

Salpeter, E. E. The Luminosity Function and Stellar Evolution. *The Astrophysical Journal*, 121: 161, 1955. doi: 10.1086/145971.

Schechter, P. L., Udalski, A., Szymański, M., Kubiak, M., Pietrzyński, G., Soszyński, I., Woźniak, P., Żebruń, K., Szewczyk, O., & Wyrzykowski, Ł. Microlensing of Relativistic Knots in the Quasar HE 1104-1805 AB. *The Astrophysical Journal*, 584(2):657–663, 2003. doi: 10.1086/345716.

Schechter, P. L., Pooley, D., Blackburne, J. A., & Wambsganss, J. A Calibration of the Stellar Mass Fundamental Plane at z ~0.5 Using the Micro-lensing-induced Flux Ratio Anomalies of Macro-lensed Quasars. *The Astrophysical Journal*, 793(2):96, 2014. doi: 10.1088/0004-637X/793/2/96.

Schmidt, M. 3C 273 : A Star-Like Object with Large Red-Shift. *Nature*, 197(4872):1040, 1963. doi: 10.1038/1971040a0.

Schmidt, R. W. Two lectures on quasar lensing and microlensing. Proceedings of the 2019 Heraeus Summer School in Jena, 2020. https://wwwstaff.ari.uni-heidelberg.de/mitarbeiter/rschmidt/papers/Jena_Proceedings_Schmidt.html.

Schmidt, R. W. The Improved Calendar of 1700 and the Interplay with Astronomical Data - Der Verbesserte Kalender des Jahres 1700 und das Wechselspiel mit astronomischen Daten. *Studia Leibnitiana*, 54(1):96–116, 2022. doi: 10.25162/SL-2022-0005.

Schmidt, R. W. & Wambsganss, J. Quasar microlensing. *General Relativity and Gravitation*, 42(9): 2127–2150, 2010. doi: 10.1007/s10714-010-0956-x.

Schmidt, R. W., Webster, R. L., & Lewis, G. F. Weighing a galaxy bar in the lens Q2237+0305. *Monthly Notices of the Royal Astronomical Society*, 295:488–496, 1998. doi: 10.1046/j.1365-8711.1998.01326.x.

Schneider, D. P., Turner, E. L., Gunn, J. E., Hewitt, J. N., Schmidt, M., & Lawrence, C. R. High-Resolution CCD Imaging and Derived Gravitational Lens Models of 2237+0305. *The Astronomical Journal*, 95:1619, 1988. doi: 10.1086/114758.

Schneider, P., Kochanek, C. S., & Wambsganss, J. *Gravitational Lensing: Strong, Weak and Micro*. Saas-Fee Advanced Course, vol. 33, Springer, Berlin, 2006. doi: 10.1007/978-3-540-30310-7.

Shajib, A. J., Vernardos, G., Collett, T. E., Motta, V., Sluse, D., Williams, L. L. R., Saha, P., Birrer, S., Spiniello, C., & Treu, T. Strong Lensing by Galaxies. *Space Science Reviews*, 220(8):87, 2024. doi: 10.1007/s11214-024-01105-x.

Shakura, N. I. & Sunyaev, R. A. Black holes in binary systems. Observational appearance. *Astronomy & Astrophysics*, 24:337–355, 1973. https://ui.adsabs.harvard.edu/abs/1973A&A....24..337S.

Skowron, J., Udalski, A., Szymański, M. K., Kubiak, M., Pietrzyński, G., Soszyński, I., Poleski, R., Ulaczyk, K., Pietrukowicz, P., Kozłowski, S., Wyrzykowski, Ł., & Gould, A. New Method to Measure Proper Motions of Microlensed Sources: Application to Candidate Free-floating-planet

Event MOA-2011-BLG-262. *The Astrophysical Journal*, 785(2):156, 2014. doi: 10.1088/0004-637X/785/2/156.

Sluse, D. & Tewes, M. Imprints of the quasar structure in time-delay light curves: Microlensing-aided reverberation mapping. *Astronomy & Astrophysics*, 571:A60, 2014. doi: 10.1051/0004-6361/201424776.

Sluse, D., Surdej, J., Claeskens, J. F., Hutsemékers, D., Jean, C., Courbin, F., Nakos, T., Billeres, M., & Khmil, S. V. A quadruply imaged quasar with an optical Einstein ring candidate: 1RXS J113155.4-123155. *Astronomy & Astrophysics*, 406:L43–L46, 2003. doi: 10.1051/0004-6361:20030904.

Sluse, D., Claeskens, J. F., Hutsemékers, D., & Surdej, J. Multi-wavelength study of the gravitational lens system RXS J1131-1231. III. Long slit spectroscopy: micro-lensing probes the QSO structure. *Astronomy & Astrophysics*, 468(3):885–901, 2007. doi: 10.1051/0004-6361:20066821.

Sluse, D., Hutsemékers, D., Courbin, F., Meylan, G., & Wambsganss, J. Microlensing of the broad line region in 17 lensed quasars. *Astronomy & Astrophysics*, 544:A62, 2012. doi: 10.1051/0004-6361/201219125.

Soldner, J. Über die Ablenkung eines Lichtstrahls von seiner geradlinigen Bewegung durch die Attraktion eines Weltkörpers, an welchem er nahe vorbeigeht. *Berliner Astronomisches Jahrbuch*, page 161, 1804.

Sorgenfrei, C., Schmidt, R. W., & Wambsganss, J. Improving the light curves of gravitationally lensed quasars with Gaia proper motion data. *Astronomy & Astrophysics*, 683:A119, 2024. doi: 10.1051/0004-6361/202347381.

Sorgenfrei, C., Schmidt, R. W., & Wambsganss, J. Detection of colour variations from gravitational microlensing observations in the quadruple quasar HE0435-1223: Implications for the accretion disk. *arXiv e-prints*, art. arXiv:2509.09341, 2025. https://ui.adsabs.harvard.edu/abs/2025arXiv250909341S.

Surdej, J., Magain, P., Swings, J.-P., Borgeest, U., Courvoisier, T. J.-L., Kayser, R., Kellermann, K. I., Kühr, H., & Refsdal, S. A new case of gravitational lensing. *Nature*, 329:695–696, 1987. doi: 10.1038/329695a0.

Suyu, S. H., Auger, M. W., Hilbert, S., Marshall, P. J., Tewes, M., Treu, T., Fassnacht, C. D., Koopmans, L. V. E., Sluse, D., Blandford, R. D., Courbin, F., & Meylan, G. Two Accurate Time-delay Distances from Strong Lensing: Implications for Cosmology. *The Astrophysical Journal*, 766(2):70, 2013. doi: 10.1088/0004-637X/766/2/70.

Suyu, S. H., Bonvin, V., Courbin, F., Fassnacht, C. D., Rusu, C. E., Sluse, D., Treu, T., Wong, K. C., Auger, M. W., Ding, X., Hilbert, S., Marshall, P. J., Rumbaugh, N., Sonnenfeld, A., Tewes, M., Tihhonova, O., Agnello, A., Blandford, R. D., Chen, G. C. F., Collett, T., Koopmans, L. V. E., Liao, K., Meylan, G., & Spiniello, C. H0LiCOW - I. H_0 Lenses in COSMOGRAIL's Wellspring: program overview. *Monthly Notices of the Royal Astronomical Society*, 468(3): 2590–2604, 2017. doi: 10.1093/mnras/stx483.

TDCOSMO Collaboration, Birrer, S., Buckley-Geer, E. J., Cappellari, M., Courbin, F., Dux, F., Fassnacht, C. D., Frieman, J. A., Galan, A., Gilman, D., Huang, X.-Y., Knabel, S., Langeroodi, D., Lin, H., Millon, M., Morishita, T., Motta, V., Mozumdar, P., Paic, E., Shajib, A. J., Sheu,

W., Sluse, D., Sonnenfeld, A., Spiniello, C., Stiavelli, M., Suyu, S. H., Tan, C. Y., Treu, T., Van de Vyvere, L., Wang, H., et al. TDCOSMO 2025: Cosmological constraints from strong lensing time delays. *arXiv e-prints*, art. arXiv:2506.03023, 2025. doi: 10.48550/arXiv.2506.03023.

Tewes, M., Courbin, F., & Meylan, G. COSMOGRAIL: the COSmological MOnitoring of GRAvItational Lenses. XI. Techniques for time delay measurement in presence of microlensing. *Astronomy & Astrophysics*, 553:A120, 2013. doi: 10.1051/0004-6361/201220123.

Thorne, K. S. Disk-Accretion onto a Black Hole. II. Evolution of the Hole. *The Astrophysical Journal*, 191:507–520, 1974. doi: 10.1086/152991.

Tsapras, Y. Microlensing Searches for Exoplanets. *Geosciences*, 8(10):365, 2018. doi: 10.3390/geosciences8100365.

Udalski, A., Szymanski, M. K., Kubiak, M., Pietrzynski, G., Soszynski, I., Zebrun, K., Szewczyk, O., Wyrzykowski, L., Ulaczyk, K., & Wiêckowski, T. The Optical Gravitational Lensing Experiment. OGLE-III Long Term Monitoring of the Gravitational Lens QSO 2237+0305. *Acta Astronomica*, 56:293–305, 2006. doi: 10.48550/arXiv.astro-ph/0701300.

Urry, C. M. & Padovani, P. Unified Schemes for Radio-Loud Active Galactic Nuclei. *Publications of the Astronomical Society of the Pacific*, 107:803, 1995. doi: 10.1086/133630.

Vakulik, V., Schild, R., Dudinov, V., Nuritdinov, S., Tsvetkova, V., Burkhonov, O., & Akhunov, T. Observational determination of the time delays in gravitational lens system Q2237+0305. *Astronomy & Astrophysics*, 447(3):905–913, 2006. doi: 10.1051/0004-6361:20053574.

Vanden Berk, D. E., Wilhite, B. C., Kron, R. G., Anderson, S. F., Brunner, R. J., Hall, P. B., Ivezić, Ž., Richards, G. T., Schneider, D. P., York, D. G., Brinkmann, J. V., Lamb, D. Q., Nichol, R. C., & Schlegel, D. J. The Ensemble Photometric Variability of ~25,000 Quasars in the Sloan Digital Sky Survey. *The Astrophysical Journal*, 601(2):692–714, 2004. doi: 10.1086/380563.

Vanderriest, C., Schneider, J., Herpe, G., Chevreton, M., Moles, M., & Wlerick, G. The value of the time delay $\Delta T(A, B)$ for the "double" quasar 0957+561 from optical photometric monitoring. *Astronomy & Astrophysics*, 215:1–13, 1989. https://ui.adsabs.harvard.edu/abs/1989A&A...215....1V.

Vegetti, S., Birrer, S., Despali, G., Fassnacht, C. D., Gilman, D., Hezaveh, Y., Perreault Levasseur, L., McKean, J. P., Powell, D. M., O'Riordan, C. M., & Vernardos, G. Strong Gravitational Lensing as a Probe of Dark Matter. *Space Science Reviews*, 220(5):58, 2024. doi: 10.1007/s11214-024-01087-w.

Vernardos, G. & Fluke, C. J. A new parameter space study of cosmological microlensing. *Monthly Notices of the Royal Astronomical Society*, 434(1):832–847, 2013. doi: 10.1093/mnras/stt1076.

Vernardos, G. & Tsagkatakis, G. Quasar microlensing light-curve analysis using deep machine learning. *Monthly Notices of the Royal Astronomical Society*, 486(2):1944–1952, 2019. doi: 10.1093/mnras/stz868.

Vernardos, G., Fluke, C. J., Bate, N. F., & Croton, D. GERLUMPH Data Release 1: High-resolution Cosmological Microlensing Magnification Maps and eResearch Tools. *The Astrophysical Journal Supplement*, 211(1):16, 2014. doi: 10.1088/0067-0049/211/1/16.

Vernardos, G., Sluse, D., Pooley, D., Schmidt, R. W., Millon, M., Weisenbach, L., Motta, V., An-

guita, T., Saha, P., O'Dowd, M., Peel, A., & Schechter, P. L. Microlensing of Strongly Lensed Quasars. *Space Science Reviews*, 220(1):14, 2024. doi: 10.1007/s11214-024-01043-8.

Vuissoz, C., Courbin, F., Sluse, D., Meylan, G., Chantry, V., Eulaers, E., Morgan, C., Eyler, M. E., Kochanek, C. S., Coles, J., Saha, P., Magain, P., & Falco, E. E. COSMOGRAIL: the COSmological MOnitoring of GRAvItational Lenses. VII. Time delays and the Hubble constant from WFI J2033-4723. *Astronomy & Astrophysics*, 488(2):481–490, 2008. doi: 10.1051/0004-6361:200809866.

Walsh, D., Carswell, R. F., & Weymann, R. J. 0957+561 A, B: twin quasistellar objects or gravitational lens? *Nature*, 279:381–384, 1979. doi: 10.1038/279381a0.

Wambsganss, J. *Gravitational microlensing*. PhD thesis, Ludwig-Maximilians-Universität München, 1990.

Wambsganss, J. Gravitational lensing: numerical simulations with a hierarchical tree code. *Journal of Computational and Applied Mathematics*, 109(1):353–372, 1999. doi: 10.1016/S0377-0427(99)00164-8.

Wambsganss, J. & Kundić, T. Gravitational Microlensing by Random Motion of Stars: Analysis of Light Curves. *The Astrophysical Journal*, 450:19, 1995. doi: 10.1086/176114.

Wambsganss, J. & Paczynski, B. Expected Color Variations of the Gravitationally Microlensed QSO 2237+0305. *The Astronomical Journal*, 102:864, 1991. doi: 10.1086/115916.

Wambsganss, J. & Paczynski, B. Parameter Degeneracy in Models of the Quadruple Lens System Q2237+0305. *The Astronomical Journal*, 108:1156, 1994. doi: 10.1086/117144.

Wambsganss, J., Paczynski, B., & Schneider, P. Interpretation of the Microlensing Event in QSO 2237+0305. *The Astrophysical Journal Letters*, 358:L33, 1990. doi: 10.1086/185773.

Wambsganss, J., Schmidt, R. W., Colley, W., Kundić, T., & Turner, E. L. Microlensing results from APO monitoring of the double quasar Q0957+561A,B between 1995 and 1998. *Astronomy & Astrophysics*, 362:L37–L40, 2000. doi: 10.48550/arXiv.astro-ph/0010232.

Weisenbach, L. A GPU code for finding microlensing critical curves and caustics. *Monthly Notices of the Royal Astronomical Society*, 541(4):3341–3352, 2025a. doi: 10.1093/mnras/staf1202.

Weisenbach, L. Efficient generation of microlensing magnification maps with GPUs. *Monthly Notices of the Royal Astronomical Society*, 541(1):281–293, 2025b. doi: 10.1093/mnras/staf994.

Wisotzki, L., Koehler, T., Kayser, R., & Reimers, D. The new double QSO HE 1104-1805: gravitational lens with microlensing or binary quasar? *Astronomy & Astrophysics*, 278:L15–L18, 1993. https://ui.adsabs.harvard.edu/abs/1993A&A...278L..15W.

Wisotzki, L., Koehler, T., Lopez, S., & Reimers, D. Discovery of a new gravitationally lensed QSO with broad absorption lines. *Astronomy & Astrophysics*, 315:405–408, 1996. https://ui.adsabs.harvard.edu/abs/1996A&A...315L.405W.

Wisotzki, L., Schechter, P. L., Bradt, H. V., Heinmüller, J., & Reimers, D. HE 0435-1223: A wide separation quadruple QSO and gravitational lens. *Astronomy & Astrophysics*, 395:17–23, 2002. doi: 10.1051/0004-6361:20021213.

Wisotzki, L., Schechter, P. L., Chen, H. W., Richstone, D., Jahnke, K., Sánchez, S. F., & Reimers,

D. HE 0047-1756: A new gravitationally lensed double QSO. *Astronomy & Astrophysics*, 419: L31–L34, 2004. doi: 10.1051/0004-6361:20040131.

Witt, H. J. Investigation of high amplification events in light curves of gravitationally lensed quasars. *Astronomy & Astrophysics*, 236:311, 1990. https://ui.adsabs.harvard.edu/abs/1990A&A...236..311W.

Woźniak, P. R., Alard, C., Udalski, A., Szymański, M., Kubiak, M., Pietrzyński, G., & Zebruń, K. The Optical Gravitational Lensing Experiment Monitoring of QSO 2237+0305. *The Astrophysical Journal*, 529(1):88–92, 2000a. doi: 10.1086/308258.

Woźniak, P. R., Udalski, A., Szymański, M., Kubiak, M., Pietrzyński, G., Soszyński, I., & Żebruń, K. The Optical Gravitational Lensing Experiment: A Hunt for Caustic Crossings in QSO 2237+0305. *The Astrophysical Journal Letters*, 540(2):L65–L67, 2000b. doi: 10.1086/312874.

Wyithe, J. S. B. & Turner, E. L. Determining the microlens mass function from quasar microlensing statistics. *Monthly Notices of the Royal Astronomical Society*, 320(1):21–30, 2001. doi: 10.1046/j.1365-8711.2001.03917.x.

Wyithe, J. S. B., Webster, R. L., & Turner, E. L. Limits on the microlens mass function of Q2237+0305. *Monthly Notices of the Royal Astronomical Society*, 315(1):51–61, 2000. doi: 10.1046/j.1365-8711.2000.03360.x.

Xu, D., Sluse, D., Gao, L., Wang, J., Frenk, C., Mao, S., Schneider, P., & Springel, V. How well can cold dark matter substructures account for the observed radio flux-ratio anomalies. *Monthly Notices of the Royal Astronomical Society*, 447(4):3189–3206, 2015. doi: 10.1093/mnras/stu2673.

Yonehara, A., Hirashita, H., & Richter, P. Origin of chromatic features in multiple quasars. Variability, dust, or microlensing. *Astronomy & Astrophysics*, 478(1):95–109, 2008. doi: 10.1051/0004-6361:20067014.

Zimmer, F., Schmidt, R. W., & Wambsganss, J. X-ray microlensing in the quadruply lensed quasar Q2237+0305. *Monthly Notices of the Royal Astronomical Society*, 413(2):1099–1106, 2011. doi: 10.1111/j.1365-2966.2011.18196.x.

Zwicky, F. Nebulae as Gravitational Lenses. *Physical Review*, 51(4):290–290, 1937a. doi: 10.1103/PhysRev.51.290.

Zwicky, F. On the Probability of Detecting Nebulae Which Act as Gravitational Lenses. *Physical Review*, 51(8):679–679, 1937b. doi: 10.1103/PhysRev.51.679.

Acknowledgments

First and foremost, I would like to thank Joachim Wambsganß, for giving me the opportunity to join his microlensing-team at ARI and work on this fascinating project. You were an amazing supervisor – scientifically and personally – and I am grateful for your support, shared advice and just in general, for the last four and a half years.

To Robert Schmidt I owe my deepest gratitude – I simply would not have managed it without you. Thank you for always having an open door, helping me, discussing and working on the science (plus some fun little side projects) with me, solving exercises from our physics tutorials on your white board, and teaching me not only about quasar microlensing, but also on various aspects – astronomical, but also historical as well as cultural – of our calendar. Finally, thank you for proof-reading this thesis, even though I did not give you much time at the end.

I would also like to thank all other members of the ARI microlensing group for their helpful advice and a supportive environment, especially to Markus Hundertmark, as well as Clément Ranc, David Kuhlbrodt, Yiannis Tsapras, Zofia Kaczmarek and the whole extended lunch group, including Jon Juaristi Campillo and many more, with whom all I shared memorable breaks e.g. discussing the accuracy of the food scale in the cafeteria.

Next, thank you to everyone on the second floor of the institute for the positive atmosphere, support and great conversations, especially to Anna Pasquali, Geneviève Parmentier, Hildrun Pisch-Papendick and Saskia Mayer, as well as everyone else at ARI. A special thanks goes to all my office mates with whom I shared our room at the end of the floor – most importantly to Pietro Facchini. Thanks for laughing with me, teaching me a few very important words in italian, and for being a friend.

I am grateful to Christian Fendt for agreeing to referee this thesis and I also thank Sabine Reffert and Werner Aeschbach for being my additional examiners.

Finally, this work would not have been possible without the constant support of my friends and family:

Daher zunächst vielen Dank an Veronika und Maximilian, die ich das große Glück hatte schon in der ersten Woche des Physikstudiums kennengelernt zu haben. Ich bin dankbar für eure Freundschaft und Unterstützung in all den Jahren, insbesondere auch jetzt aus der Ferne. Ich werde immer mit Freude an unsere gemeinsame Stu-

dienzeit zurückblicken (an Zettel rechnen, Spieleabende verbringen und natürlich an *die* Toffifeetorte) und freue mich schon auf unser nächstes Treffen!

"Ohne Musik wäre das Leben ein Irrtum" schrieb einst Friedrich Nietzsche, einem Satz dem ich aus voller Überzeugung nur zustimmen kann. Daher danke ich meinen langjährigen Freundinnen und Freunden aus Orchester und Chor – Martin, Sophie und vielen mehr – die durch unsere gemeinsame Musik mein Leben in Heidelberg seit Beginn des Studiums unermesslich bereichert haben. Ohne euch (und Bach, Brahms, Mahler, ...) hätte ich es ganz sicher nicht geschafft.

Ein besonderer Dank gebührt meiner Familie, meinem Bruder Niels, auf dessen Doktorarbeit in Detektorphysik ich schon sehr gespannt bin, und meinen Eltern Annette und Matthias, die mich letztendlich in vielerlei Hinsicht auf den Weg geführt haben auf dem ich heute bin.

Zu guter Letzt möchte ich meiner Freundin Melanie danken. Ohne deine Liebe und Unterstützung, Antrieb und Motivation, sowie deine ansteckende Freude und Begeisterung, wäre diese Doktorarbeit (und vieles mehr) nicht möglich gewesen. Ich bin sehr dankbar dich in meinem Leben zu haben.

This thesis was typeset using LaTeX
Final version as of 17. November 2025